Doctoral Dissertation
Doctoral Program in Materials Science and Technology (35th Cycle)

Development of multifunctional biomaterials for the treatment of pelvis osteoporotic fractures

By

Mattia Pagani

******

Supervisors:
Prof. Sonia Fiorilli, Supervisor
Prof. Chiara Vitale-Brovarone, Co-Supervisor

Doctoral Examination Committee:
Prof. Valeria Cannillo, Referee, Università di Modena e Reggio Emilia
Prof. Isabel Izquierdo Barba, Referee, Universidad Complutense de Madrid

Politecnico di Torino
2023

Declaration

I hereby declare that the contents and organization of this dissertation constitute my own original work and do not compromise in any way the rights of third parties, including those relating to the security of personal data.

Mattia Pagani

2023

* This dissertation is presented in fulfillment of the requirements for **Ph.D. degree** in the Graduate School of Politecnico di Torino (ScuDo).

Acknowledgment

I would like to acknowledge all the people who helped and supported in this research work. In particular, I would like to thank Prof. Sonia Fiorilli and Prof. Chiara Vitale Brovarone along with all the IRIS group of the Department of Applied Science and Technology - Politecnico di Torino.

Moreover, part of this PhD experimental work was carried out in collaboration with other research groups, as reported in detail in the thesis, which I would like to thank:

- NOVAICOS s.r.l.s, Via Amico Canobio 4/6, 28100 Novara, Italy – Dr. Casimiro Luca Gigliotti and Dr. Elena Boggio

- Department of Health Sciences, Università del Piemonte Orientale, Via Solaroli 17, 28100 Novara, Italy – Prof. Umberto Dianzani

- FLUIDINOVA, S.A., Maia, Portugal, Rua Engenheiro Frederico Ulrich, 2650, 4470-605 Moreira Da Maia, Portugal – Eng. António Azevedo, Dr. Paulo Quadros, and Dr. Catarina Coelho

Summary

The bone tissue regeneration induced by biomimetic biomaterials is a very promising and alternative method to treat the fractures caused by a trauma or disease such as osteoporosis compared to the clinical methods normally adopted. The overall goal is the design of nanostructured bioactive scaffolds that are able to reproduce the morphology and physiological features of the native tissue to guide the cells during the regeneration process. In this scenario, collagen-based scaffolds represent a promising tool to mimic the physico-chemical and nano-structural characteristics of bone extracellular matrix (ECM), moreover, the electrospinning (ESP) process can support the design of complex structures with the final shape and porosity similar to the ECM. Moreover, also mesoporous bioactive glasses (MBGs) or nano-hydroxyapatite (nano-HA) can be combined with collagen for the production of multifunctional therapeutic scaffolds; in particular, MBGs have high exposed surface area and pore volume that can be exploited for a surface grafting of different biomolecules, and both MBGs and nano-HA composition can be enriched by the incorporation of therapeutic elements (i.e., Sr). However, ESP require a complex optimization of biomaterial formulations to preserve its high biocompatibility without the loss of the native protein structure.

In this context, the research activities conducted during this PhD, were focused on the design of collagen-based constructs for bone tissue engineering, starting from the development of Sr containing MBGs grafted with a biomolecule to reversibly inhibit osteoclast activity (ICOS-Fc), followed by the optimization and characterization of the material formulations for the ESP process and the most suitable crosslinking strategy.

Concerning MBGs, two synthesis routes were selected for their production with a binary composition based on SiO_2 and CaO enriched with Sr therapeutic ions, a base-catalyzed sol-gel method and an aerosol assisted spray-drying approach. These two syntheses allowed to produce nano-sized particles and micro-sized particles, respectively, with different characteristics. Then MBGs

surface were functionalized with amino groups, and the subsequent grafting of ICOS-Fc was performed with a coupling method to link carboxyl groups of ICOS-Fc to the amino groups of MBGs, in order to obtain a multifunctional material that can reversibly and specifically inhibit only the osteoclasts migration and differentiation.

Then, the application of type I collagen was explored for the design of biomimetic scaffolds using the ESP technology, where different collagen concentrations and process parameters were indagated focalizing in particular on the preservation of the protein structure. Subsequently, MBGs or nano-HA were combined with the optimized solutions, and electrospun to obtain collagen-based constructs with a nano-fibrous morphology and a well dispersed inorganic phase. The effect of the acidic solvent used during the ESP on the grafted ICOS-Fc activity was also studied, resulting in a significant loss of activity only for nanoparticles. Finally, different chemical crosslinking methods were investigated to enhance the mechanical properties of the collagen-based membranes: an N-(3-Dimethylaminopropyl)-N′-ethylcarbodiimide (EDC)/ N-Hydroxysuccinimide (NHS) coupling and a crosslinking with a photoinitiator (Rose Bengal), in order to link the carboxyl and amino groups present in the collagen chains.

Table of contents

List of Figures

List of Tables

Thesis goals

Bone tissue, after a fracture generally fully regenerate in 6-8 weeks, under normal healing conditions[1], however, even if bone shows excellent regenerative activity, 10-15% of fractures results in an unsuccessful healing with a delay or in some cases also a non-union fracture[2]. In addition, there are some risk factors such as aging and the related bone pathologies that increase the possibility of the unsuccessful bone healing and, consequently, with the increasing of elderly people, also the number of delayed or non-union fracture is expected to affect more patients in the next future. These impaired healing outcomes are still a critical clinical challenge in particular due to the patient clinical situation such as age or osteoporosis, even if recent advancements in terms of biomaterials and surgical strategies for the treatment of these types of fractures and the support of the of the bone regeneration in compromised situations were studied[3–5].

In the last decades, many biomaterials have been studied and developed in order to repair the damaged bone tissue or for the replacement of the tissue, with the aim to overcome the clinical challenges associated to the compromised bone healing. One of these types of biomaterials includes the bioactive ceramics widely used for the excellent bioactivity for the ability to induce the formation of a hydroxyapatite layer very similar to the natural bone component, that form a chemical bonding between the bone tissues and the biomaterial[2]. The morphological and textural characteristics of the bioactive ceramics were studied and modified over the years, with the objective of improve the biological performances, also for the delivery of therapeutic agents in order to enhance the unsuccessful healing of the compromised bone tissue[1]. With this idea, the combination of the bioactivity of bioactive ceramics and the release of therapeutic agents to obtain specific biological effects is a key challenge to consider for the development of biomaterials[6].

Considering the natural composition of bone[7], the hydroxyapatite particles are often exploited in the bone tissue engineering, thanks to the ability to release calcium ions as dissolution product, moreover, in the hydroxyapatite particles therapeutic species such as Sr (similar to Ca) can be incorporated in order to obtain biological functions, in particular influence the osteoblast activity[8–10].

A considerable attention in this scenario is focused on mesoporous bioactive glasses (MBGs), that are used as multifunctional biomedical biomaterials since the proposal by Prof Zhao in 2004[11] and Prof. Vallet-Regí in 2006[12], these nano-structured bioactive glasses based on the composition SiO_2-CaO-P_2O_5 shows optimal textural properties characterized in terms of very high surface area and a regular porosity typical of silica based mesoporous materials. As for hydroxyapatite, also for MBGs, through the incorporation of specific therapeutic species, the composition of MBGs can be enriched in order to obtain different biological functions. Moreover, MBGs were used in the development of different variety of scaffold for the tissue engineering and in particular for bone regeneration due to their peculiar characteristics, in order to create scaffold with hierarchical porosity and enhanced biocompatibility and osteoconductivity[13], as well as nanocarriers thanks to the very accessible mesoporous structure and high surface area. In particular, in bone tissue regeneration conventional administration routes (i.e., injection or oral administration) are characterized by low therapeutic tissue levels and several side effects due to the non-efficient delivery to the pathological site[14]. Based on these issues, biomaterials were used to achieve a sustained drug release that enhances the delivery efficiency and maintaining the therapeutic dose over the time near the pathological site. For these reasons, the design of new systems able to exert multiple and combined effects to overcome the compromised bone healing is considered a critical issue[15]. However, some drawbacks have limited the practical use and the clinical translation of MBGs, in particular the difficulty of their administration at the pathological site in the powder form (i.e., in the bone fracture cavity), thus their combination with polymers has been widely explored to enlarge their clinical potential and to further reproduce the complex structure of bone at multiple scale levels.

For this purpose, type I collagen is a natural polymer that is present in the bone extracellular matrix; collagen has excellent biological properties due to the high density of amino acid sequences that positively influence the cells recognition and adhesion[16, 17]. However, the use of collagen in bone tissue engineering is highly limited by its low biomechanical properties[18–20], to overcome these problems, the stability of collagen can be improved after the use of different strategies of crosslinking[21].

Besides the different physico-chemical characteristics, a scaffold that mimic the architecture of the native bone at different scales may represent a promising tool in the bone tissue engineering for directing the bone tissue regeneration[16, 22]. One of the most used techniques to achieve this characteristic is the

electrospinning, this technique was typically used in order to process polymers due to the ability to design constructs that can mimic the submicrometric fibrous structure of the natural extracellular matrix[23–25]; moreover, the constructs obtained from this technique consist in flexible membranes that can be adapted to different zones, in particular in the pelvis zone. Nevertheless, several issues deriving from this technique consist in natural polymers processing (such as collagen) that should preserve the physico-chemical and structural characteristics of the native protein, and the reaching of high concentrations of inorganic phases.

In this scenario, the research conducted in this PhD was focused on the design and development of multifunctional biomimetic scaffolds able to reproduce the best native features and that can guide the healing and the restoration of the natural tissue balance in pelvis zones. Therefore, the use of type I collagen and the development of an inorganic phase (MBGs) with both pro-osteogenic and anti-osteoclastogenic effects were explored.

Most of the research activities were conducted in the frame of the GIOTTO European Project (Active aGeIng and Osteoporosis: The next challenge for smarT nanobiOmaterials and 3D technologies; NMBP-22-2018, GA 814410) aimed at designing biomimetic scaffolds for osteoporotic fractures, also able to provide biochemical and structural stimuli to rebalance the osteoblast and osteoclast activities in the case of osteoporosis.

In particular, the first aim of this PhD thesis was to produce MBGs particles with a binary composition (based on SiO_2 and CaO) with therapeutic ions incorporated into the silica framework and grafted with a biomolecule able to reversibly inhibit the osteoclasts activity. To this purpose, the Sr type of therapeutic ions and the amount added during the synthesis were selected by following the idea to exert pro-osteogenic effects, since Sr ions are well-known for their pro-osteogenic properties[26, 27]. Moreover, two types of particles production were explored to obtain nano- and micro-sized samples with different morphology, size, and structural features since and, since the method to obtain the microparticles is a process that can be easily scalable, I traveled to Porto, Portugal to perform trials to scaling-up this type of synthesis in collaboration with FLUIDINOVA company (a partner involved in the GIOTTO project) by using the industrial spray drier located in FLUIDINOVA facility. In the second step, the grafting of ICOS-Fc biomolecule (a recombinant molecule developed by NOVAICOS company[28], a partner involved in the GIOTTO project) was explored in order to enrich the therapeutic potential of the MBGs and to obtain a

synergistic effect (results reported in chapter 3). ICOS is a T-cell co-stimulatory surface receptor is normally expressed in T cells that can bind its ligand (ICOSL) expressed by several type of cells including osteoclasts, the bond between ICOS and ICOSL is also involved in the bone turnover and the administration of the soluble form of recombinant ICOS (ICOS-Fc) proved to reversibly inhibit the human osteoclast activity *in vitro* and *in vivo* in mice can inhibit the development of experimental osteoporosis[29]. The grafting of ICOS-Fc was carried out in two steps: first, an amino modification of the MBGs surface was performed by exploiting the numerous silanol groups present, while in the second step, the grafting was performed by using a carbodiimide-mediated coupling reaction to link the amino groups on MBGs surface and the carboxyl groups of ICOS-Fc molecule; moreover, since the carboxyl groups are present only in the Fc domain of ICOS-Fc[28], this approach also allows a right orientation of ICOS-Fc when grafted on MBGs surface. The biological evaluation of the obtained samples was carried out in collaboration with NOVAICOS company.

The second goal consisted in the fabrication of fibrous collagen-based constructs enriched with an inorganic phase: strontium containing nano-hydroxyapatite (Sr-nano-HA) provided by FLUIDINOVA company or the Sr containing MBGs grafted with ICOS-Fc (MBGs-Sr-ICOS-Fc). To achieve this aim, the first step consisted in testing different protein concentration in the solvent, an acetic acid solution selected as greener solvent compared to other solvents generally used for the electrospinning process, to obtain a fibrous membrane with the right feature to mimic the extracellular matrix. The preservation of the physicochemical and structural properties of the protein, alongside the morphological features of the resulting scaffolds were investigated. Then, the second goal was the incorporation of the inorganic phase in the constructs; this goal was achieved by suspending the inorganic phase in the collagen solution prior to the electrospinning at different concentration in order to study the best concentration that can be electrospun to obtain a scaffold with a good morphology of collagen fibers and with a well dispersed inorganic phase.

Finally, in order to improve the stability and the properties of the collagen constructs, two different chemical crosslinking methods were explored. In details, the crosslinking with 1-ethyl-3-(3-dimethylaminopropyl) carbodiimide-hydrochloride (EDC) and N-hydroxysuccinimide (NHS) and the chemical crosslinking using a photoinitiator called Rose Bengal (RB) were investigated. The EDC/NHS coupling is a “zero length” crosslinking that can connect amino groups with carboxyl groups in order to form amide groups; while RB is a

photoinitiator already used in clinical applications, even if the exact mechanism involved in the crosslinking with RB remains to be clarified[30], a possible mechanism where amide groups were formed is reported in literature[31]. The related results of the scaffold design and production are reported in chapter 4.

Chapter 1

State of the art

1.1 Introduction

In this PhD research work was developed a collagen-based scaffold for stimulating and supporting bone tissue regeneration in pelvis osteoporotic fractures. The developed is required to be flexible, in order to fit in the pelvis zone, and to stimulate the bone tissue regeneration and the restoration of the natural tissue balance through the combination of the following biomaterials: type I collagen, mesoporous bioactive glasses (MBGs) and strontium substituted nano-hydroxyapatite (Sr-nano-HA). Moreover, in addition to these materials, the ICOS-Fc biomolecule was exploited for its anti-osteoclastogenic effect.

In this chapter a brief overview of the fracture healing process and the osteoporosis disease is reported, as well as the limitations of the current but not very effective treatments available for osteoporotic fractures. Moreover, a more detailed overview of the various biomaterials used in this thesis for the treatment of osteoporotic fractures is reported, in particular the natural polymer type I collagen, hydroxyapatite, and bioactive glasses were detailed in sections 1.5.3, 1.5.4 and 1.5.5, respectively. Finally, the electrospinning methods of collagen and collagen with inorganic phases and its open issues were described as well, also focusing on crosslinking methods to improve the membrane properties in section 1.6.

1.2 Bone fracture healing process and osteoporosis disease

Bone is a tissue with the intrinsic capacity to self-regenerate and self-repair after suffering an injury[32], moreover, during the skeletal development and throughout the adult life this tissue undergoes a continuous remodeling[33]. Bone regeneration comprehend many biological events involving different types of cells and intracellular and extracellular signaling pathways[34, 35]. The bone fracture healing can be classified into primary and secondary healing[32], where primary healing occurs in total absence of motion and consequently fractured bone should be fixed, and in secondary healing there is a limited motion in the site promoting a formation of a callus leading an internal immobilization of the fractured bone[32, 36]. Bone healing process is divided in three overlapping phases: inflammatory phase where there is an influx of primitive mesenchymal stem cells (MSCs) into the fracture site, reparative phase in which MSCs differentiate into fibroblast, chondrocytes and osteoblasts and start the ossification and the formation of hard and soft callus then replaced with woven bone; finally, the last phase called remodeling phase involves the substitution of the woven bone with lamellar bone by osteoblasts and osteoclasts and can last up several years[32].

Despite the intrinsic self-healing properties, under normal conditions 10-15% of fractures manifest delay or non-union situations[1, 2, 32] and, additionally, with the increase of elderly people and the related pathological conditions the number of unsuccessful healing phases is expected to rise in the future[37]. One of the most known of this type of pathological conditions is osteoporosis, defined as a skeletal disorder in which a compromised bone strength causes an increased risk of fracture[38], that generally increase steeply with the age of the patient (in fact, most of the people affected by osteoporosis are over 75[39, 40]). The World Health Organization (WHO) defined osteoporosis on the basis of bone mineral density (BMD) measurements obtained on dual energy X-ray absorptiometry when the standard deviations result 2.5 or more below the normal peak bone mass[41, 42]. People affected by osteoporosis show a low bone mineral density and microarchitectural deterioration of the bone tissue[37, 42, 43]**,** this condition occurs when there is an altered balance between osteoblast bone formation and osteoclast bone resorption leading a net loss of bone, as opposed to the normal conditions where the amount of bone lost is the same of the bone formed[37]. Moreover, the causes of this disease can be categorized into primary causes further subdivided into Type I associated with menopause or estrogen deficiency and Type II that are age-related or senile osteoporosis, and secondary causes including medications, chronic renal disease, endochrine, hematopoietic,

connective tissue and nutrition and gastrointestinal disorders, immobilization, and inflammatory arthropathy[42]. In addition, there are several osteoporosis risk factors categorized by the National Osteoporosis Foundation into nonmodifiable risk factors including personal and first-degree relative history of fractures, Caucasian race, advanced age, female gender, dementia, and poor health or frailty; and potentially modifiable including the lifestyle in general (smoking, alcoholism, recurrent falls, inadequate physical activity, and low life-long calcium intake) and other risk such as low body weight, estrogen deficiency, and early menopause[42]. This disease leads to several consequences of people affected in particular the pain, physical limitations, lifestyle and skeletal changes, if untreated, that cause also psychologic effects like depression, social isolation and low self-esteem[44–46]; an example are vertebral fractures that leads to an increased thoracic kyphosis and decreased size of the thoracic and abdominal cavities[42].

Additionally, osteoporosis can also be associated with an increased morbidity and mortality[41], as demonstrated Kado et al. where the age adjusted mortality rate in women with one vertebral fracture was increased to 1.23x and with five or more wertebral fractures to 2.3x[47]. Moreover, osteoporosis disease entails also a high economic burden worldwide due to both direct and indirect costs[38].

1.3 Current treatments of osteoporosis and their limitations

Nowadays, the effects of osteoporosis can be prevented with non-pharmacologic treatments such as maintenance of an adequate dietary calcium intake and normal vitamin D status, balance and exercise training, posture training supports, and hip protectors; or treated with pharmacological interventions[41, 42]. Some pharmacological interventions include the administration of bisphosphonates, the most potent class of drugs in the prevention and treatment of osteoporosis that are pyrophosphate analogues which strongly bind the hydroxyapatite of bone inhibiting osteoclast activity; calcitonin that increases the BMD decreasing the vertebral fracture risk; strontium ranelate that reduces vertebral and non-vertebral fractures including hip fractures in postmenopausal women with osteoporosis; and parathyroid hormone that increase bone resorption and formation increasing the BMD and enhancing the bone architecture and integrity[41, 42]. Neer et al. showed that the administration of the parathyroid hormone in postmenopausal women with vertebra fractures resulted in an increase of 10% and 2.8% in lumbar and hip spine BMD, respectively, decreasing the risk of new vertebra fractures of

65% and non-vertebra fractures of 54% even if only after a 10-months treatment[48]. Unfortunately, despite the number of effective drugs to treat osteoporosis is increasing, they present some limitations. The two most important limitations are the associated side-effects and the decrease of the long-term efficacy; the side effects concern in particular the risk of atypical femur fractures and the osteonecrosis of the jaw, even if they are extremely rare and associated only with the use of bisphosphonates, in addition the risk of side-effects increases with duration of the therapy influencing the long-term efficacy of the treatment[49].

1.4 Surgical solutions for osteoporotic fractures

The well-orchestrated bone healing process resulted to be impaired in the osteoporotic bone such as the delayed expression of estrogen receptor during the healing that correlated to impairment in callus formation capacity; angiogenesis and vasculogenesis during the early to mid-phase of healing; the capacity of extracellular matrix (ECM) production and callus formation; and in particular the cell recruitment, differentiation, and proliferation during the early phase of fracture healing[50]. All these defects in the osteoporotic bone led difficulty to regenerate the bone tissue after an injury, thus, due to the current limitations of the pharmacological interventions, the design and development of new strategies to enhance the bone tissue regeneration in osteoporotic fractures are strongly needed. Moreover, generally the treatments for osteoporotic fractures occur after the injury, and are ineffective or not very effective especially in some zones like the pelvis fractures; in fact, the absence of optimal solutions, due to the difficult location of intervention, currently treated only by invasive surgery and bed rest, results to an urgency to develop ad hoc devices and personalized treatments that can be specifically adapted for the positioning in these fracture types, such as flexible devices that fit in this zone, and capable to stimulate the tissue regeneration by different and specific combined effects promoting the restoration of the natural tissue balance.

Generally, pelvis fractures can be treated in two methods based of the type of fracture derived by Fragility Fracture of the Pelvis (FFP)[51]. Isolated anterior pelvic ring fractures (FFP type I fractures) are stable, thus can be treated conservatively and with the use of analgesic, also nondisplaced fracture of the posterior pelvic ring (FFP type II fractures) can be treated conservatively but render the patient immobile for long periods, and finally, fractures characterized by a marked unilateral or bilateral instability of the posterior pelvic ring (FFP type

III and IV fractures) rarely heal spontaneously and surgical treatment using screws and plates is necessary[51, 52] (Figure 1.1). However, as mentioned above, these methods comport invasive surgery and patient immobility for long periods.

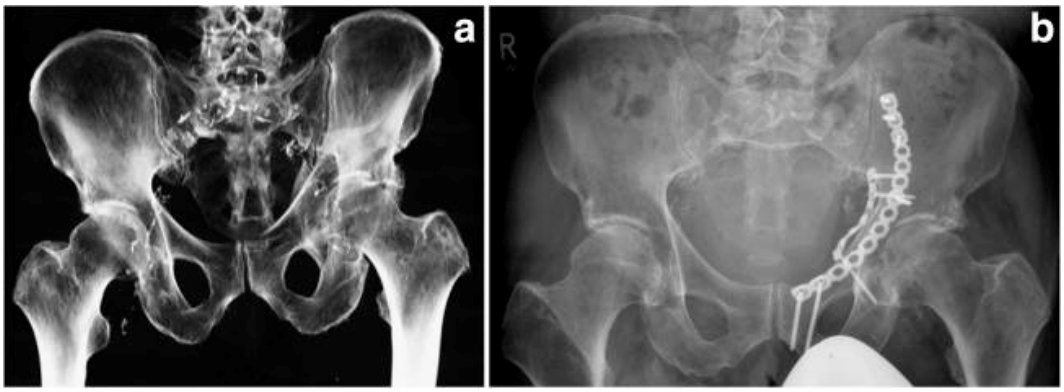

Figure 1.1:Surgical fixation of a pelvis fracture[52].

Moreover, due to the low number of possibilities for the treatment of pelvis fractures and the deleterious effects from osteoporosis disease, a device should help the healing of the osteoporotic bone fracture to achieve a diminution of the immobilization time of the patient. In order to face this unmet clinical gap and to overcome the different issues previously described such as the prolonged regeneration time or the total inhibition of the bone regeneration after the fractures in patients affected by clinical pathologies (i.e., osteoporosis), or the adaptation of the scaffold in the pelvic zone, the development of a new typology of scaffold is necessary. In this context, the tissue engineering is a discipline which exploit a combination of cells, materials, methods, and both biochemical and physicochemical factors in order to improve, restore, or replace different types of biological tissues. Therefore, this scientific area involves the use of these material combinations in the repairment or replacement of portions of tissues. Moreover, the tissues involved require different mechanical and structural properties; in fact, by exploiting the different biological, mechanical and structural properties, materials and methods of production were used to fabricate multifunctional scaffolds able to achieve different function for the repair or replacement of the tissue.

In this thesis work, a scaffold to treat pelvis osteoporotic fractures was designed and developed exploiting different natural and inorganic materials, and methods to obtain a thin and flexible membrane in order to better fit to the pelvis bone location.

1.5 Biomaterials for the bone tissue engineering

Since osteoporotic fractures does not heal due to the poor regeneration capacity of the affected bone and their number are increasing in fragile patients, this disease is the major source of both morbidity and cost of fractures especially in elderly people[53]. Consequently, the design and development of new types of scaffolds able to facilitate the bone healing and the restoration of the natural tissue balance is a critical issue. Many materials and solutions are investigated for the development of these types of scaffolds in order to improve the life of patients, such as bone grafts, biomaterials including metallic biomaterials, polymers, and ceramic biomaterials, as well as different fabrication techniques are examined.

1.5.1 Bone grafts

A common surgical method in order to improve bone regeneration in orthopedic practice is bone grafting[54, 55]. However, this method shows some issues based on the type of grafts; specifically, in autografts in which bone tissue from another part of the patient's own body is taken and integrated into the host bone rapidly and completely in terms of revascularization and remodeling[56], in order to promote bone regeneration, a problem is encountered in case of the donor site morbidity (such as in osteoporotic fractures) with some several problematics that can prevent the final successful outcome, moreover, large vessels or visceral lesions may occur when the bone tissue was taken from other parts of the body.

Instead, in allografts the bone tissue derives from a donor and in this case, there are significant risks due to immune reactions and infection carrying, moreover, the bone grafted is low osteoinductive and has no bone cells because it is devitalized and irradiated or freeze-dried, and finally, there is a restricted donor supply.

Finally, xenografts consist in taking bone tissue from a different species than the recipient, but also this method can cause immune reaction besides a rare risk of transmission of zoonotic diseases[54, 55].

1.5.2 Biomaterials

Biomaterials can limit the use of bone grafts by engineered scaffolds created exploiting the tissue engineering approach. Biomaterial scaffolds placed in the injured site can stimulate bone fracture healing and ensure certain recovery of the natural potential of repair, remodeling, and self-regeneration of the bone tissue[4,

5], moreover, a biomaterial scaffold should also have the properties to be osteoinductive by stimulating of the immature cells (MSCs) to differentiate into preosteoblasts and finally in osteoblasts, osteoconductive to easily integrate with the adjacent bone tissue, and osteointegrative for direct structural and functional integration between bone cells of the host and the scaffold[55, 57]. To assure these effects, scaffolds should be engineered with specific and multifunctional features[5], including biocompatibility, appropriate mechanical properties and architecture to promote the diffusion of both nutrients and waste products as well as cellular penetration, and finally should be bioresorbable and act as delivery of bioactive agents (Figure 1.2).

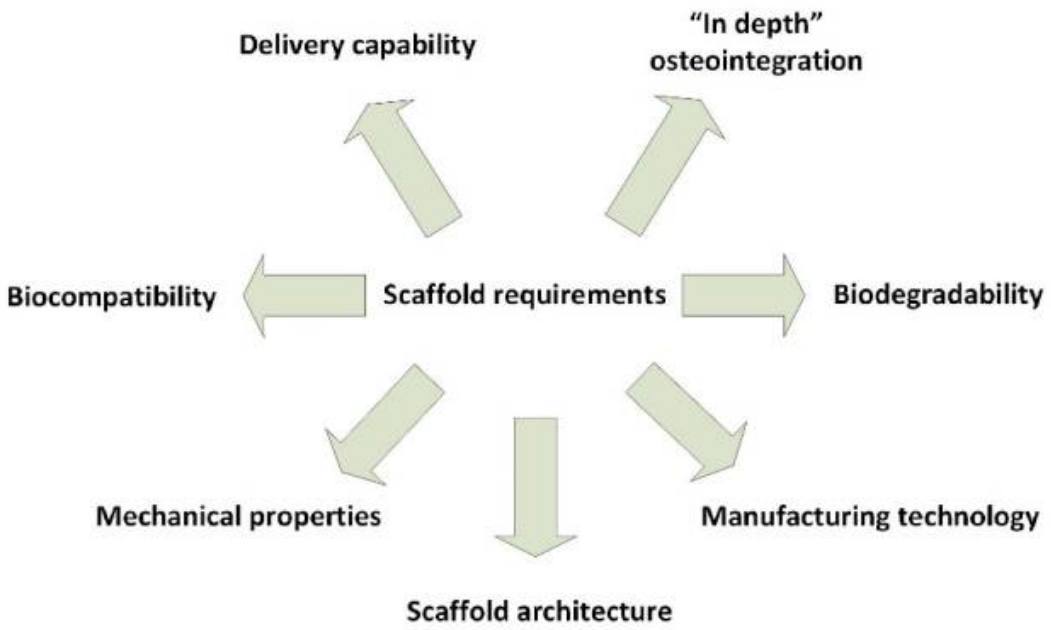

Figure 1.2: Requirements of a biomaterial scaffold[54].

The biocompatibility enables the biomaterial scaffold to reduce the immune reaction that can lead a reduced healing or cause rejection by the body; to achieves this requirement cells should adhere to the biomaterial scaffold surface, as well as migrate through the scaffold and proliferate. A biodegradable scaffold is necessary to let the space to the new native bone tissue formed, with the rate of degradation that shall be not too fast because this would hinder bone tissue regeneration and repair with the consequent scar formation, in addition, the degradation rate of the scaffold should not be too prolonged to avoid a suppression of extracellular matrix production and cell proliferation. The appropriate scaffold mechanical properties, such as the shear stresses (the ratios of

the loaded parallel forces divided by the same face area) that physiological are usually in the range of thousands of Pa, the strain (the fractional change in length of a loaded body) commonly measured in microstrain and with a physiological value usually ranging between 1500 and 3000 microstrain, the Young's modulus which represents the ratio between the stress applied and the strain occurring to a sample with a value between 15 and 25 GPa, and the Poisson's ratio (the negative ratio of the transverse strain component to the longitudinal strain component) that for bone it is usually between 0.1 and 0.33[58], need to operate from the implantation until the completion of the formation of new bone tissue. The final mechanical competence and the porous architecture should be balanced to allow the cell infiltration and the vascularization, in fact, the architectural features of the biomaterial scaffold play an essential role in osteoinduction; for example, the controlled porous microstructure and the high porous interconnectivity facilitate the penetration, proliferation, and differentiation of cells and, in particular, the two most important parameters of the porous microstructure are the pore size and the interconnective porosity, with pores that must be in the range of 50 μm to a maximum of 150 μm for the tissue ingrowth (large enough to allow the cells to penetrate inside but not too large to lose mechanical properties) and with a porosity ranging between 50% and 90%[54]. The interconnection between pores helps the loading of cells into the biomaterial scaffold due to the large internal surface area; and an adequate pores interconnection permits the diffusion of oxygen, metabolites, and growth factors, and also the waste products of the cells as well as the biomaterial can be diffused better out of the scaffold[54]. Biomaterial scaffolds should also have a delivery capability due to the release of biologically active agents that can induce different properties such as faster healing[59, 60]; and finally, another important aspect of biomaterial scaffolds to consider is the manufacturing technology used to its production that must be of low cost-effective production and with the scale-up of the material production process easily feasible from laboratory scale to industrial scale in order to be clinically and commercially viable[54, 61]. To achieve all these features in a scaffold, different biomaterials can be chosen for the fabrication, based on the characteristics each of them.

Biomaterials can be classified in three different classes based of the type of material: metal, polymers which can be further classified into natural or synthetic polymers[54], and ceramics (Figure 1.3).

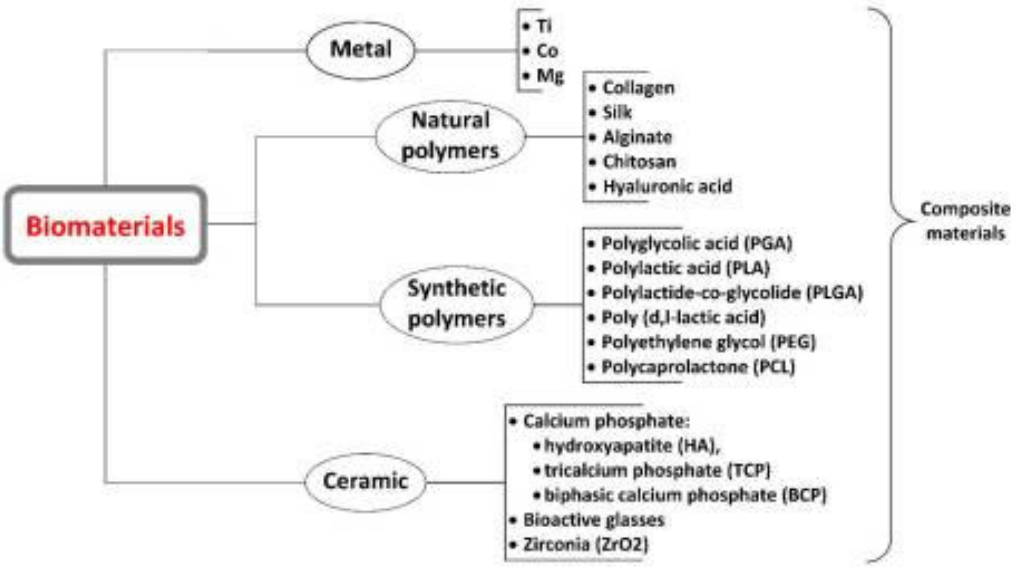

Figure 1.3: Different classes of biomaterials[54].

Metallic biomaterials

Metallic scaffolds comprise a long story of use in the field of bone repair, such as stainless steel, titanium-alloy, aluminium, and silver because they show excellent mechanical properties, either in strength and fatigue resistance besides the ability to rehabilitate the load-bearing bone defects, although they are non-degradable and require a secondary surgery for their removal or they remain in situ for the entire lifespan of the implant[55]. However, there are also several biodegradable metals with similar mechanical properties to the bone tissue, and in addition, the release of metallic ions could enhance the regeneration of the tissue[62]. For example, iron has excellent mechanical properties but also a very slow rate of biodegradation in vivo[63]; contrastingly, magnesium has more ductile properties, similar to bone, but a fast degradation rate as was found in a scaffold produced by Cheng et al.[64]. Anyway, metals can be enriched with ions like strontium or calcium to adapt the mechanical and corrosive properties and gain bone regeneration properties[65, 66].

Polymers

Natural polymers show a low immunological potential and bioactive behaviour[67]. There are many polymers investigated for bone tissue engineering, including polymers naturally presents in humans such as collagen, fibrin, and elastin but also other natural polymers like silk, chitosan, and alginate. Collagen is

the most present component of the ECM and provides structural and mechanical support for the cells, this polymer is principally extracted from animal sources and processed into hydrogels, foams, or fibers to mimic the native ECM; collagen is one of the most used biomaterials for its fast biodegradability, poor antigenicity, very good biocompatibility, and cell adhesion. Collagen scaffolds also showed the potential to induce vascularization[68–70], but on the other hand, collagen has poor elasticity and poor mechanical strength, and in fact collagen scaffolds require the adoption of methods for improve the mechanical properties such as crosslinking or blending with other polymers[71, 72].

Among the natural polymers, silk is highly used in the field of biomaterials because it can easily absorb and release water, has an excellent mechanical strength and it is resistant to UV and oxidation; silk is also highly processable (can be used to fabricate sponges, films, hydrogels, and mats), and many characteristics can be controlled via its crystallinity such as its mechanical strength and degradation rate[55]. Moreover, the structure of the silk presents a protein called sericin that must be removed in a process to avoid immunological responses[55]. Ribeiro et al. developed a composite hydrogel consisting of silk fibroin and nano-hydroxyapatite (a mineral component of the natural bone tissue with a chemical composition of $Ca^{2+}_{10}(OH^{-})_2(PO_4^{3-})_6$) with the inorganic particles uniformly dispersed within the silk fibroin matrix showing macro and microporous interconnected pores, this composite silk/nano-hydroxyapatite hydrogel showed a decrease in swelling properties and an increase in the compression modulus. Moreover, the authors demonstrate that the incorporation of nano-hydroxyapatite in the silk fibroin matrix improves the cellular metabolic and alkaline phosphatase (ALP) activities, resulting as a promising material for bone tissue engineering[73]. Instead, Li et al. studied properties of the silk fibroin-based nanofibrous scaffold produced by electrospinning incorporated with the growth factor bone morphogenetic protein 2 (BMP-2) and/or nano-hydroxyapatite, observing a significant enhance in the bone formation based on measures of mineralization and transcripts for the genes involved in the osteogenesis[74]. Finally, Mobini et al. developed a novel 3D composite scaffold with silk fibers embedded in a porous fibroin matrix prepared by freeze-drying improving the compressive moduli and stress, in addition this scaffold resulted to support attachment, proliferation and osteogenic differentiation of human mesenchymal stem cells[75].

Chitosan is a polymer extracted from chitin, a natural polymer found in invertebrates, it has antibacterial and biodegradable properties, and is biocompatible; importantly, biodegradation rate of the chitosan is inversely

related to the polymer crystallinity that is strongly dependent to the deacetylation degree: when the degree of acetylation is 0% or 100% the crystallinity reaches the maximum, in contrast when the deacetylation degree has an intermediate value the crystallinity decreases[55, 76]. Despite the good properties, chitosan is mechanically weak and need to be blended with other polymers or inorganic phases to improve its mechanical stability[55, 77]; in fact Zhang et al. developed scaffolds consisting in a hydroxyapatite scaffold with chitosan sponges nested (HC1) or chitosan scaffold incorporated with hydroxyapatite powders (HC2) to study the effects *in vitro*, cells in contact with HC1 scaffolds showed a significantly higher ALP level and osteocalcin (OC) production, while cells in contact with HC2 scaffolds exhibited only lower activity in the ALP levels and OC secretion compared to HC1 but with an increase in the ALP activity and OC production if calcium phosphate glass were added in the scaffolds[78]. Also, Thein-Han et al. successfully fabricated chitosan-based scaffolds with hydrohyapatite incorporated by freezing and lyophilization resulting in a highly porous structure, greater compression modulus, and slower degradation rate and an improved cell adhesion, higher proliferation, and well spreading morphology of pre-osteoblast cells, compared to pure chitosan scaffolds[79].

Finally, the last natural polymer widely used as biomaterial is alginate, a polysaccharide displaying good biocompatibility and low toxicity when it is with a high purity. Alginate can be gelated using divalent cations into three-dimensional (3D) structure, but a negative aspect of alginate is the non-degradability in mammalian body due to the lack of alginase enzyme. However, ionically crosslinked gel can break down because of the release of divalent cations, moreover, increasing the molecular weight of alginate, the mechanical properties will be enhanced, but also its gelatinous viscosity can cause problems during the processing. Another method to modulate the alginate mechanical properties is by changing the level of methacrylation in photocrosslinkable alginate[55]. Different researchers worked with the alginate polymer, such as Alsberg et al. that prepared an alginate hydrogel modified with a specific adhesion ligand-containing peptide in order to promote the osteoblast adhesion and spreading; the *in vitro* and *in vivo* studies demonstrated an increase rate of adhesion, osteoblast proliferation, and new bone formation. In addition, they found a limit in peptide density (resulted to be 15 femtomoles/cm^2) above which no further increase in cellular proliferation was observed[80]. Moreover, Li et al. constructed a natural polymer-based complex scaffold formed by alginate and chitosan that showed a significantly improvement in mechanical strength and structurally stable due to the strong ionic bonding between the chitosan amine

groups and alginate carboxyl groups compared to scaffolds made by only chitosan. This new scaffold showed a porosity of 92% and a three times compressive modulus and yield strength compared to the pure chitosan scaffolds, moreover, scaffolds resulted to interact with osteoblast cells allowing the attachment, proliferation, and deposition of minerals without an osteogenic medium. In addition, these scaffolds can be produced in acidic, basic, or neutral solutions providing an environment favourable to the incorporation of proteins with less risk of denaturation, and *in vivo* studies showed a rapid vascularization and deposition of connettive tissue and calcified matrix within the entire scaffold structure[81].

Synthetic polymers are synthetized under controlled conditions leading a more reproducible mechanical and physical properties. The mechanical properties and the degradative rate can be adapted by controlling the molecular weight, crystallinity, molecular groups, and the co-polymerization of aliphatic polyesters[55]. The most synthetic polymers type used are polyesters, which different types can be distinguished; in particular, poly(ε-caprolactone) (PCL), polylactide (PLA) and polyglycolic acid (PGA) are widely utilized for bone tissue engineering as well as their copolymers[82]. PCL is a biodegradable and non-toxic highly processable ductile polymer as it has a low melting point and glass transition temperature, but unfortunately, it presents some limitations like the hydrophobicity and slow degradation rate (remains in situ up to 2 years). However, by blending with different polymers or producing a composite material these disadvantages can be partially fixed. An example is the composite material PCL/calcium silicate and decellularized ECM that presents a reduced hydrophobicity and excellent bioactivity in addition to enhanced cellular adhesion, proliferation, and differentiation[83–85]. In the other hand, PLAs are composed by chiral molecules, and consequently, they include several stereoisomers like poly(L-lactide) (PLLA) and poly(D-lactide) (PDLA). This group of synthetic polymers are exceptionally biocompatible and the lactic acid (starting material for the final polymer) can be made by a fermentation process using 100% annually renewable resources (for example from the lignocellulose production by fermentation processes[86]), moreover, it is also a low-impact, greenhouse gas polymer due to the balancing of the CO_2 amount generated during PLA biodegradation and the CO_2 amount taken from the atmosphere during the growth of plant feedstocks[87]. Also in this case, they have a slow degradation rate (3-5 years[88]). PLAs properties can be improved by the combination with several calcium phosphates as in an experiment of Tanodekaew et al. where they realize a scaffold with enhanced hydrophilicity and osteoblasts activity[89].

Ceramic biomaterials

Due to their very promising biocompatibility, bioactivity, mechanical strength, and osteoconductivity, also ceramics and bioactive glasses find large application for bone tissue engineering. The abilities to both enhance the scaffold osteo-potential and promote new bone formation make ceramics a viable candidate for the use in bone tissue regeneration[90]. The most used bioceramics in this field are calcium phosphates, calcium sulphates and bioactive glasses; the calcium phosphate more frequently used is hydroxyapatite (HA), however, it also possesses some disadvantages such as the lack of osteoconductivity or the slow resorption and remodeling rate. An approach to improve the properties is to use nano-HA, in fact the nanostructured HA closely resembles the mineral size and structure present in natural bone making easier its incorporation in a regenerating bone tissue[55]. Other calcium phosphates used are tricalcium phosphates (TCP) that showed faster resorption compared with HA; both TCP and HA can also be combined to create biphasic calcium phosphates (BCP) and provide the material with the ideal resorption rate and biocompatibility, with the best ratio of BCP for the use in the bone tissue engineering founded to be 60:40 HA:TCP. Finally, bioactive glasses are oxide-based glasses (typically SiO_2, CaO, Na_2O, and/or P_2O_5) with the ability to form amorphous or crystalline HA on the surface when enter in contact with a simulated physiology solution, this formed calcium phosphate establishes bonds with hard and soft tissues. Moreover, bioactive glasses release ions (Na, Ca, Si and P) during their degradation that increase the induction of osteogenesis and angiogenesis[91], and in addition, by adding elements such as F, Mg, Sr or Zn to the bioactive glasses, their function can be reinforced[92]. Unfortunately, bioactive glasses have low mechanical properties because of their brittleness which make their use complicated in the bone tissue engineering[55].

In conclusion, scaffolds capable to enhance the fast healing of the osteoporotic bone fractures are of great importance in order to regenerate the bone tissue. These biomaterial scaffolds can be replacing the use of the autografts, allografts, and xenografts since they can be adapted based on the patient specifications for stimulate osteogenesis and consequently the regeneration of bone tissue.

In the following paragraphs are described more in detail the biomaterials used in this research work, namely collagen, hydroxyapatite and mesoporous bioactive glasses.

1.5.3 Type I collagen (structure and advantages)

Collagen is a triple-helix structure with the ability of initiate and maintain the interactions with cells and matrix, nowadays 28 different types of collagens were discovered[93]. The biocompatibility, hydrophilicity, and the low antigenicity makes collagen a good candidate material in the bone tissue engineering, moreover its high biocompatibility and bioactivity derive from the mechanism of remodeling, removal, and replacing of the collagen that are at the basis of several tissue homeostasis. More precisely, there is a recognition by cells of a specific amino acids sequence that binds the integrin receptors enabling the adhesion, furthermore cells can secrete specific enzymes for the degradation of the collagen matrix and subsequently, the collagen matrix is replaced by new collagen produced and released in the ECM[17, 94, 95]. Type I collagen is the most common in the human body, and it is present also in the bone tissue[96], its molecular mass is 300,000 Dalton and the structure consists in a hierarchical configuration that give tensile strength and stiffness properties to the protein[18, 94]. The primary structure of type I collagen is represented by a sequence of amino acids in the form of G-X-Y, where glycine (G) is an amino acid that remain constant in the structure, while X and Y are usually occupied by proline and hydroxyproline[97, 98]; these three amino acids appear as repeated units and the stability depends on the hydrogen bonds formed from the presence of the 4-hydroxyproline[99]. For the formation of the α-chain structure (secondary structure), the glycine is essential[94, 100], moreover, the non-helical domains are at the end of the structure where the C-terminus initiate the formation of the triple-helix and the N-terminus regulate the primary fibril diameters, covalent crosslinks link the short non-helical telopeptides between collagen molecules or between collagen and other ECM molecules[17]. The tertiary structure is the triple-helix where, especially for type I collagen, is formed as heterotrimer (two α_1-chains and one α_2-chain linked by hydrogen bonds) having about 1000 amino acids, 300 nm length, and 1.5 nm of diameter, the three α-chains form a left-handed, rod-like helix with the glycine residue around a central axis and the other amino acids occupy the external positions[101]. Finally, the quaternary structure are the collagen fibrils, this supramolecular structure is formed by many triple-helix due to the ability of self-assembling of the type I collagen[17]: the molecules of collagen self-package in highly oriented with 67 nm D-periodic banding structure that additionally self-assemble in micro-fibrils, then in fibrils, and finally in fibers with a scale ranging from micrometers to millimeters[16, 17, 94] (Figure 1.4).

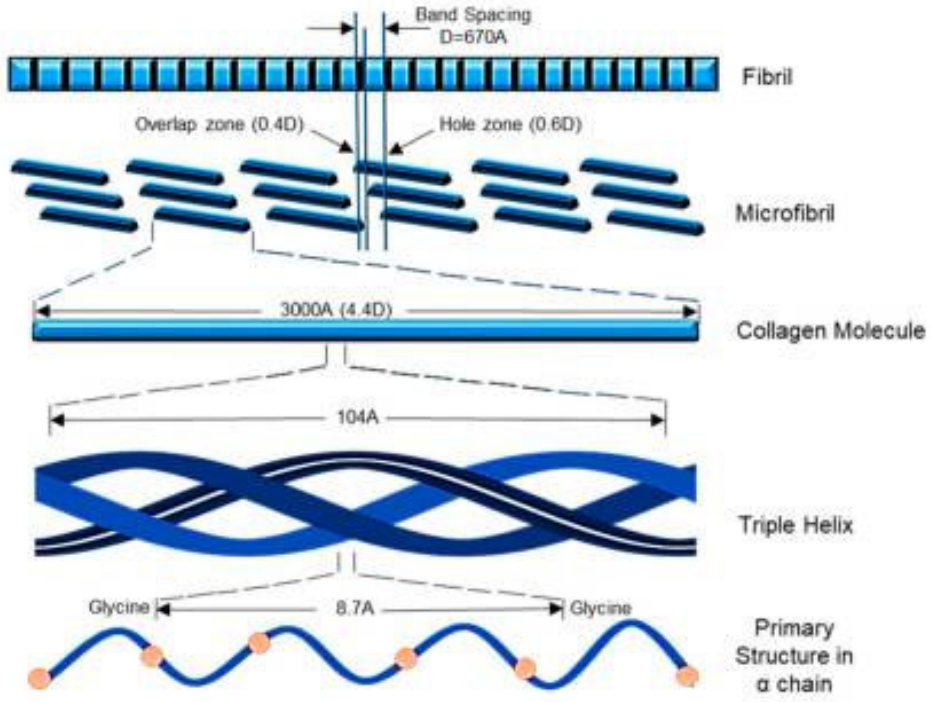

Figure 1.4: Hierarchical structure of collagen.

This process *in vitro* occurs when collagen solution is maintained at physiological conditions (pH, ionic strength, and temperature)[102], and in fact, in a pH in the range of 6.5-8 the protonation of the amino groups is inhibited, and the lysine reactivity is enhanced promoting the structured native-type fibrils reconstitution[16, 102].

1.5.4 Hydroxyapatite

As earlier specified, HA is the most used ceramic for bone tissue engineering, in fact, a lot of works has employed HA or nano-HA combined to other materials to create a scaffold for the healing of bone fractures[103–106]. In the next subsections, HA and Sr substituted nano-HA will be detailed.

1.5.4.1 Hydroxyapatite structure and properties

HA is a member of calcium phosphate ceramics and its structural and functional similarity to the bone mineral composition makes HA a very suitable material for bone tissue engineering. In fact, in the human bone HA constitutes up to 70% of the bone composition[7]. HA is composed by crystals with the chemical formula $Ca^{2+}_{10}(OH^{-})_2(PO_4^{3-})_6$ and a hexagonal unit, in the structure four Ca ions are

encircled by nine O atoms at M1 crystallographic position, while the other six Ca ions are encircled by six O atoms in the M2 crystallographic position[107] (Figure 1.5).

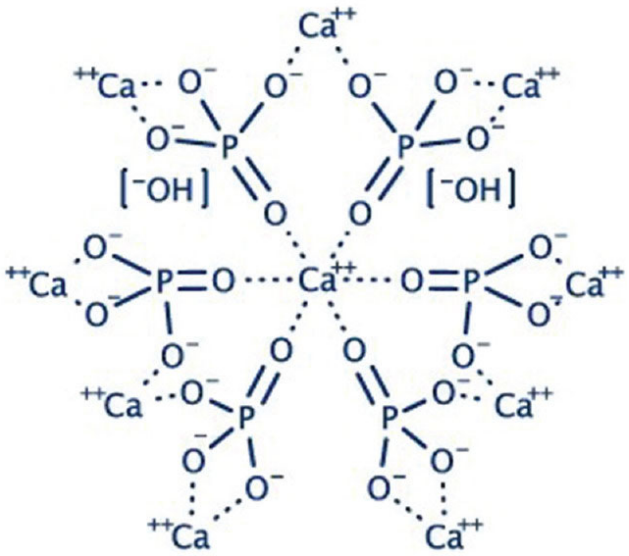

Figure 1.5: Structure of a hexagonal cell of HA.

Indeed, HA is widely used to create scaffolds for bone repair, although its characteristics can show some crystal, chemical, and micro-structural differences due to the synthesis process compared to bone HA[10], but unfortunately, it also possesses some disadvantages such as low resistance to fracture, fatigue failure, and brittleness, as well as the high Ca/P ratio and crystallinity that hinder the resorption rate by several years or decades[107]. To overcome the resorption rate issue, nano-HA can be used rather than HA because it resorbs quickly after only few weeks and is substituted by vital bone, moreover, it shows a good biocompatibility and better bioactivity compared to HA.

HA can be obtained from synthetic route or from natural sources[7], the synthetic process of the preparation consists in the combination of calcium and phosphate precursors like calcium oxide and phosphoric acid with a pH-controlled processing method; the HA obtained by these techniques has similar properties to natural bone HA, but the manufacturing costs are high[7]. HA can also be extracted from natural sources such as mammalian bones, eggshells, seashells, fish bones, and some plants, the extraction methods providing ecofriendly and cost-effective bone substituted[7, 108].

The bioactive behaviour of HA can also be improved by the introduction of substituted in both cationic and anionic parts by several therapeutic ions such as

iron, zinc, magnesium, strontium, manganese, silicate, and carbonate; that does not disrupt the configuration of the HA framework but alter the crystallinity, morphology, and solubility of HA.

1.5.4.2 Sr substituted nano-hydroxyapatite

Sr-nano-HA is commonly used in bone tissue engineering[8], in fact, strontium ions released influence osteoblast and osteoclast activity (as described in section 1.6.3). Strontium ions preferably substitute the Ca(M2) site at high concentrations, but at lower concentrations also the Ca(M1) site can be substituted[9], in addition the incorporation of Sr^{2+} ions in the HA framework reduce the crystallinity grade and the crystal size of HA. Strontium ions can totally substitute the calcium in the HA structure[10] and, since they have a larger radius than Ca ions (112 vs. 99 pm), can lead to an enlargement of the HA unit cell and the increase of cell volume; this distortion can also favor the incorporation of anions such as carbonate and HPO_4^{2-} when the Sr substituted HA is synthetized with low temperature methods[10]. Moreover, Sr substituted HA showed higher solubility than HA, with the subsequent increasing of the bioactivity and can also release Ca^{2+} ions, able to activate calcium channels and stimulate cell response[9]. Harrison et al. developed strontium substituted HA pastes and gels with two different methods (rapid-mix wet precipitation and sol-gel) where the incorporation of strontium into the final product is consistent and predictable, these materials showed a greater radiopacity proportional to its Sr content, a property with specific clinical benefits for the detection of the material during deployment and monitoring post-surgery, moreover materials can support the osteoblastic-like cells growth both with direct and indirect contact, with a biocompatibility comparable to the commercial bone graft substitute reference material[109].

1.5.5 Bioactive glasses

Glasses are materials with high biocompatibility and mechanical strength; however, a limited variety of these materials can bond directly to the bone tissue avoiding the encapsulation by fibrous tissue. As previous mentioned, the group of glasses materials that shows bioactivity is called bioactive glasses (BG)[110, 111], defined as *a glass designed to elicit specific physiological responses*[112], and are a group of synthetic silica-based bioactive materials[113]. The preparation of BG providing surface reactive silica, calcium, and phosphate groups, with a moderate alkaline interfacial pH promotes the chemical bonding with bone[114], improves

their chemical and physical properties, the microstructure, and the binding properties to bone tissue; moreover, BG can be synthetized with different compositions[110, 111]. BG has been studied principally in particulate form, although few other variants have been developed (for example glass fibers[114]), besides, some works suggested that biological properties of BG may be dependent on granule size[114]. The first BG named 45S5 developed by Hench was synthetized using a melt-quenching technique with a composition of SiO_2 of less than 60%, high content of CaO, Na_2O, and P_2O_5 (with a high CaO: P_2O_5 ratio)[115]; this BG showed the ability to create a HA layer on the surface after soaking in a solution without calcium or phosphates, comparable to the HA crystals observed in vivo[116]. This discovery has opened doors for new studies to understand the mechanism of these reactions, in fact, by exposing BG with simulated body fluid (SBF) a dissolution of this material is observed leading to the subsequent deposition of the HA layer.

BG can have different material compositions with different characteristics: one type of BG is the silica BG, this glass includes the 45S5 mentioned above and is a silicate glass with a three-dimensional glass forming SiO_2 network where the atom of Si is coordinated with four atoms of O; another kind of BG is the borate BG that shows lower chemical durability resulting in a very fast degradation and conversion in a HA-like material[117–119]. Moreover, borate BG can support the proliferation and the differentiation of the cells, but the boron released as borate ions in the solution is an issue due to its toxicity[120]. The last type is a phosphate BG in which the glass forming network is composed by P_2O_5 and CaO and Na_2O as modifiers[121–125], these glasses possess chemical affinity with bone tissue and their solubility can be controlled by the modification of their composition[126].

BG are also used in different shapes such as plates, granules, bulk, and powder for many medical and dental applications. Some examples of this applications are the reconstruction of defects of facial bone, filling frontal sinuses, augmentation of maxillary sinus floor, middle ear surgery, and very important, in the bone tissue engineering[116, 127–132]. In order to obtain a BG scaffold with the desired characteristics, different methods of production can be used to form a porous construct from particles of a melt-derived BG, the techniques can fabricate scaffolds with different critical parameters like pore architecture, porosity, pore size and interconnectivity[126]. One of the simplest methods is the thermal bonding where the scaffold is formed by thermally bonding a random and loose packing of particles or fibers in a desired geometry mold[133], some limitations of this methods concern the narrow porosity range and a constricted connectivity.

To create a more interconnected porosity scaffold can be used the polymer foam replication where a foam that can be synthetic or natural is immersed in a ceramic suspension obtaining a uniform coat on the foam, then the coated foam is dried and heat-treated at 300-600 °C and the glass struts are sintered at 600-1000 °C. The microstructure resulting is similar to the dry human trabecular bone, but the strength of the scaffold is low[133]. Another production method is the freeze casting of suspensions in which the solvent of a frozen colloidally suspension is subjected to sublimation and the particles are then sintered, with this technique, the scaffold obtained have an oriented microstructure with a higher strength in the direction of the orientation, but a disadvantage is the pore width in the range 10-40 μm that is too small to support the tissue ingrowth[133]. The sol-gel processing involve the foam formed by a surfactant of a solution, followed by reactions of condensation and gelation, used to the preparation of a hierarchical porous scaffold with a microstructure similar to the dry human trabecular bone[133], the hierarchical structure obtained simulates a physiological environment and facilitate the interaction with cells[134]. The last group of production methods are defined as solid freeform fabrication (SFF) and can used to manufacture objects layer-by-layer from a computer-aided design (CAD) file without the use of dies or molds; the structure of these scaffolds can be easily controlled and optimized to obtain the desired characteristics such as mechanical response or accelerate as well as guide the process of bone regeneration[133]. Recently, nanofibrous BG fabricated with electrospinning gained interest, in this process the electrospinning step consists in a spinning of a mixture such as tetraethyl ortosilicate (TEOS) and calcium nitrate and the fibers are obtained by the sol-gel reaction. After this step, the fibers are heated to 600-700 °C to decompose residual organic or inorganic groups and the obtained scaffold presents a rapid degradation rate due to the fine fibers diameter, and consequently in a high surface area, resulting in a rapid conversion to HA; this electrospun BG scaffold can be applicated in the regeneration of non-loaded bone defects and in the healing of soft tissue[133].

1.5.5.1 Bioactive glasses in bone healing application

As anticipated in the previous sections, the ability of BG to dissolve and form HA layer play a central role in the bonding the bone, the reaction starts on the surface of the glass and move inward, moreover, the Ca/P ratio of the HA deposited can vary between the external surface and the interior of glass[126]. The mechanism that leads the HA deposition is composed from different stages[114] (Figure 1.6).

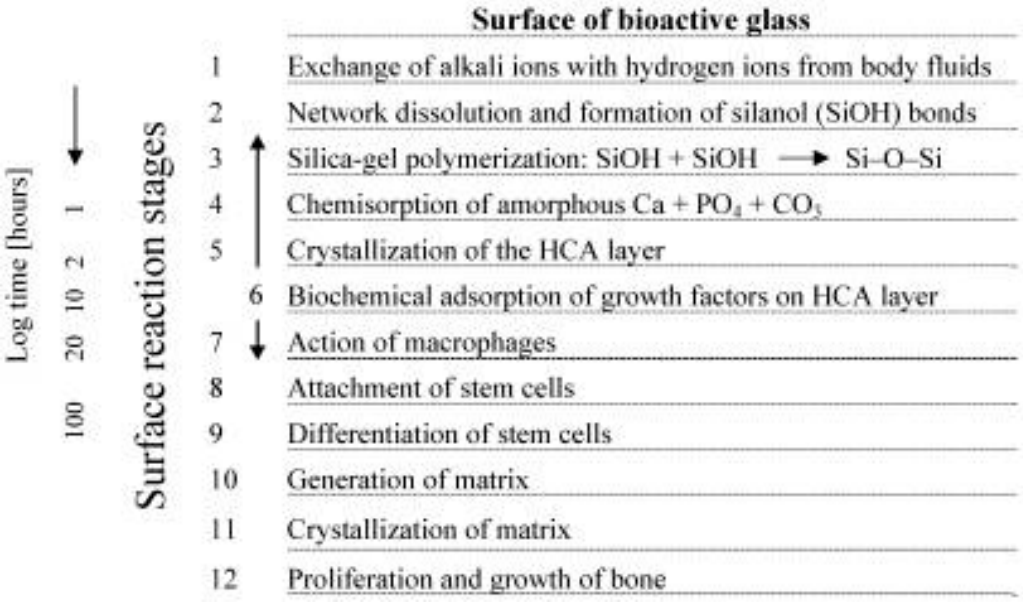

Figure 1.6: Surface reaction stages involved in forming a bond between bone and a bioactive glass[91].

In the first stage, several ion exchange reactions occur between the glass network modifiers that are replaced by hydronium ions from aqueous surroundings, the absorption of this type of ions increases the interfacial pH[126].

$$Si - O - Na^{+} + H^{+} \rightarrow Si - OH + Na^{+}(aq)[126]$$

Then, the increasing of the pH causes the silica dissolution in the form of silicic acid Si $(OH)_4$ and the continuous formation of silanol groups on the glass surface[126].

$$Si - O - Si + H_2O \rightarrow Si - OH + HO - Si$$

In the third stage the condensation and repolymerization form a silica gel rich layer on the material surface[114, 126] in which there is the chemisorption, nucleation, and growth of amorphous calcium phosphate (ACP) due to the further dissolution coupled with the migration of Ca^{2+} and $(PO_4)^{3-}$ ions from the glass through the silica rich layer[114, 126]. Finally, in the last stage the $CaO\text{-}P_2O_5$ mineral incorporates both carbonate and hydroxyl species deriving from the environment with the consequently crystallization of hydroxycarbonate apatite (HCA)[114, 126].

The formation of this apatite layer is necessary for the formation of the bond with the bone[114], the mechanism of this bonding is believed to involve the

adsorption of growth factors and the following attachment, proliferation, and differentiation of osteoprogenitor cells[135]. Then, osteoblasts create the extracellular matrix that mineralizes forming nanocrystalline mineral and collagen on the glass implant surface while the degradation and conversion of glass in HA continues over the time[136]. The product of the BG conversion commonly is a mesoporous structure of nanophase particles having a high surface area. Also, the presence of silanol groups is important for the formation of a bond with the bone[137], in fact, some investigations suggested that the existence of both silanol groups and negative charge on material surface can induce the formation of apatite and manifests bone bonding[138]. Since the formation of HCA on material surface is required to form the bone bonding, the silanol repolymerization in the BG surface is essential, besides, the surface reactions can be influenced by the crystallinity of the BG in fact[114], when the crystallization exceeds 60% the formation rate of HCA is slower[139]. In addition, the presence of calcium ions incorporated in the BG can have a beneficial effect, high concentration of calcium ions near the regenerative site can contribute to the osteogenesis by the stimulation of osteoblast proliferation, differentiation, and activity[140, 141]. Furthermore, also silica can show effects on the surface activity of BG, in fact, Bielby et al. demonstrate the increased proliferation of murine and human osteoblasts when the culture media contains 200 ppm of silica[142], moreover, Zhong et al. demonstrated that the formation of bone nodules increases in a silica-rich medium, probably because the soluble silica present in the solution can act as nuclei for the crystallization of apatite[143]. Thus, the bioactivity of BG strongly depends on their composition, macroscopically the product of this reaction can be partially converted in which there is a HA layer and an uncovered core, or fully converted to HA. Generally, silica-based BG result in a partial converted product, while borate-based BG are totally converted in HA; this activity is a consequence of the faster degradation rate of borate materials, causing a new bone formation that is almost twice respect to silica glass. Despite this promising effect, the degradation means a release of borate ions in the environment that are toxic to the cells above a threshold value[126], moreover, the microstructure can affect the ability of BG to form new bone tissue. In fact, oriented microstructure manifests more tissue infiltration than trabecular scaffolds, this happens despite the higher porosity of trabecular scaffolds compared to oriented structure, and in addition, differences in the surface roughness can change the amount of tissue infiltration. Finally, particles size can affect the BG regenerative properties, in fact, the particle size and shape may determine the compaction of the material and the interstitial spaces present between the particles, a study of Wheeler et al.

demonstrated that particles with a smaller diameter exhibit better biomechanical properties compared to larger diameter particles[144].

However, glass scaffold materials have several limitations, starting from the difficulty to process the glass into porous 3D structure, porous BG scaffolds are frequently prepared by sintering to bond particles in a strong glass phase with an interpenetrating network of pores; the difficulties encountered in this process lead to a resulting low strength. Moreover, the biological microenvironment can be influenced by the degradation of BG, with increasing of ions concentration and change in the pH, therefore, the biological effects from in vitro experiments are very difficult to predict[126].

A member of the BG family is the MBG developed by Zhao's team and Vallet-Regi's group in 2004[11, 145].

1.5.5.2 Mesoporous bioactive glasses

MBGs rapidly gained interest for their peculiar properties like a very high specific surface area (>100 m^2/g) and the high pore volume[146], they exhibit also exceptional bioactive properties[147]. The synthesis method of MBGs involves the incorporation of supramolecular chemistry to the sol-gel process, and the combination of these two strategies lead to obtain a highly ordered mesoporous arrangement resulting in a five times higher surface and porosity compared than those obtained by conventional methods. According to IUPAC (International Union of Pure and Applied Chemistry) classification, mesoporous materials category regards materials with a pore size between 2 and 50 nm[148], the ordered mesoporous structure allows the incorporation of different biomolecules and drugs to treat degenerative bone tissue and infections[149, 150]. Moreover, the synthesis of these materials requires the use of surfactants as structures that direct the assembly and the subsequent condensation of inorganic silica precursors[147], surfactants are amphiphilic molecules with both hydrophilic and hydrophobic properties due to the presence of polar and nonpolar domains; three different categories of surfactant can be distinguished: cationic (when the polar head group shows a positive charge), anionic (when the polar head group shows a negative charge), and nonionic (when the polar head group does not present charge). In aqueous solutions, surfactants can spontaneously assemble into structures called micelles, where the hydrophilic groups are in contact with the external aqueous solution and the hydrophobic groups are inside the micelle structure[151].

Synthesis of MBGs has some advantages as the fact that it requires lower temperatures compared to BG conventional production methods, an easy powder technology production with improved homogeneity and purity, a larger range of bioactive compositions (up to 90 %mol SiO_2), and the porosity is tunable[146]. In fact, after the remotion of the surfactant by calcination or extraction, MBGs obtained present some features: a stable mesoporous structure, a high specific surface area and large pore volume, homogeneous pore morphology, and a high amount of silanol groups on the surface that can be chemically functionalized[147]. As mentioned above, MBGs can be used as delivery systems because the molecules can be loaded on the material using an adsorption mechanism (impregnation method) and subsequently released via a diffusion-controlled mechanism[152].

MBGs synthesis comports some structural and textural properties that are similar to conventional sol-gel BG consisting in a vitreous network of SiO_2-CaO-P_2O_5, consequently, they are analogous at atomic level, but in addition MBGs show highly ordered mesoporous arrangement of cavities[147]. As earlier specified, the MBG synthesis combine the sol-gel strategy with the supramolecular chemistry of a surfactant as structured directing agent[147], however, this type of synthesis also requires strategies to include the presence of CaO in a multicomponent inorganic system[147] and it is based on an evaporation-induced self-assembly (EISA) process (Figure 1.7).

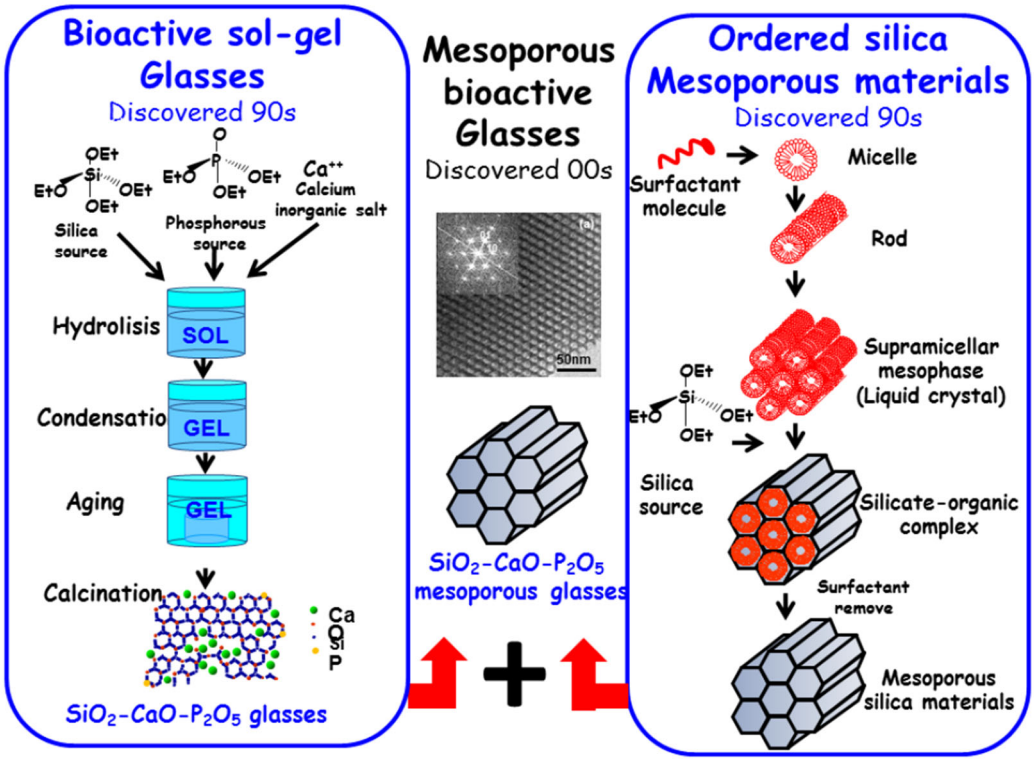

Figure 1.7: Combination of sol-gel and supramolecular routes used for the synthesis of MBGs[147].

This mechanism starts with a solution of a glass precursor and the surfactant prepared in ethanol/water with an initial concentration minor of the critical micellar concentration (CMC), the surfactant concentration progressively increases due to the evaporation of the ethanol causing the self-assembly of the surfactant in micelles and the further organization into a liquid crystalline mesophase. The EISA process is used for two reasons: gel aging and dried stages during the synthesis of SiO_2-CaO-P_2O_5 that involve temperatures of about 100 °C, incompatible with an ordered micellar phase, and the second reason concerns the use of much diluted precursor solution that overcome the not compatibility of the classic hydrothermal preparation with a multicomponent system, because the CaO can hinder the interactions between surfactant and silica[147]. In fact, EISA process consists in the gradually evaporation of a volatile solvent at room temperature until the surfactant reaches their CMC, with the following self-assembly of the micelles, the synthesis entails numerous advantages in the final characteristics of the material also including the bioactive response; moreover, based on the type of surfactant used during the synthesis (such as Pluronic® P123 and Pluronic® F127), different supramicellar mesophases structures can be

obtained. Consequently, the final pore size and volume strongly depend to the chain length and the charge of the surfactant[153, 154]. For example, the use of Pluronic® P123 leads the formation of 2D hexagonal structures consisting in unidirectional opening channels in both directions distributed in a hexagonal arrangement; however, is possible to modulate the 2D hexagonal structure to a 3D bicontinuous cubic structure, consisting in a body-centered structure with multidirectional mesoporous network, using the same surfactant but changing the CaO amount in the silica system. This behaviour can be explained by the influence of Ca^{2+} ions that act as network modifiers with the subsequent decrease in the connectivity of the silica network, and thus, the inorganic/organic ratio of the surfactant increase with the Ca content, decreasing the curvature of surfactant micelles and contributing to form hexagonal phases rather cubic structures[147]. Also, the temperature can influence the micelle structure, in fact, when the temperature rises, the micelle size system increases for the reduced micelles and water hydrogen interactions[155] and, for instance, 2D hexagonal structure is formed at lower temperature compared to 3D cubic structures[147].

Due to the high surface area and porosity derived by the synthesis method, MBGs have a better bioactivity than conventional BG, this behaviour can be explained by considering the composition of BG and MBGs, where the latter exhibit two domains: an amorphous SiO_2-CaO-(Na_2O) phase, and calcium phosphate clusters embedded inside the amorphous phase. The amorphous phase is principally formed by a network of SiO_4 thethaedra, while the calcium phosphate clusters break the Si-O-Si linkage provoking a decreasing in the network connectivity[156–158], even if the decrease of the network connectivity does not explain the accelerated bioactivity of these materials, but on the contrary, the calcium phosphate clusters can act as nucleation sites that increase the HCA layer formation kinetics. Studies showed the presence of ACP domains in the pores wall of the MBGs, and the highest surface area of MBGs provides a great accessibility of these nuclei giving a superior bioactivity compared with BG[159, 160].

In this PhD work, two different strategies were used to synthetize MBGs with a controlled morphology: the first strategy consists in a conventional base-catalyzed sol-gel method in order to produce spherical nanoparticles with a diameter in the range of 100-400 nm, and the second approach require an aerosol assisted spray drying procedure, where a similar solution of the starting solution in EISA approach is sprayed using a heated gas producing spherical micrometric particles in form of dried powders and decreasing the evaporation time required in the EISA method. Moreover, the automatic process of the aerosol assisted spray

drying procedure increases the repeatability of the particles morphology because avoid variables that can be changed by external parameters or the operator. Finally, the final composition of both nano- and microparticles was enriched by the incorporation of Sr element to confer several therapeutic properties, and synthetized MBGs were then grafted with a novel recombinant biomolecule called ICOS-Fc with the aim to further widen the ability of the particles to regenerate the osteoporotic bone fractures since ICOS-Fc proved to inhibit osteoclastogenic activity[28].

The synthesis of these type of MBGs will be discussed in the following chapter.

1.5.5.3 MBGs containing therapeutic ions

In the recent years, interest to expand the biological properties of MBGs is increased, to achieves this goal, the incorporation of metallic ions in the silica framework was studied, moreover, several metallic ions proved to exert different biological function, and in addition contrary to the use of biomolecules such as growth factors or recombinant proteins, metallic ions result less expensive[161, 162]. metallic ions are more stable and not susceptible to high temperature, solvent or pressure that can be involved during the synthesis, some ions can also be implicated in cellular functions by activating ion channels or the interaction with macromolecules or other ions, resulting in the induction of secondary cell signals[163].

Based on the type of metallic ion incorporated in the MBGs framework, different therapeutic effects can be obtained (Figure 7). Thus, incorporation of metallic ions leads to produce multifunctional platforms that can be used in different applications, even if the possible cytotoxic effects should be considered during the design of a biomaterial based on ion containing MBGs. An uncontrolled release, both in terms of concentrations and kinetics, can result undesired effects, in fact, the challenge for create a platform that can release inorganic ions in the bone tissue regeneration is to determine their therapeutic window. As shown in figure 1.8, different inorganic ions can exert different biological effects such as antibacterial function, anti-inflammatory function, osteogenesis activity or stimulate the angiogenesis[27].

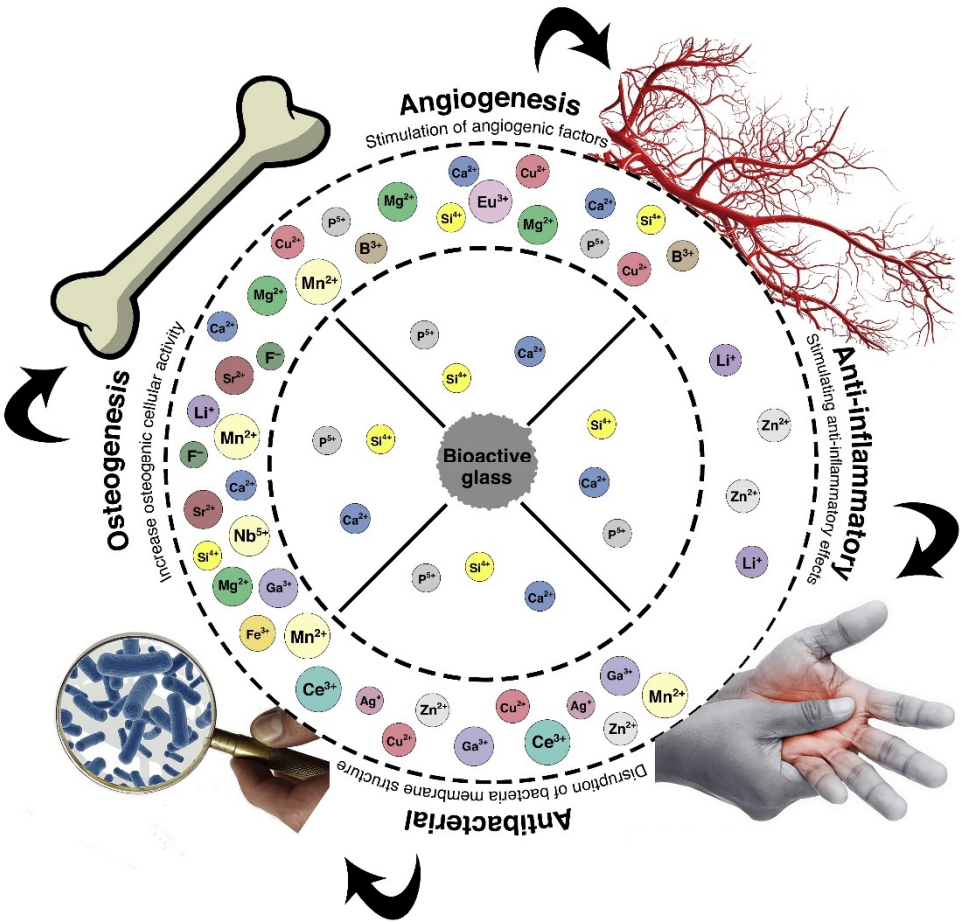

Figure 1.8: The different biological effects exerted by inorganic ions incorporated in MBGs structure[27].

As showed in the figure 7, several metallic ions have a role in the osteogenesis, in particular, the importance of the strontium in the bone healing will be discussed.

Effect of strontium (Sr)

Strontium is present in trace in human body, and in particular in bone[164], it is in the second group of the periodic table along with calcium and magnesium and due to this similarity in size and behaviour, strontium shows biological effects usually induced by calcium. In fact, Sr has the potential to stimulate bone formation due to enhancing of the osteoblast-related genes, as well as promoting osteogenic differentiation of mesenchymal stem cells, and the up-regulation of some osteogenic genes like alkaline phosphatase and osteocalcin[26]. Indeed, Sr is able to activate the calcium sensing receptor (CaSR) present in osteoblast cells,

stimulating different cell pathways and promote osteoblasts proliferation and differentiation[27], the activation of CaSR also leads to the osteoclast apoptosis. Other effects of Sr concern the inhibition of osteoclast differentiation, by the modulation of the RANK/RANKL pathway: RANKL (Receptor Activator of Nuclear Factor κ B Ligand) binds RANK (Receptor Activator of Nuclear Factor κ B) inducing the osteoclastogenesis activity; moreover, osteoprotegerin (OPG), a molecule implicated in the regulation of bone density and bone mass regulation can be overexpressed by the strontium ions, and the OPG overexpression inhibits the expression of RANKL and consequently the osteoclastogenesis[165–168]. Huang D. et al. proved that strontium ions can also disrupts the RANKL-activated p38 and NF- κ B signaling pathways[169], p38 and NF- κ B are molecules that can stimulate the NFATc1 (a transcription factor of osteoclast genes), and NF- κ B is activated by the I κ B-α degradation; Sr ions can directly inhibit the phosphorylation of p38, and simultaneously, can also inhibit the degradation of I κ B-α and thus the activation of NF- κ B (as shown in Figure 1.9) with the result of the repression of the osteoclastogenesis activity.

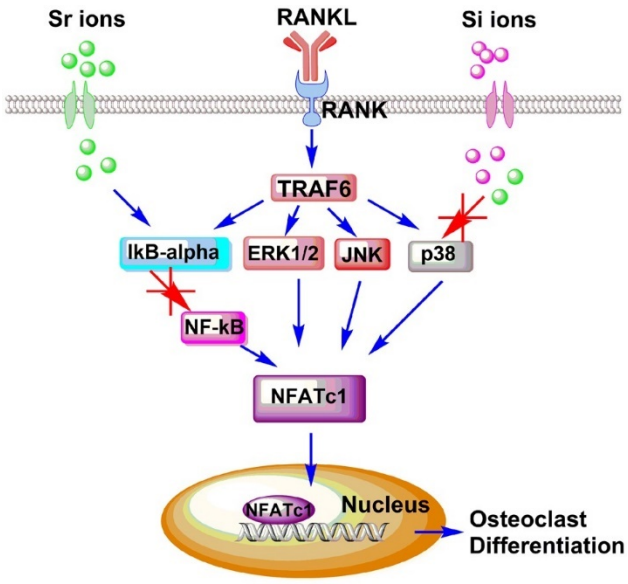

Figure 1.9: Mechanism proposed by Huang D. et al. of the Sr ion inhibition of RANKL-induced osteoclastogenic differentiation pathway[169].

Some experiments also reported the role of Sr in the angiogenesis by enhancing the basic fibroblast growth factor (bFGF) and vascular endothelial growth factor (VEGF) expression[170, 171], while other studies presented the effect of Sr to reduce the expression of pro-inflammatory factors like TNF-α, interleukin 6 (IL-6), and cytokines[172–174].

1.5.5.4 Functionalization of MBGs surface with biomolecules

As previously mentioned, the idea behind this work is to exploit both Sr ions release, and the activity of a biomolecule grafted on MBGs surface to obtain a synergistic effect in which osteoblast differentiation and activity are stimulated and at the same time osteoclast differentiation and activity are inhibited.

MBGs were used for delivering bioactive molecules (such as proteins or recombinant biomolecules), or other cargoes in a very large number of works[175–177], in fact, the high surface area and pore volume leads to an enhanced drugs adsorption, and the pores diameter can act as size selective modulator for the confinement of the bioactive molecules in the pores and limit their diffusion in the surrounding medium. Nevertheless, a disadvantage to use MBGs as carriers is an initial burst release and a not long sustained release of the loaded bioactive molecule when in contact with body fluids[175, 177]. Usually, the bioactive molecule loaded on MBGs by an impregnation method is adsorbed on the surface and not in the pores due to the pores small size that impedes the access of the molecule[149] and the interaction of the bioactive molecules and MBGs are mainly governed by the presence of a very large number of silanol groups. However, the interactions between the adsorbed molecule and the Si-OH groups are weak interactions such as Van der Waals forces or hydrogen bonds, frequently, this type of interaction is not enough to obtain a long-time release needed. To overcome this problem, it is possible to graft several bioactive molecules using different strategies where usually two steps are required: initially, the functionalization of MBGs surface by alkoxysilane chemistry to obtain a surface with different chemical properties, then, the bioactive molecule can be grafted utilizing a coupling reaction; the first step consists in a functionalization of the silanol-containing mesoporous surface with different organic groups[178, 179] (Figure 1.10).

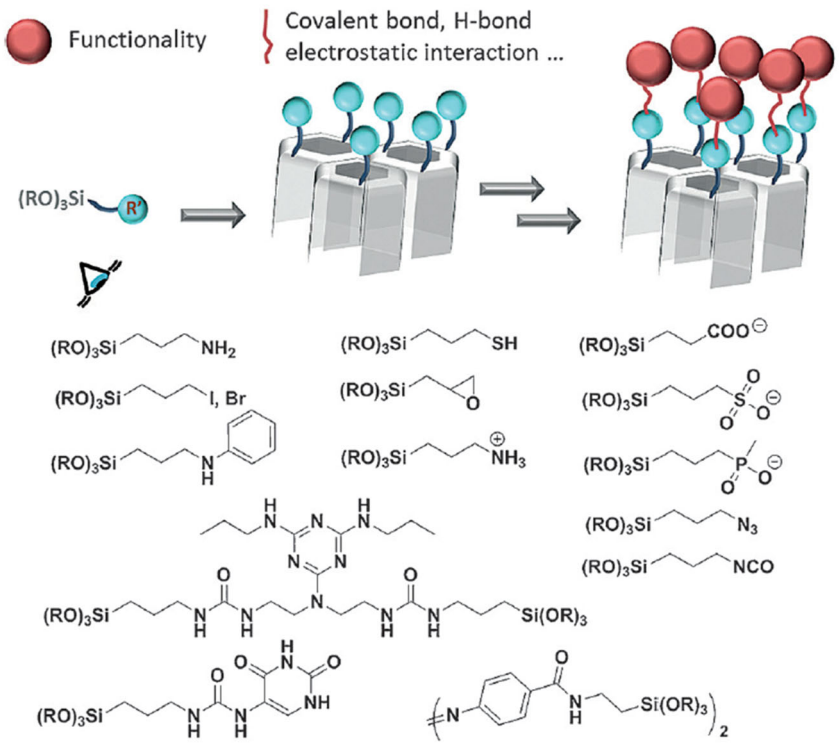

Figure 1.10: Different organosilica compounds usually functionalized on MBG surface.

To achieve the functionalization of organic groups, two main routes can be used: one-pot synthesis (co-condensation) and post-synthesis (silylation or grafting)[178], where the co-condensation method involves the simultaneous condensation of silica and organosilica precursors in the presence of the surfactant during the mesoporous synthesis, and in this case, all the functionalization process is performed at the same time during the synthesis in one step[178, 180], resulting in organic groups grafted both in the outer and in the inner part of the silica structure with consequently the degree of the mesoscopic order decreasing with the increasing of the organosilica precursors concentration in the synthesis. Due to this problem, the maximum content of organic compound does not normally exceed 40 mol%. In the other hand, in the functionalization process an organosilica precursor is grafted under anhydrous conditions on the previous formed MBG, with this method, the organic functions are located on the outer surface of MBGs obtaining a higher functionalization degree. This type of functionalization modifies the chemical properties of silica walls such as the polarity of the surface and the absorption capability, in fact, the new functional groups exposed can interact with the bioactive molecule to be adsorbed,

increasing the ability of MBGs to be loaded by it. In addition, the interaction between the functional groups and the molecule to be loaded can affect the release rate for the increasing of the diffusion resistance, but unfortunately this process leads to a reduction of textural properties such as pore diameters, pore volume and specific surface area, although dependent from the size of the organic residue[178].

However, in most cases the interaction does not prevent the burst release of the adsorbed bioactive molecule because the interactions are still not strong enough[181], and as mentioned before, the ideal MBGs carrier should not have a premature release of the bioactive molecule. To prevent it, another strategy to incorporate the bioactive molecule to MBGs surface can be used consisting of covalently linking the molecule to the modified surface of MBGs, this type of grafting can be achieved using several methods: carbodiimide-mediated coupling, maleimide/thiol coupling, disulfide bond formation, epoxy opening with amines, and diethyl squarate coupling[182] (Figure 1.11).

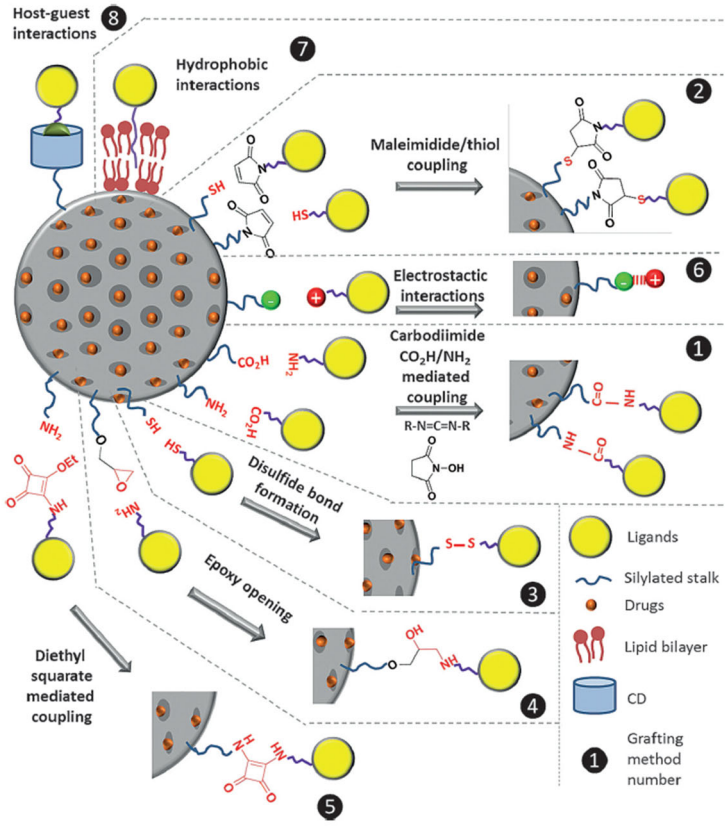

Figure 1.11: Different covalent link between MBGs surface and the active molecule.

In particular, carbodiimide-mediated coupling reaction consists in several steps to link a primary amino group with a carboxyl group, it is defined as a "zero distance" coupling since the carboxyl and amino groups are directly linked to each other. East et al. proposed a mechanism of action in which, in the first step the 1-ethyl-3-(3-dimethylaminopropyl)carbodiimide (EDC) group is protonated by the water molecules, the consequence of the protonation is an accumulation of OH^- ions in the solution that causes the deprotonation of the carboxyl group forming a carboxylate ion. Then, the carboxylate ion reacts with the N=C=N group of the EDC molecule with the formation of an isoacyl urea intermediate, and when a primary amine group encounters this structure, they react and form the amide bond between the carboxyl and amine group[183].

In this PhD work, MBGs were functionalized with amino groups on the surface using the post-synthesis method, then carbodiimide-mediated coupling reaction was used to covalently link the amino groups with the carboxyl groups present on the bioactive molecule, the selected bioactive molecule is a recombinant molecule called ICOS-Fc and it will be described in the next section.

1.5.5.5 ICOS biomolecule and its recombinant form ICOS-Fc

As specified, for this PhD work a recombinant molecule covalently linked to the MBGs surface was used to inhibit osteoclasts activity, this biomolecule named ICOS-Fc is a recombinant form of the ICOS receptor.

ICOS is a T-cell co-stimulatory surface receptor which belongs to the CD28 family receptors and is normally expressed in T cells, it can bind the inducible costimulatory ligand B7h, also known as ICOS binding ligand (ICOSL), constitutively expressed by several type of cells like B cells, macrophages, dendritic cells, and also in osteoclasts. The bond between ICOS and ICOSL is involved in the regulation of the bone turnover, and the administration of the soluble recombinant form of ICOS (ICOS-Fc) proved to reversibly inhibit the human osteoclast activity *in vitro*. Furthermore, the administration of ICOS-Fc *in vivo* in mice can inhibit and possibly reverse the development of experimental osteoporosis[28, 29].

Moreover, ICOS-Fc presents carboxyl groups in the Fc domain, allowing a right orientation when grafted on MBGs surface by the carbodiimide-mediated coupling[28].

Once ICOS-Fc was grafted on MBGs, my PhD focused on the electrospinning technique in order to fabricate the oprimal device for the treatment of the pelvis osteoporotic fractures.

1.6 Fabrication techniques

A lot of scaffolds properties were influenced by their fabrication process, in fact, a key property is the scaffold architecture based on the tissue to be replaced. Bone tissue is classified in two types: cortical bone with a porosity of 5-10%, and trabecular bone with a higher porosity that varies between 50% to 90%, with different mechanical characteristics from each other; the mechanical properties of the bone are dependent from the subject, vary from one bone to another and within different region of the same bone[126]. Indeed, to obtain a designed scaffold with good features for bone or cartilage after the fabrication is a great challenge, thus there are different techniques of fabrication of biomaterial scaffolds in order to obtain the desired characteristics. Mainly, processes can be divided into additive manufacturing and conventional methods; where additive manufacturing comprises all three-dimensional (3D) printing methods such as inkjet printing, extrusion printing, stereolithography, selective laser sintering (SLS), and bioprinting, while conventional methods include solvent casting and particulate leaching (SCPL), thermally induced phase separation (TIPS) methods, gas foaming, and electrospinning[55] (Figure 1.12).

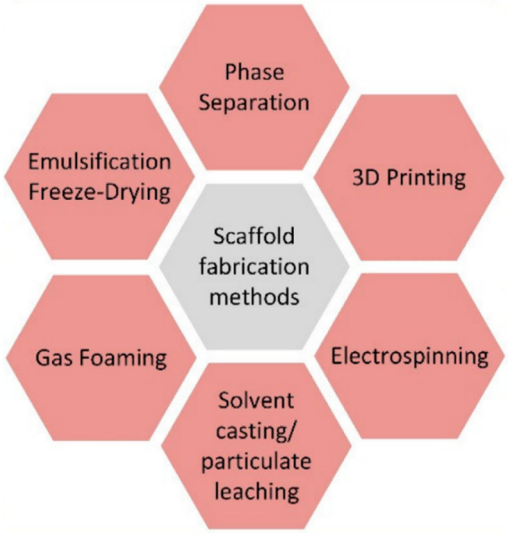

Figure 1.12: Different biomaterial scaffolds fabrication techniques[54].

The additive manufacturing techniques aims to produce scaffolds with a certain wanted pattern tailored for patient specifications, in fact, the process builds structures with macro- and microarchitecture from the bottom-up corresponding to the properties of the tissue to be replaced[55, 184].

The inkjet printing use droplets as individual building blocks to build a structure, the ejection of droplets can be driven by thermal or piezoelectric processes. Inkjet printing is a fabrication technique with low-cost, simple, and with a high speed and cell viability, but unfortunately, it also has disadvantages like the low concentration of the inks that can influence the integrity of the structure[55].

Extrusion bioprinting is the most used technique that extrudes polymers or hydrogels through a micro-nozzle, the extrusion occurs by a pressure-based mechanism that can be a pneumatic system using compressed gas and working better with highly viscous materials or piston-driven apparatus where a more direct control of the flow makes it a more precise process[184]. In general, extrusion bioprinting has a fast fabrication time and most physiologically relevant mechanical properties, but it has lower resolution compared to the other techniques[185–187].

Stereolithography (SLA) consists in the photopolymerization of a photosensitive resin layer by layer, the crosslinking is performed every layer on a downwards moving platform after each layer deposition. Unfortunately, this technique can be used only with limited materials because require the photosensitivity of the deposited material[184].

Finally, selective laser sintering (SLS) involves a laser beam that melts a compacted powder set in a platform into a pre-defined shape the sinterization occurs in each layer[184]. In this technique, the size and the morphology of the powder are very important[188]. Unfortunately, also in this method there is a limited choice of materials and of the design of the structure, moreover, because of the high temperature used, natural polymers and biomolecules cannot be used[55].

In the other hand, conventional methods are simpler and widely used. Generally, these methods start with a polymeric solution or a suspension of a polymer and inorganic phase.

The SCPL consists in the dissolution of a polymer with salt/polymer particles in a solvent, and after evaporation of the solvent, the particulates were leach out by the submersion of the matrix in water for the creation of a porous

structure[189]. Despite the simple cost-effective procedure and the controllability of pore size and porosity, this method has disadvantages like the use of organic solvents, the difficult to control the pores interconnectivity, and the low control of the spatial geometry[55, 190].

In TIPS the thermal energies of a homogeneous solution of a polymer are changed to separate it in polymer and solvent phases, and then, freeze-drying is performed to evaporate the solvent with the resulting scaffold that shows a microporous structure[191]. Although this method produces large volumes of size and morphology-controlled pores, one of the major disadvantages is the relatively higher temperatures used and consequently the impossibility to incorporate natural polymers or biomolecules during the process.

Gas foaming in a technique where polymer discs are exposed to high-pressure inert gases to create foams, the pressure is then dropped to ambient pressure to cause the nucleation of bubbles and the growth of pores is promoted by the gas diffusion through the pores. This process is fast and simple, but the resulting structure lack in interconnectivity, and in addition, it is not cost-effective because require molds to form complex structures of scaffolds[55].

Electrospinning has great possibilities for the use in bone tissue engineering because creates fibers by the use of electrostatic forces, fibers are then accumulated on a collection plate with the formed fibrous structure that mimics the ECM natural tissue. The used precursor can be a polymer solution or a molten polymer; the method is versatile, simple, and inexpensive and performed at low temperatures (therefore, also biomolecules can be incorporated); but some disadvantages regard the lack of mechanical properties, even if a way to enhance the mechanical properties and bioactivity of the electrospun scaffolds is to incorporate bioceramics particles at low concentrations[54, 55], and the requirement to perform the process under a well-controlled atmosphere.

Since macro- and microarchitecture are fundamental parameters to produce these scaffolds, the manufacturing processes used to the scaffold construction are important because can influence the structural properties like porosity degree, size of the pores and also the interconnectivity between the pores[54, 55].

In the following paragraphs were described more in detail the electrospinning (the chosen technique used in this research work), in order to obtain a device for stimulate bone tissue regeneration in pelvis osteoporotic fractures. Finally, two different crosslinking strategies to improve the mechanical properties of the electrospun scaffolds were described.

1.6.1 Electrospinning of polymers

Electrospinning is one of the most versatile techniques to produce nanofibers, in particular the scaffolds obtained by the electrospinning consist in a flexible membrane showing micro- and nanofibrous mats[192, 193], which can then be adapted in the pelvic zone, moreover the produced construct therefore can mimic the ECM at micro- and nanoscale. The interest of this method increased after 2000[194], and uses the electrostatic principle where a polymer solution or a melted polymer is pumped through a syringe needle when a high voltage is applied. The voltage leads a charge movement in the polymer solution causing a deformation and stretching of the drop, forming a Taylor cone, subsequently the electric field cause the prolongation of this cone and the successive viscoelastic jet formation that are pulled away from the needle; the process is accompanied by the solvent evaporation that cause a whipping of the filament, and finally fibers are deposited on a metallic collector (Figure 1.13).

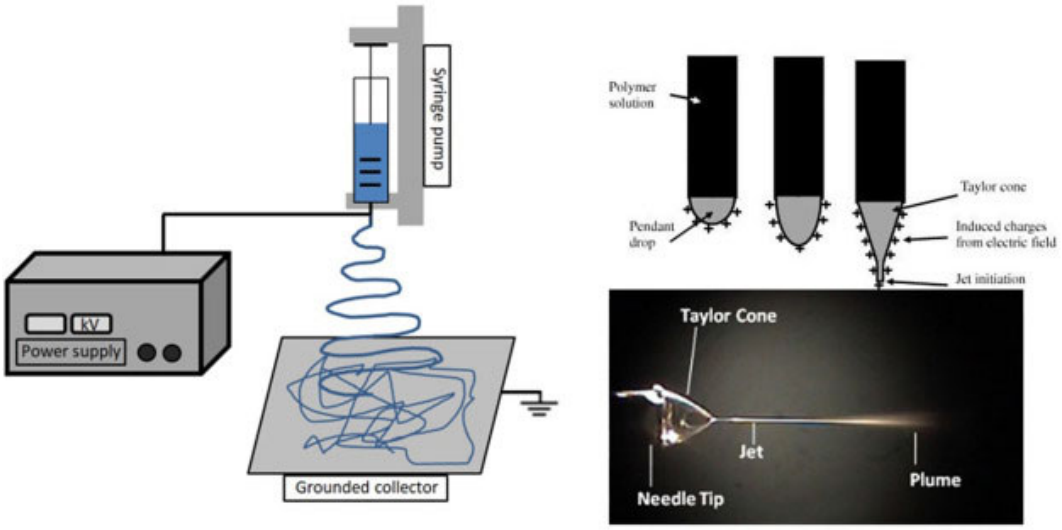

Figure 1.13: Electrospinning technology (left), and formation of Taylor cone (right).

Generally, the deposition of the fibers occurs randomly[194–196], however, several methods were developed to obtain ordered structures such as a rotating mandrel collector[197, 198]. With the electrospinning technique the production of fibers having few nanometers to micrometers in diameter can obtained by varying different parameters[199], in which the process results depend on: environmental parameters like solution temperature, humidity, and air velocity in the chamber; solution properties such as elasticity, viscosity, conductivity, and surface tension;

and governing variables for example the distance between the needle and the collector, electrical potential, and flow rate[200, 201].

A large variety of polymers can be electrospun by this technique as previously described, but for this PhD work the natural polymer type I collagen was chosen due to its biocompatibility, hydrophilicity, low antigenicity and the large presence in ECM as well as the large use in bone tissue engineering.

1.6.2 Electrospinning of type I collagen: current processes and related issues

The electrospinning method is generally chosen by the type of polymer that will be electrospun, due to the low denaturation temperature of the collagen the melt-spinning method cannot be used, thus collagen is commonly processed via solution-based methods[202]. Moreover, collagen can be extracted from different sources including mammalians, amphibians, birds, fish, marines, and human recombinant collagens[96, 203], but generally, collagens from bovine and calf dermis sources are the most used for the electrospinning, followed by collagen of rat origin. The great use of these two sources is principally due to their abundance and the commercially availability of the isolated collagen[203] but unfortunately, approximately 3% of the human population has proven to be allergic to the bovine collagen[96], therefore an alternative is the collagen from rat tail sources that is readily available and easy to extract, even if it must be treated with a high level of purification protocol and, additionally, it is easy to contaminate it[96]. Another solution is the use of recombinant technologies to produce collagen, in fact Stein H. et al. modified the tobacco plants with two genes that encode the recombinant heterotrimeric type I collagen and the human prolyl-4-hydroxylase (P4H) and lysyl hydroxylase 3 (LH3) enzymes resulting in the formation of rhCOL1 that is then extracted, this extract forms a thermally stable triple helical structure[204].

In order to solubilize and electrospinning the collagen, often some level of denaturation occurs that is commonly associated with the type of solvent used, for example the fluoroalcohol family such as 1,1,1,3,3,3-hexafluoro-2-propanol (HFP) or the 2,2,2-trifluoroethanol (TFE)[192]. Thus, the use of HFP or other fluoroalcohol solvents is conventionally thought to denature the collagen with little to no recovery of the structure during fabrication[203], but other solvents can be used to solubilize the collagen polymer like aqueous acidic solvents that showed improvement in the structure, but with some disadvantages, indeed, the slower evaporation rate of the solution compared with fluoroalcohols results in a slower flow rate during the electrospinning limiting the fiber size and the

collection over time. Moreover, electrospun fibers are more wet when deposited causing a union with other fibers around them with the possibility to decrease the porosity and the mechanical behaviour.

1.6.3 Electrospun collagen-inorganic phases scaffolds

As previously described, bioactive ceramics exhibit the ability of bond formation directly with living tissues, in particular of bone tissue, once they are implanted into the body. In the other hand, collagen scaffolds show biocompatibility and low antigenicity, but have poor mechanical strength. Therefore, to increase mechanical properties and osteogenic characteristics of the collagen scaffolds can be produced a composite material by mixing the collagen with a ceramic phase[55], and the idea behind this PhD work is to combine in a collagen scaffold the properties of both bioactive ceramics (MBGs and HA) and crosslinked electrospun collagen.

A composite scaffold for bone tissue engineering should be mimic the bone ECM constituted mainly of collagenous fibers embedded with HA nanocrystallites[205], thus the incorporation of an inorganic phase such as HA in the final scaffold can provide the stiffness and strength of bone, while type I collagen can be responsible to give flexibility and resilience[206]. Different works studied the effects of create composite materials: Venugopal et al. created a composite electrospun collagen scaffold loading crystalline HA founding an increase in the mineralization of osteoblast cells compared to pure collagen, due to the HA presence that acts as a chelating agent and induces the mineralization[207]. Other workers investigated the activity of HA in gelatin electrospun scaffolds concluding that they can enhance the cell attachment, proliferation, and ECM production, moreover, by improving the fiber orientation, also mechanical properties were increased, in addition they founded the presence of some nanoscale interactions between gelatin and HA[208]. Other studies showed an increasing of osteogenesis *in vitro* for HA/core-shell based electrospun scaffolds[209, 210]: Song et al. use a co-precipitation processing to obtain a very well dispersed inorganic phase in the collagen matrix, with this method they were able to implement 20 wt% of HA in the organic matrix without beads and the produced scaffolds can stimulate osteoblastic differentiation and support good cell adhesion[211]. Moreover, Zhou et al. electrospun and crosslinked collagen with HA as inorganic phase with a new method, results of this experiment showed HA particles well dispersed and with an oriented alignment. Furthermore, scaffolds showed 40 times higher tensile strength compared to previous scaffolds and promoting cell viability without showing *in vitro* cytotoxicity[212]. While many

works describe the incorporation of HA in collagen electrospun scaffolds, not many reported the incorporation of BG in collagen, however some researchers studied the incorporation of BG in other natural polymers: Saatchi et al. incorporated cerium substituted BGs in polyethylene oxide (PEO) electrospun fibers with the result of an increased wettability and cell viability[213]; Talebian et al. studied the effects of the incorporation of sol-gel BGs in core-shell PEO fibers, noting an increase in the mechanical strength probably due to the formation of ionic and hydrogen bonds between BGs and polymers, these scaffolds showed the ability to form a plate-like hydroxyl-carbonate apatite layer and displayed the potential to induce the osteogenic differentiation in human MSCs[214]. Finally, Chen et al. investigated three-layer composite scaffolds, the loading of 5 and 10% of Bioglass® increased the mechanical properties and *in vivo* studies showed a positive effect on promoting cell proliferation and the expression of bFGF, VEGF and collagen I[215].

Despite the many studies with the promising results, combining natural polymers with bioactive inorganic materials during the course of electrospinning remains a considerable challenge. For example, when HA nanopowder is mixed directly with a polymer solution, electrospinning into nanofibers is impeded significantly creating a large number of beads, moreover inorganic nanoparticles generally agglomerate easily and cannot be homogenized with the polymer solution[205].

Furthermore, as previously described, the collagen scaffolds produced by electrospinning lack in mechanical properties; in order to enhance these properties, membranes can be crosslinked. In the following section, a general overview of the main methods to crosslink was described, then the two crosslinking strategies used in this work was described more specifically.

1.6.4 Strategies for collagen crosslinking

As already mentioned, collagen materials are very good choice in the field of tissue engineering due to the very high biocompatibility, hydrophilicity, and low antigenicity, unfortunately, collagen scaffolds result in poor mechanical strength, reduced elasticity, rapid degradation rate, and low resistance to external factors such as the presence of enzymes[202, 216]; an approach to improve these properties can be the use of chemical, physical, and enzymatic crosslinking methods.

In the case of chemical crosslinking, chemical agents can be used to interact with collagen functional groups (carboxyl- and amino groups), this leads to the

formation of crosslinks between collagen molecules[217]. There is a large number of chemical crosslinking: the use of glutaraldehyde (GA) compound crosslinks the amine groups of lysine or hydroxylysine of the collagen by the reaction with the aldehyde group of GA[218, 219], however, the exact mechanism of this reaction still is not completely elucidated[220]; the GA is principally selected for its low cost, high reactivity, and high solubility in water solution[216, 221–224], but some studies reported the toxicity of GA for human health[220, 225]. Another method is the use of genipin, a chemical compound obtained from a glucoside[226] that possesses antimicrobial, antitumor, and anti-inflammatory properties, it is also less toxic than GA and can interact with amino acids or proteins in a reversible chemical attachment[216, 227], but unfortunately genipin results cytotoxic for concentration above of 5 mM[216]. According to Yan et al. *in vitro* studies on collagen/chitosan scaffolds crosslinked with genipin show an improved biostability and an elasticity modulus increased with the increasing of genipic concentration, in addition scaffolds showed a good biocompatibility, moreover condrocyte's adhesion, spread, and viability can be supported by the fabricated scaffolds as *in vitro* studies demonstrated[228]. The EDC/ (N-Hydroxysuccinimide) NHS method is a "zero length" crosslinking process that chemical activate the molecules, this process crosslinks the amino- and carboxyl groups present in the collagen molecules[229, 230], this method is widely used because increase stability to the enzymatic digestion[216]. The dialdehyde starch (DAS) is a macromolecular aldehyde produced in the reaction between native starch and periodic acid[231] that shows low toxicity, biodegradability, and antiviral activity[232, 233], but materials crosslinked with this compound tends to age as Langmaier et al. described[234]. Finally, chitosan is a linear polysaccharide with its hydroxyl and amino groups can covalently bond other reagents[235]. Chitosan is biocompatible, biodegradable, non-toxic, and exhibits antibacterial and antifungal properties[76, 236, 237], the combination with collagen can enhance the mechanical and biological properties of the scaffold[238], however it has low solubility in water solutions and only the addition of an acidic medium can increase its solubility[216] and in addition, since it is a natural-based compound, chitosan can be contaminated by organic or inorganic impurities[216].

Also, the physically induced crosslinking can improve the collagen scaffold properties, to perform this process two types of methods are commonly used: temperature and UV irradiation[216]. The method using the temperature is called dehydrothermal (DHT) method and in this case, collagen is exposed to elevate temperature (higher that 90 °C) under vacuum conditions[239], a study confirms that the crosslinking using DHT did not change the fibers diameter or the

interfiber distance and improved the mechanical strength[240] and in addition, the process is not cytotoxic and provides sterilization[241], nevertheless, during the process collagen denaturation occurs, with the rearrangement of the tertiary structure in a less ordered structure, due to the high temperature involved resulting in a loss of the protein bioactivity[242]. The UV light crosslinking methods is faster and more effective compared to DHT treatment, during the process, using a UV light at 254 nm free radicals are formed on the aromatic groups of tyrosine and phenylalanine that interact with each other to form chemical bonds[243]. The procedure does not require additional reagents but causes a partial denaturation[244], however the technique sterilizes the material because UV light at 254 nm damages the microorganism genetic material[245], but unfortunately the UV light alone not produce a high density of crosslinking[246]. More recently, combined methods in which a reaction between UV light and a photo-activable reagent produce intra- and intermolecular crosslinks were developed and these methods appear more effective than UV light only, such as riboflavin and UV-A crosslinking or UV-EDC/NHS-induced crosslinking[216].

Finally, enzyme induced crosslinking provides the use of enzymes to crosslink the collagen molecules, collagen fibrils are stabilized with enzymatical post-translational modifications in physiological conditions[247]. In the past, lysyl oxidase (LOX) enzyme was used to crosslink collagen molecules, this enzyme modifies the amino groups of lysines and hydroxylysines of the collagen into aldehyde groups that consequently interact with the unmodified amino groups[248], but nowadays a microbial transglutaminase (MTG) is widely used, the MTG crosslinking improves the collagen stability and enhances the mechanical properties, moreover the resulting material showed good cytocompatibility and a not changed morphology of collagen fibrils[249].

In this PhD work, two types of crosslinking to enhance the electrospun collagen matrices were investigated: a chemical crosslinking using the “zero distance” EDC/NHS method and a UV crosslinking with a photo-activable compound called Rose Bengal (RB).

1.6.4.1 Crosslinking by EDC/NHS coupling

EDC/NHS coupling is a “zero length” crosslinking able to connect an amino group with a carboxyl group, as described in 1.4.5.4 section, the formed link is a covalent bond that enhance the physicochemical properties of the collagen matrix. This method is able to mimics the enzymes that stabilize the collagen structure *in vivo*[250], in fact, the use of this methods reported to increase five-sixfold the

tensile modulus of collagen matrices[251] and the resulting crosslinked collagen shows a more ordered 3-dimensional structure that increase the thermal stability and facilitates the cell attachment and proliferation[251–253], creating an adequate environment for cell viability (including osteoblast-like cells[252]). Moreover, this crosslinking reaction also increase the stability to enzymatic digestion by bacterial collagenase, probably because collagenase cannot recognize the cleavage sites covered in the crosslinking[216]. However, even if this method has numerous advantages, some disadvantages are also present: the topographic cues of the collagen could be altered by the use of ethanol present during the crosslinking reaction and the reaction is principally limited to the collagen surface due to the slow penetration of EDC and NHS caused by the high-ethanol environment[254].

1.6.4.2 Crosslinking by Rose Bengal

RB is a halide derivative of fluorescein[255] (Figure 1.14) widely used in clinical applications both for enhance the visualization of corneal lesions as well as in the inhibition of microorganisms' growth such as bacterial and fungal infection by a photochemical mechanism[255, 256].

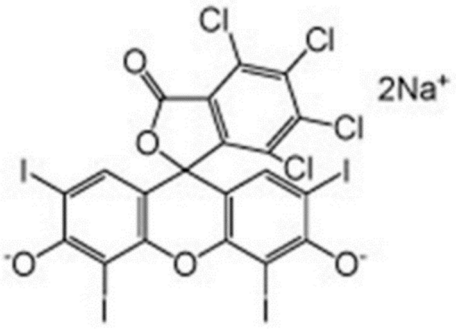

Figure 1.14: RB structure.

Nevertheless, this molecule can also be used to crosslink collagen materials improving their properties; although the exact mechanism involved in the binding and interaction between RB and collagen remains to be clarified[30], an hypothesis of Redmond and Kochevar suggests that RB through aggregates rather than individuals monomers binds the collagen positively charged groups (amines and lysines) mainly via hydrogen bond, since RB have two negative charges, and proline via hydrophobic forces, and then amino acids in collagen act as electron donors to donate an additional negative charge to RB with a subsequent de-

iodination and a formation of amino acid radicals that can form covalent crosslinks between collagen chains. But also, a mechanism involving oxygen can occurs where RB reactive oxygen species (singlet oxygen) were generated by energy transfer[31]. Eckes et al. demonstrate that when RB is used to crosslink collagen sheets, the resulting materials show reduced swelling degree and a huge increase in the resistance of mechanical pressure, moreover, the crosslinked sheets showed an increase collagen rigidity leading to an improvement of primary osteoblasts and muscle cells proliferation[257]. Another work of Chan and So demonstrated the improvement in the physicochemical properties of a collagen gel after the crosslinking with RB[258], however, these authors used a method in aqueous conditions that can results in a loss of topographic cues for collagen electrospun fibers. Liu T. et al. overcome this problem by modifying this protocol, they founded a well-maintained morphology of the scaffolds loaded with at least 0.1% (w/v) of RB[30], moreover, they exposed the collagen electrospun fibers encapsulated with RB to water or ethanol before the laser irradiation to avoid the fast loss of fibrous morphology. This probably is due because water and ethanol provide ground state oxygen able to interact with RB producing reactive singlet oxygen to oxidize surrounding molecules. Finally, Liu T. et al. demonstrated that these scaffolds provide a beneficial environment for proliferation and differentiation of cells[30].

Chapter 2

Materials and methods

List of acronyms

AA: Acetic Acid

APST: (3-aminopropyl) silanetriol

BET: Brunauer-Emmett-Teller

COL: Rat Type I Collagen

CTAB: Cetyltrimethylammonium Bromide

DFT: Density Functional Theory

ddH_2O: Double Distilled Water

DMEM: Dulbecco's Modified Eagle's Medium

DPBS: Dulbecco's Phosphate-Buffered Saline

ECM: Extracellular Matrix

EDC: N-(3-Dimethylaminopropyl)-N′-ethylcarbodiimide

EDS: Energy Dispersive Spectroscopy

ELISA: Enzyme-Linked Immunosorbent Assay

FBS: Fetal Bovine Serum

FESEM: Field Emission Scanning Electron Microscopy

FTIR: Fourier Transform Infrared

HA: Hydroxyapatite

HFP: Hexafluoroisopropanol

HRP: Horseradish Peroxidase

ICP-AES: Inductively Coupled Plasma Atomic Emission Spectroscopy

MBGs: Mesoporous Bioactive Glasses

MBGs-Sr: Strontium containing Mesoporous Bioactive Glasses

MDOCs: Monocyte-Derived Osteoclasts

NHS: N-Hydroxysuccinimide

OD: Optical Density

PBS: Phosphate-Buffered Saline

RB: Rose Bengal

SBF: Simulated Body Fluid

SD-Sr: Strontium containing Mesoporous Bioactive Glasses microparticles

SD-Sr-ICOS-Fc: Strontium containing Mesoporous Bioactive Glasses microparticles grafted with ICOS-Fc

SD-Sr-NH_2: Amino modified strontium containing Mesoporous Bioactive Glasses microparticles

SDS-PAGE: Sodium Dodecyl Sulphate - Polyacrylamide Gel Electrophoresis

SEM: Scanning Electron Microscopy

SG-Sr: Strontium containing Mesoporous Bioactive Glasses nanoparticles

SG-Sr-ICOS-Fc: Strontium containing Mesoporous Bioactive Glasses nanoparticles grafted with ICOS-Fc

SG-Sr-NH_2: Amino modified strontium containing Mesoporous Bioactive Glasses nanoparticles

Sr-nano-HA: Strontium substituted nano-hydroxyapatite

SSA: Specific Surface Area

TEOS: Tetraethyl Orthosilicate

TGA: Thermogravimetric Analysis

TMB: Tetra-Methyl-Benzidine

TNBS: 2,4,6-Trinitrobenzene Sulfonic Acid

TRAP: Tartrate-Resistant Acid Phosphatase

XRD: X-ray Diffraction

XTT: 2,3-Bis(2-methoxy-4-nitro-5-sulfophenyl)-2H-tetrazolium-5-carbox-anilide

2.1 Introduction

The general aim of the present PhD thesis was to develop a flexible multifunctional scaffold that can be specifically adapted for pelvis location in order to treat osteoporotic fractures, by exerting different therapeutic effects and promoting overall bone tissue regeneration. In this chapter, the general scheme of the synthesis procedures and technologies for the fabrication of the final scaffold are reported (schematically outlined in figure 2.1).

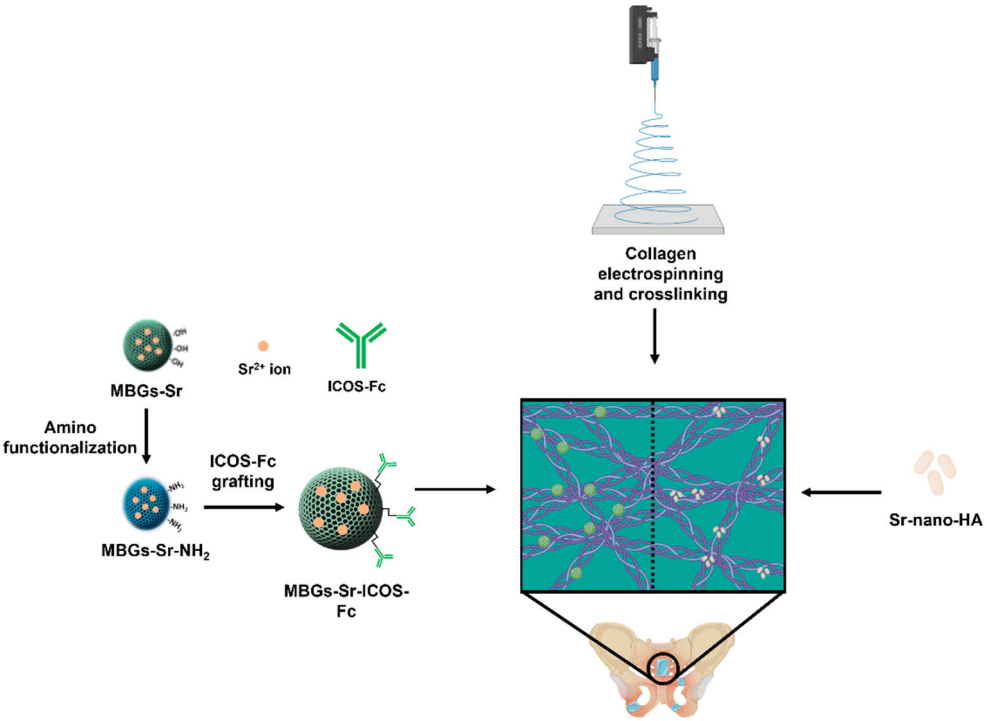

Figure 2.1: Materials and technologies for the scaffold development.

Firstly, MBGs and Sr-nano-HA inorganic phases able to stimulate the bone fracture healing and promote the restoration of the normal tissue balance were selected and synthetized. For MBGs two synthesis methods were explored that allow to obtain nano- and micro-sized particles, whereas Sr-nano-HA were produced by FLUIDINOVA company by a wet chemical precipitation method; the amount of strontium as therapeutic ion added in the synthesis both for MBGs and Sr-nano-HA was selected in order to exert the characteristic pro-osteogenic effects of Sr ions.

Subsequently, the bone healing properties of MBGs have been enhanced by grafting of ICOS-Fc biomolecule, in order to exploit both the pro-osteogenic effects imparted by Sr ions and the anti-osteoclastogenic activity of ICOS-Fc, thus achieving a synergistic effect. Prior to the grafting MBGs surface were modified with amino groups, then EDC/NHS chemistry was exploited in order to link the amino groups with the carboxyl groups present on the Fc domain of the biomolecule to form an amide bond.

Thereafter, type I collagen was electrospun with and without the selected inorganic phases in order to obtain flexible membranes with a morphology that can mimic the human bone ECM.

Since the collagen-based electrospun membranes result in poor mechanical properties and fast degradation rate, two methods to crosslink membranes were investigated. The first method implies the use of an EDC/NHS coupling to link the amino and carboxyl groups both present in the collagen molecules, while the second method used the Rose Bengal molecule as the photoinitiator.

2.2 Synthesis of nano-sized mesoporous bioactive glasses

Part of the work described in this chapter has been already published during the PhD period[259].

The synthesis of nano-sized particles was conducted by using a modified procedure of base catalyzed sol-gel method developed by Wu et al.[260], in order to obtain particles with a composition of SiO_2, CaO and SrO (ratio 85/5/10, named SG-Sr) and a mesopore size ranging between 2-4 nm. The preparation was conducted as follows: 6.6 g of CTAB (≥98%, Sigma Aldrich, Italy) was dissolved in 600 mL of ddH_2O and 12 mL of NH_4OH (Ammonium hydroxide solution, Sigma Aldrich, Italy) for 30 min. Then, 28.2 g of TEOS (reagent grade 98%, Sigma Aldrich, Italy) was added drop by drop, and 1.88 g of calcium nitrate tetrahydrate ($Ca(NO_3)_2$•$4H_2O$, 99%, Sigma Aldrich, Italy) and 4.25 g of strontium chloride hexahydrate ($SrCl_2$•$6H_2O$ 99%, Sigma Aldrich, Italy) were dissolved, and the solution was vigorously stirred for 3 h. The formed powder was collected by centrifugation (Hermle Labortechnik Z326) at 13000 rpm for 3 min and washed two times with ddH_2O and one time with absolute ethanol (Ethanol absolute = 99.8%, Sigma Aldrich, Italy). The collected particles were then dried at 70 °C with a STF-F 52 stove (FALC INSTRUMENTS s.r.l.) for 12 h and calcined using a FALC FM 8,2 furnace (FALC INSTRUMENTS s.r.l.) at 600 °C in air for 5 h (heating ramp 1°C min^{-1}) in order to remove all the residual CTAB.

All the reagents were purchased from Sigma Aldrich, Italy, and used as received.

2.3 Synthesis of micro-sized mesoporous bioactive glasses

Part of the work described in this chapter has been already published during the PhD period[259].

In order to obtain micro-sized MBGs, a process based on an aerosol assisted spray-drying approach under mild acidic conditions was exploited by modifying the procedure reported by Pontiroli et al[261]. The major advantage of this

technique is due to its good repeatability and the promising scalability to an industrial level. The preparation to obtain particles with a composition of SiO_2, CaO and SrO (ratio 85/5/10, named SD-Sr) and a mesopore size ranging between 8-10 nm was carried out as follows: 2.03 g of the non-ionic block copolymer Pluronic P123 ($EO_{20}PO_{70}EO_{20}$, average Mn ~5,800, Sigma Aldrich, Italy) were dissolved in 85 g of ddH_2O for 3 h; in a separate batch 10.73 g of TEOS were pre-hydrolyzed using 5 g of an aqueous HCl solution (pH 2) until the solution obtained was transparent (about 3 h of stirring). The TEOS solution was then added drop by drop into the Pluronic solution and 0.72 g of $Ca(NO_3)_2 \cdot 4H_2O$ and 1.62 g of $SrCl_2 \cdot 6H_2O$ were dissolved in the final solution. The resulting solution was sprayed (Büchi, Mini Spray-Dryer B-290) with nitrogen as atomizing gas using the following parameters: nozzle diameter 0.7 mm, inlet temperature 220 °C, N_2 pressure 55 mmHg and feed rate 3.5 mL/min. The obtained particles were then collected and calcined using a FALC FM 8,2 furnace (FALC INSTRUMENTS s.r.l.) at 600 °C in air for 5 h (heating ramp 1°C min^{-1}) in order to remove the Pluronic P123 residual.

All the reagents were purchased from Sigma Aldrich, Italy, and used as received.

2.3.1 Scaling-up to industrial scale of micro-sized mesoporous bioactive glasses

Since the synthesis of SD-Sr is an easily scalable process, in this PhD thesis the scaling-up from lab scale to industrial scale of this process was explored using an industrial spray dryer located in FLUIDINOVA company in Porto, Portugal (Figure 2.2).

Figure 2.2: Industrial spray dryer used for the scaling-up trials.

To perform the scaling-up of the MBGs spray drying with a composition of SiO_2, CaO and SrO (ratio 85/5/10) and a mesopore size ranging between 8-10 nm, the protocol developed at laboratory scale was adapted in term of reagent amounts (Table 2.1).

Table 2.1: Amounts of reagents for industrial scaling-up trials compared to lab scale synthesis.

	Reagents	**Lab scale synthesis quantities**	**Industrial scale synthesis quantities**
Non-ionic block copolymer solution	Pluronic P123	2.03 g	304.5 g
	ddH_2O	85 g	12.75 Kg
Pre-hydrolyzation solution	TEOS	10.73 g	1.61 Kg
	HCl solution (pH 2)	5 g	750 g
Ions precursors	$Ca(NO_3)_2 \cdot 4H_2O$	0.72 g	108 g
	$SrCl_2 \cdot 6H_2O$	1.62 g	243 g

The optimization of the overall procedure required several step-by-step adjustments. The procedure for preparing the surfactant solution consisted as follows: 304.5 g of the non-ionic block copolymer Pluronic P123 were dissolved in 12.75 Kg of ddH_2O for 4.30 h. The complete dissolution required longer time compared to TRL3 process due to the higher amount of the surfactant. The procedure for preparing the solution of hydrolyzed silica precursor consisted as follows: 3.219 Kg of TEOS were pre-hydrolyzed using 1.5 Kg of an aqueous HCl solution (pH 2) until the solution obtained was transparent (about 4 h of stirring); in the preliminary trials the silica precursor solution has reached high temperatures (up to 64 °C) due to the exothermic hydrolyzation reaction of TEOS hydrolysis, which involves the early curing of the solution, to overcome this problem the solution was prepared in an ice bath in the subsequent trials. The TEOS solution was then added into the Pluronic solution (flow rate of 7 L/h) and 108 g of $Ca(NO_3)_2$•$4H_2O$ and 243 g of $SrCl_2$ were dissolved in the final solution. The final solution was then sprayed by an industrial spray dryer with air as atomizing gas with the following parameters: nozzle diameter 2 mm, inlet temperature 220 °C, outlet temperature 115 °C, and air flow 90 L/h. The obtained particles were then collected and calcined using a FALC FM 8,2 furnace (FALC INSTRUMENTS s.r.l.) at 600 °C in air for 5 h (heating ramp 1°C min^{-1}) in order to remove the Pluronic P123 residual.

All the reagents were purchased from Sigma Aldrich, Italy and used as received.

2.4 ICOS-Fc grafting on mesoporous bioactive glasses surface

The functionalization with amino groups has been used to insert reactive groups at the surface of MBG enabling the grafting of ICOS-Fc biomolecule through the carboxyl moieties present on Fc residue of the biomolecule.

2.4.1 Surface modification of mesoporous bioactive glasses

Part of the work described in this chapter has been already published during the PhD period[259].

MBGs shows on their surface a high number of terminal hydroxyl groups that easily allow the grafting of alkoxysilane moieties in order to achieve several

targets like reducing the aggregation among particles, nonspecific surface adhesion or, as in this case, exploit the amino group for a subsequent grafting reaction. The selected functionalization route was based on the post-grafting of APST (22-25% in water, ALFA Chemistry) (Figure 2.3).

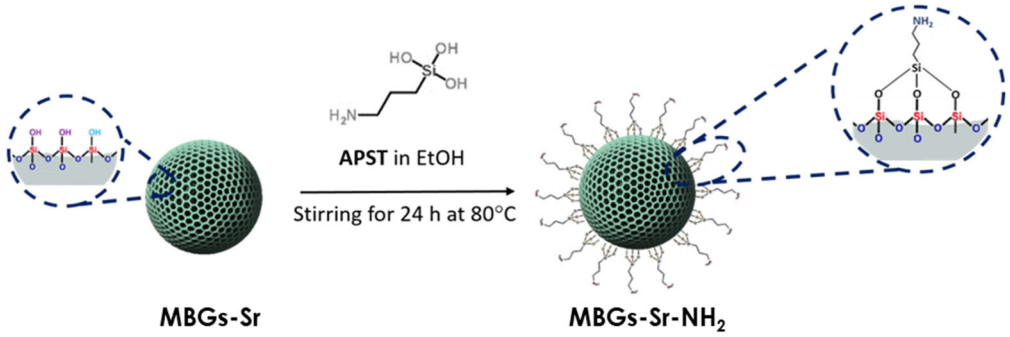

Figure 2.3: Amino modification of MBGs-Sr surface.

The amount of APST to be added during the functionalization procedure was calculated based to the Zhuravlev number widely used in the literature to estimate the organosilane precursors for the post-grafting reactions of MBGs and mesoporous silica[262]. According with the Zhuravlev number a density of 4.9 SiOH/nm^2 should be considered, and based on the specific surface area of MBGs the overall number of the exposed hydroxyl groups was estimated and the amount of organosilane was calculated.

In particular, the procedure generally reported for mesoporous silicas was used[263–265], where 0.6 g of the previous described SG-Sr and SD-Sr were outgassed overnight in vacuum in order to remove all the water residual on the surface and then dispersed in 50 mL of absolute ethanol (P.A., absolute = 99.8%, Sigma Aldrich, Italy) then the optimized amount of APST (0.9 mmol for SG-Sr and 0.6 mmol for SD-Sr) was added and refluxed 24 h under stirring (400 rpm) at 80 °C under nitrogen atmosphere. The obtained functionalized powder (SG-Sr-NH_2 and SD-Sr-NH_2) was collected by centrifugation (Hermle Labortechnik Z326) 3 min at 13000 rpm for SG-Sr-NH_2 and 5 min at 10000 rpm for SD-Sr-NH_2, washed three times with absolute ethanol and dried at 70 °C for 12 h.

2.4.2 Grafting of ICOS-Fc on mesoporous bioactive glasses surface

Part of the work described in this chapter has been already published during the PhD period[259].

The grafting of ICOS-Fc biomolecule was conducted on SG-Sr-NH_2 and SD-Sr-NH_2, the major challenge underlaying this procedure is the grafting of the biomolecule showing the correct orientation for preserving its biological functionality. To ensure the correct orientation, an EDC (Sigma Aldrich, Italy)/ NHS (Sigma Aldrich, Italy) coupling reaction described by Wang et al[266]. and optimized in terms of reagents amounts and EDC/NHS ratio was used, since the carboxyl group present on ICOS-Fc that in the reaction were linked to amino groups of the particles are present in the Fc domain and not in the active site (Figure 2.4).

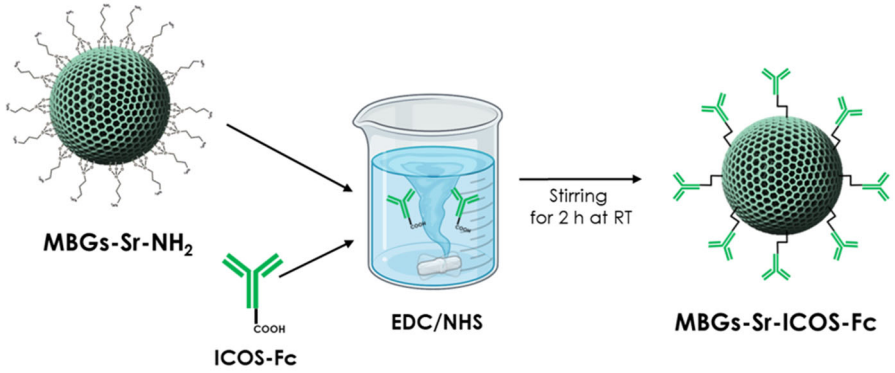

Figure 2.4: ICOS-Fc grafting on MBGs surface procedure.

In particular, 1 mg of ICOS-Fc was dissolved in 6.2 mL of DPBS and 200 µL of a solution containing 50 mg/mL EDC and 75 mg/mL NHS were added, the resulting solution was stirred at 500 rpm for 15 min at room temperature. Then, 100 mg of SG-Sr-NH_2 or SD-Sr-NH_2 were added and stirred at 500 rpm for 2 h at room temperature. The grafted powder was then collected by centrifugation (Hermle Labortechnik Z326) 15 min at 8500 rpm and washed five times with ddH_2O, while supernatants were collected for the ELISA-like assay (see section 2.9.1). Finally, the powder was dry under vacuum for 12 h.

2.5 Synthesis of strontium containing nano-hydroxyapatite

The Sr-nano-HA (50% Sr in the crystalline structure) used in this PhD work was provided by FLUIDINOVA company and synthetized by a wet chemical precipitation method through NETmix® reactor, a static mixing device for continuous mode operation available at the company that produces nanoparticles

with high reproducibility in terms of size distribution, allowing the control of the formation of nano-HA at molecular scale (by controlling the mixing between the different substances), moreover strontium ions were incorporated into the nano-HA structure by the addition of strontium chloride hexahydrate as precursor to the reactant solution following the equation:

$$(10-x)\,Ca^{2+}_{(aq)} + xSr^{2+}_{(aq)} + {}_6PO_4^{3-}{}_{(aq)} + 2OH^{-}_{(aq)} \rightarrow Ca_{10-x}Sr_x(PO_4)_6(OH)_{2(s)}$$

Where x is the content of strontium.

More precisely, the synthesis of Sr-nano-HA consisted in feeding a solution containing calcium ($CaCl_2$)/strontium ($SrCl_2 \cdot 6H_2O$) and a phosphate (KH_2PO_4) solution, containing KOH as alkaline reactant in order to control the solution pH in the range of 10-13, through the NETmix reactor in order to produce a milky suspension of doped hydroxyapatite by wet chemical precipitation method (flowrate 285 L/h) at room temperature. The precipitated Sr-nano-HA was collected and washed with distilled water to eliminate the residual ions.

All the reagents were purchased from Sigma Aldrich and used as received.

2.6 Electrospinning

An electrospinning technology for collagen-based systems focusing on the preservation of the protein structure and to obtain a nanofibrous homogeneous fibrous matrix was optimized, in order to obtain fibrous biomimetic scaffolds to be used for bone tissue engineering. Electrospinning is a comparatively versatile technique to fabricate nanofibers, membranes, and scaffolds; the basic setup of the electrospinning technique consists in a spinneret section and an electric field applied in order to form a liquid jet that due to different types of forces (electrostatic forces, surface tension, viscoelastic force, gravity) is able to produce sub-millimetric and sub-micrometrics fibers, then collected on a metal collector. In the process a drop of the polymer solution is created on the needle that not falls due to the surface tension, when a sufficient high voltage applied the solution becomes charged and the electrostatic repulsion counteracts the surface tension, resulting in a stretching of the drop; at a critical point a jet of the liquid solution erupts from the drop surface and, with a sufficient molecular cohesion of the liquid, the breakup of the jet does not occurs, this point where the jet starts is known as the Taylor cone. After the liquid polymer jet is created from a needle it elongates under the forces mentioned above, and when the polymer solution is drawn to the collector, the rapid evaporation of the solvent allows to obtain a

deposition of dry fibers, whose size is strictly dependent on the process parameters and the physico-chemical characteristic of the material, as represented in Figure 2.5. Furthermore, the type of collector used can result in a different orientation of the deposited fibers; for example, a plate collector can be used to obtain membranes with not ordered nanofibers deposition to mimic ECM, a rotating drum collector is used to collect aligned nanofiber sheets and producing a homogenous nanofiber mats, moreover using different length/ diameter ratio with different rotating speed an even fiber sheet or aligned fibers can be made; fibers can be collected in large areas but the fabrication of highly aligned fibers is difficult. In contrast, a rotating wire collector, composed of thin stainless-steel wires arranged at the same distance from the axis of rotation, is also used to collect aligned fibers, but the realization of highly aligned fibers happens with more simplicity. Finally, the mandrel collector is similar to the drum collector, but the smaller diameter allows to make tubular nanofiber samples.

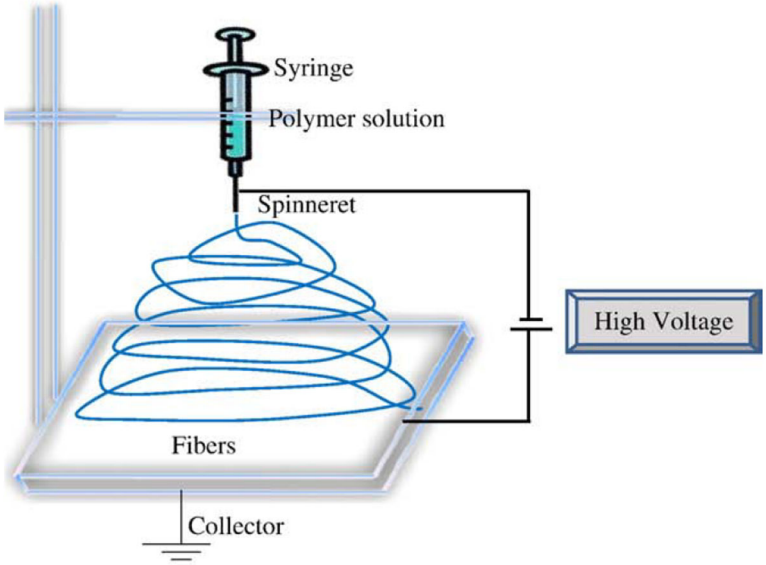

Figure 2.5: Schematic diagram of electrospinning apparatus with a vertical set[267].

For the optimization of a suitable system for the electrospinning, collagen dissolution was investigated and then electrospun, different critical aspects were considered: the dissolution of the collagen in a solvent suitable for the electrospinning but at the same time not harmful to the protein, the process to suspend MBG-Sr or Sr-nano-HA into the collagen solution in order to obtain fibers with a well dispersed inorganic phase, and the methods to enhance the poor mechanical properties and fast degradation time of electrospun collagen membranes. The electrospinning tests were conducted using a custom-made

electrospinning setup placed under a chemical hood and a control system of temperature and room humidity. In order to obtain fibers with a random orientation, for all tests a plate collector was used with a needle of 21 G (internal diameter of 0.8 mm).

2.6.1 Type I collagen extraction from rat tail tendon

Type I collagen used to the electrospinning studies was extracted from rat tail tendon by NOVAICOS company (Novara, Italy). In details, collagen fibers were first dissected into small parts, transferred in 0.2% AA, and stirred at 4 °C for three days; the obtained viscous solution was blended in a house-ware blender in ice to avoid the overheating and then centrifugated at 3500 rpm at 4 °C, filtered and kept at 4 °C. This method of extraction allows to maintain the structural integrity of the collagen protein. Moreover, each preparation of collagen was then jellified and incubated at 37 °C, 5% CO_2 in sterile complete medium in order to test the sterility of the preparations, microbial growth was not detected; preparations were also analyzed by SDS-PAGE in a 10% polyacrylamide gel to detect the presence of contaminant proteins or degraded collagen chains; SDS-PAGE is a technique where proteins were linked to the sodium dodecyl sulphate molecule (every 2 amino acids one molecule of SDS is bonded) that breaks the non-covalent interactions making the proteins linear with a negative charge proportional to the protein mass, proteins were then separated based on their mass on a polyacrylamide gel by electrophoresis; the preparations resulted not contaminated and not degraded. Finally, COL was also analyzed with FTIR in order to investigate the reproducibility of the process.

2.6.2 Preparation and electrospinning of type I collagen solutions

In order to obtain a polymer solution suitable for the electrospinning with preserved structure and biological functionality of collagen, 40% AA (glacial ≥99%, Sigma Aldrich, Italy) in water was investigated for dissolving COL, and compared with HFP (≥99%, Sigma Aldrich, Italy) widely used in the literature for the dissolution of collagen in the electrospinning processes. COL was obtained by the lyophilization with a Lyovapor L-200 freeze-dryer (Büchi, Switzerland) of a solution of 1% w/v rat type I collagen in PBS provided by NOVAICOS company and stored at -20 °C before the use. To detect the preservation of the structural properties of the collagen dissolved, FTIR and SDS-PAGE were performed. Since the COL dissolved in HFP solvent did not preserve its structural properties on the contrary of the COL dissolved in 40% AA as demonstrated FTIR spectra and

SDS-PAGE, the solutions for the electrospinning were prepared by dissolving the collagen in 40% AA. The selection of collagen concentrations was based on previous studies aimed to obtain a solution that can be easily electrospun avoiding the formation of non-homogeneous fibrous matrices and beads.

2.6.2.1 Preparation and electrospinning of 20% collagen solution

The COL solution was prepared by the dissolution of COL in 40% AA solution with a concentration of 20% w/v. In particular, 1 g of lyophilized COL was dissolved in 5 mL of 40% AA, the solution of COL was then covered and stirred at 300 rpm overnight at room temperature, under a chemical hood. The obtained solution (called 20COL) was then transferred in a 5 mL syringe and centrifuged (Hermle Labortechnik Z326) for 2 min at 2000 rpm in order to remove all the bubbles formed during the dissolution before the electrospinning. Before starting the process, an aluminium foil was placed on the plate collector in order to easily remove the electrospun matrix without damage it. The 20COL solution was then electrospun with a distance between the emitter and the collector of 10 cm with a voltage ranging from 22 to 24 kV and a flow rate of 300-350 µL/h. The formation of a stable Taylor cone was observed during the application of the selected voltage (Figure 2.6). The temperature and the room humidity were maintained constant (23 °C and 35%, respectively) and the solution was electrospun for a total time of 3 h in order to obtain a thick matrix that can be easily characterized. The obtained electrospun matrices were removed from the collector and dried overnight at room temperature and then analyzed.

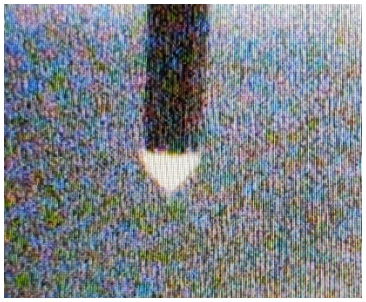

Figure 2.6: Taylor cone formed during the electrospinning process.

2.6.2.2 Preparation and electrospinning of 20% collagen and strontium containing mesoporous bioactive glasses suspension

The COL solution was prepared by the dissolution of COL in 40% AA solution and separately MBG-Sr were suspended in 40% AA. The volumes of 40% AA for

the dissolution of COL and the suspension of MBG-Sr were selected in order to obtain a final COL concentration of 20% w/v upon mixing. Different concentrations of MBG-Sr micro- or nanoparticles (5% w/v, 7.5% w/v, 10% w/v, 12.5% w/v, and 15% w/v) in the final suspension were tested to identify the best choice in term of incorporated amount and homogeneous dispersion within the electrospun matrix. In particular, 1 g of lyophilized COL was dissolved in 3 mL of 40% AA, covered and stirred at 300 rpm overnight at room temperature, under a chemical hood. In another batch, 750 mg of MBG-Sr were suspended in 2 mL of 40% AA, stirred for 1 h at 500 rpm and sonicated using an ultrasonic bath (Digitec DT 103H, Bandelin) for 1 h. Subsequently, MBG-Sr suspension was further stirred at 500 rpm, and once the two solution was prepared, MBG-Sr suspension was added drop by drop in the COL solution and the resulted suspension was stirred at 300 rpm for 1 h at room temperature. The obtained 20COL/MBG-Sr suspension was then transferred in a 5 mL syringe and centrifuged (Hermle Labortechnik Z326) for 2 min at 1000 rpm in order to remove all the bubbles formed during the dissolution and the mixing before the electrospinning and avoiding the precipitation of the inorganic phase. Before starting the process, an aluminium foil was placed on the plate collector in order to easily remove the electrospun matrix without damage it. The 20COL/MBG-Sr suspension was then electrospun with a distance between the emitter and the collector of 10 cm with a voltage ranging from 22 to 24 kV and a flow rate of 300-350 μL/h. The formation of a stable Taylor cone was observed during the application of the selected voltage, the temperature and the room humidity were maintained constant (23 °C and 35%, respectively) and the suspension was electrospun for a total time of 3 h in order to obtain a thick matrix that can be easily characterized. The obtained electrospun matrices were then removed from the collector, dried overnight at room temperature, and analyzed.

2.6.2.3 Preparation and electrospinning of 20% collagen and strontium substituted nano-hydroxyapatite suspension

The COL solution was prepared by dissolving COL in 40% AA solution and in a separately solution of 40% AA the Sr-nano-HA (50% Sr in the crystalline structure, provided by FLUIDINOVA, Portugal) were suspended. The quantity of 40% AA used for the dissolution of COL and for the suspension of Sr-nano-HA were calculated for obtaining a final COL concentration of 20% w/v and different tested concentrations of Sr-nano-HA (5% w/v, 7.5% w/v, 10% w/v, 12.5% w/v, and 15% w/v), to obtain a matrix with a well dispersed inorganic phase. In particular, 1 g of lyophilized COL was dissolved in 3 mL of 40% AA, covered

and stirred at 300 rpm overnight at room temperature, under a chemical hood. In another batch, 500 mg of Sr-nano-HA were suspended in 2 mL of 40% AA, stirred for 1 h at 500 rpm, sonicated using an ultrasonic bath (Digitec DT 103H, Bandelin) for 1 h, and further stirred at 500 rpm. Once the collagen solution and the Sr-nano-HA suspension were prepared, Sr-nano-HA suspension was added drop by drop in the COL solution and the resulted suspension was still stirred at 300 rpm for 1 h at room temperature before the electrospinning. The obtained 20COL/Sr-nano-HA suspension was then transferred in a 5 mL syringe and centrifuged (Hermle Labortechnik Z326) for 1 min at 1000 rpm to remove all the bubbles formed during the dissolution and the mixing without the precipitation of Sr-nano-HA. Before starting the process, an aluminium foil was placed on the plate collector to easily remove the electrospun matrix without damage it. The 20COL/Sr-nano-HA suspension was then electrospun with a distance between the emitter and the collector of 10 cm with a voltage ranging from 23 to 24 kV and a flow rate of 300-350 µL/h, the formation of a stable Taylor cone was observed during the application of the selected voltage. The temperature and the room humidity were maintained constant (23 °C and 35%, respectively). The suspension was electrospun for a total time of 3 h to obtain a thick matrix that can be easily characterized. The obtained electrospun matrices were then removed from the collector and dried overnight at room temperature and finally analyzed.

2.6.2.4 Preparation and electrospinning of 20% collagen and 0.1% Rose Bengal solution

The 20% collagen and 0.1% Rose Bengal solution (20COL/0.1%RB) solution was prepared by the dissolution of COL and RB (Dye content ≥80 %, Sigma Aldrich, Italy) in 40% AA solution with a concentration of 20% w/v and 0.1% w/v, respectively. In particular, 1 g of lyophilized COL and 5 mg of RB were dissolved in 5 mL of 40% AA. The resulting 20COL/0.1%RB solution was then covered and stirred at 300 rpm overnight at room temperature, under a chemical hood. The obtained solution was then transferred in a 5 mL syringe and centrifuged (Hermle Labortechnik Z326) for 2 min at 2000 rpm in order to remove all the bubbles formed during the dissolution before the electrospinning. Before starting the process, an aluminium foil was placed on the plate collector in order to easily remove the electrospun matrix without damage it. The 20COL/0.1%RB solution was then electrospun with a distance between the emitter and the collector of 10 cm with a voltage ranging from 22 to 24 kV and a flow rate of 300-350 µL/h. The temperature and the room humidity were maintained constant (23 °C and 35%, respectively). The solution was electrospun for a total time of 3 h in order to

obtain a thick matrix that can be easily characterized. The obtained electrospun matrices were removed from the collector and dried overnight at room temperature and then analyzed.

All the steps with the RB dye (starting from the dissolution to the drying of the obtained electrospun matrices) were performed keeping away the direct light to avoid premature activation of RB dye.

2.6.3 Crosslinking methods

Since the collagen electrospun matrices result in poor mechanical properties and fast degradation times, two types of crosslinking methods were investigated with the aim to enhance these properties. The analyzed crosslinking methods are both chemical crosslinking: an EDC/NHS coupling which exploit the amino and carboxyl groups both present in the collagen protein to link them to each other, and a crosslinking method using a photoinitiator called Rose Bengal and using a 514 nm light to activate it (Figure 2.7).

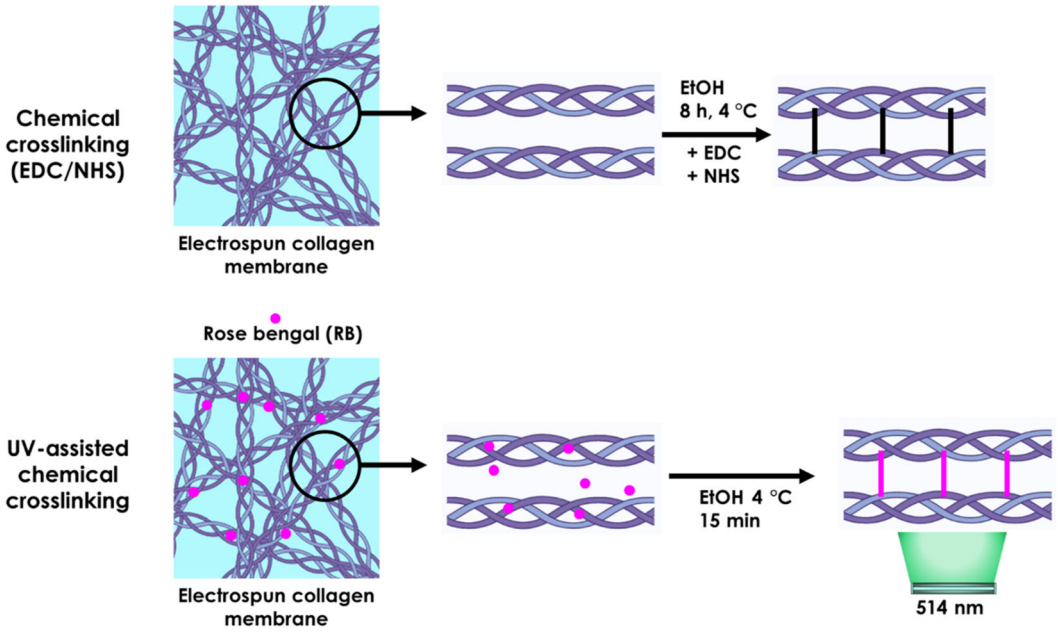

Figure 2.7: EDC/NHS chemical crosslinking and crosslinking method using Rose Bengal as photoinitiator of electrospun collagen membranes.

2.6.3.1 EDC/NHS coupling crosslinking method

Electrospun collagen membrane crosslinking with the EDC/NHS coupling was investigated using a modified procedure previous described by Ribeiro et al[193].

In detail, collagen membranes obtained after the electrospinning were soaked in a solution of absolute ethanol (Ethanol puriss. P.A., absolute = 99.8%, Sigma Aldrich, Italy) containing both EDC (Sigma Aldrich, Italy) and NHS (Sigma Aldrich, Italy) reagent, with a respectively concentration of 30 mM and 15 mM, for 8 h at 4 °C in order to allow the complete reaction without the degradation of the collagen protein. Then, membranes were washed two times with absolute ethanol and stored at -20 °C before the lyophilization with a Lyovapor L-200 freeze-dryer (Büchi, Switzerland) to remove all the ethanol residual. After the lyophilization, membranes were manually detached from the aluminium foil and stored at 4 °C.

2.6.3.2 crosslinking method using Rose Bengal as photoinitiator

Another method to crosslink the electrospun membranes was investigated by the use of the RB photoinitiator, able to be activated by a 514 nm, radiation using a modified procedure developed by Liu T. et al[30]. In order to include the photoinitiator in the collagen membranes for the subsequent activation, the electrospinning procedure was performed by the preliminary addition of RB dye immediately after the dissolution of the collagen in the 40% AA solution and later the resulting solution was electrospun as described in the 2.5.1.4 section. Once the electrospun collagen matrices with RB were obtained, membranes were soaked in a solution of 95% absolute ethanol (Ethanol puriss. P.A., absolute = 99.8%, Sigma Aldrich, Italy) for 15 min at 4 °C, then ethanol was removed, and the membranes impregnated of ethanol were irradiated at 514 nm for 100 s and stored at -20 °C before the lyophilization with a Lyovapor L-200 freeze-dryer (Büchi, Switzerland) to remove all the ethanol residual. After the lyophilization, membranes were manually detached from the aluminium foil and stored at 4 °C.

All the steps from the dissolution of RB until the irradiation were performed keeping away the direct light to avoid premature activation of RB dye.

2.7 Morphological, structural and compositional characterization

In the following section the morphological, structural and compositional analyses performed to investigate and characterize the different morphology, size, structural features and compositions of the produced materials and scaffolds will be described. Collected data allowed the selection of the best suitable material and scaffold.

2.7.1 Morphological analysis by Field Emission Scanning Electron Microscopy and Scanning Electron Microscopy

The FESEM and the SEM are non-destructive techniques which efficiently give morphology, compositional and structure information of the analyzed material. An electron gun generates a high energy electron beam on the sample, scanning the material surface at very low potentials ranging between 0.02 and 5 kV with a very good spatial resolution. Whenever samples are not electrically conductive, to reduce the obstructing of the electron path caused by the surface charging, preceding the imaging a samples preparation process is required. To eliminate the charges on the sample surface, a deposition of a generally very thin (5-10 nm) conductive heavy metal layer such as Pt, Cr or Au is performed. On all the above-mentioned MBGs samples a FESEM characterization was performed to evaluate their morphology, size, and shape, moreover, FESEM analysis was assessed on MBGs samples after soaking in SBF to investigate the formation of a hydroxyapatite layer (see section 2.8). For the preparation of the samples, 5 mg of nano-sized MBGs samples, synthetized by the base-catalyzed sol-gel method, were dispersed in 5 mL of isopropanol in an ultrasonic bath (Digitec DT 103H, Bandelin) for 10 min to obtain a stable suspension. Then, the suspension was dropped on a copper grid (3.05 mm Diam.200 MESH, TAAB), dried in air and coated with Cr (layer of ~7 nm) prior the imaging. On the contrary, micro-sized MBGs synthetized by the aerosol assisted spray dryer approach were dispersed on a conductive carbon tape adhered on a stub as dried powder and then coated with a Cr layer of about 7 nm. All MBGs samples were analyzed with a ZEISS MERLIN instrument. Conversely, collagen membranes were directly placed on a carbon tape adhered on a stub and coated with a 7 nm thin platinum layer before the imaging, all collagen membrane samples were analyzed with a PHENOM XL instrument.

2.7.2 N_2 adsorption-desorption analysis

N_2 adsorption-desorption measurements analyzes the sample SSA, pore volume and size, as well as the pore shape and distribution used to the determination of the textural properties of a large assortment of solid materials (for example catalysts, pigments, or glasses/ceramics)[148]. When an adsorbable gas called adsorptive got in contact with the solid surface called adsorbent, a physisorption phenomenon in which intermolecular forces (in particular van der Waals forces) are involved occurs[268]. The temperature of the performed measurement for most of the adsorption analyses is above the freezing point of the gas used but

lower than its triple point[269]. After the definition of the adsorbent (MBGs-based samples) and the adsorptive (nitrogen at 77 K), the amount of gas adsorbed was measured as a function of relative pressure (p/p_0) at constant temperature and reported as an adsorption isotherm.

When the analysis is concluded, the instrument report a different adsorption isotherm for different types of samples, in fact, according to IUPAC classification there are six types of isotherms (Figure 2.8)[148, 270]:

- Type I isotherm typically concerns materials with a small external surface and with micropores (pore size <2 nm); two different types of isotherms can be obtained by the use of nitrogen at 77 K and argon at 87 K: the type I(a) isotherm when the microporous material possesses narrow micropores with a width of about 1 nm, and the type I(b) isotherm when the material presents a broader pore size distribution ranging from micropores to narrow mesopores (<~2.5 nm).
- Type II isotherm is obtained by nonporous or microporous (pore size >50 nm) materials, the unrestricted monolayer-multilayer adsorption up to high p/p_0 determines its shape. The completion of the monolayer coverage is reported in the figure 2.8 by the point B.
- Type III isotherm is typical of nonporous or microporous materials, and it is the result of weak interactions between the adsorbent and the adsorbate.
- Type IV isotherm is typical of mesoporous materials, where the adsorption depends both on the adsorbent-adsorptive interaction and on the molecules in the condensed state. In this case, a gas condensation in the pores follows the initial monolayer-multilayer adsorption phase, in fact, in the isotherm the monolayer-multilayer adsorption of nitrogen molecules on the walls of the mesopores corresponds to the adsorption to low p/p_0, and the condensation of the nitrogen gas in the pores follow this phase at pressure $<p_0$. Generally, these types of isotherms end with a saturation plateau.

Also in this case, two different type IV isotherms can be obtained: type IV(a) isotherm typical of mesoporous materials exhibiting pores larger than a critical width (4 nm if nitrogen at 77 K is used as adsorptive) presenting a hysteresis loop in the capillary condensation region; and type IV(b) isotherm typical of mesoporous materials with smaller mesopores, usually conical or cylindrical mesopores.

- Type V isotherm is typical to weak adsorbent-adsorbate interactions such as the adsorption of water in hydrophobic microporous and mesoporous materials; this type of isotherm is very similar to type III isotherm.

- Type VI isotherm is typical when a highly uniform nonporous surface presents a layer-by-layer adsorption.

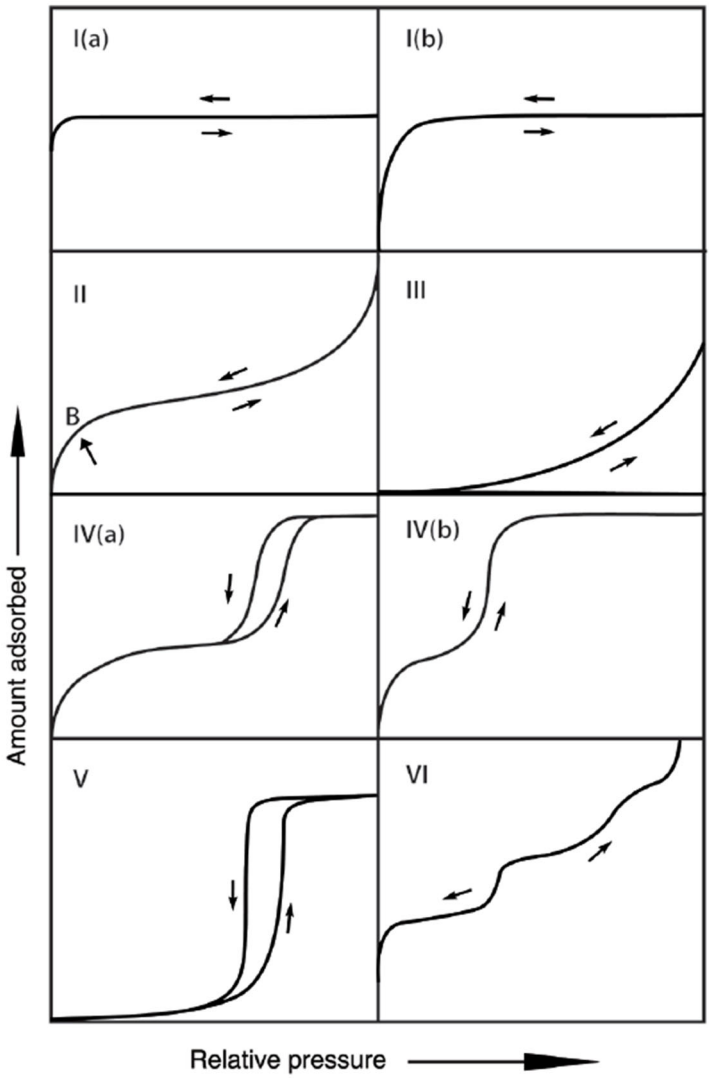

Figure 2.8: IUPAC classification of physisorption isotherms[270].

Moreover, in the multilayer range of physisorption isotherms can be noticed a hysteresis loop generally associated to the capillary condensation. Normally, can be generated five types of hysteresis loops (H1, H2, H3, H4 and H5) based on the structure of pores and the adsorption mechanism (Figure 2.9):

- H1 hysteresis loop is generated when mesoporous materials show a narrow range of uniform mesopores.

- H2 hysteresis loop generally is associated to more complex pore features; specifically, H2(a) could be attributed to the block of pores in a narrow pore range while H2(b) could be ascribed to the pore blocking with pores with larger neck widths.
- H3 hysteresis loop occurs when there are aggregates of plate-like particles.
- H4 hysteresis loop is typical of materials showing narrow and elongated pore size.
- H5 hysteresis loop regards materials with both open and partially blocked pores.

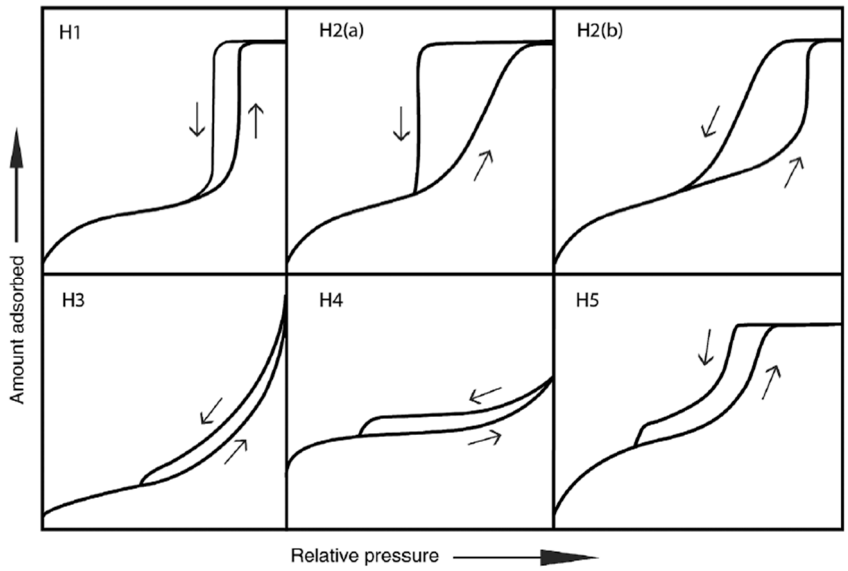

Figure 2.9: IUPAC classification of hysteresis loops[270].

The analysis of the data acquired by the N_2 adsorption-desorption measurements allows to obtain different material properties such as SSA value, pore volume, and pore size. To analyze the data can be adopted different methods. In particular, the BET gas adsorption method is one of the most used to calculate the SSA of mesoporous materials[148, 270]. The theory that the adsorption enthalpy remains constant during the multilayer formation is the basis of this method. The BET equation is the following:

$$\frac{\mathrm{p}}{\mathrm{V}(p_0 - \mathrm{p})} = \frac{1}{V_m C} + \frac{C-1}{V_m C}\frac{p}{p_0}$$

Where p is the equilibrium pressure (torr), V is the adsorbed volume for every gram of solid, p_0 is the saturation pressure at 77 K (torr), V_m is the monolayer

volume of N_2 (mL), and C is the parameter associated to the energy of the monolayer adsorption.

The values of V_m and C can be calculated after the measuring of the linear correlation in a limited range of p/p_0 (0.05 and 0.3), made possible by plotting of $p/(V(p_0-p))$ as a function of p/p_0. Then, SSA value is determined by the following equation[271]:

$$SSA = \frac{\sigma V_m N_a}{v}$$

Where SSA is the specific surface area in m^2/g, σ is the molecular cross-sectional area occupied by the molecules of adsorbate in the monolayer (for N_2 is 13.5 Å), N_a is the Avogadro number ($6.022 \cdot 10^{23}$), and v is the molar volume of the adsorbed gas that for N_2 is 22.414 mL/mol.

To calculate the pore size distribution and the total pore volume, one of the most used methods is based on the established principles of statistical mechanics and is the one of Non-Local DFT, where the calculation of the function of pore size distribution derives from an equation able to correlate the isotherm kernel with the experimental isotherm[270].

All the MBGs-based samples were analyzed by the N_2 adsorption-desorption measurements to evaluate both the SSA and the structure of mesopores. Before the analysis, in order to avoid a change in the surface structure the samples were outgassed to remove all the species that are physiosorbed. Nano-sized particles were outgassed at 200 °C for 3 h, while micro-sized particles were outgassed at 150 °C for 3 h. Finally, in order to avoid the denaturation of ICOS-Fc biomolecule, all the samples grafted with ICOS-Fc were outgassed at 37 °C for 5 h. To calculate the SSA from the adsorption data (relative pressure 0.04-0.2) was used the BET equation, while for the pore size distribution was used the DFT method using the Non-Local DFT kernel of equilibrium isotherm (desorption branch). All the samples were analyzed with an ASAP2020 (Micrometrics) instrument with nitrogen as adsorptive (77 K).

2.7.3 Compositional characterization

Energy Dispersive Spectroscopy. The EDS technique is widely used to examine and evaluate the elemental composition of the analyzed samples, during the analysis, after the exposure of the sample surface to a high-energy electron beam the electrons from the atoms are ejected, then the formed electron vacancies are filled by electrons present in the higher states with the consequent emission of

an X-ray for the balancing of the difference of energy of the two electrons states. The characteristic set of peaks detected from the instrument is unique for each element.

The EDS analysis was performed on all above-mentioned MBGs-based samples with the aim to identify the elemental composition and confirm the incorporation of the therapeutic ions in the silica framework: samples in dry powder form were dispersed on a conductive carbon tape adhered on a stub and coated with a Cr layer of 7 nm before the analysis performed by an Aztec EDS equipment.

Inductively Coupled Plasma Atomic Emission Spectroscopy. In the ICP-AES method, atoms and ions were excited by a plasma causing the emission of an electromagnetic radiation with a wavelength unique for each element. Consequently, this technique can evaluate the quantity of a specific element present in a water-based medium, even if very low concentrations (ppb) of element is present. During the analysis, the liquid sample is prior converted in an aerosol, then the aerosol was atomized using an argon plasma which is a neutral conducting gas with the same number of cations and electrons. The atomization give energy to excite the electrons with the subsequent electron transfer in high energy levels and, after the decay of the electrons in their ground energy state, a radiation is emitted. The emitted light allows to identify the element due to the specific wavelengths of each element, furthermore, the intensity of the radiation is proportional to the element concentration in the sample. This technique possesses high sensitivity, good precision and accuracy.

This technique was used to evaluate the ions concentration release from the collected supernatant of the MBGs-based samples tested using the procedure reported in section 2.7. Before the measurements, in order to obtain a suitable detectable ions concentration for the ICP-AES instrument, all the collected supernatants were diluted in ddH_2O and, in addition, the effective amount of incorporated ions in the MBGs-based samples was also evaluated using this technique by the dissolution of the samples in a mixture of nitric and hydrofluoric acids (0.5 mL of HNO3 and 2 mL of HF every 10 mg of samples) and the measurement via ICP analysis of the obtained solutions. An ICP-MS, Thermoscientific, ICAP Q instrument was used for all the analyses.

Fourier Transform Infrared. FTIR spectroscopy exploits the infrared radiation to scanning the samples and analyze and identify organic, inorganic, and polymeric materials. Normally, a FTIR spectrometer is composed by a source of the radiation, a cell with the sample, the detector, an amplifier, an A/D convertor

to convert the radiation signal in a digital signal, and a computer (Figure 2.10); the generated radiation transits in an interferometer and reaches the detector, then the signal is amplified and subsequent converted to a digital signal and transferred to the computer where is executed the Fourier transform. The infrared radiation passes on the sample and a part is absorbed by the sample and converted in vibrational and rotational energy, and the remanent part passes through the sample and is transmitted. The resultant signal obtained at the detector is a spectrum from 4000 to 400 cm^{-1} representing the molecular fingerprint of the sample, every material possesses a unique specific fingerprint where the absorption peaks represent the vibration frequencies of the bonds of the atoms, and consequently, FTIR spectroscopy is a key tool for the chemical identification.

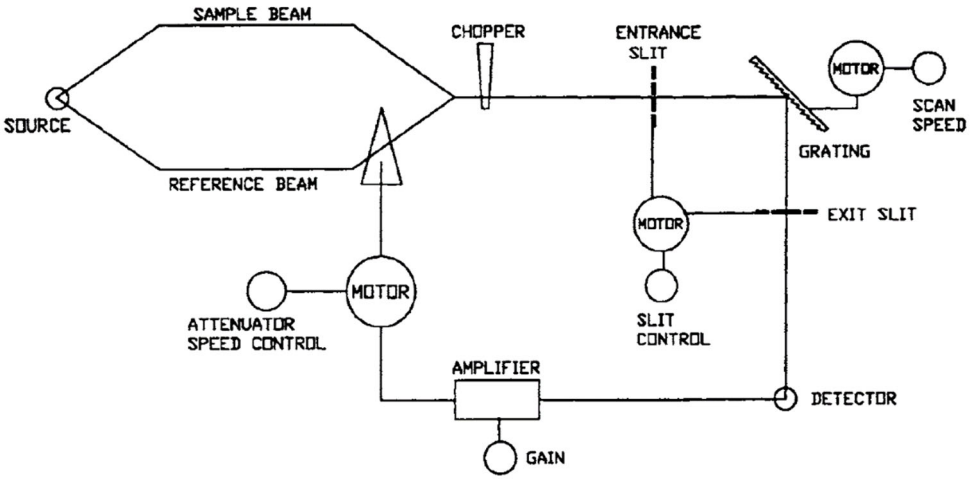

Figure 2.10: Schematic representation of the FTIR instrument[272].

In this PhD work, FTIR spectroscopy was used to confirm the successful functionalization of amino groups on the MBGs surface and the successful grafting of ICOS-Fc on MBGs surface as well as the preservation of the structural properties of the collagen dissolved for the electrospinning. FTIR spectra were collected by a Bruker Equinox 55 spectrometer (range of wavenumbers from 4000 to 400 cm^{-1} with a resolution of 2 cm^{-1}).

Thermogravimetric analysis. TGA measure the change in weight of a material under a controlled atmosphere as a function of the temperature and can identify different features of the material (such as the thermal stability, filler content in polymers, solvent content, and in particular the percent composition of components in a specific compound). During the analysis, the sample positioned in a furnace gradually increase the temperature while the weight is constantly

monitored by an analytical balance and when thermal events that involve a loss of volatile compound occurs, a weight loss is observed. The weight of the sample is then plotted against temperature.

In this PhD work, TGA was performed on amino functionalized MBGs, and ICOS-Fc grafted MBGs to confirm the presence of amino groups and ICOS-Fc biomolecule grafted. The ICOS-Fc amount was determined from the weight loss of MBGs-Sr-ICOS-Fc compared to MBGs-Sr-NH_2 and MBGs-Sr. Moreover, TGA was also performed on crosslinked collagen membranes to evaluate the successful crosslinking, and the weight loss was determined between 250 and 420 °C. Analyses were performed using a STA 2500 Regulus (Netzsch) instrument over a temperature range of 25-600 °C for MBGs-based samples and 25-800 °C for crosslinked collagen membranes, under air flux (flow of 50 mL/min) at heating rate of 10 °C min^{-1}, and data were collected using a Proteus® (Netzsch) software.

X-ray Diffraction. XRD is a non-destructive technique to characterize crystalline materials, providing both qualitative and quantitative information about the structure of the samples. This technique exploits the diffraction of X-rays by the crystal lattice of the analyzed solid; if $n\lambda=2d \sin\theta$ (Bragg's Law) is satisfied, when an X-ray monochromatic beam pass on the sample with a certain wavelength λ and a certain angle θ, the sample produces a constructive interference and a diffracted ray, as shown in Figure 2.11. The Bragg's Law correlate the wavelength to the diffraction angle and the lattice spacing in a crystalline sample, and by varying the angle θ, different d-spacings satisfy the Bragg's Law conditions in crystalline samples. Then, the diffracted X-ray is detected, processed, and counted, all the possible diffraction directions of the lattice can be reached by varying 2θ angles. Usually, the X-ray diffractometer use a Cu Kα X-rays (λ= 0.15406 nm) and operate at room temperature at known voltages and current over the 2θ range from 10 to 100 degrees in the steps of 0.01 degree in open quartz sample holders. The diffractogram is then obtained by plotting the diffracted X-ray intensities as a function of all the angular positions and it is characteristic for each material; in the diffractograms can be determined two different regions: an amorphous region characterized by broad peaks centered around the θ, which show a sharp peak for crystalline materials with the same composition; and a crystalline region characterized by sharp peaks resulting from the diffracted beams arising from different planes, several data can be obtained from the analysis of the diffractogram (such as the crystal cell symmetry and the type of phases, the quantitative composition by the derivation of the intensity of the peaks, and information of the crystal dimension).

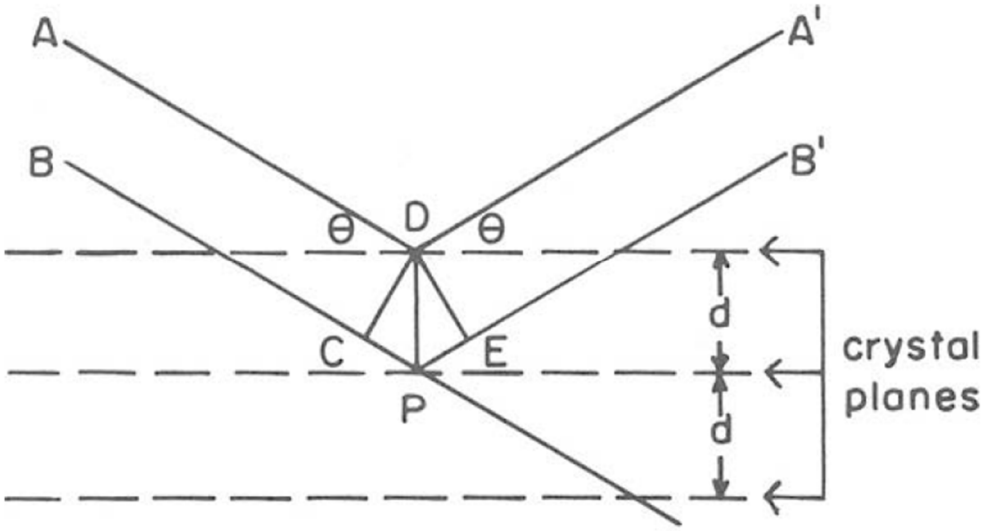

Figure 2.11: Diffraction from crystal planes according to Bragg's law[273].

All the MBGs-based samples and collagen membranes were analyzed through XRD using a Philips X'Pert diffractometer with a Cu K (40 kV, 20 mA) source in a 2θ range of 10–70 with a scan speed of 0.05°/s, to obtain different information on the material structure; MBGs-based samples were analyzed in order to investigate the possible presence of undesired segregated oxidic phases of the incorporated therapeutic metallic ions in the silica framework, moreover, the formation of hydroxyapatite layer after the soaking in SBF of MBGs-based samples (see section 2.8) was investigated in order to confirm the bioactive behaviour. Finally, collagen scaffolds with inorganic phases were analyzed through XRD to investigate the Sr-nano-HA presence in the membranes.

UV-Vis spectroscopy. UV-Vis spectroscopy is a quantitative technique used to measure the quantity of absorbed radiation by a chemical substance determining the intensity of the radiation that passes through the sample compared to the intensity passed through a blank or a reference sample. The basis of this method is the absorption of a monochromatic electromagnetic radiation in the ultraviolet (200-350 nm) and visible (350-700 nm) spectral region by species composed by particular atoms or a group of atoms responsible for ultraviolet and/or visible light absorption (chromophores). In particular, when a chromophore is excited with a specific amount of energy, atoms absorb the UV-visible radiation and electrons are excited from a lower to a higher energy level. Basically, an UV-visible spectrometer is composed by a light source, a monochromator, and a

detector; the light from the source is split by the monochromator into its component colors of different wavelengths, then the radiation passes through the sample and reach the detector which converts the light intensity in an electric signal, then amplified, and returns a diagram reporting the absorbance as a function of the wavelength. During the passage of the monochromatic radiation through the sample, part of the light can be absorbed while the rest is transmitted, the ratio between the intensity of the incoming radiation (I) and the resulting radiation after the sample absorption (I_0) is called transmittance, and the negative logarithm of the transmittance is called absorbance (A):

$$A = -log(I/I_0)$$

If the absorbance is known, the Lambert-Beer law can be used in order to calculate the concentration of the substance:

$$A = \varepsilon\, c\, d$$

Where ε is the molar extinction coefficient, peculiar for a substance (mol^{-1} L cm^{-1}), d is the optical path length, and c is the concentration of the solution (mol/L).

UV-visible spectroscopy was used to investigate the crosslinking degree of crosslinked collagen membranes by the measurement of the free amine presence (see section 2.11). For the analysis, using a blank solution containing the reaction mixture without the collagen, a baseline was recorded, then, the reaction mixtures with collagen or crosslinked collagen were analyzed after a dilution of 1:20 in ddH_2O by using a Thermo Scientific Multiskan GO, scanning from 200 nm to 600 nm and reading the absorbance value at 346 nm in order to compare the free amine groups between non-crosslinked collagen and the crosslinked collagen. All tests were performed in triplicate.

2.8 Ions release analysis on mesoporous bioactive glasses

Part of the work described in this chapter has been already published during the PhD period[259].

Strontium ions release tests were performed in order to investigate the ability of MBGs-Sr and MBGs-Sr-ICOS-Fc to release the incorporated therapeutic ions, even after the biomolecule grafting, by modifying the procedure described by Shi et al[274].

MBGs-Sr or MBGs-Sr-ICOS-Fc with a concentration of 250 μg mL^{-1} were soaked in Tris HCl buffer (Tris(hydroxymethyl)aminomethane (Trizma, Sigma Aldrich)) at 0.1 M and pH 7.4. Specifically, 5 mg of powder were suspended in 20 mL of Tris HCl buffer at 37 °C for different time steps (3 h, 1 day, 3 days, 7 days, and 14 days) in an orbital shaker (Excella E24, Eppendorf) using an agitation rate of 150 rpm. After each time point, the suspensions were centrifuged (Hermle Labortechnik Z326) for 3 min at 13000 rpm or for 5 min at 10000 rpm for nano-sized and micro-sized particles, respectively, half of the supernatant was collected, and the same volume of fresh Tris HCl buffer solution was added in order to maintain constant the total volume of the release medium, finally, the ion released concentration was measured by ICP-AES technique after an appropriate dilution. All the tests were performed in triplicate, moreover, to express the released percentage of the powder during the tests and to evaluate the total amount of the incorporated ions in the MBGs silica framework during the synthesis, particles were dissolved in a mixture of nitric acid and hydrofluoric acid (0.5 mL and 2 mL of HNO_3 and HF respectively, every 10 mg of powder) and measured with ICP analysis. Each test was performed in triplicate and the data are presented as means ± standard deviations.

2.9 Bioactivity test on mesoporous bioactive glasses

Part of the work described in this chapter has been already published during the PhD period[259].

The ability to create a hydroxyapatite layer of MBGs is an essential characteristic and a fundamental property of the material in order to promote the bone tissue regeneration and, since the bioactivity of MBGs is very important, bioactivity tests were performed, by following the protocol reported by Maçon et al.[275], where a unified method was used to evaluate the ability to form a hydroxyapatite layer of the bioactive glasses.

With the intention to evaluate the *in vitro* bioactivity, both MBGs-Sr and MBGs-Sr-ICOS-Fc were tested. In particular, 30 mg of sample was soaked in 30 mL of SBF (prepared with the reagents reported in Table 2.2) following the protocol reported in the literature at 37 °C in an orbital shaker (Excella E24, Eppendorf) with an agitation rate of 150 rpm[275]; the experiments were carried out up to 14 days and, at each time point (3 h, 1 day, 3 days, 7 days, and 14 days) powders were collected by centrifugation (Hermle Labortechnik Z326) for 3 min at 13000 rpm or for 5 min at 10000 rpm for nano-sized and micro-sized particles, respectively, washed two times with ddH_2O and dried at 70 °C for 12 h. Dried

samples were then analyzed with FESEM and XRD analysis in order to analyze the hydroxyapatite layer formation.

Table 2.2: Reagents for the preparation of SBF solution, the order in the table represents the order of addition.

Reagent	Amount (g L^{-1})	CAS number
NaCl	8.035	7647-14-5
$NaHCO_3$	0.355	144-55-8
KCl	0.225	7447-40-7
$K_2HPO_3 \cdot 3H_2O$	0.231	16788-57-1
$MgCl_2 \cdot 6H_2O$	0.311	7791-18-6
HCl 1 M	38 mL	7647-01-0
$CaCl_2 \cdot 2H_2O$	0.386	10035-04-8
Na_2SO_4	0.072	7757-82-6
Tris	6.118	77-86-1

2.10 Assessment of grafted ICOS-Fc functionality

Part of the work described in this chapter has been already published during the PhD period[259].

Since the challenge in the ICOS-Fc grafting procedure on MBGs surface is the preservation of the biomolecule biological functionality, meaning a correct orientation in which ICOS-Fc biomolecule and amino groups on MBGs-Sr-NH_2 are linked, without a denaturation of the biomolecule during the procedure, several tests (non-biological and biological) were performed on the grafted samples.

2.10.1 Enzyme-Linked Immunosorbent Assay-like assay

The ELISA technique is an assay system for the quantitative determination of antigens and antibodies, ELISA assay is very simple, rapid, sensitive, reliable, and versatile analysis and can be classified into two types[276]: a competitive assay using an antigen-enzyme conjugate or an antibody-enzyme conjugate, and noncompetitive assay using a double antibody "sandwich" technique with an indicator enzyme linked to the second antibody. To perform the test, an immunoreactant (antibody or antigen) is immobilized on a solid support by adsorption with noncovalent interactions (Figure 2.12A) and incubated with the test solution containing the analyte of interest that will interact and binds the immunoreactant (Figure 2.12B). After the incubation period, the support is washed and the bound antigen is detected by adding an enzyme-conjugated antibody which binds the antigenic site of the analyte linked to the immunoreactant (Figure 2.12C), and the amount of analyte of interest is visualized by the addition of a chromogenic or fluorogenic substrate (Figure 2.12D). The concentration of the product derived from the reaction of the added substrate is directly proportional to the concentration of the analyte antigen.

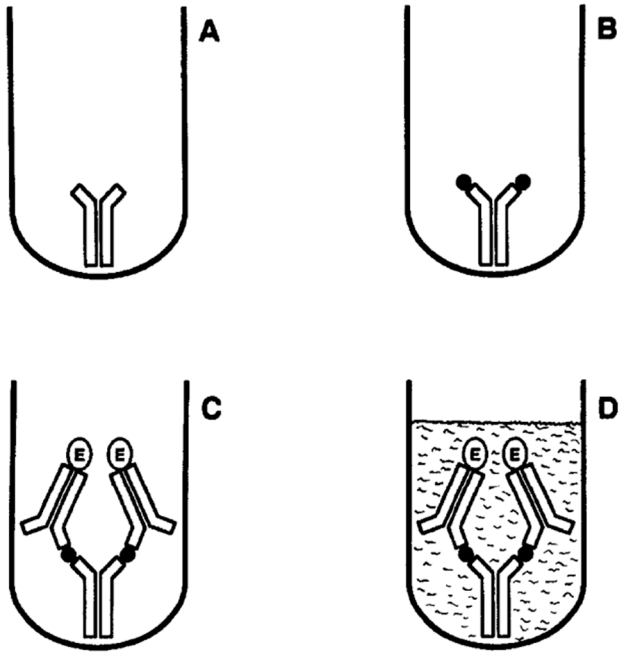

Figure 2.12: ELISA assay steps[276].

ELISA-like assay plates were prepared by coating with 1 µg/mL of human ICOSL-His (Sino-Biological, Beijing, China) in PBS at pH 7.4 overnight at 4 °C,

washed five times with 0.05% Tween-20 (Merck Life Science) in PBS (pH 7.4), and the non-specific binding was blocked by the incubation with the same washing solution for 1 h at room temperature. All the MBGs-Sr-ICOS-Fc were tested by the ELISA-like assay performed by NOVAICOS company in duplicate, using MBGs-Sr as negative controls, in order to indagate the correct orientation and the maintained functionality of the grafted ICOS-Fc. Moreover, were also tested the unbounded reaction supernatants in order to measure the amount of residual ICOS-Fc not grafted during the reactions (since the amount of ICOS-Fc grafted on particles cannot be directly calculated on particles samples) and the medium obtained after the bound stability tests (see section 2.10) to indagate the binding stability of ICOS-Fc biomolecule in DMEM (Sigma Aldrich) medium up to 21 days. Specifically, 1 h after the preparation of the plates, samples were added, incubated at 37 °C for 2 h and washed five times. Then, HRP-conjugated goat anti-human immunoglobulin (Ig)G (Dako, Santa Clara, CA, USA) was added, incubated for 1 h at room temperature and washed five times before the addition of TMB (Merck Life Science, Darmstadt, Germany) for the reaction to detect the ICOS-Fc presence, the reaction was then stopped by the addition of H_2SO_4 2N (Merck Life Science). Plates were then analyzed with a spectrophotometer at 450 nm (Packard SpectraCount, Meriden, CT, USA) and results recorded as OD value. The OD value, also defined as absorbance, is obtained by calculating the $\log_{10}$ with the exponent the result of the intensity of the light sent to the sample divided by the intensity after passing through the sample:

$$OD = log \frac{I_0}{I}$$

where I_0 is the intensity of the monochromatic radiation sent to the sample and I is the intensity of the monochromatic transmitted radiation.

2.10.2 Biological tests

Biological tests were performed by NOVAICOS company in order to indagate the biocompatibility of grafted samples as well as their effects on cells exhibiting the ICOSL molecule on the cell surface.

Biocompatibility test. For the biocompatibility tests, murine pre-osteoblast MC3T3-E1 cells (American Type Culture Collection, Manassas, VA, USA) were used to analyze if the MBGs grafted with ICOS-Fc samples show an effect on the cell vitality. Cells were grown as a monolayer in a DMEM supplemented with

10% FBS, 100 U/mL penicillin, and 100 µg/mL streptomycin (Gibco) and maintained at 37 °C in a 5% CO_2 in a humified atmosphere. After 24 h, the medium was removed and cells were incubated for different time steps (2, 4, and 7 days) in a medium containing titrated amounts of MBGs-Sr-ICOS-Fc (200, 100, and 10 µg/mL), after each time step, viable cells were evaluated by the addition of XTT reagent (Trevigen, Helgerman CT, Gaithersburg, MD, USA) for 3 h at 37 °C and read with a spectrophotometer at 450 nm (Packard SpectraCount, Meriden, CT, USA). The cell viability was calculated using the following formula:

$$cell\ viability = \frac{absrbance\ of\ sample}{absorbance\ of\ control\ (untreated\ cells)} \times 100$$

All the tests were performed in triplicate and the statistical analyses were performed using a GraphPad Prism 3.0 software (San Diego, CA, USA) and a one-way ANOVA and Dunnett Multiple Comparison tests.

Migration tests (Boyden chamber migration assay). For migration tests, prostate cancer PC-3 (ICOSL-positive) cells from human prostate carcinoma (American Type Culture Collection, Manassas, VA, USA) were used in order to examine the potential motility inhibition of grafted samples on the ICOSL-positive cells into a Boyden chamber (BD Biosciences, Milan, Italy) migration assay. This type of assay is based on a chamber with two media separated in compartments by a microporous membrane. Cells are placed in the upper compartment and allowed to migrate through the membrane pores into the lower compartment where chemotactic agents are present, after the incubation time, the membrane is fixed and stained, and the number of the migrated cells is determined[277].

Cells were grown in RPMI 1640 (Gibco, Life Technologies, Carlsbad, CA, USA) medium supplemented with 10% FBS, 100 U/mL penicillin, and 100 µg/mL streptomycin (Gibco) and maintained at 37 °C in a 5% CO_2 in a humified atmosphere. For the assay, PC-3 cells were plated onto the apical side of 50 µg/mL Matrigel-coated filters (8.2 mm diameter and 0.5 µm pore size; Neuro Probe, Inc.; BIOMAP snc, Milan, Italy) in a serum-free medium with or without the presence of grafted samples at different concentrations (2, 0.2, 0.02, and 0.002 µg/mL), while a medium containing 20% FBS was placed in the basolateral chamber as a chemoattractant, and incubated for 6 h. Cells on the apical side were wiped off with Q-tips and the cells on the bottom of the filter were stained with crystal-violet and all counted with an inverted microscope. All the tests were performed in quintuplicate, and data were reported as percentages of the inhibition

of treated cells. Statistical analyses were performed using a GraphPad Prism 3.0 software (San Diego, CA, USA) and a one-way ANOVA and Dunnett Multiple Comparison tests.

Clonogenic assay. For the clonogenic assays, osteosarcoma cells were seeded on six-well plates; after one day, the cells were exposed at different concentrations of SG-Sr-ICOS-Fc and SD-Sr-ICOS-Fc for 72 h, then the medium was changed, and the cells were cultured for other 7 days in a medium without MBGs. Later, cells were fixed and stained with a solution of 80% crystal violet (Sigma Aldrich) and 20% methanol, then colonies were photographed; after, cells were washed, and 30% v/v acetic acid was added in order to induce a complete dissolution of the crystal violet. Finally, absorbance was recorded at 595 nm by a 96-well-plate ELISA reader. Five different experiments were performed.

Differentiation tests. For the differentiation tests, were used MDOCs prepared from $CD14^+$ monocytes isolated with the Easy Sep Human CD14 Negative Selection Kit (STEMCELL Technologies, Vancouver, BC, Canada) in order to investigate the potential of the differentiation inhibition of the ICOS-Fc biomolecule present on the grafted samples. Monocytes were plated and cultured for 21 days in a differentiation medium (DMEM (Lonza, Basel, Switzerland), 2mM of L-glutamine, 10% FBS (Invitrogen, Carlsbad, CA, USA), recombinant human M-CSF (25 ng/mL; R&D System, Minneapolis, MN, USA), and RANK-L (30 ng/mL; R&D System)). Every 3 days, the differentiation medium was changed, and cells were treated with MBGs-Sr-ICOS-Fc (2 μg/mL) and compared with the treatment using free ICOS-Fc or bare samples (MBGs-Sr). Then, phase-contrast images were acquired by Axiovert 40 CFL microscope (Zeiss, Oberkochen, Germany) equipped with a Q imaging camera and Image Pro Plus 7.0 software (Media Cybernetics Inc, Rockville, MD, USA). Moreover, the total RNA was isolated from MDOCs cultures in the day 21 by the use of TRIzol reagent (Invitrogen) and retrotranscribed with a QuantiTect Reverse Transcription Kit (Qiagen, Hilden, Germany) for the evaluation of the expression of the differentiation genes DC-STAMP, OSCAR, and NFATc1 using a gene expression assay (Assay-on Demand; Applied Biosystems, FosterCity, CA, USA); GAPDH gene expression was used in order to normalize the cDNA amounts. Then, a Real-time PCR was performed in duplicate using the CFX96 System (Bio-Rad Laboratories, Hercules, CA, USA) in a final volume of 10 μL containing 1 μL of diluted cDNA, 5 μL of TaqMan Universal PCR Master Mix (Applied Biosystems), and 0.5 μL of Assay-on Demand mix, and results were analyzed using the ΔΔ threshold cycle method. Finally, also the TRAP activity was evaluated; TRAP is a critical enzyme for the bone turnover highly expressed in

osteoclasts and it is generally used as a specific histochemical marker for these cells[278, 279], the evaluation of TRAP activity was assessed using the Acid Phosphatase kit (Sigma Aldrich) according to the manufacturer's instructions. In particular, cells after the treatment with MBGs-Sr-ICOS-Fc (compared with free ICOS-Fc and with MBGs-Sr) were fixed using a citrate solution (0.038 mol/L in 60% Acetone), washed, and incubated in a pre-warmed labeling solution (Fast Garnet GBC Base Solution 7 mg/mL dissolved in Acetate Solution 2.5 mol/L, pH 5.2, Naphtol AS-BI phosphoric acid solution 12.5 mg/mL, Tartrate Solution 0.67 mol/L, pH 5.2) at 37 °C for 1 h. Finally, microphotographs of TRAP staining were acquired using an EVOS FLoid Cell Imaging System (Life Technologies, Carlsbad, CA, USA).

2.11 Bound stability test on strontium containing mesoporous bioactive glasses grafted with ICOS-Fc

Part of the work described in this chapter has been already published during the PhD period[259].

As described in section 2.4.2, MBGs-Sr-ICOS-Fc were prepared using an EDC/NHS coupling reaction, this reaction link amino groups with carboxyl groups tartrateto form an amide bond. In order to confirm the presence of a stable bond between ICOS-Fc biomolecule and the MBGs-Sr surface, bound stability tests were performed; in particular, in a multiwell plate 3 mg of MBGs-Sr-ICOS-Fc samples were placed and 2 mL of DMEM supplemented with 10% heat-inactivated FBS (Lonza BioWhittaker, Spain), 1 mM Lglutamine (Lonza BioWhittaker, Spain), 200 mg/mL penicillin (Lonza BioWhittaker, Spain) and 200 mg/mL streptomycin (Lonza BioWhittaker, Spain) were added. Then, samples were soaked at room temperature for different time points (3, 7, 14, and 21 days) specifically chosen to mimic the time-course of osteoclast differentiation in vitro. At each time point, the supernatant and the samples were recovered separately, and an ELISA-like assay was performed (see section 2.9.1) both on supernatants and particles. All tests were performed in triplicate.

2.12 Crosslinking degree of electrospun collagen membranes (free amine test)

In order to investigate the crosslinking degree of crosslinked collagen membranes, a measurement of the free amine presence was performed. Basically, since the crosslinking exploits amino and carboxyl groups both present in the collagen

molecule, a diminution of the non-bonded amino groups in a crosslinked sample compared to a non-crosslinked sample denotes that the reaction between the two functional groups occurred. Thus, an UV-absorbing chromophore, called TNBS, was used in order to investigate changes in the free primary amino groups of crosslinked collagen membranes compared to non-crosslinked collagen.

In particular, tests were performed by following a procedure reported both by Tronci et al. and Davidenko et al. modified in terms of time and temperature of the process[280, 281], where 11 mg of COL or crosslinked collagen membrane were reacted with 1 mL of a $NaHCO_3$ solution (4% w/v, pH ~ 8.5) (Sigma Aldrich, Italy) and 1 mL of TNBS solution (0.5% w/v) (Sigma Aldrich, Italy) under stirring for 3 h at 40 °C. Then, 3 mL of a HCl (Sigma Aldrich, Italy) solution (6 M) was added and the resulting solution was further stirred for 1 h at 90 °C, the collected solution was diluted in ddH_2O (1:20) before reading in a UV-visible spectrophotometer at 346 nm (see section 2.6.3). All samples were prepared in triplicate and a buffer made of TNBS-only solution was used as control.

Chapter 3

Development, characterization and *in vitro* studies of the biomaterials developed for the electrospun multifunctional scaffold

3.1 Introduction

With the final aim to develop a bioactive collagen-based multifunctional scaffold fabricated by electrospinning technology, type I collagen (COL) with mesoporous bioactive glasses (MBGs) or nano-hydroxyapatite (nano-HA) as inorganic phase were combined to stimulate the healing of pelvis osteoporotic fractures. COL and hydroxyapatite are the main organic and inorganic phases of bone tissue, respectively, and MBGs are known for their high bioactive and pro-osteogenic properties. In addition, strontium ions were incorporated into the inorganic phases in order to exert a specific pro-osteogenic effect and ICOS-Fc biomolecule was grafted on the MBGs surface in order to synergistically provide an anti-osteoclastogenic effect to the final scaffold. Indeed, ICOS-Fc has been proven to reversibly inhibit the activity of osteoclasts and the combination of its effect with the strontium ions effects is expected to restore the normal bone tissue balance.

In this PhD work, COL and nano-HA were provided by two different companies (NOVAICOS and FLUIDINOVA, respectively), while MBGs-based

materials were fully developed and characterized. The present chapter will present and discuss the results of the characterization of MBGs-based materials.

For the synthesis of the inorganic phase, consisting of MBGs, two synthesis procedures have been selected to produce the samples with a composition based on SiO_2, CaO, and SrO (molar ratio 85/5/10). The first procedure is a base-catalyzed sol-gel method where ammonia was used as a catalyst to produce nano-sized particles with a diameter in the range of 100 and 300 nm and pores around 4 nm, while the second procedure consists in an aerosol-assisted spray-drying approach to produce micro-sized particles having a size ranging between 1 and 5 μm and pores in the range of 5-7 nm. The amount of therapeutic ions added during the synthesis was selected to obtain specific effects in terms of efficacy and biocompatibility, and the related results are described in sections 3.2.1 and 3.2.2. In addition, scale-up trials from lab scale to pilot scale were performed for the materials synthesized by the aerosol-assisted spray-drying approach and related results will be reported in section 3.2.3.3.

Once characterized the strontium containing MBGs, ICOS-Fc was grafted on the MBGs surface by exploiting surface functionalization with amino groups followed by an EDC/NHS coupling procedure. The results of the characterization related to strontium containing MBGs grafted with ICOS-Fc will be reported in section 3.3, with a focus on *in vitro* biological tests in section 3.3.3.

3.2 Morphological and structural characterization of strontium containing MBGs nano- and microparticles

3.2.1 Strontium containing mesoporous bioactive glasses nanoparticles

Part of the work described in this chapter has been previously published[259].

In this section, all the results of the characterization of strontium containing nano-sized particles (85 SiO_2/ 5 CaO/ 10 SrO %mol, hereafter named SG-Sr) are presented.

3.2.1.1 Morphological and structural characterization of SG-Sr

Synthetized SG-Sr powders were fully characterized in terms of morphology, textural features, composition, therapeutic ions release and bioactivity. FESEM images of SG-Sr (Figure 3.1A) showed monodispersed nanoparticles with a

spherical morphology and with a diameter size ranging between 100 and 300 nm. EDS analysis on the particles confirms the incorporation of both calcium and strontium ions in the silica framework during the synthesis (Figure 3.1B); however, since the Sr peak in the EDS analysis partially overlapped with the Si peak, results showed a lower atomic percentage of incorporated strontium compared to the theoretical percentage. Therefore to detect the effective incorporated amount of strontium ions, ICP-AES analysis on powder after the acidic dissolution was performed, the results evidenced an incorporated percentage for Ca and Sr of 6.2 % and 10.9 %, respectively, the percentage of strontium resulted slightly higher compared with the theoretical one and also the incorporated calcium demonstrate a higher percentage compared with the theoretical percentage, confirming that the incorporation of the two elements was overall satisfactory.

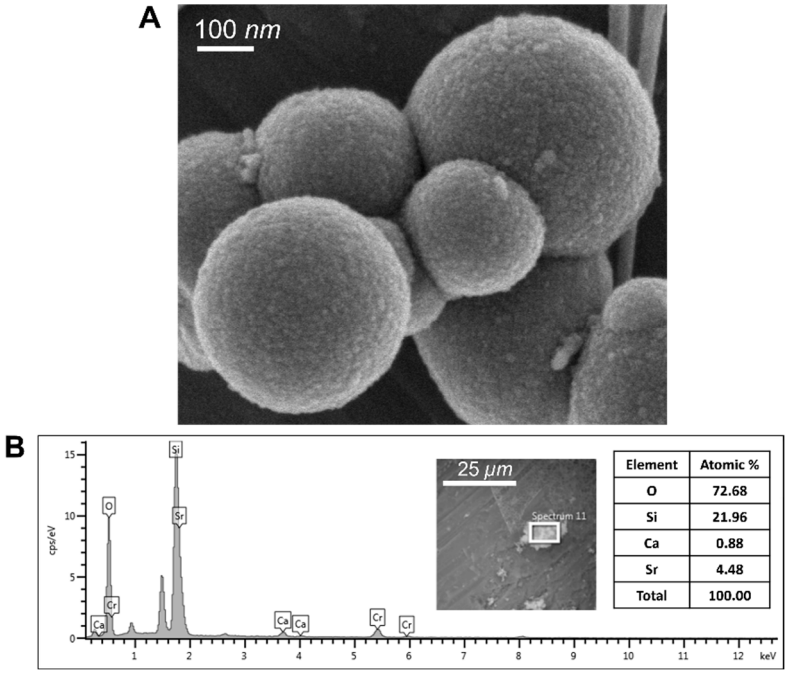

Element	Atomic %
O	72.68
Si	21.96
Ca	0.88
Sr	4.48
Total	100.00

Figure 3.1: (A) FESEM image of SG-Sr, and (B) EDS spectrum and atomic % of the components of SG-Sr.

XRD analysis (Figure 3.2) showed an amorphous structure of SG-Sr, without peaks due to crystalline oxide-based phases, confirming that strontium did not form oxide clusters into the silica framework after the powder calcination.

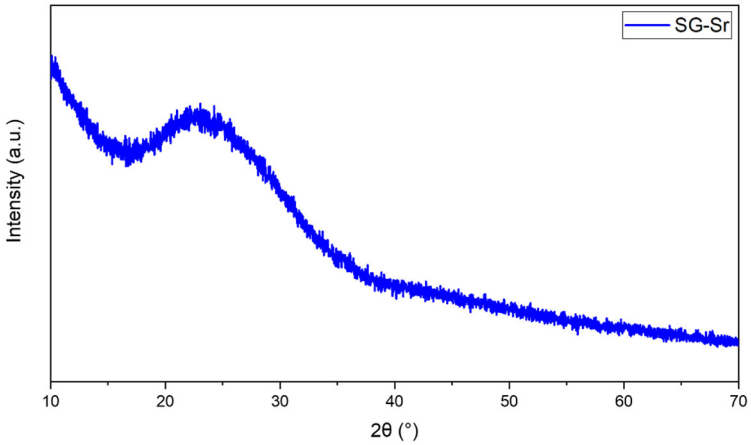

Figure 3.2: XRD spectrum of SG-Sr.

N_2 adsorption-desorption analysis showed a type IV isotherm typical of mesoporous materials (Figure 3.3), confirming the mesoporous structure of SG-Sr samples, the DFT pore size distribution (graph inset in the figure 3.3) confirmed the presence of uniform mesopores having an average diameter of about 3 nm. The BET specific surface area and the pore volume of SG-Sr resulted to be very high (as reported in table 3.1) even if lower with respect to the specific surface area of analogue materials without the presence of strontium into the silica framework, where the average surface area and pore volume generally are close to 1000 m^2/g and 1 cm^3/g[147, 282], respectively, Taghvaei et al. already found that the specific surface area is altered by the presence of Sr species since Sr^{2+} cations have a larger size compared to Ca^{2+}[283]. However, the specific surface area of SG-Sr resulted very similar to the area observed for the Sr containing MBGs by Taghvaei et al.[283].

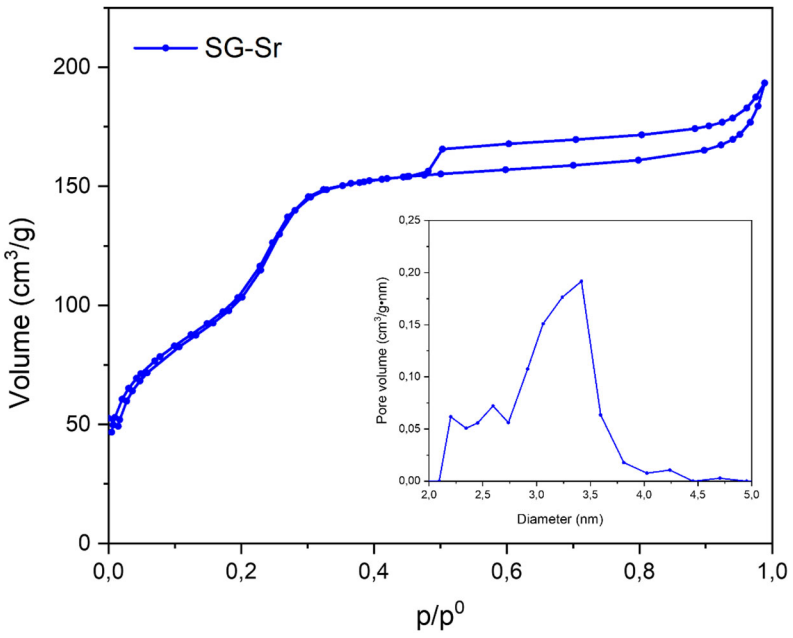

Figure 3.3: N_2 adsorption-desorption isotherm of SG-Sr samples, and DFT pore size distribution (inset the figure).

Tabella 3.1: Specific surface area, pore size and volume of SG-Sr.

Sample	**Specific surface area (m^2/g)**	**Pore size (nm)**	**Pore volume (cm^3/g)**
SG-Sr	465	3	0.33

3.2.1.2 Strontium ions release from SG-Sr in tris HCl

Strontium exhibits pro-osteogenic effects, previously reported in the literature[284]; consequently, strontium ions represent very promising therapeutic agents for boosting the regeneration of osteoporotic bone fractures. Sr ion release of this type of ions was analyzed, soaking the sample in Tris HCl and figure 3.4 reports the obtained release kinetics. The released amount of Sr^{2+} ions detected in the supernatants recovered at each time point was referred to the amount of strontium incorporated into the particles to obtain the released percentages. The release tests showed that almost the total amount of incorporated strontium was released with a burst release in the first 3 h of incubation. This burst ion release kinetics was expected due to the high surface area and small average size of the

particles, which allow a fast ion diffusion through the open porous structure. Moreover, the ppm of strontium ions released after 1 day and 7 days were compared with the literature; after 1 day the total amount of strontium ions released resulted to be 155 ppm, a higher value compared with MBGs containing the 6 %mol of strontium in the silica framework (70 ppm) of the work of Kermani et al.[285], but a very similar value compared with MBGs containing 10 %mol of Sr that was reported by Wu et al. to be around 150 ppm[286]. However, the value of released Sr in SG-Sr after 7 days was higher compared with the work of Wu et al. (238 ppm vs 160 ppm), this difference probably depends on the different media employed for the release studies by Wu et al. (Simulated Body Fluid) that slightly affect the ion release from the samples[286], this effect could be due to the deposition of HA un the particles that hinders the ions diffusion.

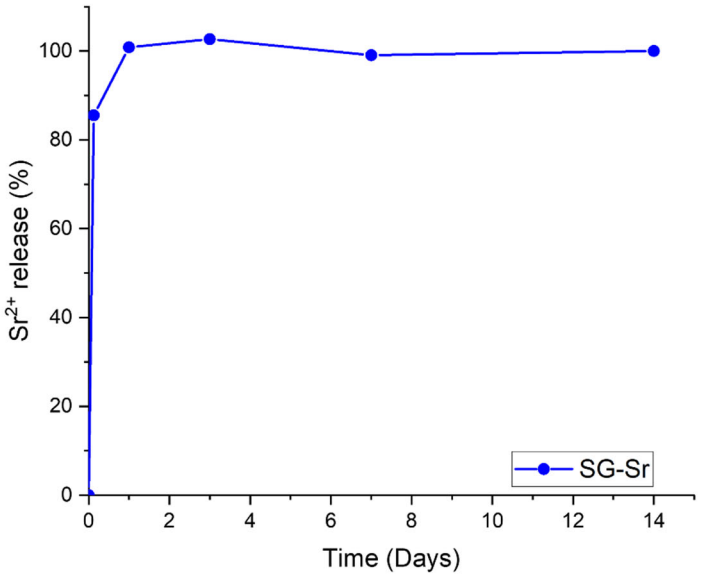

Figure 3.4: Profile of the strontium ions releases of SG-Sr.

3.2.1.3 Bioactivity of SG-Sr in SBF

SG-Sr bioactivity was tested by soaking the powder in SBF medium up to 14 days in order to investigate the ability to form the hydroxyapatite (HA) layer of the particles. After 3 days of soaking, SG-Sr not showed the formation of HA layer (Figure 3.5A), but after 7 days a response in terms of bioactivity was observed, since samples started to form particles of HA (Figure 3.5B), and after 14 days of soaking in SBF, SG-Sr particles continued the formation of HA (Figure 3.5C),

suggesting that the bioactivity response from SG-Sr particles was maintained also after the incorporation of strontium, even if lower compared with MBGs that not contain the Sr ions, as reported in the literature[287, 288], where MBGs showed the formation of HA after 1 day and in some cases even after 4 h[283, 289–292], thus the incorporation of strontium probably influence in part the bioactivity of the particles, this influence can be due to the Ca substitution with the Sr species that could decrease the amount of the released calcium ions, with a consequent reduction of the apatite-forming ability[293, 294].

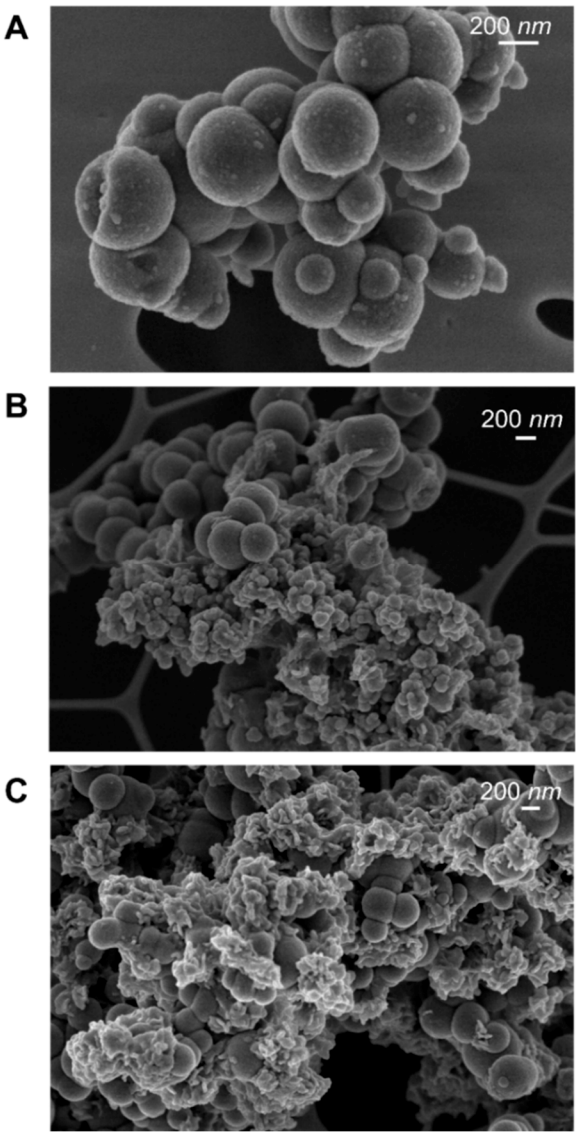

Figure 3.5: FESEM image of SG-Sr after (A) 3, (B) 7, and (C) 14 days of soaking in SBF.

To further confirm the HA layer formation kinetics, a XRD analysis was performed on SG-Sr after each time point (Figure 3.6). XRD spectra of day 7 and day 14 showed the presence of crystalline peaks at 25.81 and 32.02 2θ degrees, matching with the HA peaks (reference 01-074-0565). As expected after the analysis of FESEM images, on day 3 SG-Sr not showed peaks ascribable to the HA suggesting a slower bioactivity compared to the MBGs reported in literature[291, 292], or the amount of the formed HA is too low to be detected by XRD analysis.

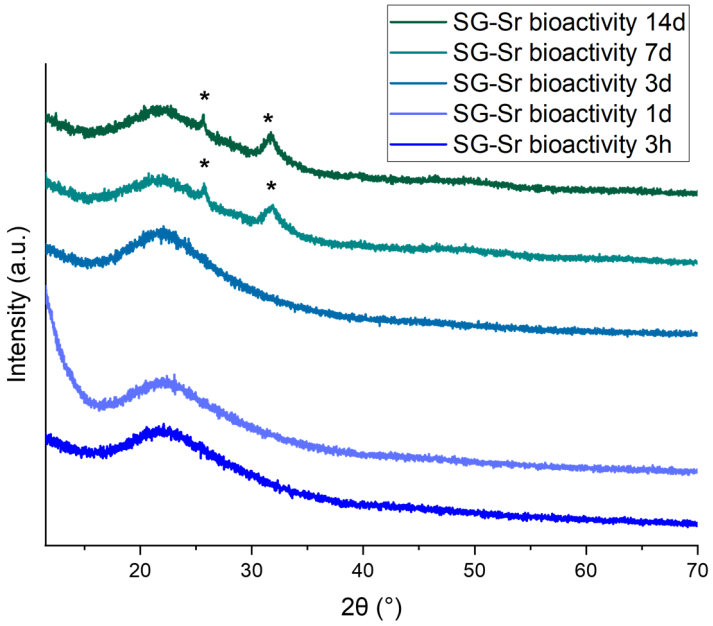

Figure 3.6: XRD spectra of SG-Sr after 3h, 1 day, 3 days, 7 days, and 14 days of soaking in SBF medium. Asterisks show the HA peaks.

3.2.2 Strontium containing mesoporous bioactive glasses microparticles

Part of the work described in this chapter has been previously published[259].

In this section are reported the characterization of strontium containing microparticles (SD-Sr) with a ratio of 85 SiO_2/ 5CaO/ 10SrO %mol. The microparticles were produced using a modified method of the procedure reported by Pontiroli et al.[261].

3.2.2.1 Morphological and structural characterization of SD-Sr

The fully characterization in terms of composition, morphology, and textural features as well as ions release and bioactivity properties was performed on SD-Sr powder. The morphological characterization of SD-Sr was performed with the FESEM technique, FESEM images of SD-Sr (reported in figure 3.7A) showed a spherical morphology with a diameter ranging between 1 and 5 μm. An EDS analysis was performed on the microparticles confirming the presence of calcium and strontium indicating their incorporation during the synthesis procedure (Figure 3.7B). As previously discussed, the peak of Sr in the EDS spectra is partially covered by the Si peak, affecting the detection of Sr atomic percentage. The effective strontium atomic percentage inside SD-Sr particles was confirmed by an ICP-AES analysis resulting in a percentage of Ca and Sr of 5.5 % and 8.8 %, respectively. This difference compared to the SG-Sr particles can be ascribable to the short time in which the strontium precursor remains into the solution before the spraying, since the larger ions radius of Sr^{2+} compared to Ca^{2+}, that is about 16% than Ca^{2+} (1.18 Å vs 0.99 Å), resulting in a lower field strength of Sr ions compared to calcium ions and consequently establishes weaker interactions with the silica framework[295].

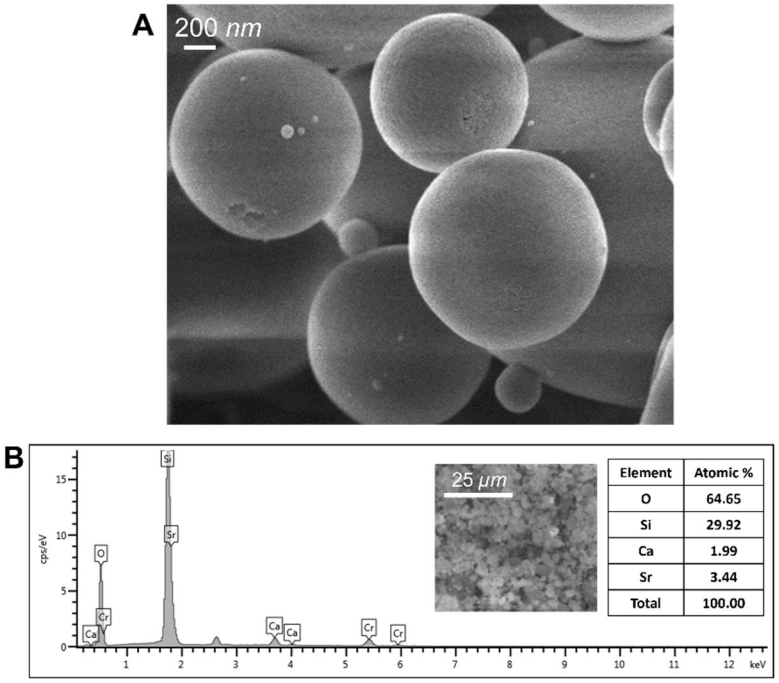

Figure 3.7: (A) FESEM image of SD-Sr, and (B) EDS spectrum and atomic % of the components of SD-Sr.

The XRD spectrum of SD-Sr (Figure 3.8) demonstrated that strontium did not form oxide clusters during the synthesis and the subsequent calcination, as suggests the absence of crystalline peaks in the spectra.

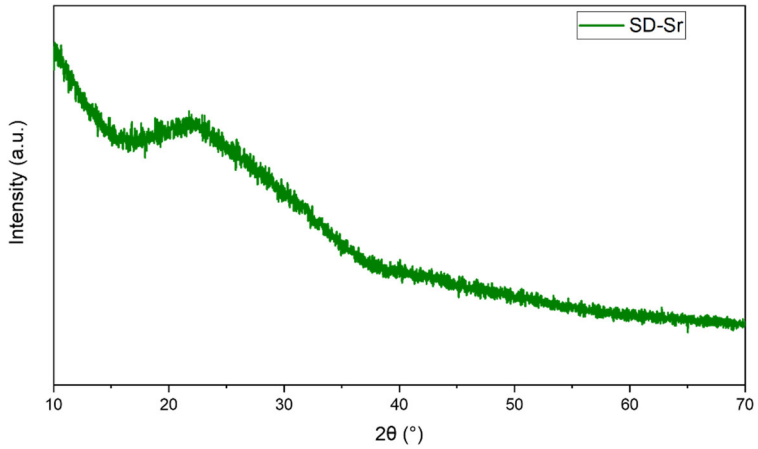

Figure 3.8: XRD spectrum of SD-Sr.

The N_2 adsorption-desorption analysis was performed on SD-Sr and results confirm the mesoporous structure of SD-Sr since a type IV isotherm typical of mesoporous materials were obtained by the analysis (Figure 3.9) with a specific surface area of 133 m^2/g, a very similar value compared to the literature for Sr containing microparticles[296]; moreover, also the DFT pore size distribution results (inset in the figure 3.9) showed a uniform mesopores distribution with a diameter ranging from 5 to 7 nm. As mentioned, the specific surface area and the pore volume of SD-Sr resulted to be high (reported in the table 3.2) and similar to the literature[296]. However, the specific area resulted very lower compared to SG-Sr, this feature is due to the particle size, the use of a different surfactant for the pore formation, and finally for the acidic environment used for the hydrolysis of the silica precursor. The specific surface area resulted also lower respect similar particles without the presence of strontium that normally is above to 300 m^2/g[297, 298].

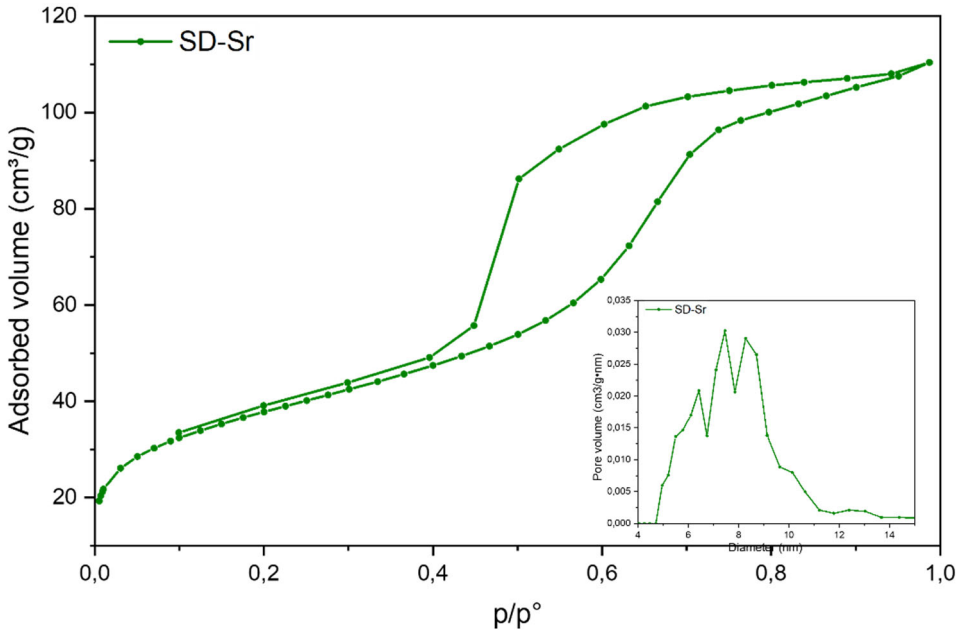

Figure 3.9: N_2 adsorption-desorption isotherm of SD-Sr samples, and DFT pore size distribution (inset the figure).

Table 3.2: Specific surface area, pore size and volume of SD-Sr.

Sample	**Specific surface area (m^2/g)**	**Pore size (nm)**	**Pore volume (cm^3/g)**
SD-Sr	133	5-7	0.16

3.2.2.2 Strontium ions release from SD-Sr in Tris HCl

In the figure 3.10 the release of strontium ions from SD-Sr in Tris HCl analyzed by ICP-AES is reported; in order to obtain the percentages released, the released Sr^{2+} ions detected in the supernatants recovered at each time point was referred to the total amount of strontium incorporated into the particles during the synthesis, Sr^{2+} results to be totally released, and as well as SG-Sr, also in this case results showed a burst release in the first 3 h of incubation ending with a plateau phase till the end of the 14 days. As for SG-Sr, the burst release during the first 3 h of SD-Sr can be related to the high surface and accessible porous structure that allow a fast ion diffusion through the porous structure. The ppm values resulted slightly

lower compared to the SG-Sr samples, with a value of 134 ppm after 1 day and 223 ppm after 7 days, however these values do not differ too much from the literature[285, 286]; this difference is most likely due to the total amount of Sr present in the SD-Sr that was lower compared to the Sr amount in the SG-Sr.

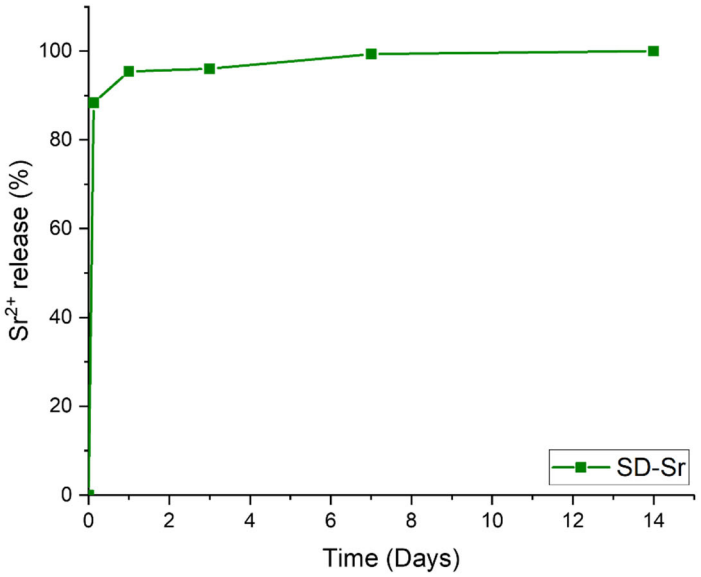

Figure 3.10: profile of the strontium ions releases of SD-Sr.

3.2.2.3 Bioactivity of SD-Sr in SBF

SD-Sr were soaked in SBF medium up to 14 days in order to investigate the bioactivity behaviour to form a HA layer on the surface. After 3 days, results of FESEM images on SD-Sr showed a beginning of formation of HA on their surface, with the typical elongated needle-like structures morphology (Figure 3.11A). After 7 days of soaking part of particles started to be covered by an HA layer (Figure 3.11B), until 14 days where the HA layer continued to be formed covering a larger part of the surface of the SD-Sr particles (Figure 3.11C); these results suggesting an better bioactivity response from SD-Sr particles compared to SG-Sr that can be explained by the lower interconnections into the silica framework due to the incorporation of strontium[287, 288] and the spray dryer synthesis, as reported by Pontiroli et al.[261].

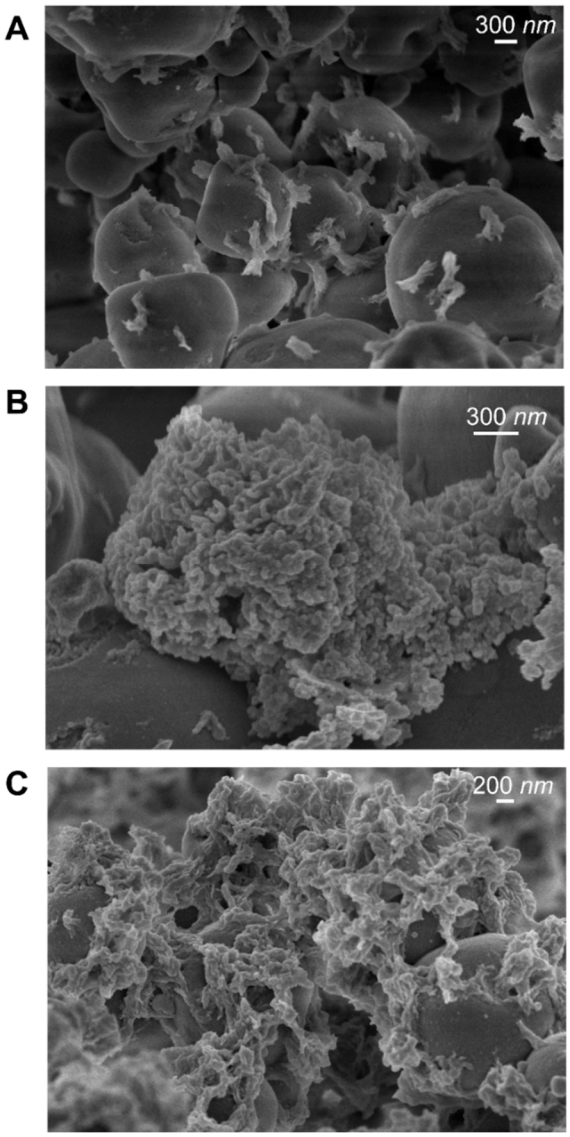

Figure 3.11: FESEM image of SD-Sr after (A) 3, (B) 7, and (C) 14 days of soaking in SBF.

The further confirmation of the formation kinetics of the HA layer was given by the XRD analysis, performed on SD-Sr after each time point (Figure 3.12). Crystalline peaks at 25.48 appears in the XRD spectra after the day 1 and another peak at 31.59 appears after the day 14, these peaks matching with the HA peaks (reference 01-074-0565). As suggested by FESEM images and confirmed with XRD analysis, SD-Sr showed a better bioactivity compared to SG-Sr, however, compared with MBGs without strontium species, the bioactivity of SD-Sr resulted

slightly lower[283, 289–292], indicating again that the cause may be due to the strontium species that substitute the calcium species during the synthesis.

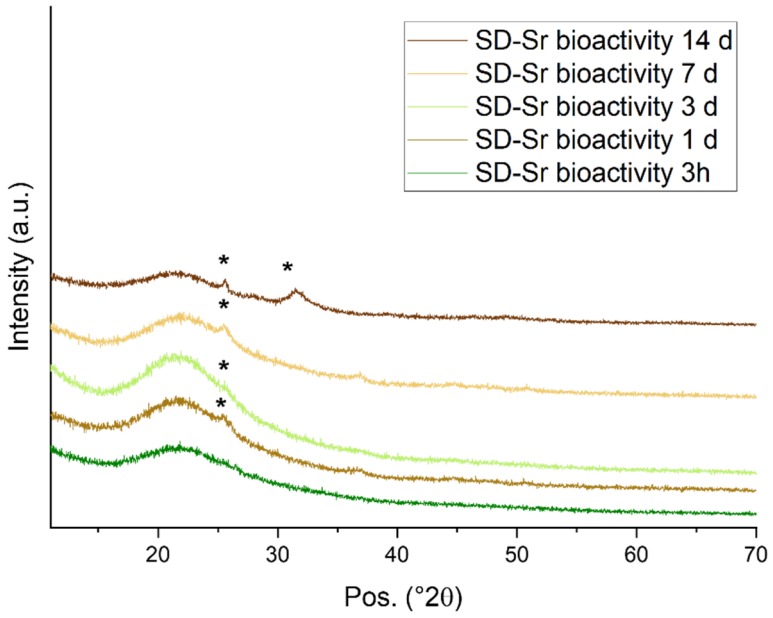

Figure 3.12: XRD spectra of SD-Sr after 3h, 1 day, 3 days, 7 days, and 14 days of soaking in SBF medium. Asterisks show the HA peaks.

3.2.3 Scaling-up of strontium containing mesoporous bioactive glasses microparticles

In this section the characterization of the microparticles obtained after scaling-up tests (hereafter named SD-Sr_S) is reported. The produced powder using an industrial spray-drier situated in the FLUIDINOVA company were characterized in terms of morphology, composition and specific surface area.

3.2.3.1 Morphological and structural characterization of SD-Sr_S

The characterization in terms of composition, morphology, and textural features SD-Sr_S powder after calcination was performed. SD-Sr_S morphological characterization was carried out with the SEM analysis, and images showed little crumpled small particles and bigger particles with a size ranging from 1 to 10-15 μm and non-spherical precipitate blocks (figure 3.13). EDS analysis reported the presence of Sr ions in the particles with an atomic percentage close to the theoretical one, while the aggregates are principally composed of pure silica

without Sr (Table 3.3). The results suggest that the aggregates were formed before the spraying and during the addition of the TEOS solution into the Pluronic solution which cause early precipitation of the silica precursor; the moderately number of crumpled particles and the presence of the precipitate suggest that other trials should be performed in order to obtain a better morphology without silica precipitate.

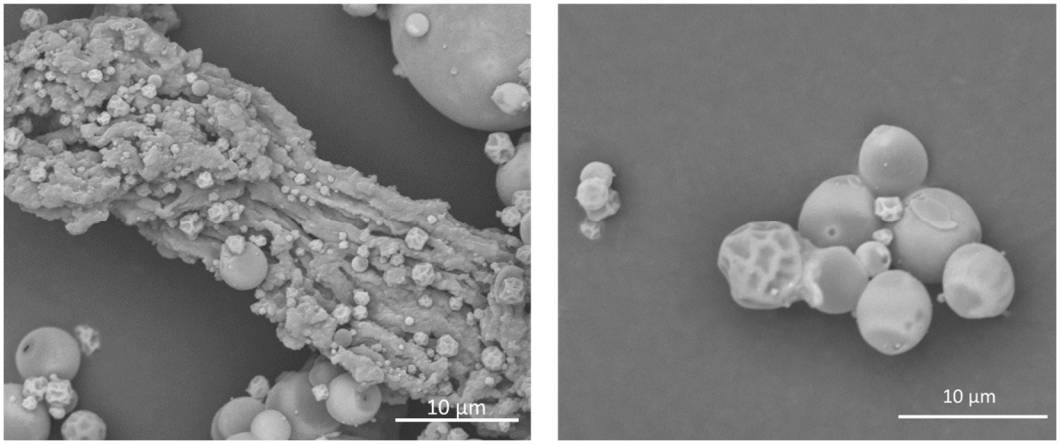

Figure 3.13: SEM images of SD-Sr_S aggregates (left) and particles (right).

Table 3.3: EDS analysis results of SD-Sr_S.

	SD-Sr_S aggregates	**SD-Sr_S particles**
Element	Atomic %	Atomic %
Si	99.0	80.3
Sr	0.0	9.6
Ca	1.0	10.1

The XRD analysis on SD-Sr_S (Figure 3.14) showed the non-formation of oxide clusters of strontium during the synthesis and calcination, since in the spectra crystalline peaks are absent.

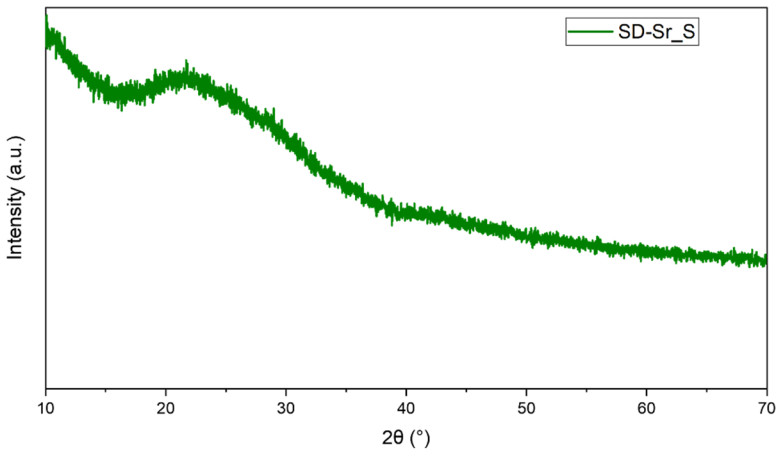

Figure 3.14: XRD spectrum of SD-Sr_S.

N_2 adsorption-desorption analysis results showed a type IV isotherm typical of mesoporous materials, indicating that the particles present in the SD-Sr_S powders have a mesoporous structure (Figure 3.15), the specific surface area of 166 m^2/g is similar to the lab scale particles, and also the DFT pore size distribution analysis (inset in the figure 3.15) reported a uniform mesopores distribution with a diameter very similar to SD-Sr (ranging from 4 to 5 nm). Since the high specific surface area and the pore volume of SD-Sr_S (reported in the table 3.4) are similar to the SD-Sr particles, the performed scaling-up method, after other subsequent optimizations to avoid the early precipitation, can be a very promising approach to obtain industrial quantities of microparticles.

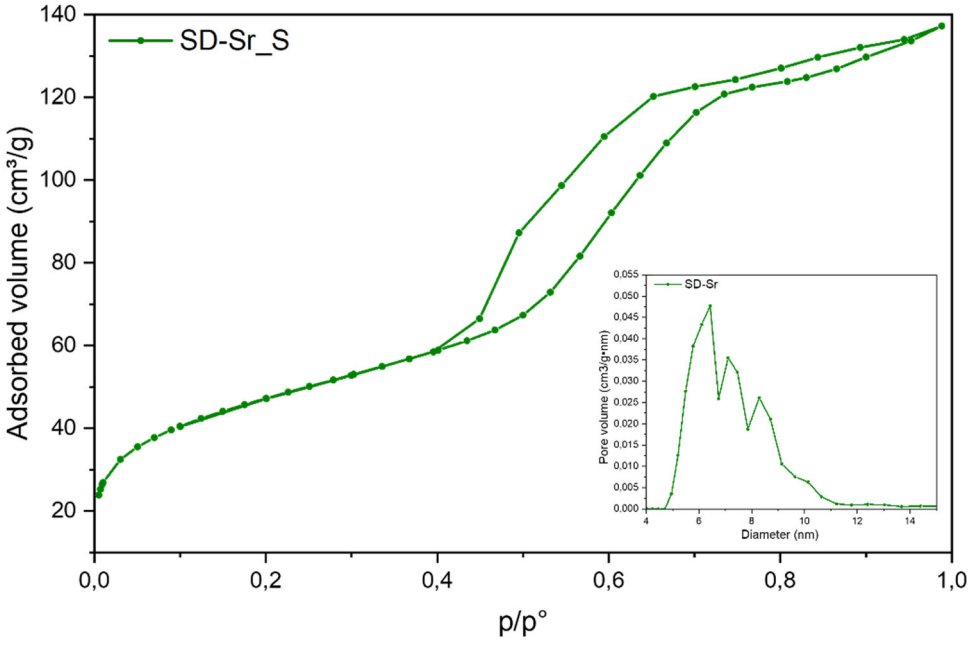

Figure 3.15: N_2 adsorption-desorption isotherm of SD-Sr_S samples, and DFT pore size distribution (inset the figure).

Table 3.4: Specific surface area, pore size and volume of SD-Sr_S.

Sample	**Specific surface area (m^2/g)**	**Pore size (nm)**	**Pore volume (cm^3/g)**
SD-Sr	166	4-5	0.20

3.3 Morphological and structural characterization of strontium containing MBGs nano- and microparticles grafted with ICOS-Fc

3.3.1 Strontium containing mesoporous bioactive glasses nanoparticles grafted with ICOS-Fc

Part of the work described in this chapter has been previously published[259].

The aim of activity was to confer anti-osteoclastogenic activity to the MBGs-Sr particles in order to inhibit reversibly the resorption activity of osteoclasts and support the restoration of bone in osteoporotic fractures. The grafting of the biomolecule consisted of two steps: a functionalization of the particles surface with amino groups obtaining amino-functionalized SG-Sr (hereafter named SG-Sr-NH_2), and the subsequent grafting of the ICOS-Fc to amino groups using a zero-length coupling reaction (as described in the second chapter, section 2.4), obtaining ICOS-Fc grafted SG-Sr particles (hereafter named SG-Sr-ICOS-Fc). In this section, all the results of the characterization of strontium containing nano-sized particles grafted with ICOS-Fc are presented.

3.3.1.1 Morphological and structural characterization of SG-Sr-ICOS-Fc

SG-Sr-ICOS-Fc were fully characterized in terms of morphology, textural features, composition, therapeutic ions release and bioactivity. FESEM analysis was performed in order to investigate the maintained morphology of the particles after the grafting procedure, and images of SG-Sr-ICOS-Fc (Figure 3.16A) showed nanoparticles with a spherical morphology and with a diameter size ranging between 100 and 300 nm, similar to the bare samples. EDS analysis on the particles was performed to examine any change in the atomic percentage of SG-Sr-ICOS-Fc after the grafting. Results showed that calcium and strontium elements are present into the particles (Figure 3.16B) and, as for bare samples, since the Sr peak in the EDS analysis is partially overlapped to the Si peak the effective amount of strontium in SG-Sr-ICOS-Fc has been detected by ICP-AES analysis; related results showed an atomic percentage of Ca and Sr close to the percentages previously detected in SG-Sr samples (5.0 % and 9.8 %, respectively), with only a small decrease of the percentages of both ions, confirming that the grafting procedure does not affect much the amount of incorporated calcium and strontium.

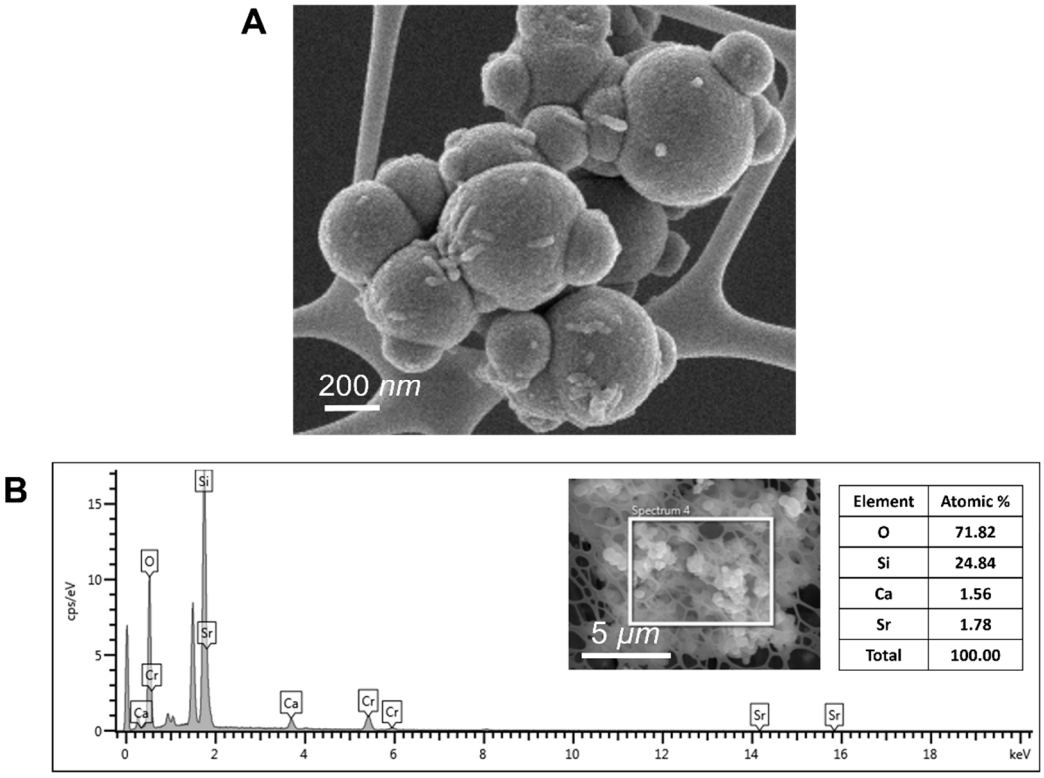

Figure 3.16: (A) FESEM image of SG-Sr-ICOS-Fc, and (B) EDS spectrum and atomic % of the components of SG-Sr-ICOS-Fc.

XRD analysis (Figure 3.17) showed an amorphous structure of SG-Sr-ICOS-Fc, indicating that the grafting procedure did not form crystalline structures after the amino functionalization or ICOS-Fc grafting processes, as expected.

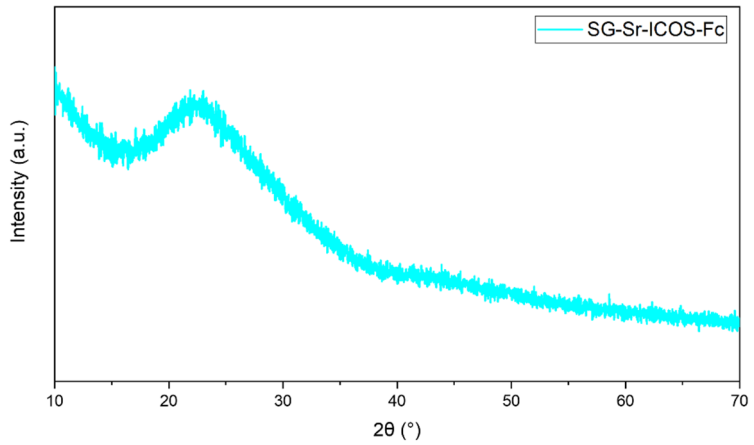

Figure 3.17: XRD spectrum of SG-Sr-ICOS-Fc.

N_2 adsorption-desorption analysis was performed both on amino functionalized and ICOS-Fc grafted particles to detect a reduction of the specific surface area after each step due to the presence of grafted amino groups and biomolecules. Results showed a type IV isotherm typical of mesoporous materials (Figure 3.18 left), confirming the maintained mesoporous structure of both SG-Sr-NH_2 and SG-Sr-ICOS-Fc, the DFT pore size distribution (Figure 3.18 right) confirmed the presence of uniform mesopores having a total pore volume of about 0.07 cm^3/g for SG-Sr-NH_2 and 0.09 cm^3/g for SG-Sr-ICOS-Fc. The BET specific surface area and the pore volume of SG-Sr-NH_2 and SG-Sr-ICOS-Fc resulted to be reduced compared to SG-Sr (as reported in the table 3.5) confirming the successful functionalization and grafting of the biomolecule on the SG-Sr surface; this effect is due to the steric hindrance of ICOS-Fc, the biomolecule expected to react mostly with amino groups at the mesopore entrances during the initial phases of reaction, that leads to partial or full pore occlusion[299–301].

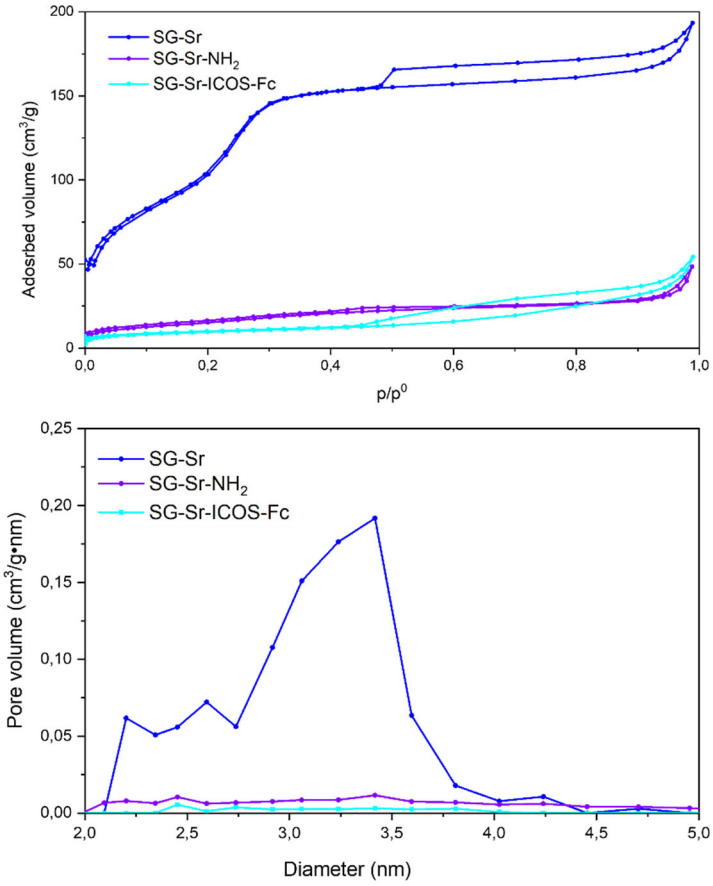

Figure 3.18: N_2 adsorption-desorption isotherm of SG-Sr-NH2 and SG-Sr-ICOS-Fc samples compared with SG-Sr (above), and their DFT pore size distribution (below).

Table 3.5: Specific surface area, pore size and volume of SG-Sr, SG-Sr-NH2 and SG-Sr-ICOS-Fc.

Sample	**Specific surface area (m^2/g)**	**Pore volume (cm^3/g)**
SG-Sr	465	0.33
SG-Sr-NH_2	57	0.07
SG-Sr-ICOS-Fc	34	0.09

The bond between ICOS-Fc and the SG-Sr surface resulting from the grafting procedure where amino groups present on the particles surface are linked to the carboxyl groups of the ICOS-Fc molecule forming an amide bond, and in order to confirm the occurred grafting, different tests were performed.

FTIR analysis was performed to confirm the presence of ICOS-Fc on SG-Sr surface. FTIR difference spectrum, obtained by subtracting the spectra of SG-Sr to the SG-Sr-ICOS-Fc spectra, showed a peak ascribable to the stretching of the amide carbonyl group in the range 1680-1650 cm^{-1} (free and H-bonded carbonyl), moreover, at lower frequencies the N-H and C-H bending modes of amine functionalities and ICOS-Fc structure, respectively, are visible (Figure 3.19), suggesting the presence of the biomolecule on the sample surface.

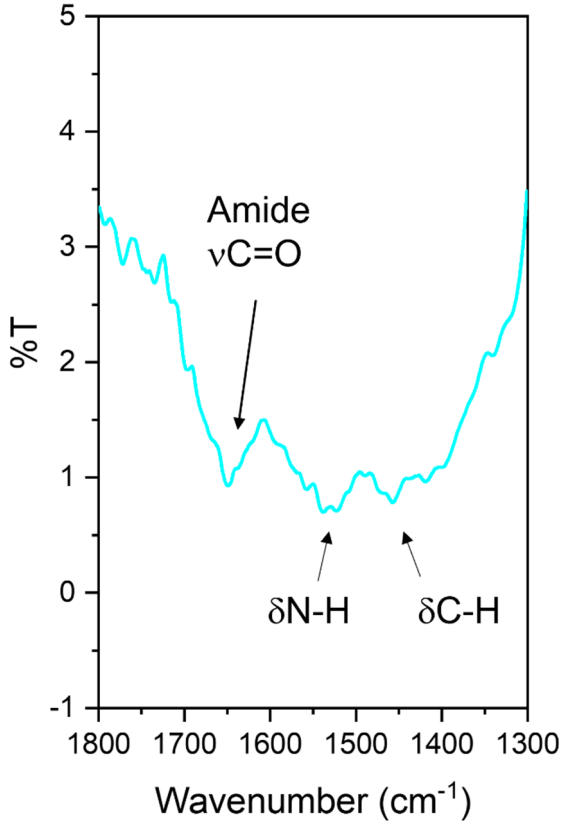

Figure 3.19: FTIR spectra of SG-Sr-ICOS-Fc in the 1300-1800 cm^{-1} range.

An ELISA-like assay was performed to verify the successful grafting of ICOS-Fc on samples and to check if ICOS-Fc maintained its ability to bind ICOS-L (the ICOS binding partner). Results of ELISA-like assay expressed in optical density (O.D.) value of SG-Sr-ICOS-Fc showed a greater signal compared to SG-Sr (Figure 3.20), indicating the presence of ICOS-Fc and the maintained ability of the biomolecule to bind its ligand ICOS-L, results also indicate that ICOS-Fc was grafted with the active site in the correct position. The same assay was conducted to detect the unbounded ICOS-Fc present in the supernatant recovered after the grafting procedure in order to calculating the amount of ICOS-Fc molecules grafted on SG-Sr samples by exploiting a subtractive calculation method, since the directly calculation on spherical SG-Sr-ICOS-Fc resulted not possible; the amount obtained by the collection from SG-Sr-ICOS-Fc suspensions was subtracted from the initial amount of ICOS-Fc used during the grafting reaction, subsequently the average ICOS-Fc grafted amount was calculated to be 0.4 μg/mg of SG-Sr particles.

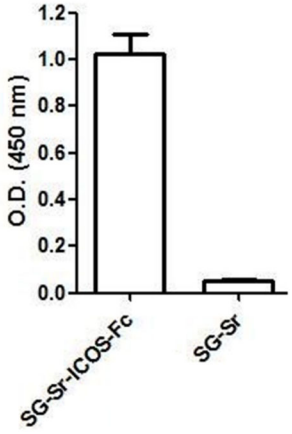

Figure 3.20: Results of ELISA-like assay expressed in O.D. value of SG-Sr-ICOS-Fc compared with bare samples.

Finally, to examine the stability of the bond formed between the particles surface and ICOS-Fc to hydrolysis reaction in aqueous medium, bond stability tests were performed by soaking the SG-Sr-ICOS-Fc particles in DMEM for different time points, up to 21 days (3, 7, 14, and 21 days); later the collected supernatants were analyzed by an ELISA-like assay in order to quantify the amount of ICOS-Fc present in the medium. The time points were specifically selected to mimic the time-course of osteoclast differentiation *in vitro*, where for 21 days the monocytes are cultured in a differentiation medium that are changed every 3 days. The stability of the bond between ICOS-Fc and the MBGs surface is

important, since if ICOS-Fc molecule is anchored to the particles, it inhibits the osteoclast only when they are active and enter in contact with the particles, resulting in a specific inhibition activity only in the site where osteoclasts are active (Figure 3.21).

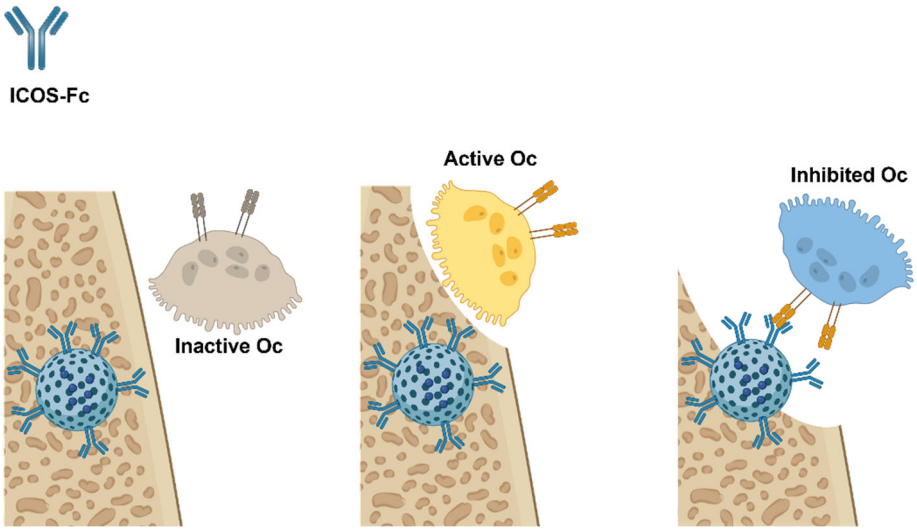

Figure 3.21: Schematic representation of the inhibition mechanism on Oc due to ICOS-Fc anchored to MBG surface.

Results of the bond stability test (Table 3.6) showed a very limited amount of ICOS-Fc present in the supernatants, indicating that the most of ICOS-Fc biomolecule is anchored on the particles surface with a stable bond.

Table 3.6: Stability test of ICOS-Fc binding to SG-Sr-ICOS-Fc surface.

SG-Sr-ICOS-Fc				
Time (Days)	3	7	14	21
ICOS-Fc in medium (%)	4.2	5.4	5.6	6.7

3.3.1.2 Strontium ions release from SG-Sr-ICOS-Fc in Tris HCl

In order to investigate if the grafting procedure affected the ability of the particles to release Sr ions, the releases from SG-Sr-ICOS-Fc in Tris HCl has been monitored by ICP-AES (reported in the figure 3.22). Results showed that the total

amount of strontium present in the particles was released, with a burst release in the first 3 h of incubation, as occurred for SG-Sr samples, demonstrating that the two steps for the grafting method did not affect the capability of SG-Sr-ICOS-Fc to release Sr^{2+} ions.

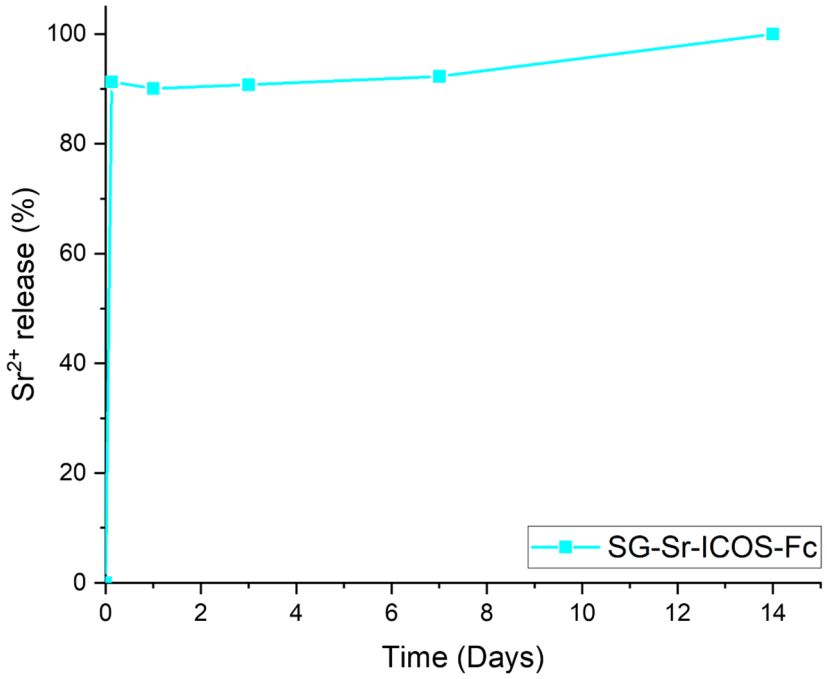

Figure 3.22: profile of the strontium ions releases of SG-Sr-ICOS-Fc.

3.3.1.3 Bioactivity of SG-Sr-ICOS-Fc in SBF

The bioactive behaviour of SG-Sr-ICOS-Fc was tested up to 14 days to investigate if the grafting process affected the particles' ability to form the HA layer. FESEM images showed that after 3 days of soaking SG-Sr-ICOS-Fc manifested a rapid formation of HA (Figure 3.23A), this bioactivity resulted faster compared to bare SG-Sr. Then, samples continued to form a HA layer after 7 days of soaking starting to cover the particles (Figure 3.23B), and after 14 days particles were almost fully covered by the HA layer (Figure 3.23C), suggesting that the grafting of ICOS-Fc biomolecule does not affect the high bioactivity response of SG-Sr-ICOS-Fc, indeed the bioactivity resulted slightly higher, even if still lower compared to MBGs without strontium[289–292].

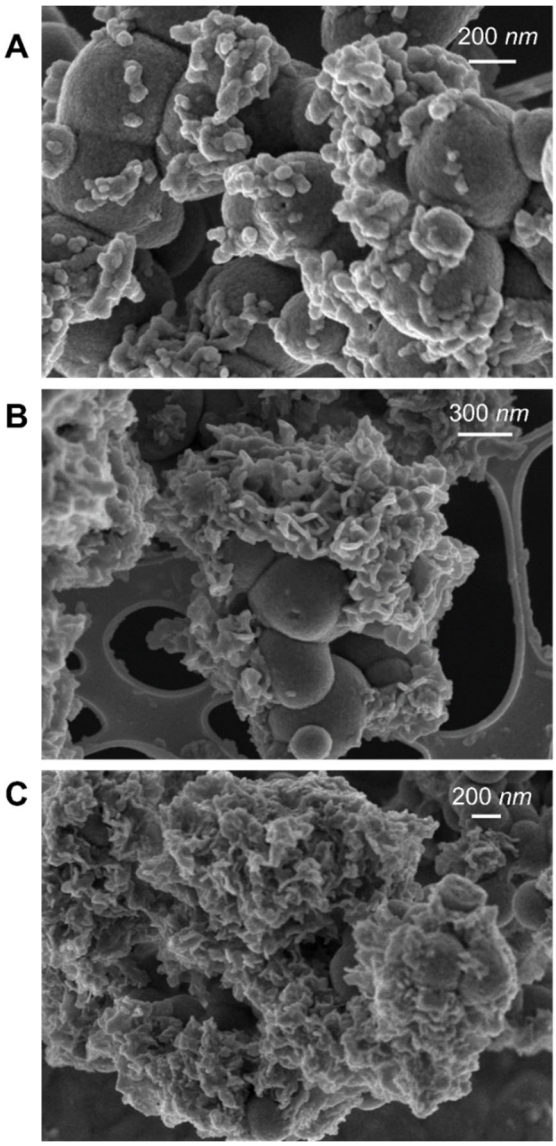

Figure 3.23: FESEM image of SG-Sr-ICOS-Fc after (A) 3, (B) 7, and (C) 14 days of soaking in SBF.

XRD analysis was performed to further confirm the HA layer formation after each time point (Figure 3.24). The spectra of day 7 and day 14 showed the presence of crystalline peaks at 25.58 and 31.74 2θ degrees, matching with the HA peaks (reference 01-074-0565), as occurred for SG-Sr, while probably the formed HA at day 3 is too low to be detected by XRD analysis.

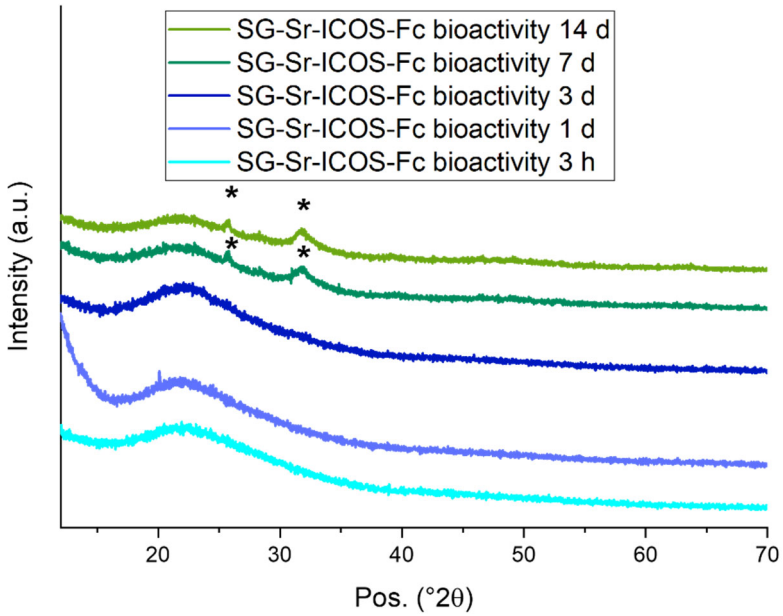

Figure 3.24: XRD spectra of SG-Sr-ICOS-Fc after 3h, 1 day, 3 days, 7 days, and 14 days of soaking in SBF medium. Asterisks show the HA peaks.

3.3.2 Strontium containing mesoporous bioactive glasses microparticles grafted with ICOS-Fc

Part of the work described in this chapter has been previously published[259].

The aim of this part of work was to confer anti-osteoclastogenic activity to the MBGs-Sr microparticles that already contain strontium which exhibits pro-osteogenic effects, in order to obtain the synergistic effect that guide the recovery of osteoporotic bone fracture and the restoration of the normal bone tissue balance. As for SG-Sr-ICOS-Fc the grafting consisted in a functionalization of the surface with amino groups (the obtained sample after the first step hereafter is named SD-Sr-NH_2), and the following zero-length grafting of ICOS-Fc (as described in the second chapter, section 2.4) obtaining particles hereafter named SD-Sr-ICOS-Fc. In this section, all the results of the characterization of strontium containing micro-sized particles grafted with ICOS-Fc are presented.

3.3.2.1 Morphological and structural characterization of SD-Sr-ICOS-Fc

The fully characterization of the morphology, textural features, composition, therapeutic ions release and bioactivity of SD-Sr-ICOS-Fc were performed in

order to investigate the possibility that the grafting changed some property of the particles. FESEM images of SD-Sr-ICOS-Fc (Figure 3.25A) showed spherical monodispersed microparticles with a diameter size of 1-5 µm, very similar to the bare samples. The EDS analysis (Figure 3.25B) showed the presence of calcium and strontium in the particles and the effective atomic percentage of strontium in SD-Sr-ICOS-Fc was analyzed by the ICP-AES, that reports an atomic percentage of Ca and Sr of 4.1 % and 7.9 %, respectively, a small decrease as found for SG-Sr, confirming that the grafting procedure affects only minimally the amount of calcium and strontium incorporated.

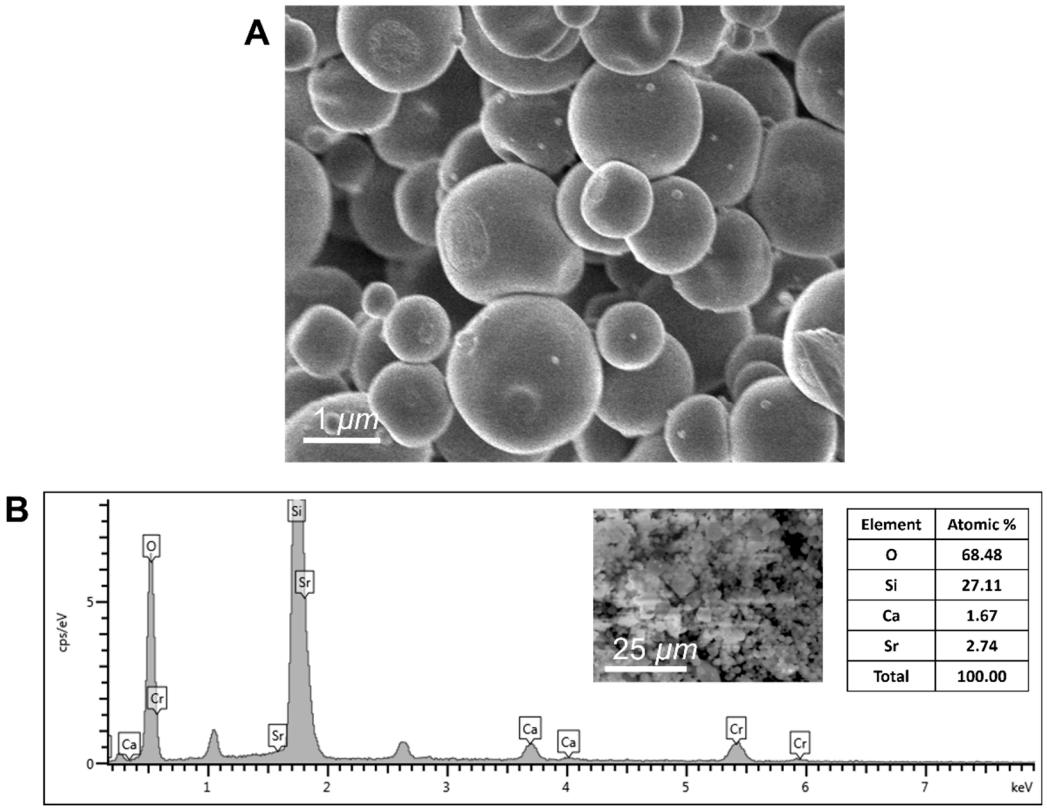

Figure 3.25: (A) FESEM image of SD-Sr-ICOS-Fc, and (B) EDS spectrum and atomic % of the components of SD-Sr-ICOS-Fc.

The formation of crystalline structures after the steps of the grafting procedure was monitored by XRD analysis (Figure 3.26), results showed an absence of peaks due to crystalline phases, confirming the amorphous morphology of SD-Sr-ICOS-Fc.

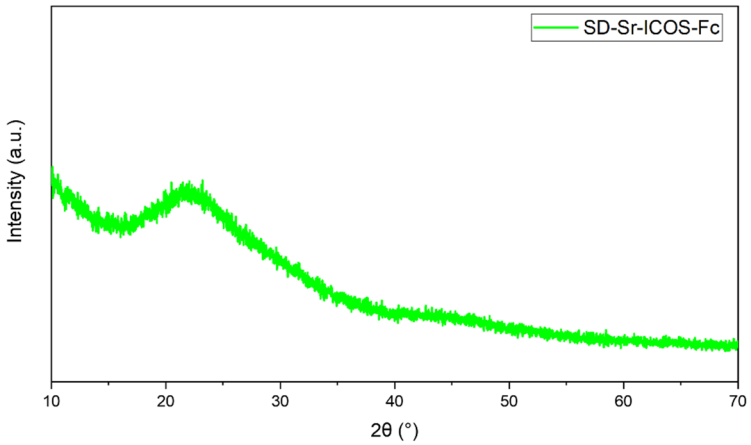

Figure 3.26: XRD spectrum of SD-Sr-ICOS-Fc.

The N_2 adsorption-desorption analysis was performed on amino functionalized and ICOS-Fc grafted particles in order to examine a reduction of the specific surface area due to the presence of amino groups or ICOS-Fc. Results showed an isotherm (type IV) typical of mesoporous materials (Figure 3.27 left), indicating that the mesoporous structure of both SD-Sr-NH_2 and SD-Sr-ICOS-Fc was maintained, in addition, the DFT pore size distribution (figure 3.27 right) revealed a total volume of about 0.04 cm^3/g for SD-Sr-NH_2 and 0.03 cm^3/g for SD-Sr-ICOS-Fc. The reduced specific surface area and the pore volume of SD-Sr-NH_2 and SD-Sr-ICOS-Fc compared to SD-Sr (as reported in the table 3.7) confirming the successful functionalization and grafting of the biomolecule on the SD-Sr surface. As for SG-Sr-ICOS-Fc, the steric hindrance of ICOS-Fc can lead to a partially or fully pore occlusion[299, 301, 302] that explains the reduced specific surface area and pore volume, even if the hysteresis loop in the isotherm is still visible, indicating that pores are not completely occluded probably because ICOS-Fc biomolecules are mainly at the pores entrance.

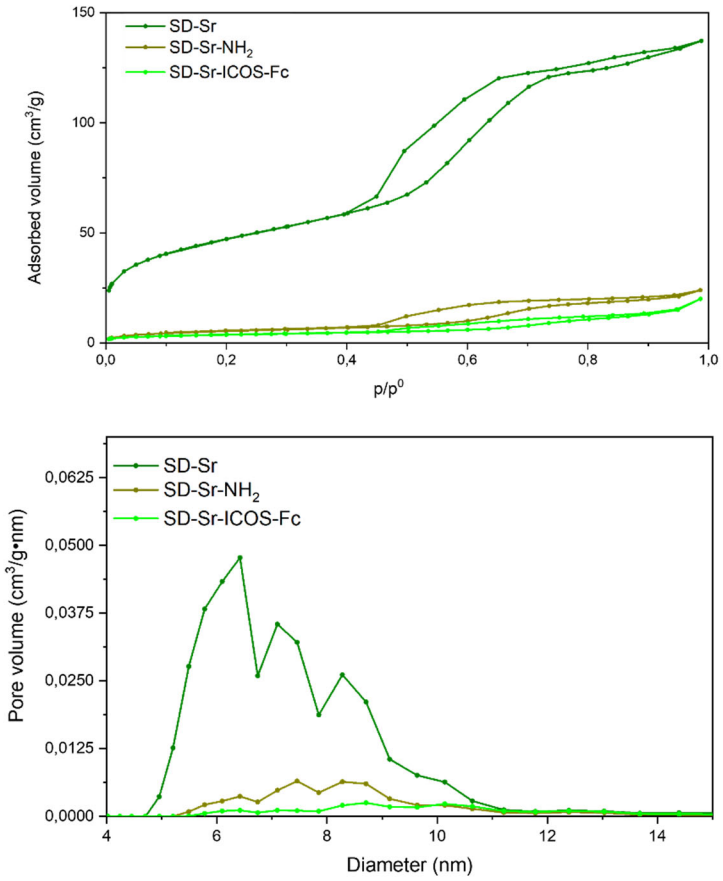

Figure 3.27: N_2 adsorption-desorption isotherm of SD-Sr-NH2 and SD-Sr-ICOS-Fc samples compared with SG-Sr (left), and their DFT pore size distribution (right).

Table 3.7: Specific surface area, pore size and volume of SD-Sr, SD-Sr-NH2 and SD-Sr-ICOS-Fc.

Sample	**Specific surface area (m^2/g)**	**Pore volume (cm^3/g)**
SD-Sr	133	0.16
SD-Sr-NH_2	19	0.04
SD-Sr-ICOS-Fc	13	0.03

The confirmation of the successful grafting of ICOS-Fc was indagated by different tests.

The presence of ICOS-Fc on the sample surface on SG-Sr surface was indagated by FTIR analysis. Spectra obtained by the subtraction of SD-Sr spectra to the SD-Sr-ICOS-Fc spectra showed two peaks, the first peak is ascribable to the amide C=O bonds stretching in the range of 1680-1650 cm^{-1} and the second to the C-H bonds bending of ICOS-Fc aliphatic chains around 1480 cm^{-1} range (Figure 3.28). Contrary to SG-Sr-ICOS-Fc spectra, the peak of N-H functionalities is not present, suggesting a lower number of residual amines not reacted with ICOS-Fc, most likely due to the greater pore size and the consequent higher reactivity at the pore entrances.

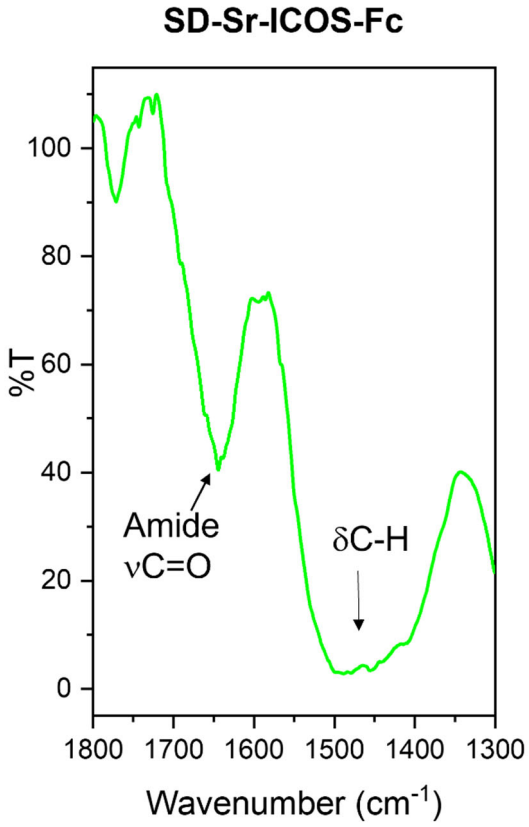

Figure 3.28: FTIR spectra of SD-Sr-ICOS-Fc in the 1300-1800 cm-1 range.

The last test performed, as for SG-Sr-ICOS-Fc, was an ELISA-like assay. Results expressed in O.D. value showed a greater O.D. signal of SD-Sr-ICOS-Fc compared to bare samples (Figure 3.29), confirming the presence and the

maintained ability to bind ICOS-L of ICOS-Fc grafted on the sample surface, and in addition, results suggesting also that ICOS-Fc was grafted with the correct position of the active site. The real amount of ICOS-Fc grafted on the particles surface was calculated by subtraction with the values obtained with the ELISA-like assay on the unbounded ICOS-Fc present in the supernatant of the reaction, as for SG-Sr-ICOS-Fc; results revealed that the average ICOS-Fc grafted was about 0.4 μg each mg of particles, very close to SG-Sr-ICOS-Fc samples, suggesting that the grafting of ICOS-Fc was not affected by the size of particles or by their pore size.

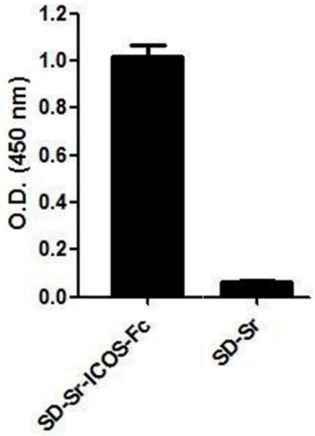

Figure 3.29: Results of ELISA-like assay expressed in O.D. value of SD-Sr-ICOS-Fc compared with bare samples.

The investigation of the bond stability formed on microparticles surface with ICOS-Fc was performed with the same procedure used for SG-Sr-ICOS-Fc for different time points, up to 21 days. The amount of ICOS-Fc present in the collected supernatants was analyzed by an ELISA-like assay and results (Table 3.8) indicate a limited amount of the biomolecule present in the supernatants, denoting that ICOS-Fc formed a stable bond with the particles surface.

Table 3.8: Stability test of ICOS-Fc binding to SD-Sr-ICOS-Fc surface.

SD-Sr-ICOS-Fc				
Time (Days)	3	7	14	21
ICOS-Fc in medium (%)	5.6	5.3	5.4	6.6

3.3.2.2 Strontium ions release from SD-Sr-ICOS-Fc in tris HCl

Strontium ions release of SD-Sr-ICOS-Fc was analyzed by ICP-AES (reported in the figure 3.30); results of the tests, performed to investigate changes of the release ability of SD-Sr-ICOS-Fc after the grafting procedure, showed that the total amount of strontium was released in tris HCl, also in this case with a burst release in the first 3 h that reach a plateau phase between the day 7 and the day 14, similar to SD-Sr samples, but the profile of the release graph was slightly different from the SD-Sr release graph, this behaviour can be ascribable to the pore entrance that is limited by the grafting but with the ion exchange still allowed.

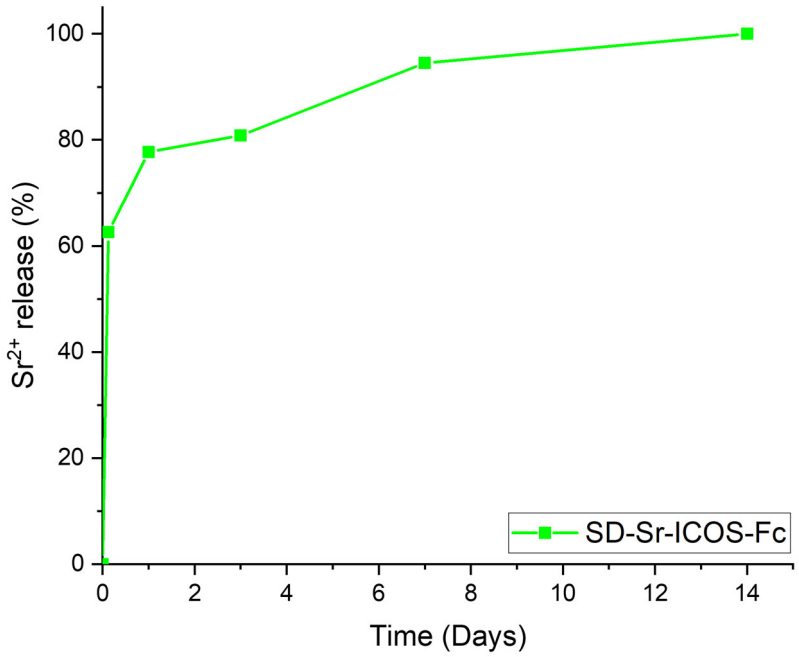

Figure 3.30: Profile of the strontium ions releases of SD-Sr-ICOS-Fc.

3.3.2.3 Bioactivity of SD-Sr in SBF

The SD-Sr-ICOS-Fc bioactivity, tested in SBF medium up to 14 days, was performed to inspect the possibility that the grafting method can affected the ability to form the HA layer of SD-Sr-ICOS-Fc. As for SD-Sr, after 3 days of soaking a rapid formation of a HA was detected for SD-Sr-ICOS-Fc (Figure 3.31A), with a formation of a layer that partially covers the particles after 7 days of soaking (Figure 3.31B) and that totally covers them after 14 days (Figure

3.31C), evincing that the grafting does not affect the excellent bioactivity of SD-Sr-ICOS-Fc and, indeed, as occurred for SG-Sr-ICOS-Fc samples, resulted accentuated.

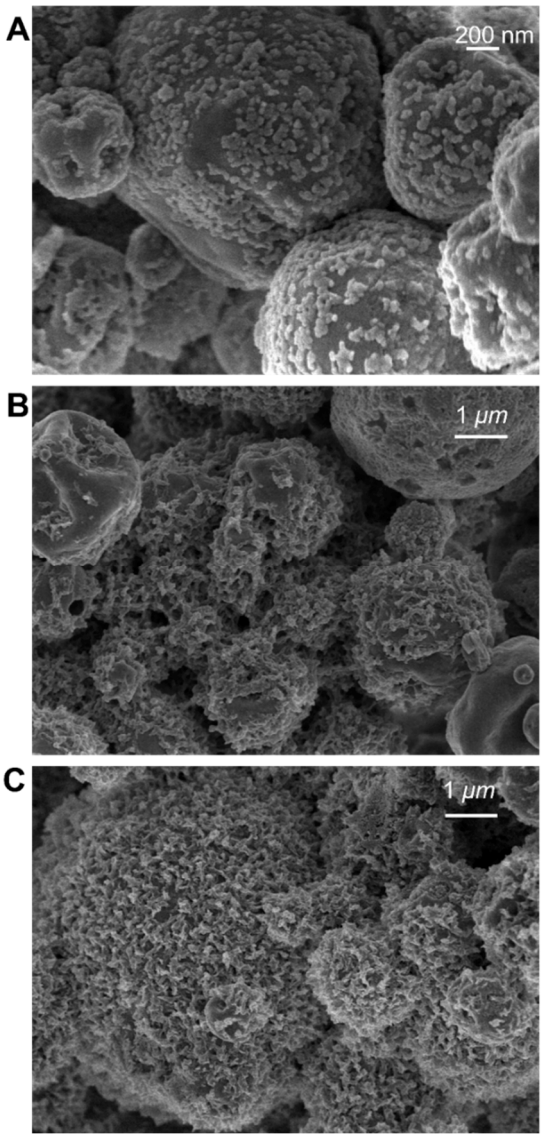

Figure 3.31: FESEM image of SD-Sr-ICOS-Fc after (A) 3, (B) 7, and (C) 14 days of soaking in SBF.

Moreover, XRD analysis was performed to the further confirmation of the HA layer formation (Figure 3.32). The spectra of day 7 and day 14 showed crystalline HA peaks at 25.62 and 31.78 2θ degrees (reference 01-074-0565), as occurred for SD-Sr; also in this case, the absence of peaks at 3 days can be due to the too low concentration of HA formed in this time step.

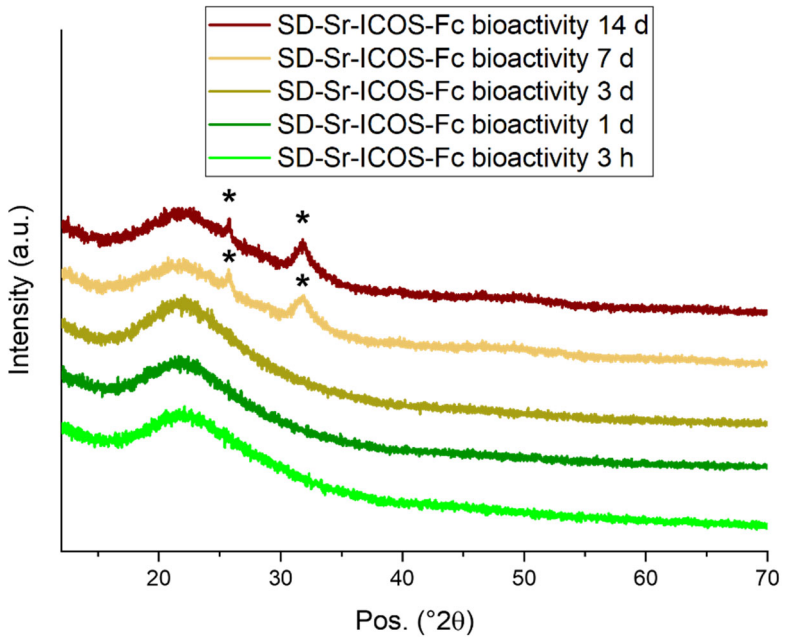

Figure 3.32: XRD spectra of SD-Sr-ICOS-Fc after 3h, 1 day, 3 days, 7 days, and 14 days of soaking in SBF medium. Asterisks show the HA peaks.

3.3.3 Biological tests of SG-Sr-ICOS-Fc and SD-Sr-ICOS-Fc

Part of the work described in this chapter has been previously published[259].

The aim of this part of work was to investigate the biocompatibility, and the ability to inhibit the osteoclasts migration and differentiation of the developed multifunctional materials. Both SG-Sr-ICOS-Fc and SD-Sr-ICOS-Fc were tested by NOVAICOS company comparing the results with the effects of free ICOS-Fc in terms of the potentiality of migration and differentiation inhibition.

3.3.3.1 Biocompatibility of SG-Sr-ICOS-Fc and SD-Sr-ICOS-Fc

In order to evaluate the cytotoxicity of the samples, different amounts of SG-Sr-ICOS-Fc and SD-Sr-ICOS-Fc (200, 100, and 10 µg/mL) were incubated with MC3T3-E1 cells; then, after different time points (2,4 and 7 days) the cell viability was evaluated (Figure 3.33). Results showed an optimal biocompatibility of both SG-Sr-ICOS-Fc and SD-Sr-ICOS-Fc; in fact, SG-Sr-ICOS-Fc did not affect the cell viability for all the tested concentrations, compared with the control cells, while only for the highest tested concentration of SD-Sr-ICOS-Fc the cell viability ranging from 70% to 45% that resulted lower compared to the other

concentrations and the untreated cells which did not show significant modifications in cell viability.

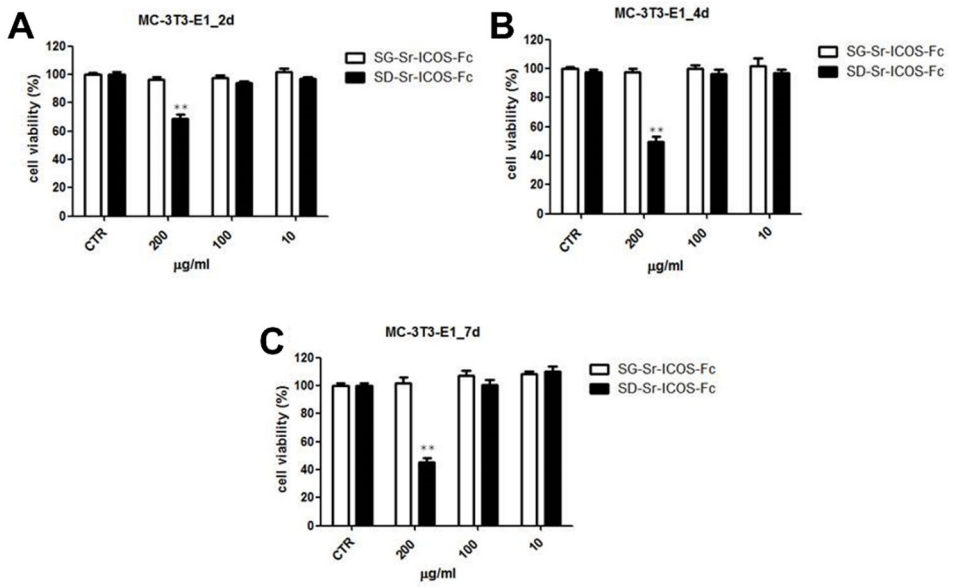

Figure 3.33: MC3T3-E1 cell viability after SG-Sr-ICOS-Fc (white bars) and SD-Sr-ICOS-Fc (black bars) treatment at different times of exposure (A) 2 d, (B) 4 d, and (C) 7 d and at different concentrations.

3.3.3.2 Effects of SG-Sr-ICOS-Fc and SD-Sr-ICOS-Fc on cell migration and proliferation

The effect of free ICOS-Fc on the osteoclasts migratory activity was well reported in the literature[303, 304]; to compare the effects of SG-Sr-ICOS-Fc and SD-Sr-ICOS-Fc samples on the osteoclast's migration Boyden chamber migration assays with ICOS-L positive cell lines, or ICOS-L negative cell line as control, were performed as described in chapter 2, section 2.10.2. Results showed an affected migration of ICOS-L positive cells (PC-3 and U2OS) when treated with SG-Sr-ICOS-Fc or SD-Sr-ICOS-Fc in a dose dependent manner in analogy to free ICOS-Fc compared to ICOS-L negative cells (HOS), contrary to bare samples, evidencing that the grafted ICOS-Fc retained the ability to specifically inhibit only the ICOS-L positive cells motility (Figure 3.34).

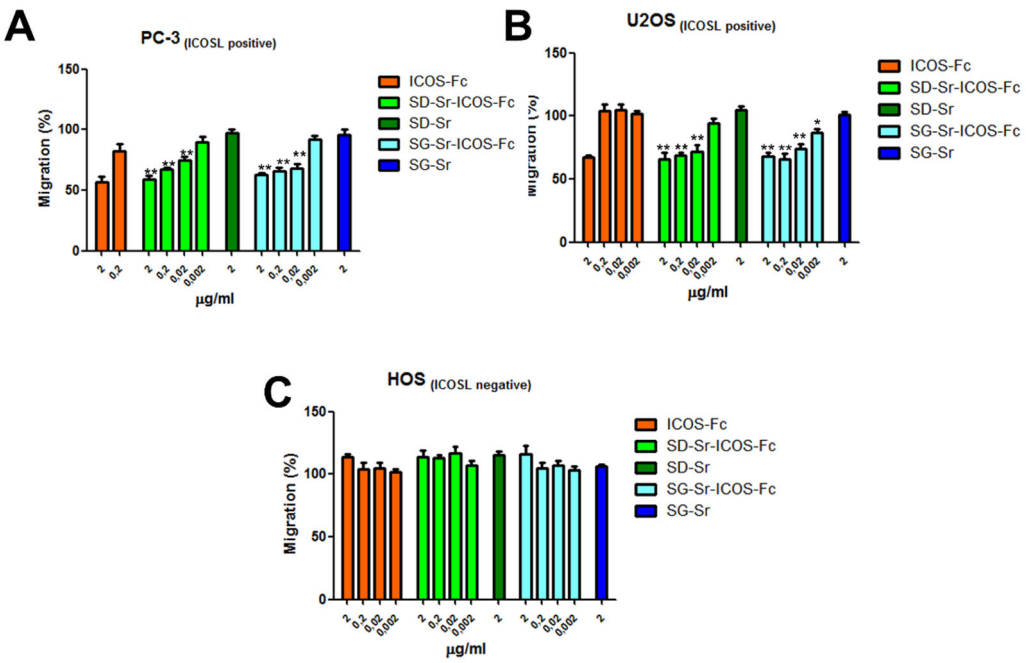

Figure 3.34: Results of the Boyden chamber migration assay of SG-Sr-ICOS-Fc and SD-Sr-ICOS-Fc at different concentrations on PC-3 (A) and U2OS (B) ICOS-L positive cells, and on HOS (C) ICOS-L negative cells.

The effects on cells proliferations of SG-Sr-ICOS-Fc and SD-Sr-ICOS-Fc were tested with clonogenic proliferation assays, and results (reported in Figure 3.35) showed that SG-Sr-ICOS-Fc and SD-Sr-ICOS-Fc did not affect the proliferation of the cells.

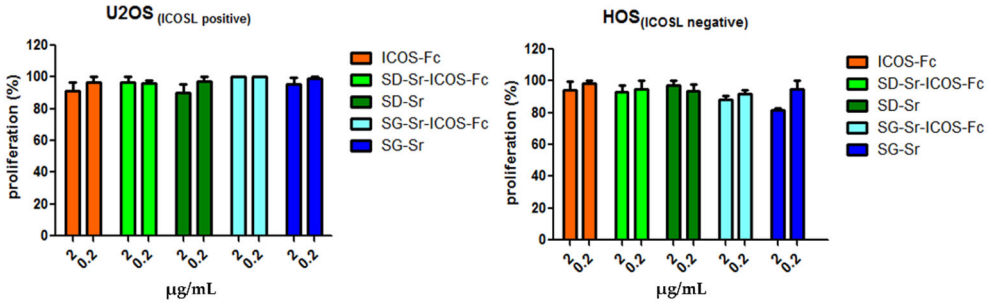

Figure 3.35:Clonogenic assay on U2OS (left) and HOS (right) cells treated with SG-Sr-ICOS-Fc and SD-Sr-ICOS-Fc, compared with free ICOS-Fc.

3.3.3.3 Effects of SG-Sr-ICOS-Fc and SD-Sr-ICOS-Fc on monocyte-derived osteoclasts differentiation

The inhibitory effects on the monocyte-derived osteoclasts (MDOCs) differentiation of SG-Sr-ICOS-Fc and SD-Sr-ICOS-Fc were tested comparing the results with the inhibition ability of free ICOS-Fc reported in literature[29]. MDOCs were placed in contact with SG-Sr-ICOS-Fc and SD-Sr-ICOS-Fc and the differentiation of the cells was monitored up to 21 days; results (showed in Figure 3.36) evidenced that the MDOCs differentiation was strongly inhibited by the ICOS-Fc grafted on particles surface, in analogy to free ICOS-Fc. Moreover, the cells after the treatments with SG-Sr-ICOS-Fc and SD-Sr-ICOS-Fc resulted to be with a round shape and a spindle-like morphology, very similar to cells treated with free ICOS-Fc, while cells treated with SG-Sr or SD-Sr did not show differences in the differentiation compared to the negative control. Furthermore, the treatment with SG-Sr-ICOS-Fc and SD-Sr-ICOS-Fc displayed a decrease in the formation of multinuclear TRAP positive cells, confirming the potential ability of SG-Sr-ICOS-Fc and SD-Sr-ICOS-Fc to inhibit the osteoclast cells differentiation.

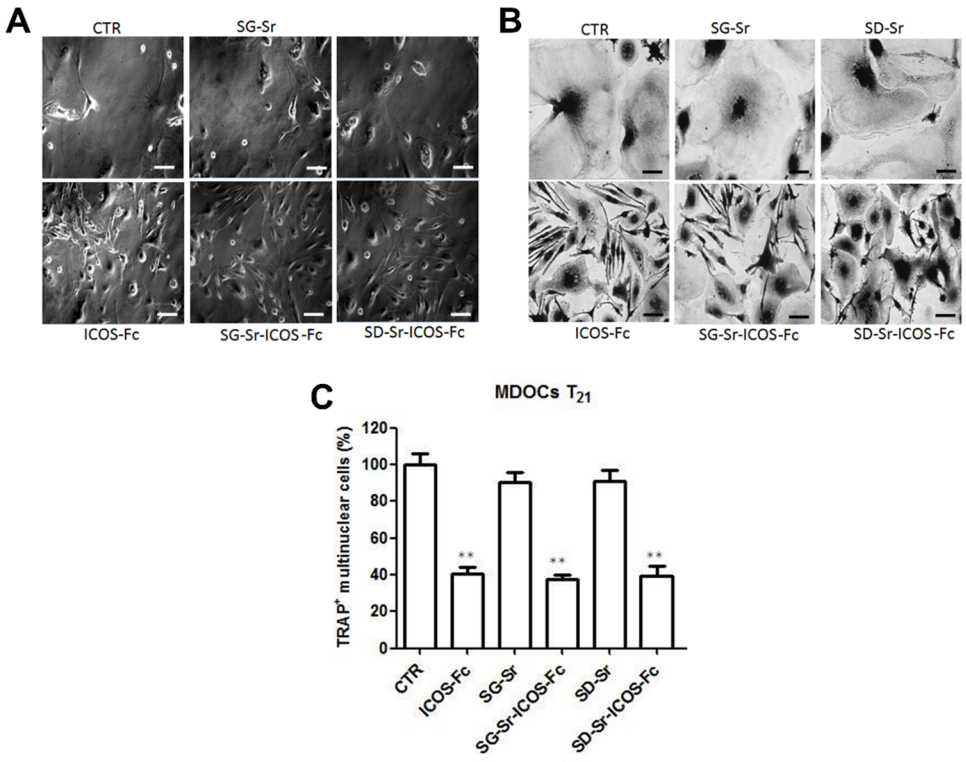

Figure 3.36: MDOCs morphology after the treatment with SG-Sr-ICOS-Fc and SD-Sr-ICOS-Fc compared with free ICOS-Fc and SG-Sr and SD-Sr showed by phase-contrast microscopy (A) and microphotographs (B). (C) Percentage of multinuclear TRAP positive cells at day 21 after the treatment with with SG-Sr-ICOS-Fc and SD-Sr-ICOS-Fc compared with free ICOS-Fc and SG-Sr and SD-Sr.

To further confirm the differentiation inhibition of SG-Sr-ICOS-Fc and SD-Sr-ICOS-Fc, differentiation marker genes (DC-STAMP, NFATc1, and OSCAR) expression was evaluated by real-time PCR at day 21 (Figure 3.37), since in the differentiation phase these marker genes are upregulated[305]. Results showed a significant decrease of the expression of all these genes for cell treated with SG-Sr-ICOS-Fc and SD-Sr-ICOS-Fc compared with untreated cells and cells treated with SG-Sr and SD-Sr, in analogy to cells treated with free ICOS-Fc, providing a further confirmation that the developed SG-Sr-ICOS-Fc and SD-Sr-ICOS-Fc have the ability to inhibit the differentiation of osteoclasts.

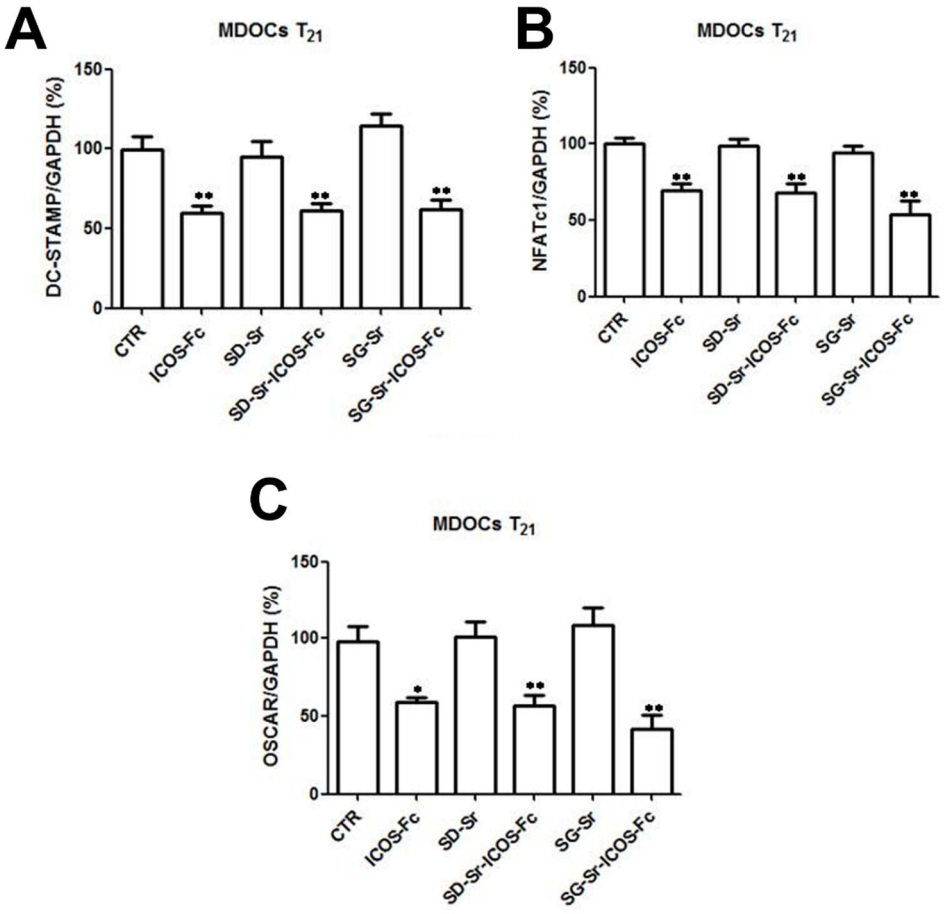

Figure 3.37: DC-STAMP (A), NFATc1 (B), and OSCAR (C) marker genes expression of cells treated with SG-Sr-ICOS-Fc and SD-Sr-ICOS-Fc at day 21 compared with cells untreated or treated with SG-Sr, SD-Sr, and free ICOS-Fc.

3.4 Final considerations

Different types of MBGs were successfully synthetized by a base catalyzed sol-gel method and an aerosol-assisted spray-drying procedure, allowing to produce nanoparticles and microparticles, respectively. The base catalyzed sol-gel method allowed to obtain well dispersed nanoparticles with a uniform diameter ranging between 100 and 300 nm having a spherical shape, while the aerosol-assisted spray drying approach allowed to obtain well dispersed spherical microparticles with a diameter ranging between 1 and 5 μm.

Both synthesis methods led to particles with an internal mesoporous structure, with a pore diameter of 3 nm due to the use of cetyltrimethylammonium bromide (CTAB) for SG-Sr and with pores with a diameter of 5-7 nm due to the use of

P123, for the base catalyzed sol-gel method and aerosol-assisted spray drying approach, respectively. The specific surface area and pore volume resulted very high compared to the not-templated conventional glasses[306], even if lower compared to similar particles without the presence of strontium in the silica framework, in particular, SG-Sr surface area resulted to be the 46% of the normal surface area of silica nanoparticles without Sr[282], and SD-Sr surface area resulted to be the 44% compared to silica microparticles without Sr[297, 298].

Both types of synthesis allowed to incorporate strontium ions into the silica framework to a percentage close to the theoretical one, even if slightly different; the lower amount encountered for SD-Sr respect SG-Sr can be ascribed to the larger ionic radius of strontium (1.18 Å) compared to that of calcium (0.99 Å)[295, 307], that can partially limit the incorporation into the silica framework during the spray-drying process[308].

The ions release tests showed a burst release during the first 3 h for both types of particles that can be related to the high surface area of the particles allowing a fast ion diffusion through the porous structure, the amount of the Sr ions released does not differ too much from the literature[285, 286]. Moreover, both types of particles showed bioactivity in SBF proving that the incorporation of different ions did not inhibit the bioactive behaviour of silica mesoporous glasses, even if it was lower compared with MBGs that do not contain the Sr ions as reported in the literature[283, 289–292].

Since the aerosol assisted spray-drying approach is a process that can be easily scalable, some trials to scaling-up the synthesis of SD-Sr were performed obtaining samples with incorporated Ca and Sr and with a specific surface area and pore volume comparable to the lab-scale microparticles, even if the morphology showed the presence of aggregates consisting of amorphous silica-based precipitates. Results suggested that the process is in principle feasible but requires further optimization in order to obtain final microparticles with structural and morphological features similar to powders produced at lab-scale. Since the main problem is the early precipitation prior to the spraying, this can be mitigated by using an ice bath both during the solution preparation and the spraying of the final solution.

Furthermore, both types of particles were grafted with ICOS-Fc in a method consisting in two following steps, obtaining SG-Sr-ICOS-Fc and SD-Sr-ICOS-Fc samples. Both SG-Sr-ICOS-Fc and SD-Sr-ICOS-Fc resulted to maintain all the characteristics exhibited by bare samples in terms of morphology, textural features, ions release properties, and an even greater bioactivity. Moreover, ICOS-

Fc biomolecule resulted to be successful grafted on the particles surface with a stable bond and with the correct orientation without change its ability to bind ICOS-L.

Finally, grafted samples demonstrate to possess a good biocompatibility, as well as the ability to specifically inhibit the migration and differentiation of only ICOS-L positive cells as confirmed by the Boyden chamber assays and the analysis of the differentiation of MDOCs and marker genes expression, respectively.

To conclude, the developed SG-Sr-ICOS-Fc and SD-Sr-ICOS-Fc can be used in the study of the design of the final scaffold in order to confer both pro-osteogenic and anti-osteoclastogenic properties.

Chapter 4

Electrospinning of the collagen-based suspensions and crosslinking to obtain the multifunctional scaffold

4.1 Introduction

In this chapter, with the final aim to develop a scaffold to treat pelvis osteoporotic fractures, the electrospinning (ESP) and the subsequent crosslinking of type I collagen (COL) combined with inorganic phases will be presented. Two different inorganic phases were used: strontium containing mesoporous bioactive glasses (MBGs) grafted with ICOS-Fc biomolecule (described in chapter 3), and strontium containing nano-hydroxyapatite (Sr-nano-HA) provided by FLUIDINOVA company.

ESP is a promising technique to develop biomimetic scaffolds, in fact, this method permits to produce constructs mimicking the extracellular matrix (ECM), enabling the production of micro- and nanofibrous mats[192, 193]. The construct produced by ESP consists in flexible membranes that can be adapted to different parts of the pelvis zone. The use of different process parameters allows for controlling the deposition, the morphological characteristics, and the physico-chemical properties of the membrane that will be obtained[24, 192, 309].

However, the use of collagen material in the ESP technique shows some critical aspects consisting in the potential denaturation of the protein due to the used solvents and process parameters[192, 212, 310].

Firstly, the potential denaturation of collagen in acetic acid (AA) solution and different collagen concentrations has been explored in order to obtain a homogeneous solution that can be electrospun. Then, different ESP conditions have been investigated to realize the final fibrous electrospun membrane and the morphology of electrospun membranes was assessed by scanning electron microscopy (SEM), to define the influence of the different ESP parameters; collected data led to define the best collagen formulation and ESP conditions in order to obtain homogeneous nano-fibrous matrix.

After the preliminary optimization of the ESP process for collagen alone, MBGs or nano-HA were introduced in the collagen solutions as inorganic phases, and the ESP process has been optimized for the resulting hybrid suspensions to obtain composite membranes with inorganic phases homogenously distributed inside the membrane. The obtained membranes were characterized by SEM to confirm both the maintained fiber morphology and the presence of a homogeneous inorganic phase.

Finally, since collagen-based matrices generally lack mechanical properties and chemical stability[311], strategies to enhance these properties were explored. In detail, two chemical crosslinking methods were investigated: an 1-ethyl-3-(3-dimethylaminopropyl)carbodiimide (EDC)/ N-Hydroxysuccinimide (NHS) coupling in order to link amino and carboxyl groups of the collagen structure, and a crosslinking using a photoinitiator called Rose Bengal (RB), that is already used in clinical applications[255, 256] to induce the binding of collagen fibres by using a 514 nm radiation. Cross-linked membranes were then characterized by SEM to confirm the maintained morphology upon the crosslinking reactions, and by free amine tests in order to confirm the occurred crosslinking.

4.2 Electrospinning of the collagen solutions

Critical roles in the electrospinning fabrication are played by the solvent and the polymer concentration, as well as the ESP parameters such as the applied voltage, the flow rate and the distance of the collector. Moreover, additional other issues have been reported for the ESP of natural polymers due to their high

viscosity and low solubility, often requiring the addition of other synthetic polymers or the dissolution into organic toxic solvents.

Generally, one of the most used solvents for the collagen ESP is the 1,1,1,3,3,3 hexafluoro-2-propanol (HFP) which exhibits a low boiling point (61 °C), which is a desirable characteristic in ESP applications promoting the evaporation of the solvent under atmospheric conditions, resulting in the deposition of collagen fibers in a dry state[312]. However, normally the harsh and toxic environment of the HFP solvent significantly influences the physico-chemical properties of the native collagen[24, 192, 193], even if in some cases the electrospun collagen maintained its characteristics[313]. On the other hand, the use of non-toxic solvents (ethanol or phosphate-buffered saline solutions) results in less homogeneous larger fibers as well as presents deposited salts in the final membrane[314].

In order to overcome the issues related to the use of harmful organic solvents and promote the deposition of functional collagen nanofibers, in this PhD thesis, the use of AA solution, as a benign solvent, was optimized to solubilize collagen at high concentrations (ranging from 15 wt% to 25 wt%) preserving the overall native structure of the protein.

4.2.1 Characterization of collagen dissolved in acetic acid solution

At first, different batches of COL extracted and provided by NOVAICOS company were characterized with FTIR analysis and compared to literature data in order to evaluate that the extraction process did not alter biological functionality and create a reference before the dissolution and the ESP (Figure 4.1).

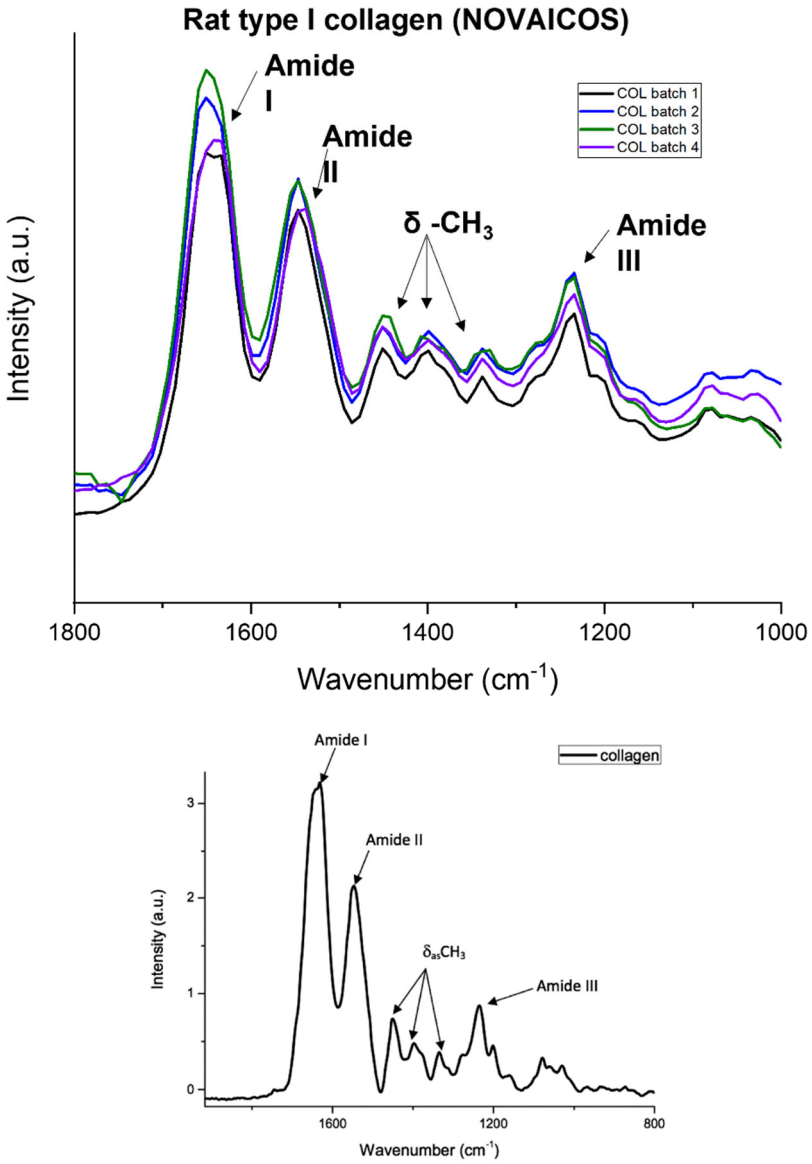

Figure 4.1: FTIR spectra of the COL batches provided by NOVAICOS company (above), FTIR spectrum of the type I collagen by Júnior et al. [315] (below).

The spectra of all COL batches showed three peaks at 1239 cm^{-1}, 1555 cm^{-1}, and 1650 cm^{-1} ascribable to the amide III (C-N stretching and N-H bending), amide II (N-H bending), and amide I (C=O stretching), respectively; moreover, three peaks ascribable to the C-H bending were founded at 1320 cm^{-1}, 1400 cm^{-1}, and 1450 cm^{-1}. Comparing the registered spectra with the spectrum reported by Júnior et al.[315], similar positions and intensity ratio of the peaks suggest that the

different COL batches overall show the typical spectroscopic features of collagen structure.

The preservation of the native structure of the COL after the dissolution in a solution of 40% AA in water was then investigated by FTIR analysis and compared with the dissolution in HFP solvent. Prior the FTIR analysis, COL was dissolved in the solvent (40% AA solution or HFP), frozen at -20 °C, and lyophilized. FTIR spectra of COL dissolved in 40% AA solution compared with the COL not dissolved showed analogous absorption peaks, at variance with COL dissolved in HFP solvent (Figure 4.2).

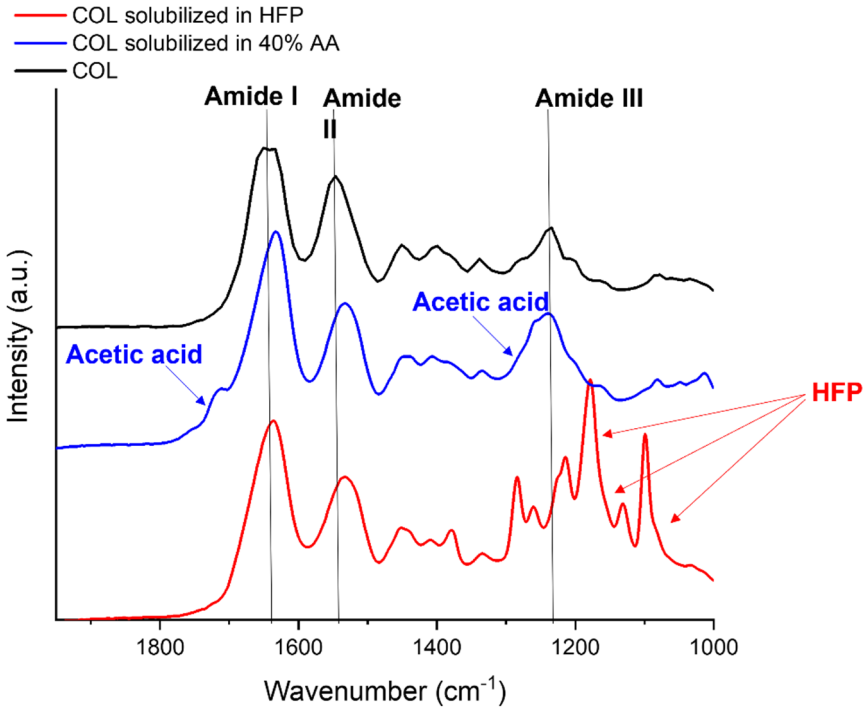

Figure 4.2: FTIR spectra of COL dissolved in 40% AA solution (blue line), compared with not dissolved COL (black line) and COL dissolved in HFP (red line).

For both spectra of collagen after dissolution residuals of the solvents were evidenced: COL dissolved in 40% AA peaks at 1740 cm^{-1} and at 1387 cm^{-1}, corresponding to the C=O carbonyl stretch and to the C-H symmetric deformation[316], respectively, and for COL dissolved in HFP a group of bands in the region between 1100 cm^{-1} and 1250 cm^{-1} ascribable to the HFP solvent[317]. Moreover, the three peaks at 1320 cm^{-1}, 1400 cm^{-1}, and 1450 cm^{-1} were present for all three samples, but while the bands of amide I at 1650 cm^{-1} and amide II at 1555 cm^{-1} showed only a slight shift after the dissolution in the

two solvents, the amide III band at 1239 cm^{-1} was not observed in the COL sample dissolved in HFP compared to both COL before and after dissolution in 40% AA solution, suggesting a more extensive loss of the collagen structure[309], in particular the β-sheet secondary structures[318], when dissolved in HFP.

To further confirm the maintenance of the structure for COL dissolved in 40% AA solution, SDS-PAGE was performed by NOVAICOS company comparing the dissolved samples with the COL pre-dissolution and commercial collagen (type I collagen from rat tail, Roche) (Figure 4.3).

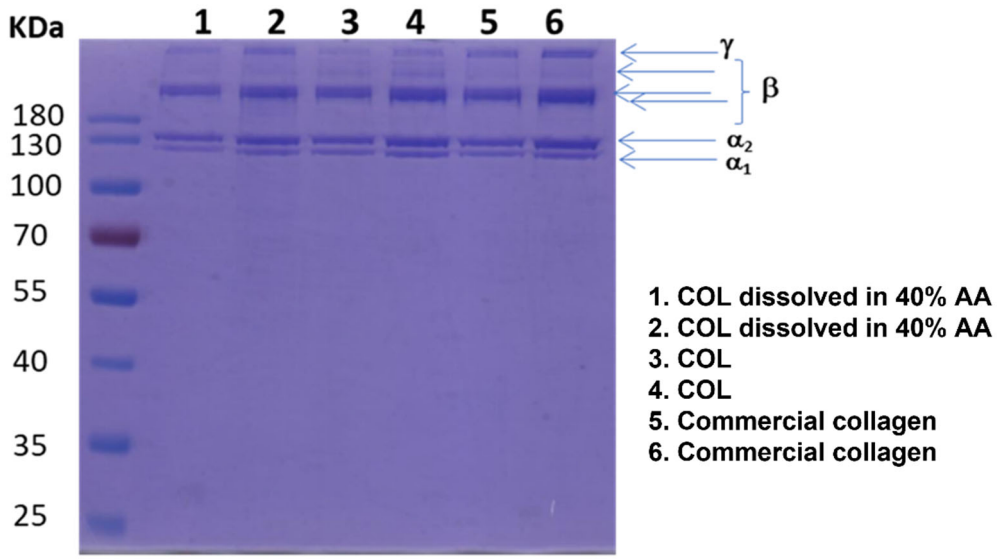

Figure 4.3: SDS-PAGE of COL dissolved in 40% AA solution, compared to COL provided by NOVAICOS and commercial collagen.

Since the acidic pH of the 40% AA solution caused problems on the electrophoretic run, the following protocol has been optimized before the electrophoretic analysis: COL was dissolved in 40% AA, frozen and subsequently lyophilized (-54 °C, pressure of 0.08 mbar for 48 h). The obtained lyophilized sample was added to the loading buffer and heated for 5 min at 95 °C for the SDS-PAGE analysis. Results of COL dissolved in 40% AA showed the presence of the α bands, as well as β and γ bands as for COL and commercial collagen, confirming the identity and purity of the collagen protein[319], moreover, the pattern of the sample was similar to COL as extracted and to the commercial collagen, indicating that the chains of the protein were not degraded.

4.2.2 Electrospinning of collagen dissolved in AA solution

After the confirmation that the dissolution in AA does not significantly degrade the collagen structure, the activity mostly focused on identifying the ideal concentration of collagen for the ESP process. With this perspective, COL was dissolved in 40% AA solution at different concentrations, 15 wt%, 20 wt% and 25 wt%, by adding the COL to the 40% AA solution and leaving the resulting solutions to stir overnight at RT. Prior to ESP, centrifugation was performed in order to remove all the formed bubbles, then the solution was electrospun.

The trials started with the processing of 15 wt% of COL in 40% AA, however, the formation of the Taylor cone and the jet stability were not optimal for the parameters used; consequently, parameters were slowly changed one by one until the stabilization of the jet was attained. Therefore, the final voltage and flow rate in which the solution was successfully electrospun with a formation of the Taylor cone and a stable jet were 18 kV and 150 µL/h, respectively, while the distance of the collector for a stable ESP resulted in 15 cm. The obtained membrane was analyzed by SEM and images showed a homogeneous fiber mat with the undesired formation of beads (Figure 4.4), indicating that 15 wt% was not an optimal concentration for electrospinning the collagen with 40% AA solution. The average size of electrospun fibers was about 80 nm-100 nm.

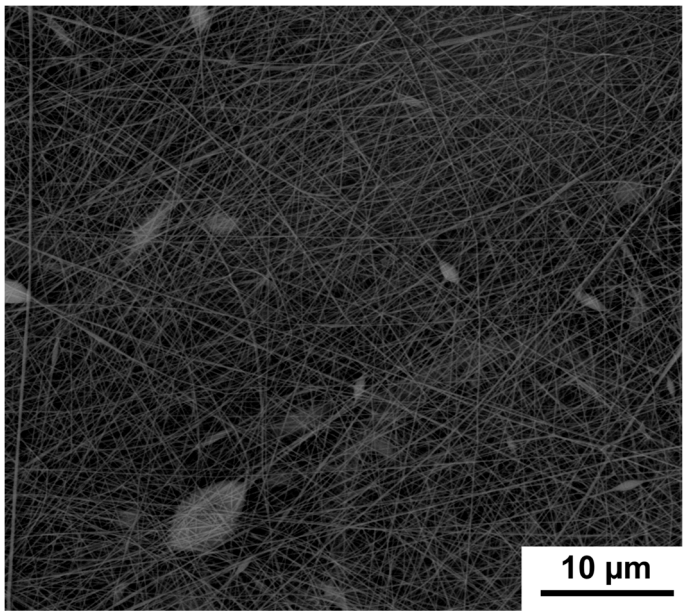

Figure 4.4: SEM image of the collagen membrane obtained by ESP at the concentration of 15 wt% with a voltage of 18 kV, a flow rate of 150 µL/h, and a distance from the collector of 15 cm.

According to the literature, beads formation can be prevented by increasing the concentration of the solution[320]. Consequently, the concentration of the COL was increased to 25 wt% and the resulting solution was electrospun, however the parameters used for the ESP of the 15 wt% collagen solution did not allow a stable jet, consequently voltage, flow rate, and the collector distance were changed one by one in order to stabilize the jet and obtain a Taylor cone. A stable jet was obtained by setting the voltage at 20 kV and a flow rate of 80 µL/h, the optimal working distance of the collector resulted in 12 cm. The obtained membrane resulted in dense homogeneous fiber mats without the presence of beads, as shown in figure 4.5.

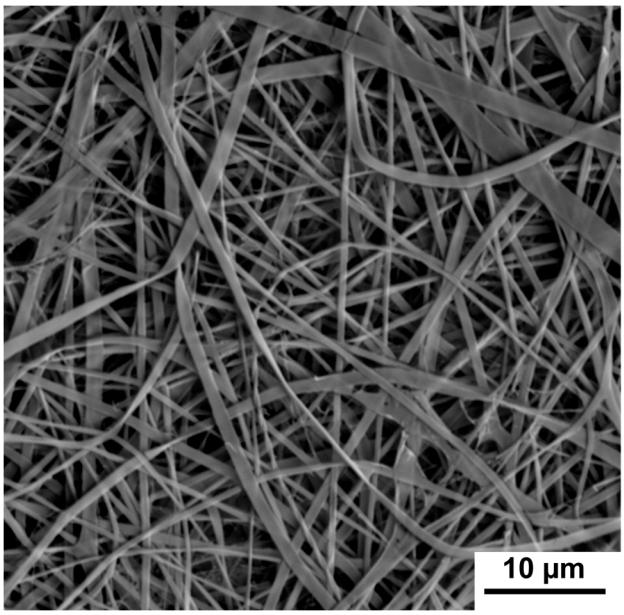

Figure 4.5: SEM image of the collagen membrane obtained by ESP at the concentration of 25 wt% with a voltage of 20 kV, a flow rate of 80 µL/h, and a distance from the collector of 12 cm.

The increase in collagen concentration leads to the formation of fibers with a larger diameter (around 450 nm-500 nm), moreover, fibers morphology was flat and irregular, indicating that this concentration hindered the achievement of fiber with the targeted morphology.

To find a compromise between the concentrations, a new solution of COL at a concentration of 20 wt% was prepared and electrospun. As occurred for the increasing of the concentration from 15 wt% to 25 wt%, also the decrease to 20 wt% required again the change of the parameters one at a time to get a stable stream during the ESP process; the final parameters used to electrospun the 20

wt% collagen solution were reported in table 4.1. Using this collagen concentration, a dense homogeneous fiber mat was obtained (Figure 4.6).

Table 4.1: ESP parameters applied for processing the COL solution at 20 wt%.

COL concentration (wt%)	**Voltage (kV)**	**Flow rate (µL/h)**	**Collector distance (cm)**
20	22-24	300-350	12

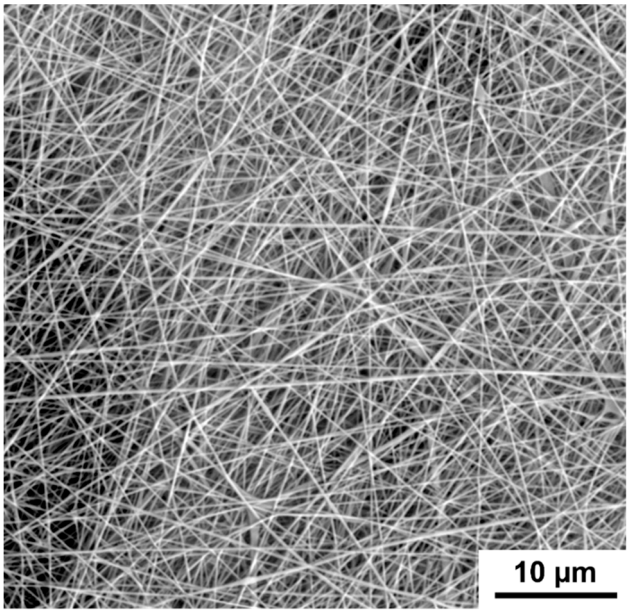

Figure 4.6: SEM image of the collagen membrane obtained by ESP at the concentration of 20 wt% with a voltage of 22-24 kV, a flow rate of 300-350 µL/h, and a distance from the collector of 12 cm.

Fiber's diameter resulted to be around 100 nm, smaller compared to those obtained with the 25 wt% solution and slightly greater than those resulting with the 15 wt% solution, within the range defined in the literature for collagen fibers[321]. Moreover, the possible problems arising from the increasing from 25 wt% to 20 wt% are the anew formation of beads and a a non-optimal morphology of the formed fibers due to a non-stable process, however, the formation of fibres with a diameter within the range defined in the literature and the absence of beads indicate that the concentration of 20% by weight is sufficient both for the

formation of fibers with an optimal morphology and for a stable process that not forming beads.

4.3 Optimization of the electrospinning of the collagen-inorganic phase suspensions

Once the concentration and the parameters for a successful electrospinning of the collagen solution were identified, the combination of the collagen solution with MBGs and nano-HA was investigated in order to obtain a composite electrospun collagen-based membrane.

4.3.1 Incorporation of the MBGs microparticles in the collagen fibrous matrix

The first inorganic phase incorporated into the 20 wt% COL solution was the strontium containing MBGs microparticles (SD-Sr) whose synthesis was reported and discussed in chapter 3. SD-Sr rather than SD-Sr-ICOS-Fc was chosen for the trials to optimize the overall process due to the high cost of the ICOS-Fc biomolecule. Since the ICOS-Fc grafting does not cause any substantial change in SD-Sr size and morphology, the obtained results are considered valid also for the functionalized particles.

Different concentrations of SD-Sr were tested in order to prepare the suspensions to be electrospun, namely 5 w/v%, 7.5 w/v%, 10 w/v%, and 15 w/v%, while higher concentrations caused the needle blockage during the process. Each suspension was electrospun with a 5 mL syringe; however, changes in the ESP environment by the addition of the inorganic phase will also affect the process[322], consequently, the addition of SD-Sr affected the formation of the Taylor cone and the stabilization of the jet. Several trials were performed in order to investigate how the process could be stabilized for longer time frames. The suspensions were processed in order to find the optimal conditions for the ESP, in particular for each concentration of the inorganic phase the parameters were changed one by one to achieve a stable process. Table 4.2 reports the best parameters found for each concentration of the inorganic phase, allowing to obtain a stable process.

Table 4.2: The best ESP parameters found for each of the investigated SD-Sr suspensions.

Suspension	Voltage (kV)	Flow rate (µL/h)	Collector distance (cm)
5 w/v%	18	100	15
7.5 w/v%	24	100	12
10 w/v%	24	200	10
15 w/v%	22-24	300-350	10

The resulting membranes for each concentration were characterized by SEM; images showed fibers with regular size and shape (Figure 4.7) for all the electrospun membranes, moreover, the inorganic phase was distributed homogeneously, and particles were integrated within the fibrous matrix, as well as inside the collagen fibers.

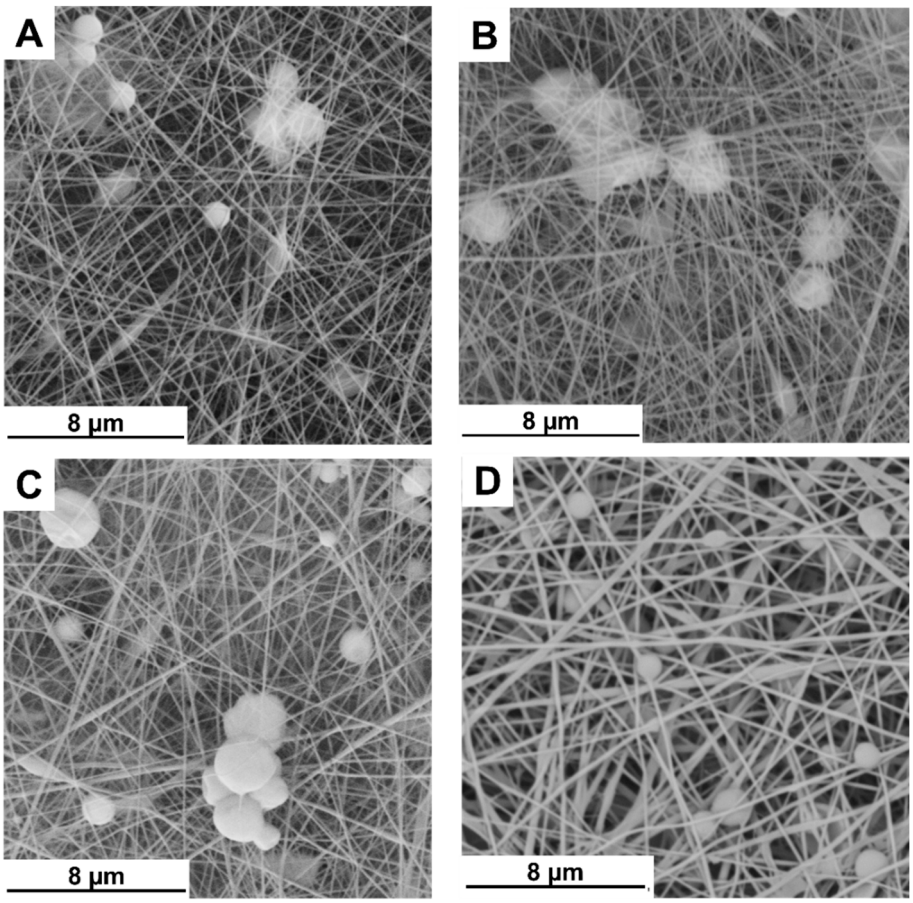

Figure 4.7: SEM images of the electrospun COL suspensions with 5 w/v% (A), 7.5 w/v% (B), 10 w/v% (C), and 15 w/v% (D) of SD-Sr.

Moreover, images also showed the presence of small aggregates smaller than 12 µm for the 5 w/v%, 7.5 w/v%, and 10 w/v% concentrations, while 15 w/v% concentration did not show these types of aggregates and the processability was satisfactory whilst maintaining a high concentration of inorganic phase. Fibers of all the tested concentrations attained a diameter falling in the desired range as described in the literature[321], with an average size of about 120 nm. The 15 w/v% concentration represented the best compromise between the overall processability of the formulation and the amount of incorporated inorganic phase inside the fibrous mat.

4.3.2 Incorporation of the MBGs nanoparticles in the collagen fibrous matrix

Strontium containing MBGs nanoparticles (SG-Sr), whose synthesis is discussed in chapter 3, was also incorporated into the 20 wt% COL solution.

The tested concentrations were 5 w/v%, 7.5 w/v%, 10 w/v%, and 15 w/v% since higher concentrations involved the needle blockage, as for the suspension with SD-Sr. In all the trials with SG-Sr it was observed that higher voltages led to higher material accumulation which could be associated with solvent evaporation excessively fast, and consequently requiring more frequent interruptions of the process to clean the needle and remove the accumulated material. However, the ESP of every concentration of SG-Sr of the suspensions was performed by changing the parameters one by one to make the process more stable. The final set of parameters for each suspension are reported in table 4.3.

Table 4.3: The best ESP parameters applied to each concentration of the SG-Sr in the COL and inorganic phase suspensions.

Suspension	Voltage (kV)	Flow rate (µL/h)	Collector distance (cm)
5 w/v%	20	100	10
7.5 w/v%	18	100	10
10 w/v%	20	100	10
15 w/v%	25	200	10

The matrices obtained from the ESP for each concentration showed the presence of a homogenous mat, made of fibers with regular size and cylindrical shape (Figure 4.8); however, a large number of agglomerates was observed for all trials, on the contrary respect to the suspensions with microparticles, even if the observed agglomerates were smaller than 10 µm.

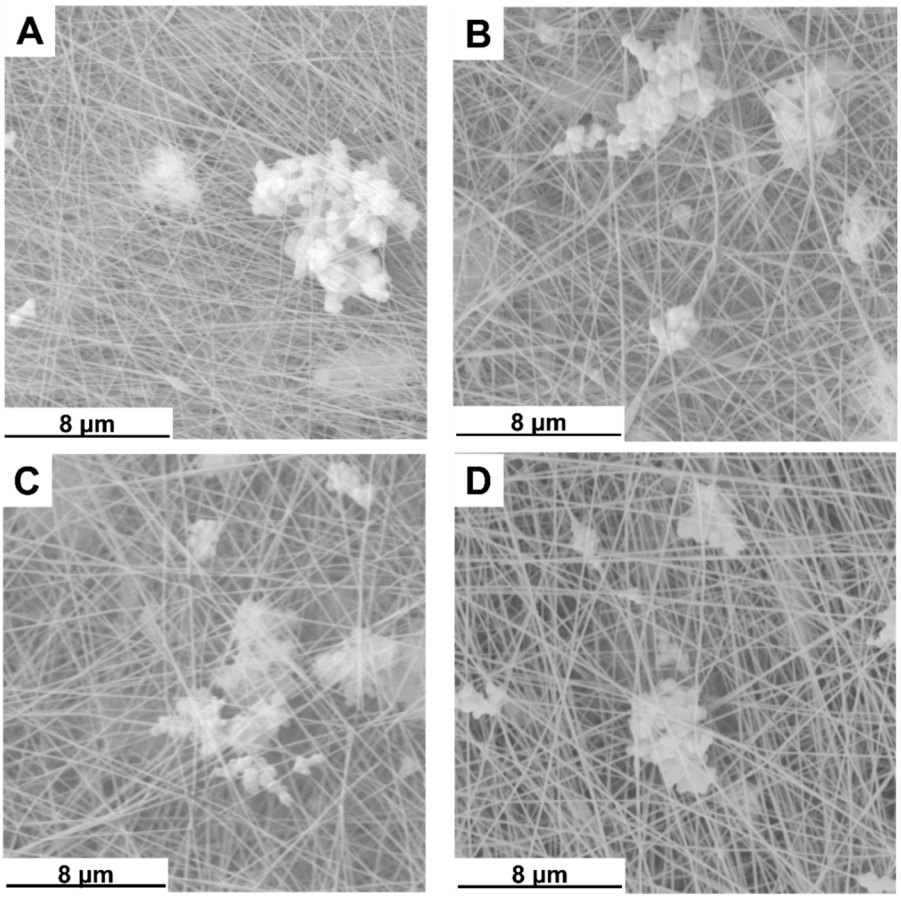

Figure 4.8: SEM images of the electrospun COL suspensions with 5 w/v% (A), 7.5 w/v% (B), 10 w/v% (C), and 15 w/v% (D) of SG-Sr.

In this case, as for the SD-Sr suspensions, the 15 w/v% concentration of the electrospun suspension represented the best compromise between the processability of the hybrid formulation and the amount of incorporated inorganic phase, with a formation of a fibrous mat having fibers with an average size of about 100 nm in line with the size reported in the literature[321].

4.3.3 Effect of the acetic acid on MBGs grafted with ICOS-Fc

In the experiments described in the previous sections, due to the cost of ICOS-Fc unfunctionalized samples were used. However, even if the set of optimized ESP parameters are expected to be not influenced by the presence of the biomolecule grafted on MBGs surface, the effect of the acidic solvent on the biological functionality of ICOS-Fc is a key aspect and needed a dedicated investigation in view of the final scaffold development as well as the possible cleavage of the

amide bond formed between ICOS-Fc and the MBGs surface, since the break of the amide bond during the ESP process leads to a loss of ICOS-Fc during the process and in addition a stable bond results in a specific osteoclasts inhibition only in the site where they are active as discussed in chapter 3, section 3.3.1.1.

With this purpose, MBGs (both SD and SG) grafted with ICOS-Fc were incubated in the 40% AA solution at 15 w/v% in order to mimic the maximum concentration defined for the MBGs in the ESP trials. With the aim of mimicking the minimum and maximum time in which the particles and the solution are in contact, two different time points were considered: 4 hours (the time needed for the preparation of the suspension and the subsequent addition to the COL solution prior to the ESP), and 7 hours (the duration of the whole ESP process). At the defined time points, the assessment of functional ICOS-Fc was evaluated by NOVAICOS company with an ELISA-like assay on the collected supernatants to indagate the possible cleavage of the bond between ICOS-Fc and MBGs and on the particles in order to indagate the maintained activity of ICOS-Fc after the exposition of AA; but, since AA can interfere with the test, supernatants were prior dialyzed against PBS in order to remove all the AA residues, while the particles were washed with water and re-suspended in PBS.

Results were expressed in optical density (OD) value, this value in the results of the following equation:

$$OD = log \frac{I_0}{I}$$

where I_0 is the intensity of the monochromatic radiation sent to the sample and I is the intensity of the monochromatic transmitted radiation.

The obtained results showed no significant differences between the samples contacted with 40% AA for 4 h or 7 h, but differences were instead evidenced before and after the contact, in particular for SG-Sr-ICOS-Fc samples (Figure 4.9). Specifically, SD-Sr-ICOS-Fc presents similar OD, before and after contact with 40% AA, meaning that only a limited number of ICOS-Fc molecules, when grafted on MBG microparticles, lost functionality. On the other hand, for ICOS-Fc grafted on SG-Sr the functionality significantly decreases after contact with the solvent, even if before the contact higher OD value was found if compared to SD-Sr-ICOS-Fc.

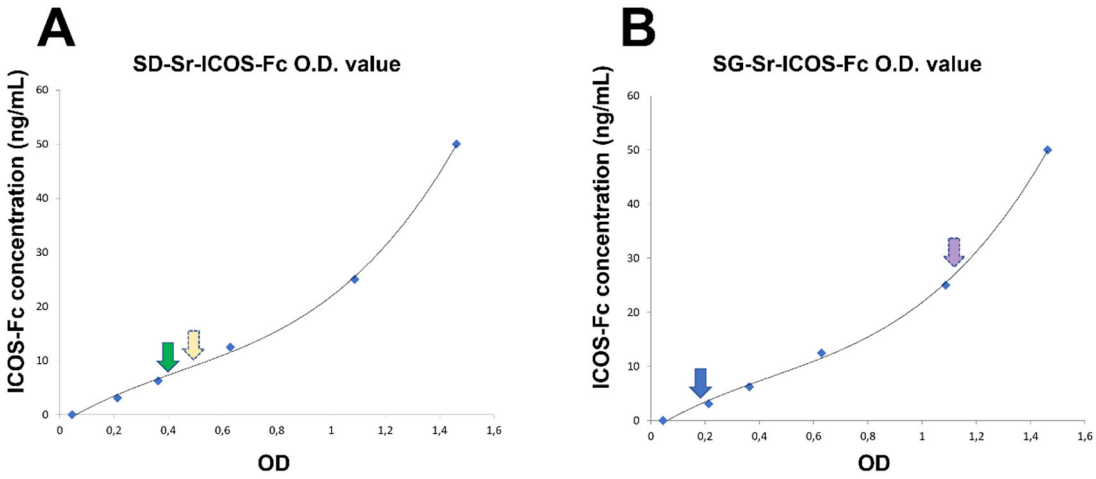

Figure 4.9: OD calibration lines of free ICOS-Fc at different concentrations. (A) shows the OD and relative concentration detected for SD-Sr-ICOS-Fc before (yellow dashed arrow) and after (green arrow) the contact with 40% AA, while (B) shows the OD and relative concentration detected for SG-Sr-ICOS-Fc before (violet dashed arrow) and after (blue arrow) the contact with 40% AA.

These results probably are due to the characteristics of MBGs microparticles, in fact, SD-Sr has larger pore size compared to SG-Sr, consequently, the ICOS-Fc biomolecules are grafted mainly at the entrance of the pores, differently from SG-Sr-ICOS-Fc, whose pore size does not allow to accommodate the bulky molecules inside the porous structure. The less exposed position of ICOS-Fc in SD-Sr-ICOS-Fc samples is expected to reduce the contact of the biomolecule with AA. Moreover, concerning the tests on the supernatants to detect if the acidic solvent can break the amide bond, only a very little amount of free ICOS-Fc was detected in the collected and dialyzed supernatants, implying that the bond between ICOS-Fc and MBGs is not damaged during the process.

4.3.4 Incorporation of the Sr-nano-HA in the collagen matrix

For this part of experiments, Sr-nano-HA produced and provided by FLUIDINOVA company was used at different concentrations; however, since the maximum processable limit of the concentration in the suspension resulted to be 12.5 w/v%, differently from the MBGs particles the concentrations tested were 5 w/v%, 7.5 w/v%, 10 w/v% and 12.5 w/v%, even if, as expected, the suspension with the higher percentage of Sr-nano-HA appeared more viscous compared to the others.

After the preparation, suspensions were transferred in a syringe and processed by ESP. Also in this case, starting from the parameters set for the ESP of the 20 wt% COL solution, the different parameters were changed separately and one at a time in order to achieve a Taylor cone and a stable jet during the ESP process; however, despite the more concentrated suspension resulted to be processable, after 15 minutes of ESP the needle was blocked, hindering the deposition of fibers, hence, the maximum condition processable for longer time was defined as 10 w/v% (over 1 hour without needle blockage). The best parameters of each suspension to obtain the desired characteristics of the process are reported in table 4.4.

Table 4.4: The best ESP parameters applied to each concentration of the Sr-nano-HA in the COL and inorganic phase suspensions.

Suspension	**Voltage (kV)**	**Flow rate (µL/h)**	**Collector distance (cm)**
5 w/v%	16	80	10
7.5 w/v%	20	100	12
10 w/v%	23-24	300-350	10
12.5 w/v%	26	200	10

The obtained membranes were analyzed with SEM and images showed COL fibers with regular size and shape, and with a homogeneous distribution of the inorganic phase, with Sr-nano-HA particles visibly integrated within the matrix (Figure 4.10). As mentioned above, based on the time to be processable and the amount of the inorganic phase incorporated, the optimal concentration of Sr-nano-HA was defined to be 10 w/v%, which showed COL fibers with a diameter in the range of 100 nm.

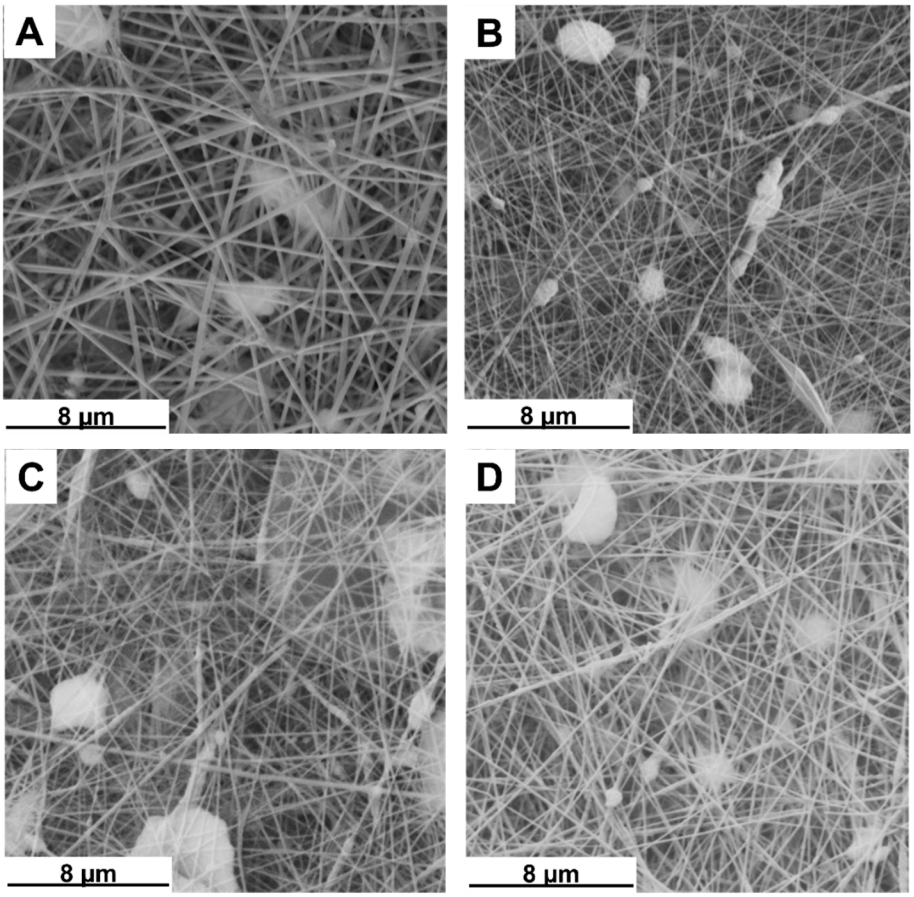

Figure 4.10: SEM images of the electrospun COL suspensions with 5 w/v% (A), 7.5 w/v% (B), 10 w/v% (C), and 12.5 w/v% (D) of Sr-nano-HA.

4.4 Crosslinking of the collagen membranes

Since the electrospun membranes result in poor mechanical properties[311], two approaches were explored to improve these properties: EDC/NHS coupling and crosslinking using Rose Bengal (Figure 4.11). These processing steps are expected to provide adequate mechanical and chemical stability for the collagen-based fibrous mats in view of the selected application.

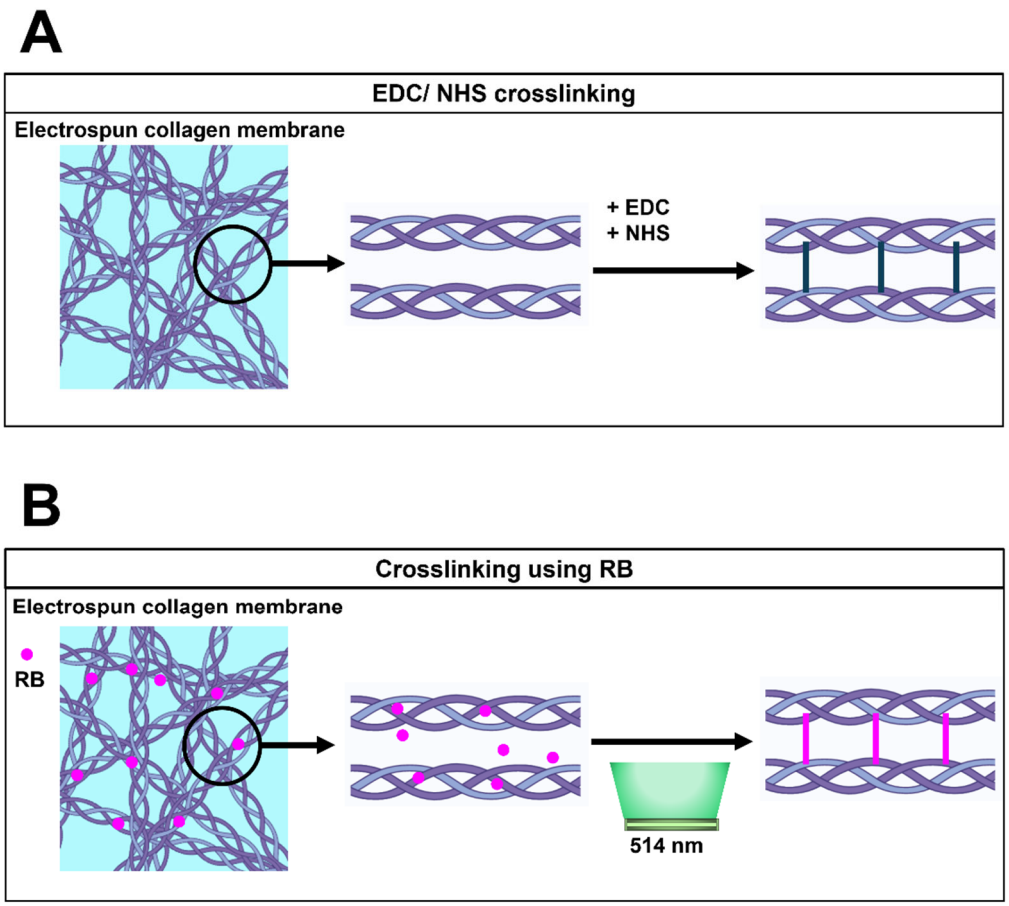

Figure 4.11: (A) EDC/NHS crosslinking and (B) crosslinking using Rose Bengal.

4.4.1 Crosslinking of collagen membranes using EDC/NHS coupling

In order to crosslink the electrospun COL membranes, the first followed approach was a procedure described by Ribeiro et al.[193], where membranes were stored at 4 °C in a solution of 90 % ethanol/ water containing EDC and NHS reagents for 12 h, then membranes were dried at room temperature under hood. SEM images of the membranes obtained after this process showed densification due to the loss of its fibrous structure (Figure 4.12).

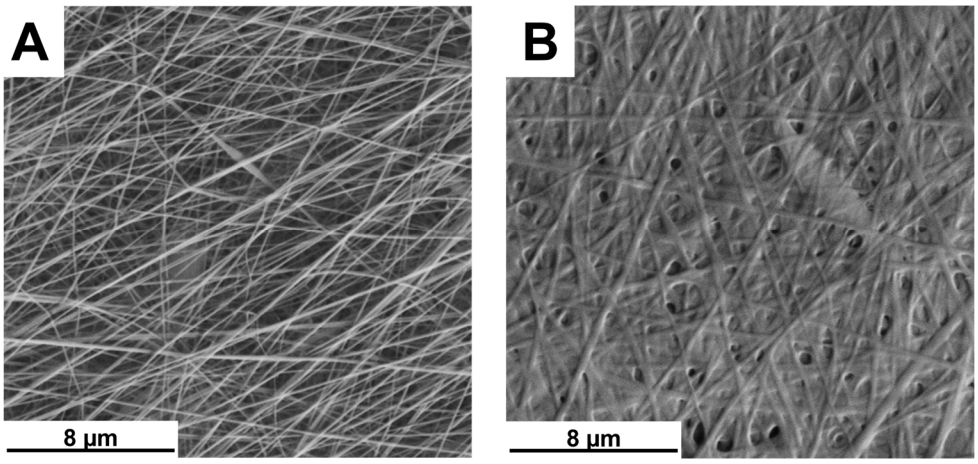

Figure 4.12: SEM images reporting the morphology of electrospun COL matrices prior to crosslinking (A) and after crosslinking for 12 h in 90 % ethanol/ water (B).

Consequently, the protocol was changed in order to improve the porosity and obtain a final morphology that matched the initial one; the change regarded the use of pure ethanol to eliminate all the water involved in the process and the drying of the membranes after the crosslinking by lyophilization at -54 °C. The results obtained by following this protocol reported a moderately encouraging improvement in the final morphology of the fibrous mats, showing a slightly improved porosity, even if they still present a fairly dense structure (Figure 4.13).

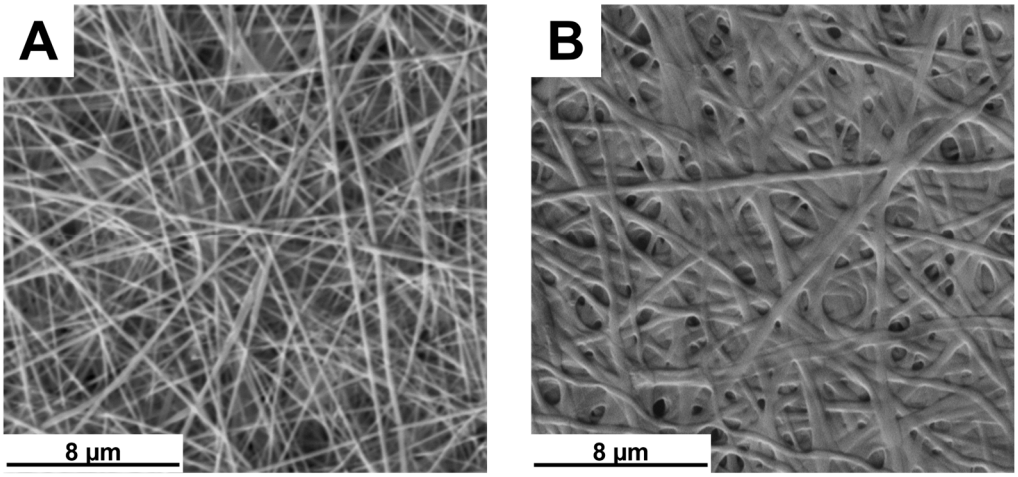

Figure 4.13: SEM images reporting the morphology of electrospun COL matrices prior to crosslinking (A) and after crosslinking for 12 h in pure ethanol and lyophilized (B).

To further improve the morphology of the membranes, trials at different times of incubation were indagated, where membranes were incubated in the

crosslinking solution for 12 h, 10 h, 8 h, and 6 h. Results showed significant progress of the final morphology, which matches with the original sample, for the incubation times of 6 h and 8 h; while the densification is more prevalent for incubation of 10 h and 12 h, indicating that long incubation times are excessive (Figure 4.14).

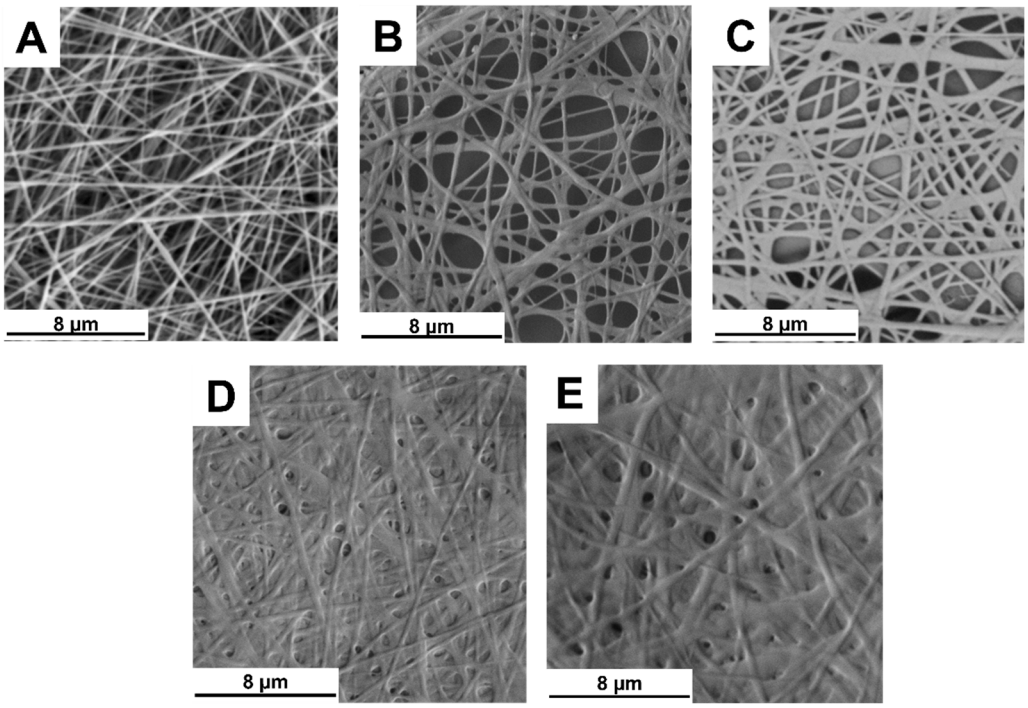

Figure 4.14: SEM images reporting the morphology of electrospun COL matrices prior to crosslinking (A) and after crosslinking for 6h (B), 8 h (C), 10 h (D), and 12 h (E).

Consequently, the optimal incubation time was defined as 8 h, which ensures the crosslinking without a substantial losing the structure of the fibrous mat.

Then, to determine the degree of the crosslinking of the collagen, a 2,4,6-trinitrobenzensulfonic acid (TNBS) colorimetric assay was carried out by using a procedure reported in the literature[280, 281], as described in chapter 2, section 2.12, where samples are prepared by the reaction of the dissolved collagen membranes in a solution containing $NaHCO_3$ and TNBS for 3 h at 40 °C, and another subsequent reaction after the addition of HCl for 1 h at 90 °C. After the preparation of the samples, the absorption of the solutions was analyzed at 346 nm and compared to the non-crosslinked collagen (Figure 4.15).

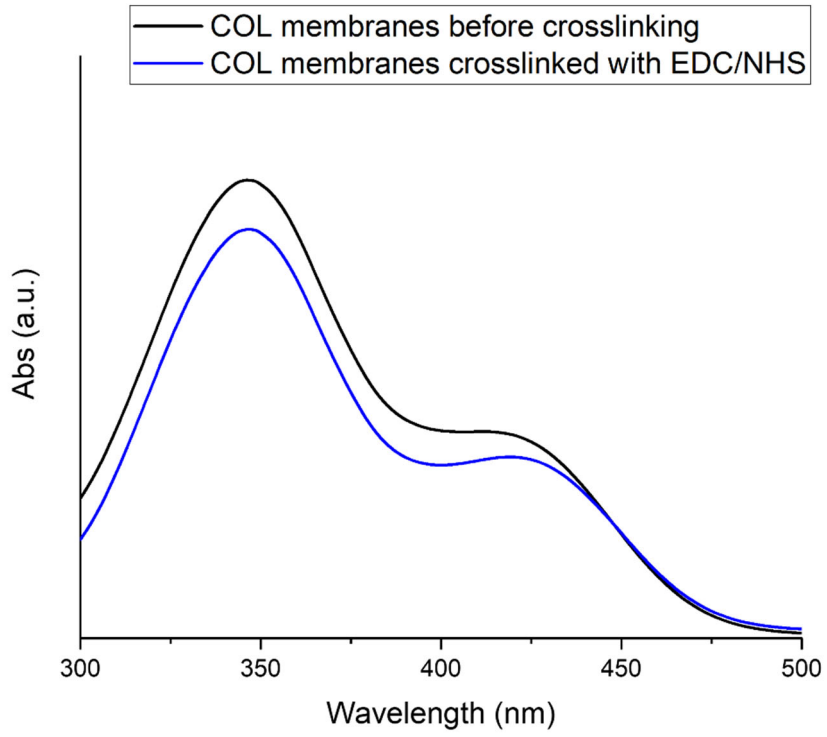

Figure 4.15: Absorption value after the TNBS treatment of COL membranes crosslinked with EDC/NHS coupling (blue line) and native COL (black line).

As expected, results showed that the absorption value of the solutions obtained by the reaction with crosslinked COL resulted lower to the absorption value of the solutions obtained by the reaction with native COL, indicating that the crosslinking occurred. Moreover, the total number of free amines was calculated using the formulas reported by Tronci et al.[280]:

$$\frac{mol\ (free\ amines)}{g\ (COL)} = \frac{2 \times Abs(346\ nm) \times 0.02}{1.4 \times 10^4 \times b \times x}$$

$$Crosslinking\ degree = 1 - \frac{moles(free\ amines)_{crosslinked\ COL}}{moles\ (free\ amines)_{native\ COL}}$$

Where Abs(346 nm) is the absorbance value at 346 nm, $1.4 \cdot 10^4$ is the molar absorption coefficient for the TNBS bound to the amines (in $L/mol \cdot cm^{-1}$), b is the cell path length (1 cm), x is the sample weight, and moles (free amines)$_{crosslinked\ COL}$ and moles (free amines)$_{COL}$ represent the free amines molar content in crosslinked and native collagen, respectively.

Results of the calculations showed a total number of free amines of about $34 \cdot 10^{-4} \pm 2.6 \cdot 10^{-4}$ moles (free amines) $\cdot g^{-1}$ for the native COL, while the number of free amines of the EDC/NHS crosslinked collagen resulted to be about $26 \cdot 10^{-4} \pm 1.7 \cdot 10^{-4}$ moles (free amines) $\cdot g^{-1}$, a lower number compared to the native COL amount, indicating that the crosslinking occurred. The degree of crosslinking was found to be about 27 %, a lower value compared to that reported by Davidenko et al.[281][21] where the average resulted to be 39%; probably the cause is that the crosslinking was carried out on COL electrospun membranes, and many amine sites were foreclosed due to the electrospun membrane thickness (100-150 μm).

4.4.2 Crosslinking of collagen membranes using Rose Bengal

The second approach indagated to crosslink COL membranes was a procedure described by Liu et al.[30] where a molecule called Rose Bengal (RB) was used as a photoinitiator, as described in chapter 2. A possible mechanism of this crosslinking process by using RB was described Redmond and Kochevar[323], suggesting that RB aggregates bind the collagen positively charged groups such as amines and lysines via hydrogen bond and proline via hydrophobic forces; then, after the activation of the RB due to the radiation at 514 nm (^{3}RB*), amino acids in the collagen molecule donate an additional negative or positive charge to the RB molecule causing a subsequent formation of amino acid radicals ($AA\bullet^+$, $AA\bullet^-$) and charged RB radicals ($RB\bullet^+$, $RB\bullet^-$), then the coupling of these radicals forms covalent crosslinks between collagen chains (Figure 4.16).

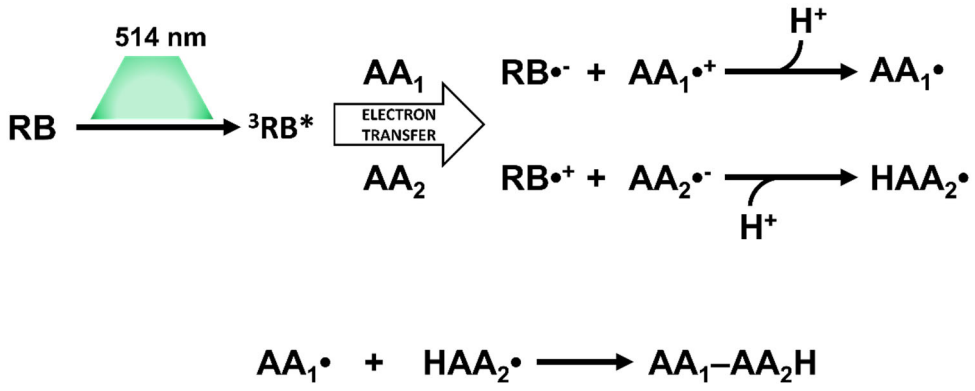

Figure 4.16: The possible mechanism of the RB crosslinking described by Redmond and Kochevar.

SEM images of the crosslinked membranes showed that the morphology was maintained after the crosslinking, with only a slight enlargement compared to

COL membranes before the crosslinking (Figure 4.17). On the other hand, the crosslinking with RB induced significantly less enlargement compared to the membranes crosslinked with EDC/NHS, probably due to the shorter time of immersion in the solution required by the followed protocol.

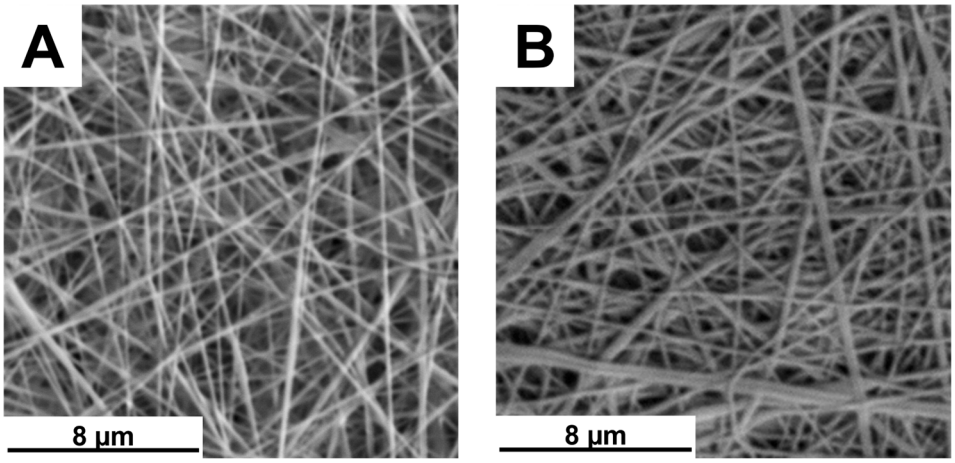

Figure 4.17: SEM images reporting the morphology of electrospun COL matrices prior to crosslinking (A) and after crosslinking using the RB photoinitiator (B).

As for EDC/ NHS crosslinking, also for the COL membranes crosslinked with the RB method was performed the TNBS assay in order to determine the degree of functionalization (Figure 4.18).

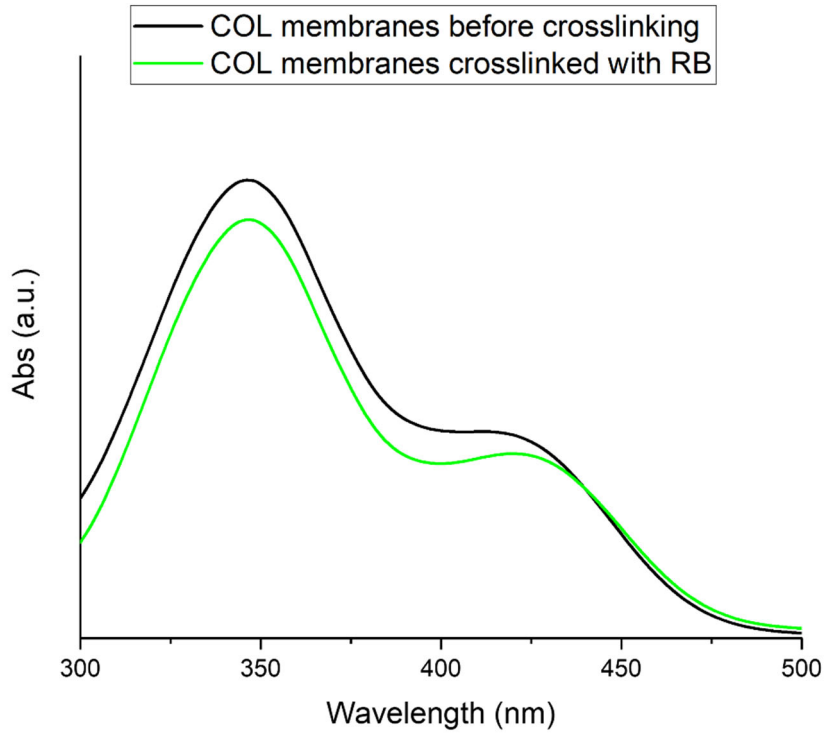

Figure 4.18: Absorption value after the TNBS treatment of COL membranes crosslinked with RB method (green line) and native COL (black line).

The minor absorbance of crosslinked samples compared to native COL was expected, as for EDC/NHS crosslinked membranes, due to the minor number of the free amines present in the sample, consequently indicating that the crosslinking occurred. The number of free amines of the crosslinked collagen with RB resulted about $29 \cdot 10^{-4} \pm 1.4 \cdot 10^{-4}$ moles (free amines) $\cdot g^{-1}$, which compared to the number of the native COL ($34 \cdot 10^{-4} \pm 2.6 \cdot 10^{-4}$ moles (free amines) $\cdot g^{-1}$) was lower, indicating also in this case that the crosslinking occurred. Moreover, the degree of crosslinking resulted to be about 17 %, a lower number compared to the EDC/NHS crosslinked samples, this value can be explained considering that the light at 514 nm for the activation of RB probably does not penetrate completely the electrospun membrane, that have a width of about 100-150 µm, and many RB molecules present in depth of the membranes were not activated during the irradiation, with the consequent crosslinking only at the membranes surface; another explanation another explanation can be that there be not enough RB compared to amines present in the collagen, since the possible mechanism is that aggregates of RB instead of a single molecule interacts with an amino group.

4.5 Final considerations

Biopolymers, among which collagen, have demonstrated several complications during processing with the electrospinning technologies, both due to the use of harsh and toxic solvents that compromise the cytocompatibility of the material, and the loss of the physico-chemical properties during the processing[324]. Different conflicting results were reported in the literature in the processing of type I collagen for the production of polymeric scaffolds using the electrospinning process, the selection of the right solvent and the electrospinning conditions, as well as the source of collagen and the method of extraction from the native tissue, resulted to be crucial, justifying the several contrasting results in the literature[16, 20, 309]. Moreover, the preservation of the collagen physico-chemical properties and the final morphological features of the scaffolds are still open issue in literature, as well as the developed scaffold that should be flexible to fit in different types of zones (such as the pelvis zone), biocompatible, with appropriate mechanical properties and architecture, bioresorbable and finally should stimulate the bone tissue regeneration and the restoration of the natural tissue balance using different types of biomaterials.

To obtain these properties, in this PhD work, different steps were followed; first, to dissolve high concentrations of rat type I collagen (20 wt%) was used a solution of 40% acetic acid in water as more green solvent compared to the solvents frequently used in order to obtain a final solution that can be processed by the electrospinning technique, forming a homogeneous fibrous mat with fibers with a diameter in the range of about 100 nm, replicating the nano- and micro-architecture of the bone tissue[321, 325, 326], several previous tests with different concentrations of the collagen (15 wt% and 25 wt%) showed a non-optimal morphology with a membrane presenting numerous defects such as the presence of beads or fibers with a flat and irregular morphology. Moreover, the introduction of an inorganic bioactive phase was explored, in order to boost the regenerative effect of the final scaffold; thus, both strontium containing MBGs and Sr-nano-HA were successfully incorporated into the previously optimized collagen system. The resulting scaffolds showed a uniform morphology consisting of fibers with a diameter around 120 nm and 100 nm for COL electrospun with MBGs and Sr-nano-HA, respectively, and an inorganic phase homogeneously distributed throughout the collagen matrix.

Although ICOS-Fc grafted MBGs were not used for the ESP, due to the cost of the biomolecule ICOS-Fc and the quantities of MBGs used during the ESP trials and since the ICOS-Fc grafting does not cause any substantial change in the

size and morphology of MBGs, the effect of AA on the grafted particles was studied and results showed a severely impaired activity of ICOS-Fc in SG-Sr-ICOS-Fc samples, but on the other hand the activity of the biomolecule of SD-Sr-ICOS-Fc resulted only slightly impaired probably due to the less exposed ICOS-Fc in these types of samples.

Finally, since the collagen scaffolds result in poor mechanical properties[311], two crosslinking strategies were explored in order to increase the stability and the final strength of the electrospun collagen scaffold. The occurred crosslinking was confirmed by free amine test both on membranes crosslinked with the EDC/ NHS method and with RB as photoinitiator. Since the crosslinking procedure should increase the mechanical properties of the scaffolds, key properties of the scaffolds for the bone tissue engineering, mechanical and biological tests are currently under investigation, to ensure a stable bioactive and nanostructured scaffold able to promote the regeneration of bone osteoporotic fractures in the pelvis zone.

To conclude, results described in this chapter confirmed that collagen-based formulations can be processable by electrospinning technology for the design of biomimetic scaffolds to treat fractures in the pelvis zone, moreover, future studies on the potential scalability of the electrospinning technique can be performed, since the process can be easily scaled up after some modifications.

Chapter 5

Conclusions and future perspectives

The aim of this PhD work was the design and the development of biomimetic collagen-based scaffolds for bone tissue engineering and in particular for the treatment of osteoporotic fractures in the pelvis zone. The development was carried out by exploring the use of type I collagen combined with two different inorganic phases: strontium containing mesoporous bioactive glasses grafted with ICOS-Fc biomolecule (MBGs-Sr-ICOS-Fc) or strontium containing nano-hydroxyapatite (Sr-nano-HA), and the processing by means electrospinning technology, as well as the optimization of different strategies to improve the properties of the electrospun collagen-based membranes to obtain a biomimetic flexible construct that can be adapted in the pelvis zone, stimulate the fracture healing and restore the natural tissue balance for fractures in people affected by osteoporosis.

To achieve this objective, the first aim of this PhD thesis was the design and the development of MBGs-Sr-ICOS-Fc, where first, mesoporous bioactive glasses (MBGs) particles with a binary composition based on SiO_2 and CaO enriched with Sr therapeutic ions were synthetized in form of nano- and microparticles, subsequently the MBGs surface was functionalized with amino groups, and finally the ICOS-Fc molecule was grafted on MBGs surface by using the N-(3-Dimethylaminopropyl)-N′-ethylcarbodiimide (EDC)/ N-Hydroxysuccinimide (NHS) coupling to link the carboxyl groups present in the Fc domain of the

biomolecule with the amino groups to form an amide bond. In this frame, also the possible scaling up of the synthesis of MBGs microparticles was explored by using an industrial spray drier situated in FLUIDINOVA company. The second aim in the work focused on the electrospinning of collagen and collagen-based suspension and the subsequent crosslinking of the scaffold; first the optimal concentration to dissolve the collagen in the acetic acid solution used in the electrospinning process was studied in order to obtain a construct with a good morphology in terms of collagen fibers, and then the incorporation of the two selected inorganic phases in the collagen-based scaffolds was indagated with the objective of the development of a construct with the desired characteristics in terms of fibers morphology and dispersion of the inorganic phase. The last part of the PhD thesis was dedicated to exploring different crosslinking methods in order to enhance the properties of the collagen-based constructs.

Nano- and micro-sized particles containing strontium as therapeutic specie (10% mol) in their silica framework were successfully produced by using a base-catalyzed sol-gel method and an aerosol assisted spray-drying approach, respectively. The two different methods allowed the production of particles with different morphology, size, and structural features in order to obtain different systems for the incorporation in the collagen-based scaffolds for the bone tissue healing.

Regarding the morphology, with the base-catalyzed sol-gel method, particles with a spheroidal shape and with a uniform size ranging from 100 nm to 300 nm were obtained, while for particles synthetized by the aerosol assisted spray-drying approach the obtained morphology consisted in spheric particles with a diameter size ranging between 1 and 5 μm. Both types of particles showed mesoporous structure with pores of about 3 nm for nanoparticles and 5-7 nm for microparticles; the related specific surface area resulted in line with similar ion containing MBGs particles[283, 296]. Concerning the release kinetics, the release profile of Sr^{2+} species were evaluated in Tris HCl medium, and results showed a burst release in the first 3 h for both particle types, followed by a plateau phase. Since the bioactivity is a key feature in the MBGs particles for the osteointegration, the effect of the incorporation of strontium on the bioactivity was evaluated by soaking the particles in simulated body fluid (SBF) medium; both types of particles resulted to possess bioactivity proving that the incorporation of different ions did not inhibit their bioactive behaviour, even the showed bioactivity resulted lower compared with MBGs that do not contain the Sr ions as reported in the literature[283, 289–292].

Since the aerosol assisted spray-drying approach is a process that can be easily scalable, some trials to scaling-up the synthesis of microparticles were performed in collaboration with FLUIDINOVA by using the industrial spray drier situated in their facility, obtaining samples with Ca and Sr incorporated and showing a specific surface area and pore volume comparable to the lab-scale microparticles, even if the presence of amorphous silica-based precipitates was found; thus, the process requires further optimization such as the use of an ice bath during the solution preparation and the spraying of the final solution in order to mitigate the early precipitation and obtain microparticles with structural and morphological features similar to powders produced at lab-scale.

Then, MBGs-Sr were grafted with ICOS-Fc, after their functionalization with amino groups, through the zero length EDC/NHS coupling. Based on the obtained results, the particle morphology, size, structural features and strontium release kinetics did not result affected by this type of grafting, in fact, FESEM images and EDS analysis suggested that ICOS-Fc grafting does not significantly alter the morphological characteristics of MBGs-Sr that remained very similar to the features of bare samples. However, the specific surface area drastically reduced for both types of samples, as a consequence of ICOS-Fc grafting, even if the hysteresis loop in the isotherm of grafted microparticles resulted still visible, probably due to the pores that are not completely occluded because ICOS-Fc biomolecules are mainly at the pores entrance. X-ray diffraction (XRD) analyses were performed to assess the amorphous state of the biomolecule and to exclude the presence of crystalline aggregates, results confirmed the amorphous state of ICOS-Fc grafted irrespective of the particle type, confirming that the crystallization did not occur after the grafting procedure. For both type of particles, FTIR indicated the presence of ICOS-Fc on the MBGs surface and ELISA-like assay (performed in collaboration with NOVAICOS) confirmed both the presence and the maintained ability of ICOS-Fc to bind its ligand, indicating that the biomolecule was grafted in the right orientation and not damaged after the grafting procedure. Moreover, the stability of the bond between ICOS-Fc and MBGs were indagated since it is important for a specific inhibition activity only in the site where osteoclasts are active. The release profile of Sr ions evaluated in Tris HCl resulted very similar to the bare samples with a burst release after 3 h and subsequently followed by a plateau phase, however, the release kinetics of grafted microparticles resulted slightly different compared to bare samples, ascribable to the limited pore entrance but with the ion exchange still allowed. Finally, the bioactivity of both grafted samples resulted maintained, confirming

that the grafting does not affect the bioactivity, on the contrary, it resulted increased.

Then, biological tests were performed in collaboration with NOVAICOS, in order to investigate the biocompatibility, and the ability to inhibit the osteoclasts migration and differentiation of the developed multifunctional materials. Biocompatibility tests were performed using different concentrations of grafted particles, and results confirmed that the grafted MBGs did not affect the cell viability, only the highest tested concentration of grafted microparticles resulted lower compared to the other concentrations. Boyden chamber migration assays with ICOS-L positive cell lines or ICOS-L negative cell line as control were performed in order to investigate the effects of grafted samples on the osteoclast's migration; results confirmed that grafted ICOS-Fc retained the ability to specifically and reversibly inhibit only the ICOS-L positive cells motility, as expected. Clonogenic proliferation assays were performed to test the effects on cells proliferations, for cells treated with the samples, the results showed that grafted MBGs did not affect the proliferation of the cells. Moreover, the inhibitory effects on the monocyte-derived osteoclasts (MDOCs) differentiation of samples were tested comparing the results with the inhibition ability of free ICOS-Fc, results evidenced that the MDOCs differentiation was strongly inhibited by the ICOS-Fc grafted on samples in analogy to free ICOS-Fc, and the differentiation marker genes expression confirmed that samples have the ability to inhibit the differentiation of osteoclasts.

Subsequently, the electrospinning of type I collagen, provided by NOVAICOS, combined with inorganic phases and the subsequent crosslinking were performed. Prior to the electrospinning, since solvent and the polymer concentration have a critical role in the process, the use of an acetic acid solution, as greener solvent, for the solubilization of the collagen at high concentrations, preserving the structure of the protein, were indagated. In order to evaluate if the extraction process alter the biological functionality of collagen and create a reference FTIR analysis were performed and compared to literature data; then, the preservation of the collagen structure after the dissolution was investigated by FTIR analysis and SDS-PAGE (performed by NOVAICOS) and results confirmed that the collagen was not degraded after the dissolution in acetic acid. After the confirmation of the maintained structure of the collagen, the dissolution at different concentration and the subsequent electrospinning of the collagen was performed. Results of SEM analysis confirmed that, with the lower (15 wt%) and the higher (25 wt%) concentrations of collagen, the obtained membranes did not

show a good morphology, on the other hand, the concentration of 20 wt% resulted to be optimal for obtaining membranes with a fibrous structure similar to that reported in literature[321]. Subsequently, the incorporation of different concentration of the inorganic phases (grafted MBGs or Sr-nano-HA provided by FLUIDINOVA) was indagated. Concerning the incorporation of grafted microparticles in the collagen-based construct, SEM images showed that the inorganic phase was distributed homogeneously, and particles resulted integrated within the fibrous matrix; moreover, the 15 w/v% concentration represented the best compromise between the formulation processability, and the amount incorporated. Results of nano-sized particles incorporation showed the presence of a homogenous mat, but with a large number of agglomerates, even if smaller than 10 μm; also in this case, the 15 w/v% concentration represented the best compromise. In addition, since unfunctionalized samples were used due to the cost of ICOS-Fc, the effect of the acidic solvent on the biological functionality of ICOS-Fc was indagated, and results confirmed that only a limited number of ICOS-Fc grafted on MBG microparticles lost functionality, while for ICOS-Fc grafted on nanoparticles the functionality significantly decreases after contact with acetic acid, probably this effect is due to the larger pore size of MBGs microparticles compared to SG-Sr which allows the ICOS-Fc to be grafted at the pores entrance, and this less exposed position reduce the contact of the biomolecule with the acidic solution. For Sr-nano-HA, the maximum concentration resulted to be processed was 12.5 w/v%, and the best concentration for the processability, the obtaining of a good morphology of fibers and a well dispersed inorganic phase, resulted to be 10 w/v%.

Finally, since the mechanical properties of the collagen-based constructs generally result not adequate to the bone tissue engineering[311], two crosslinking procedures were investigated. The first followed approach was an EDC/NHS coupling that links amino and carboxyl groups to form an amide group; the procedure described in literature[193] was optimized in several steps until obtaining a good fibers morphology, and free amine assay were performed to indagate the degree of crosslinking with the resulting degree of 27 %, a lower value compared to that reported in literature[281] probably due to many amine sites that were foreclosed due to the electrospun membrane thickness. In the second approach was used the Rose Bengal (RB) molecule as photoinitiator by following a procedure described in literature[30] with some optimization, the possible mechanism described in literature[31] results in a formation of an amide bond between positively and negatively charged groups in the collagen chains. The crosslinked membrane morphology resulted from SEM images showed a

significantly less enlargement compared to the EDC/NHS crosslinked membranes, and the degree of crosslinking obtained from the free amine assay resulted to be 17 %, lower compared to the EDC/NHS crosslinked samples that can be explained by the light at 514 nm that cannot penetrate completely the electrospun membrane for the RB activation, or by the not enough RB compared to amines in the collagen. These preliminary results of the crosslinking methods are currently under investigation to indagate the increased mechanical properties.

In conclusion, the possibility to grafting the ICOS-Fc biomolecule on MBGs-Sr surface represents a very attracting candidates to the development of personalized and multifunctional devices with a synergistic effect of pro-osteogenesis and anti-osteoclastogenesis, due to the presence of both ICOS-Fc biomolecule and Sr, able to stimulate the healing in the bone remodeling process. In addition, future trials can be performed to further optimize the scaling up of the aerosol assisted spray-drying approach, in order to obtain a large amount of microparticles without the presence of precipitate. Moreover, since electrospinning represent one of the most interesting fabrication routes to the formation of nanometric fibrous scaffolds that is similar to the morphological features of bone extracellular matrix at the nanoscale, the developed scaffolds with MBGs-Sr grafted with ICOS-Fc or Sr-nano-HA in a collagen-based matrix resulted a possible route to obtain multifunctional scaffolds that can be applied for the treatment of osteoporotic fractures in different locations such as in the pelvis zone. While the mechanical tests of these constructs are still under investigation, future studies can be focused on the opportunity to obtain more complex architectures, by exploiting the direct writing electrospinning, and on a comprehensive biological assessment to indagate the high bioactive features of the constructs.

References

1. Winkler T, Sass FA, Duda GN, Schmidt-Bleek K (2018) A review of biomaterials in bone defect healing, remaining shortcomings and future opportunities for bone tissue engineering. Bone Joint Res 7:232–243. https://doi.org/10.1302/2046-3758.73.BJR-2017-0270.R1

2. Haas NP (2000) Callusmodulation Fiktion oder Realität? Chirurg 71:987–988

3. Schlundt C, Bucher CH, Tsitsilonis S, et al (2018) Clinical and Research Approaches to Treat Non-union Fracture. Curr Osteoporos Rep 16:155–168. https://doi.org/10.1007/s11914-018-0432-1

4. McHale MK, Bergmann NM, West JL (2018) Histogenesis in Three-Dimensional Scaffolds. Elsevier Inc.

5. Tripathy N, Perumal E, Ahmad R, et al (2018) Hybrid Composite Biomaterials. Elsevier Inc.

6. Vallet-Regí M (2010) Evolution of bioceramics within the field of biomaterials. Comptes Rendus Chimie 13:174–185. https://doi.org/10.1016/j.crci.2009.03.004

7. Ramesh N, Moratti SC, Dias GJ (2018) Hydroxyapatite–polymer biocomposites for bone regeneration: A review of current trends. J Biomed Mater Res B Appl Biomater 106:2046–2057. https://doi.org/10.1002/jbm.b.33950

8. Hassan M, Sulaiman M, Yuvaraju PD, et al (2022) Biomimetic PLGA/Strontium-Zinc Nano Hydroxyapatite Composite Scaffolds for Bone Regeneration. J Funct Biomater 13:

9. Ratnayake JTB, Mucalo M, Dias GJ (2017) Substituted hydroxyapatites for bone regeneration: A review of current trends. J Biomed Mater Res B Appl Biomater 105:1285–1299. https://doi.org/10.1002/jbm.b.33651

10. Arcos D, Vallet-regí M (2021) Substituted hydroxyapatite coatings of bone implants Daniel. J Mater Chem B 8:1781–1800. https://doi.org/10.1039/c9tb02710f.Substituted

11. Yan X, Yu C, Zhou X, et al (2004) Highly ordered mesoporous bioactive glasses with superior in vitro bone-forming bioactivities. Angewandte Chemie - International Edition 43:5980–5984. https://doi.org/10.1002/anie.200460598

12. López-Noriega A, Arcos D, Izquierdo-Barba I, et al (2006) Ordered mesoporous bioactive glasses for bone tissue regeneration. Chemistry of Materials 18:3137–3144. https://doi.org/10.1021/cm060488o

13. Baino F, Fiorilli S, Vitale-Brovarone C (2016) Bioactive glass-based materials with hierarchical porosity for medical applications: Review of recent advances. Acta Biomater 42:18–32. https://doi.org/10.1016/j.actbio.2016.06.033

14. Li Y, Liu Y-Z, Long T, et al (2013) Mesoporous bioactive glass as a drug delivery system: fabrication, bactericidal properties and biocompatibility. J Mater Sci Mater Med 24:1951–1961. https://doi.org/10.1007/s10856-013-4960-z

15. Anand A, Das P, Nandi SK, Kundu B (2020) Development of antibiotic loaded mesoporous bioactive glass and its drug release kinetics. Ceram Int 46:5477–5483. https://doi.org/10.1016/j.ceramint.2019.10.264

16. Griffanti G, Nazhat SN (2020) Dense fibrillar collagen-based hydrogels as functional osteoid-mimicking scaffolds. International Materials Reviews 65:502–521. https://doi.org/10.1080/09506608.2020.1735828

17. Ferreira AM, Gentile P, Chiono V, Ciardelli G (2012) Collagen for bone tissue regeneration. Acta Biomater 8:3191–3200. https://doi.org/10.1016/j.actbio.2012.06.014

18. Cunniffe GM, O'Brien FJ (2011) Collagen scaffolds for orthopedic regenerative medicine. Jom 63:66–73. https://doi.org/10.1007/s11837-011-0061-y

19. Cen L, Liu WEI, Cui LEI, et al (2000) Collagen Tissue Engineering: Development of Novel Biomaterials and Applications. 63:492–496

20. Angele P, Abke J, Kujat R, et al (2004) Influence of different collagen species on physico-chemical properties of crosslinked collagen matrices.

Biomaterials 25:2831–2841. https://doi.org/10.1016/j.biomaterials.2003.09.066

21. Delgado LM, Fuller K, Zeugolis DI (2017) Collagen Cross-Linking: Biophysical, Biochemical, and Biological Response Analysis. Tissue Eng Part A 23:1064–1077. https://doi.org/10.1089/ten.tea.2016.0415

22. Tang D, Tare RS, Yang LY, et al (2016) Biofabrication of bone tissue: Approaches, challenges and translation for bone regeneration. Biomaterials 83:363–382. https://doi.org/10.1016/j.biomaterials.2016.01.024

23. Chen H, Malheiro ADBFB, Van Blitterswijk C, et al (2017) Direct Writing Electrospinning of Scaffolds with Multidimensional Fiber Architecture for Hierarchical Tissue Engineering. ACS Appl Mater Interfaces 9:38187–38200. https://doi.org/10.1021/acsami.7b07151

24. Sell SA, McClure MJ, Garg K, et al (2009) Electrospinning of collagen/biopolymers for regenerative medicine and cardiovascular tissue engineering. Adv Drug Deliv Rev 61:1007–1019. https://doi.org/10.1016/j.addr.2009.07.012

25. Jun I, Han HS, Edwards JR, Jeon H (2018) Electrospun fibrous scaffolds for tissue engineering: Viewpoints on architecture and fabrication. Int J Mol Sci 19:. https://doi.org/10.3390/ijms19030745

26. Peng S, Zhou G, Luk KDK, et al (2009) Strontium promotes osteogenic differentiation of mesenchymal stem cells through the Ras/MAPK signaling pathway. Cellular Physiology and Biochemistry 23:165–174. https://doi.org/10.1159/000204105

27. Kargozar S, Baino F, Hamzehlou S, et al (2018) Bioactive glasses entering the mainstream. Drug Discov Today 23:1700–1704. https://doi.org/10.1016/j.drudis.2018.05.027

28. Dianzani U, Gigliotti CL, Boggio E WO-2016-189428

29. Gigliotti CL, Boggio E, Clemente N, et al (2016) ICOS-Ligand Triggering Impairs Osteoclast Differentiation and Function In Vitro and In Vivo. The Journal of Immunology 197:3905–3916. https://doi.org/10.4049/jimmunol.1600424

30. Liu T, Teng WK, Chan BP, Chew SY (2010) Photochemical crosslinked electrospun collagen nanofibers: Synthesis, characterization and neural stem cell interactions. J Biomed Mater Res A 95:276–282. https://doi.org/10.1002/jbm.a.32831

31. Redmond RW, Kochevar IE (2019) Medical Applications of Rose Bengal- and Riboflavin-Photosensitized Protein Crosslinking. Photochem Photobiol 95:1097–1115. https://doi.org/10.1111/php.13126

32. Cottrell JA, Turner JC, Arinzeh TL, O'Connor JP (2016) The Biology of Bone and Ligament Healing. Foot Ankle Clin 21:739–761. https://doi.org/10.1016/j.fcl.2016.07.017

33. Dimitriou R, Jones E, McGonagle D, Giannoudis P V. (2011) Bone regeneration: Current concepts and future directions. BMC Med 9:66. https://doi.org/10.1186/1741-7015-9-66

34. Einhorn TA (1998) The cell and molecular biology of fracture healing. Clin Orthop Relat Res 355:7–21. https://doi.org/10.1097/00003086-199810001-00003

35. Cho TJ, Gerstenfeld LC, Einhorn TA (2002) Differential temporal expression of members of the transforming growth factor β superfamily during murine fracture healing. Journal of Bone and Mineral Research 17:513–520. https://doi.org/10.1359/jbmr.2002.17.3.513

36. Maruyama M, Rhee C, Utsunomiya T, et al (2020) Modulation of the Inflammatory Response and Bone Healing. Front Endocrinol (Lausanne) 11:1–14. https://doi.org/10.3389/fendo.2020.00386

37. Coughlan T, Dockery F (2014) Osteoporosis and fracture risk in older people. Clinical Medicine 14:187–91

38. Lane NE (2006) Epidemiology, etiology, and diagnosis of osteoporosis. Am J Obstet Gynecol 194:. https://doi.org/10.1016/j.ajog.2005.08.047

39. Dolan P, Torgerson DJ (1998) The cost of treating osteoporotic fractures in the United Kingdom female population. Osteoporosis International 8:611–617. https://doi.org/10.1007/s001980050107

40. Cummings SR, Melton LJ (2002) Osteoporosis I: Epidemiology and outcomes of osteoporotic fractures. Lancet 359:1761–1767. https://doi.org/10.1016/S0140-6736(02)08657-9

41. Poole KES, Compston JE (2006) Osteoporosis and its management. Clinical review 333:

42. Lin JT, Lane JM (2004) Osteoporosis: A review. Clin Orthop Relat Res 425:126–134. https://doi.org/10.1097/01.blo.0000132404.30139.f2

43. David L Glaser, Frederick S Kaplan (1997) Osteoporosis: Definition and Clinical Presentation. Spine (Phila Pa 1976) 22:12S-16S

44. Coelho R, Silva C, Maia A, et al (1999) Bone mineral density and depression. J Psychosom Res 46:29–35. https://doi.org/10.1016/s0022-3999(98)00064-6

45. Gold DT, Bales CW, Lyles KW, Drezner MK (1989) Treatment of Osteoporosis The Psychological Impactof a Medical Education Program on Older Patients. 37:

46. Gold DT, Shipp KM, Lyles KW (1998) Managing patients with complications of osteoporosis. Endocrinol Metab Clin North Am 27:485–496. https://doi.org/10.1016/S0889-8529(05)70018-9

47. Kado DM, Browner WS, Palermo L, et al (1999) Vertebral fractures and mortality in older women: A prospective study. Arch Intern Med 159:1215–1220. https://doi.org/10.1001/archinte.159.11.1215

48. Neer R, Arnaud C, Zanchetta J, et al (2001) EFFECT OF PARATHYROID HORMONE (1-34) ON FRACTURES AND BONE MINERAL DENSITY IN POSTMENOPAUSAL WOMEN WITH OSTEOPOROSIS. N Engl J Med 344:1434–1441

49. Khosla S, Hofbauer LC (2017) Osteoporosis treatment: recent developments and ongoing challenges. Lancet Diabetes Endocrinol 5:898–907. https://doi.org/10.1016/S2213-8587(17)30188-2

50. Cheung WH, Miclau T, Chow SKH, et al (2016) Fracture healing in osteoporotic bone. Injury 47:S21–S26. https://doi.org/10.1016/S0020-1383(16)47004-X

51. Oberkircher L, Ruchholtz S, Rommens PM, et al (2018) Osteoporotic Pelvic Fractures. Dtsch Arztebl Int 115:70–80. https://doi.org/10.3238/arztebl.2018.0070

52. Hollensteiner M, Sandriesser S, Bliven E, et al (2019) Biomechanics of Osteoporotic Fracture Fixation. Curr Osteoporos Rep 17:363–374. https://doi.org/10.1007/s11914-019-00535-9

53. De Laet CEDH, Pols HAP (2000) Fractures in the elderly: Epidemiology and demography. Bailliere's Best Practice and Research in Clinical Endocrinology and Metabolism 14:171–179. https://doi.org/10.1053/beem.2000.0067

54. Codrea CI, Croitoru A-M, Constantin Baciu C, et al (2021) Advances in Osteoporotic Bone Tissue Engineering. J Clin Med 10

55. Perić Kačarević Ž, Rider P, Alkildani S, et al (2020) An introduction to bone tissue engineering. International Journal of Artificial Organs 43:69–86. https://doi.org/10.1177/0391398819876286

56. Goldberg VM, Stevenson S (1993) The biology of bone grafts. Semin Arthroplasty 4:58–63

57. Kacarevic ZP, Kavehei F, Houshmand A, et al (2018) Purification processes of xenogeneic bone substitutes and their impact on tissue reactions and regeneration. International Journal of Artificial Organs 41:789–800. https://doi.org/10.1177/0391398818771530

58. Sharir A, Barak MM, Shahar R (2008) Whole bone mechanics and mechanical testing. Veterinary Journal 177:8–17. https://doi.org/10.1016/j.tvjl.2007.09.012

59. Mahanta AK, Patel DK, Maiti P (2019) Nanohybrid Scaffold of Chitosan and Functionalized Graphene Oxide for Controlled Drug Delivery and Bone Regeneration. ACS Biomater Sci Eng 5:5139–5149. https://doi.org/10.1021/acsbiomaterials.9b00829

60. Zhang S, Chen J, Yu Y, et al (2019) Accelerated Bone Regenerative Efficiency by Regulating Sequential Release of BMP-2 and VEGF and Synergism with Sulfated Chitosan. ACS Biomater Sci Eng 5:1944–1955. https://doi.org/10.1021/acsbiomaterials.8b01490

61. O'Brien FJ (2011) Biomaterials & scaffolds for tissue engineering. Materials Today 14:88–95. https://doi.org/10.1016/S1369-7021(11)70058-X

62. Ghosh D, Singha PSS, Firdaus SB, et al (2016) BIOMETALS IN HEALTH AND DISEASE: A REVIEW. World J Pharm Res 5:390–399. https://doi.org/10.20959/wjpr201612-7471

63. Zheng YF, Gu XN, Witte F (2014) Biodegradable metals. Materials Science and Engineering R: Reports 77:1–34. https://doi.org/10.1016/j.mser.2014.01.001

64. Cheng MQ, Wahafu T, Jiang GF, et al (2016) A novel open-porous magnesium scaffold with controllable microstructures and properties for bone regeneration. Sci Rep 6:1–14. https://doi.org/10.1038/srep24134

65. Glenske K, Donkiewicz P, Köwitsch A, et al (2018) Applications of metals for bone regeneration

66. Bornapour M, Celikin M, Cerruti M, Pekguleryuz M (2014) Magnesium implant alloy with low levels of strontium and calcium: The third element effect and phase selection improve bio-corrosion resistance and mechanical performance. Materials Science and Engineering C 35:267–282. https://doi.org/10.1016/j.msec.2013.11.011

67. Cortizo MS, Belluzo MS (2017) Biodegradable Polymers for Bone Tissue Engineering. Industrial Applications of Renewable Biomass Products. https://doi.org/10.1007/978-3-319-61288-1_2

68. Parenteau-Bareil R, Gauvin R, Berthod F (2010) Collagen-based biomaterials for tissue engineering applications. Materials 3:1863–1887. https://doi.org/10.3390/ma3031863

69. Pina S, Oliveira JM, Reis RL (2015) Natural-based nanocomposites for bone tissue engineering and regenerative medicine: A review. Advanced Materials 27:1143–1169. https://doi.org/10.1002/adma.201403354

70. Pabst AM, Lehmann KM, Walter C, et al (2016) Influence of porcine-derived collagen matrix on endothelial progenitor cells: an in vitro study. Odontology 104:19–26. https://doi.org/10.1007/s10266-014-0186-x

71. Lin S, Gu L (2015) Influence of crosslink density and stiffness on mechanical properties of type I collagen gel. Materials 8:551–560. https://doi.org/10.3390/ma8020551

72. Gentile P, McColgan-Bannon K, Gianone NC, et al (2017) Biosynthetic PCL-graft-collagen bulk material for tissue engineering applications. Materials 10:1–17. https://doi.org/10.3390/ma10070693

73. Ribeiro M, De Moraes MA, Beppu MM, et al (2015) Development of silk fibroin/nanohydroxyapatite composite hydrogels for bone tissue engineering. Eur Polym J 67:66–77. https://doi.org/10.1016/j.eurpolymj.2015.03.056

74. Li C, Vepari C, Jin HJ, et al (2006) Electrospun silk-BMP-2 scaffolds for bone tissue engineering. Biomaterials 27:3115–3124. https://doi.org/10.1016/j.biomaterials.2006.01.022

75. Mobini S, Hoyer B, Solati-Hashjin M, et al (2013) Fabrication and characterization of regenerated silk scaffolds reinforced with natural silk fibers for bone tissue engineering. J Biomed Mater Res A 101 A:2392–2404. https://doi.org/10.1002/jbm.a.34537

76. Croisier F, Jérôme C (2013) Chitosan-based biomaterials for tissue engineering. Eur Polym J 49:780–792. https://doi.org/10.1016/j.eurpolymj.2012.12.009

77. Abraham A, Soloman PA, Rejini VO (2016) Preparation of Chitosan-Polyvinyl Alcohol Blends and Studies on Thermal and Mechanical Properties. Procedia Technology 24:741–748. https://doi.org/10.1016/j.protcy.2016.05.206

78. Zhang Y, Ni M, Zhang M, Ratner B (2003) Calcium Phosphate – Chitosan Composite Scaffolds for Bone Tissue Engineering. Tissue Eng 9:

79. Thein-Han WW, Misra RDK (2009) Biomimetic chitosan-nanohydroxyapatite composite scaffolds for bone tissue engineering. Acta Biomater 5:1182–1197. https://doi.org/10.1016/j.actbio.2008.11.025

80. Alsberg E, Anderson KW, Albeiruti A, et al (2001) Cell-interactive alginate hydrogels for bone tissue engineering. J Dent Res 80:2025–2029. https://doi.org/10.1177/00220345010800111501

81. Li Z, Ramay HR, Hauch KD, et al (2005) Chitosan-alginate hybrid scaffolds for bone tissue engineering. Biomaterials 26:3919–3928. https://doi.org/10.1016/j.biomaterials.2004.09.062

82. Guo B, Ma PX (2014) Synthetic biodegradable functional polymers for tissue engineering: A brief review. Sci China Chem 57:490–500. https://doi.org/10.1007/s11426-014-5086-y

83. Nair LS, Laurencin CT (2007) Biodegradable polymers as biomaterials. Progress in Polymer Science (Oxford) 32:762–798. https://doi.org/10.1016/j.progpolymsci.2007.05.017

84. Liu F, Huang B, Hinduja S, Silva Bartolo PJ (2019) Biofabrication Techniques for Ceramics and Composite Bone Scaffolds. Bioceramics and Biocomposites 17–37. https://doi.org/10.1002/9781119372097.ch2

85. Andrew Wu YH, Chiu YC, Lin YH, et al (2019) 3D-Printed bioactive calcium silicate/poly-ε-Caprolactone bioscaffolds modified with biomimetic extracellular matrices for bone regeneration. Int J Mol Sci 20:. https://doi.org/10.3390/ijms20040942

86. Garrison TF, Murawski A, Quirino RL (2016) Bio-based polymers with potential for biodegradability. Polymers (Basel) 8:1–22. https://doi.org/10.3390/polym8070262

87. Henton DE, Gruber P, Lunt J, Randall J (2005) Polylactic acid technology. Natural Fibers, Biopolymers, and Biocomposites 527–577. https://doi.org/10.1002/1521-4095(200012)12:23<1841::aid-adma1841>3.3.co;2-5

88. Farah S, Anderson DG, Langer R (2016) Physical and mechanical properties of PLA, and their functions in widespread applications — A comprehensive review. Adv Drug Deliv Rev 107:367–392. https://doi.org/10.1016/j.addr.2016.06.012

89. Tanodekaew S, Channasanon S, Uppanan P (2014) Preparation and degradation study of photocurable oligolactide-HA composite: A potential resin for stereolithography application. J Biomed Mater Res B Appl Biomater 102:604–611. https://doi.org/10.1002/jbm.b.33040

90. Ginebra MP, Espanol M, Maazouz Y, et al (2018) Bioceramics and bone healing. EFORT Open Rev 3:173–183. https://doi.org/10.1302/2058-5241.3.170056

91. Gerhardt LC, Boccaccini AR (2010) Bioactive glass and glass-ceramic scaffolds for bone tissue engineering. Materials 3:3867–3910. https://doi.org/10.3390/ma3073867

92. Jones JR (2013) Review of bioactive glass: From Hench to hybrids. Acta Biomater 9:4457–4486. https://doi.org/10.1016/j.actbio.2012.08.023

93. Holmes DF, Lu Y, Starborg T, Kadler KE (2018) Collagen Fibril Assembly and Function, 1st ed. Elsevier Inc.

94. Walters BD, Stegemann JP (2014) Strategies for directing the structure and function of three-dimensional collagen biomaterials across length scales. Acta Biomater 10:1488–1501. https://doi.org/10.1016/j.actbio.2013.08.038

95. Sherman VR, Yang W, Meyers MA (2015) The materials science of collagen. J Mech Behav Biomed Mater 52:22–50. https://doi.org/10.1016/j.jmbbm.2015.05.023

96. Naomi R, Ridzuan PM, Bahari H (2021) Current insights into collagen type i. Polymers (Basel) 13:1–19. https://doi.org/10.3390/polym13162642

97. Bou-Gharios G, Abraham D, de Crombrugghe B (2019) Type I collagen structure, synthesis, and regulation. Elsevier Inc.

98. Henriksen K, Karsdal MA (2016) Type I Collagen. Elsevier Inc.

99. Theocharis AD, Skandalis SS, Gialeli C, Karamanos NK (2016) Extracellular matrix structure. Adv Drug Deliv Rev 97:4–27. https://doi.org/10.1016/j.addr.2015.11.001

100. Boraschi-Diaz I, Wang J, Mort JS, Komarova S V. (2017) Collagen type i as a ligand for receptor-mediated signaling. Front Phys 5:1–11. https://doi.org/10.3389/fphy.2017.00012

101. Fratzl P (2003) Cellulose and collagen: From fibres to tissues. Curr Opin Colloid Interface Sci 8:32–39. https://doi.org/10.1016/S1359-0294(03)00011-6

102. Tronci G, Russell SJ, Wood DJ (2013) Photo-active collagen systems with controlled triple helix architecture. J Mater Chem B 1:3705–3715. https://doi.org/10.1039/c3tb20720j

103. Kikuchi M (2013) Hydroxyapatite/Collagen Bone-Like Nanocomposite Masanori. Biol Pharm Bull 36:1666–1669. https://doi.org/https://doi.org/10.1248/bpb.b13-00460

104. Xing F, Chi Z, Yang R, et al (2021) Chitin-hydroxyapatite-collagen composite scaffolds for bone regeneration. Int J Biol Macromol 184:170–180. https://doi.org/10.1016/j.ijbiomac.2021.05.019

105. Song Y, Wu H, Gao Y, et al (2020) Zinc Silicate/Nano-Hydroxyapatite/Collagen Scaffolds Promote Angiogenesis and Bone Regeneration via the p38 MAPK Pathway in Activated Monocytes. ACS Appl Mater Interfaces 12:16058–16075. https://doi.org/10.1021/acsami.0c00470

106. Pighinelli L, Kucharska M (2013) Chitosan-hydroxyapatite composites. Carbohydr Polym 93:256–262. https://doi.org/10.1016/j.carbpol.2012.06.004

107. Rajula MPB, Narayanan V, Venkatasubbu GD, et al (2021) Nano-hydroxyapatite: A Driving Force for Bone Tissue Engineering. J Pharm Bioall Sci. https://doi.org/10.4103/jpbs.JPBS_683_20

108. Radulescu DE, Neacsu IA, Grumezescu AM, Andronescu E (2022) Novel Trends into the Development of Natural Hydroxyapatite-Based Polymeric Composites for Bone Tissue Engineering. Polymers (Basel) 14:. https://doi.org/10.3390/polym14050899

109. Harrison CJ, Hatton P V., Gentile P, Miller CA (2021) Nanoscale strontium-substituted hydroxyapatite pastes and gels for bone tissue regeneration. Nanomaterials 11:. https://doi.org/10.3390/nano11061611

110. Hench LL (1994) Bioactive ceramics. Annals of New York Academy of Sciences 523:54–71. https://doi.org/https://doi.org/10.1111/j.1749-6632.1988.tb38500.x

111. Kasuga T (2005) Bioactive calcium pyrophosphate glasses and glass-ceramics. Acta Biomater 1:55–64. https://doi.org/10.1016/j.actbio.2004.08.001

112. Clark AE, Hench LL, Paschall HA (1976) The influence of surface chemistry on implant interface histology: A theoretical basis for implant materials selection. J Biomed Mater Res 10:161–174. https://doi.org/10.1002/jbm.820100202

113. Välimäki V V., Aro HT (2006) Molecular basis for action of bioactive glasses as bone graft substitute. Scandinavian Journal of Surgery 95:95–102. https://doi.org/10.1177/145749690609500204

114. Thomas M V., Puleo DA, Al-Sabbagh M (2005) Bioactive glass three decades on. J Long Term Eff Med Implants 15:585–597. https://doi.org/10.1615/JLongTermEffMedImplants.v15.i6.20

115. Cao W, Hench LL (1996) Bioactive materials. Ceram Int 22:493–507. https://doi.org/10.1016/0272-8842(95)00126-3

116. Hench LL (2006) The story of Bioglass®. J Mater Sci Mater Med 17:967–978. https://doi.org/10.1007/s10856-006-0432-z

117. Huang W, Day DE, Kittiratanapiboon K, Rahaman MN (2006) Kinetics and mechanisms of the conversion of silicate (45S5), borate, and borosilicate glasses to hydroxyapatite in dilute phosphate solutions. J Mater Sci Mater Med 17:583–596. https://doi.org/10.1007/s10856-006-9220-z

118. Yao A, Wang D, Huang W, et al (2007) In vitro bioactive characteristics of borate-based glasses with controllable degradation behavior. Journal of the American Ceramic Society 90:303–306. https://doi.org/10.1111/j.1551-2916.2006.01358.x

119. Fu Q, Rahaman MN, Fu H, Liu X (2010) Silicate, borosilicate, and borate bioactive glass scaffolds with controllable degradation rate for bone tissue engineering applications. I. Preparation and in vitro degradation. J Biomed Mater Res A 95:164–171. https://doi.org/10.1002/jbm.a.32824

120. Brown RF, Rahaman MN, Dwilewicz AB, et al (2009) Effect of borate glass composition on its conversion to hydroxyapatite and on the

proliferation of MC3T3-E1 cells. J Biomed Mater Res A 88:392–400. https://doi.org/10.1002/jbm.a.31679

121. Uo M, Mizuno M, Kuboki Y, et al (1998) Properties and cytotoxicity of water soluble Na2O-CaO-P2O5 glasses. Biomaterials 19:2277–2284. https://doi.org/10.1016/S0142-9612(98)00136-7

122. Franks K, Abrahams I, Knowles JC (2000) Development of soluble glasses for biomedical use part I: In vitro solubility measurement. J Mater Sci Mater Med 11:609–614. https://doi.org/10.1023/A:1008949527695

123. Salih V, Franks K, James M, et al (2000) Development of soluble glasses for biomedical use part II: The biological response of human osteoblast cell lines to phosphate-based soluble glasses. J Mater Sci Mater Med 11:615–620. https://doi.org/10.1023/A:1008901612674

124. Ahmed I, Lewis M, Olsen I, Knowles JC (2004) Phosphate glasses for tissue engineering: Part 1. Processing and characterisation of a ternary-based P2O5-CaO-Na 2O glass system. Biomaterials 25:491–499. https://doi.org/10.1016/S0142-9612(03)00546-5

125. Ahmed I, Lewis M, Olsen I, Knowles JC (2004) Phosphate glasses for tissue engineering: Part 2. Processing and characterisation of a ternary-based P2O5-CaO-Na 2O glass fibre system. Biomaterials 25:501–507. https://doi.org/10.1016/S0142-9612(03)00547-7

126. Rahaman MN, Day DE, Bal BS, et al (2011) Bioactive glass in tissue engineering. Acta Biomater 7:2355–2373. https://doi.org/10.1016/j.actbio.2011.03.016

127. Aitasalo K, Kinnunen I, Palmgren J, Varpula J (2001) Repair of orbital floor fractures with bioactive glass implants. Journal of Oral and Maxillofacial Surgery 59:1390–1395. https://doi.org/10.1053/joms.2001.27524

128. Suominen E, Kinnunen J (1996) Bioactive glass granules and plates in the reconstruction of defects of the facial bones. Scand J Plast Reconstr Surg Hand Surg 30:281–289. https://doi.org/10.3109/02844319609056406

129. Peltola M, Suonpää J, Aitasalo K, et al (1998) Obliteration of the frontal sinus cavity with bioactive glass. Head Neck 20:315–319.

https://doi.org/10.1002/(SICI)1097-0347(199807)20:4<315::AID-HED6>3.0.CO;2-1

130. Stanley HR, Hall MB, Colaizzi F, Clark AE (1987) Residual alveolar ridge maintenance with a new endosseous implant material. J Prosthet Dent 58:607–613. https://doi.org/10.1016/0022-3913(87)90393-3

131. Turunen T, Peltola J, Yli-Urpo A, Happonen RP (2004) Bioactive glass granules as a bone adjunctive material in maxillary sinus floor augmentation. Clin Oral Implants Res 15:135–141. https://doi.org/10.1111/j.1600-0501.2004.00989.x

132. Lamars E, Sewon L, Luostarinen T, et al (1995) Bioactive glass in periodontal defects. Initial findings of soft tissue and osseous repair. Bioceramics 8:279–284

133. Fu Q, Saiz E, Rahaman MN, Tomsia AP (2011) Bioactive glass scaffolds for bone tissue engineering: State of the art and future perspectives. Materials Science and Engineering C 31:1245–1256. https://doi.org/10.1016/j.msec.2011.04.022

134. Wu L, Zhou C, Zhang B, et al (2020) Construction of Biomimetic Natural Wood Hierarchical Porous-Structure Bioceramic with Micro/Nanowhisker Coating to Modulate Cellular Behavior and Osteoinductive Activity. ACS Appl Mater Interfaces 12:48395–48407. https://doi.org/10.1021/acsami.0c15205

135. larry L. Hench, Julia M. Polak (2002) Third-Generation Biomedical Materials. Science (1979) 295:1014–1017

136. Ducheyne P, Qiu Q (1999) Bioactive ceramics: The effect of surface reactivity on bone formation and bone cell function. Biomaterials 20:2287–2303. https://doi.org/10.1016/S0142-9612(99)00181-7

137. Filgueiras MR, La Torre G, Hench LL (1993) Solution effects on the surface reactions of a bioactive glass. J Biomed Mater Res 27:445–453. https://doi.org/10.1002/jbm.820270405

138. Li P, Ohtsuki C, Kokubo T, et al (1994) The role of hydrated silica, titania, and alumina in inducing apatite on implants. J Biomed Mater Res 28:7–15. https://doi.org/10.1002/jbm.820280103

139. Peitl O, Federal U, Peitl O (1996) Effect of crystallization on apatite-layer formation of bioactive glass 45S5. J Biomed Mater Res 30:509–514

140. Yamauchi M, Yamaguchi T, Kaji H, et al (2005) Involvement of calcium-sensing receptor in osteoblastic differentiation of mouse MC3T3-E1 cells. Am J Physiol Endocrinol Metab 288:608–616. https://doi.org/10.1152/ajpendo.00229.2004

141. Park EK, Lee YE, Choi JY, et al (2004) Cellular biocompatibility and stimulatory effects of calcium metaphosphate on osteoblastic differentiation of human bone marrow-derived stromal cells. Biomaterials 25:3403–3411. https://doi.org/10.1016/j.biomaterials.2003.10.031

142. Bielby RC, Christodoulou IS, Pryce RS, et al (2004) Time- and concentration-dependent effects of dissolution products of 58S sol-gel bioactive glass on proliferation and differentiation of murine and human osteoblasts. Tissue Eng 10:1018–1026. https://doi.org/10.1089/ten.2004.10.1018

143. Zhong JP, Greenspan DC, Feng JW (2002) A microstructural examination of apatite induced by Bioglass® in vitro. J Mater Sci Mater Med 13:321–326. https://doi.org/10.1023/A:1014075320987

144. Wheeler DL, Stokes KE, Hoellrich RG, et al (1999) Effect of bioactive glass particle size on osseous regeneration of cancellous defects. J Biomed Mater Res 46:301–303. https://doi.org/10.1002/(sici)1097-4636(199908)46:2<301::aid-jbm20>3.0.co;2-%23

145. Vallet-Regí M, Salinas AJ, Arcos D (2006) From the bioactive glasses to the star gels. J Mater Sci Mater Med 17:1011–1017. https://doi.org/10.1007/s10856-006-0437-7

146. Kargozar S, Montazerian M, Hamzehlou S, et al (2018) Mesoporous bioactive glasses: Promising platforms for antibacterial strategies

147. Izquierdo-Barba I, Vallet-Regí M (2015) Mesoporous bioactive glasses: Relevance of their porous structure compared to that of classical bioglasses. Biomedical Glasses 1:140–150. https://doi.org/10.1515/bglass-2015-0014

148. Sing KSW, Everett DH, Haul RAW, et al (1985) Reporting physisorption data for gas-solid systems with special reference to the determination of

surface area and porosity (Recommendations 1984). Pure & Appl Chem 57:603–619. https://doi.org/https://doi.org/10.1351/pac198557040603

149. Vallet-Regí M (2010) Nanostructured mesoporous silica matrices in nanomedicine. J Intern Med 267:22–43. https://doi.org/10.1111/j.1365-2796.2009.02190.x

150. Vallet-Regí M (2006) Revisiting ceramics for medical applications. Dalton Transactions 5211–5220. https://doi.org/10.1039/b610219k

151. Raman NK, Anderson MT, Brinker CJ (1996) Template-based approaches to the preparation of amorphous, nanoporous silicas. Chemistry of Materials 8:1682–1701. https://doi.org/10.1021/cm960138+

152. Manzano M, Colilla M, Vallet-Reg M (2009) Drug delivery from ordered mesoporous matrices. Expert Opin Drug Deliv 6:1383–1400. https://doi.org/10.1517/17425240903304024

153. Arcos D, López-Noriega A, Ruiz-Hernández E, et al (2009) Ordered mesoporous microspheres for bone grafting and drug delivery. Chemistry of Materials 21:1000–1009. https://doi.org/10.1021/cm801649z

154. Hoffmann F, Cornelius M, Morell J, Fröba M (2006) Silica-based mesoporous organic-inorganic hybrid materials. Angewandte Chemie - International Edition 45:3216–3251. https://doi.org/10.1002/anie.200503075

155. Li Z, Chen D, Tu B, Zhao D (2007) Synthesis and phase behaviors of bicontinuous cubic mesoporous silica from triblock copolymer mixed anionic surfactant. Microporous and Mesoporous Materials 105:34–40. https://doi.org/10.1016/j.micromeso.2007.05.017

156. Pedone A (2009) Properties calculations of silica-based glasses by atomistic simulations techniques: A review. Journal of Physical Chemistry C 113:20773–20784. https://doi.org/10.1021/jp9071263

157. Tilocca A, Cormack AN (2010) Surface signatures of bioactivity: MD simulations of 45S and 65S silicate glasses. Langmuir 26:545–551. https://doi.org/10.1021/la902548f

158. Tilocca A (2009) Structural models of bioactive glasses from molecular dynamics simulations. Proceedings of the Royal Society A: Mathematical, Physical and Engineering Sciences 465:1003–1027. https://doi.org/10.1098/rspa.2008.0462

159. Mathew R, Turdean-Ionescu C, Stevensson B, et al (2013) Direct probing of the phosphate-ion distribution in bioactive silicate glasses by solid-state NMR: Evidence for transitions between random/clustered scenarios. Chemistry of Materials 25:1877–1885. https://doi.org/10.1021/cm400487a

160. Izquierdo-Barba I, Arcos D, Sakamoto Y, et al (2008) High-performance mesoporous bioceramics mimicking bone mineralization. Chemistry of Materials 20:3191–3198. https://doi.org/10.1021/cm800172x

161. Bose S, Tarafder S, Banerjee SS, et al (2011) Understanding In Vivo Response and Mechanical Property Variation in MgO, SrO and SiO2 doped β-TCP. Bone 48:1282–1290. https://doi.org/10.1016/j.bone.2011.03.685

162. Mouriño V, Cattalini JP, Boccaccini AR (2012) Metallic ions as therapeutic agents in tissue engineering scaffolds: An overview of their biological applications and strategies for new developments. J R Soc Interface 9:401–419. https://doi.org/10.1098/rsif.2011.0611

163. Habibovic P, Barralet JE (2011) Bioinorganics and biomaterials: Bone repair. Acta Biomater 7:3013–3026. https://doi.org/10.1016/j.actbio.2011.03.027

164. Mehrabi T, Mesgar AS, Mohammadi Z (2020) Bioactive Glasses: A Promising Therapeutic Ion Release Strategy for Enhancing Wound Healing. ACS Biomater Sci Eng 6:5399–5430. https://doi.org/10.1021/acsbiomaterials.0c00528

165. Coulombe J, Faure H, Robin B, Ruat M (2004) In vitro effects of strontium ranelate on the extracellular calcium-sensing receptor. Biochem Biophys Res Commun 323:1184–1190. https://doi.org/10.1016/j.bbrc.2004.08.209

166. Brown EM (2003) Is the calcium receptor a molecular target for the actions of strontium on bone? Osteoporos Int 14 Suppl 3:25–34. https://doi.org/10.1007/s00198-002-1343-6

167. Peng S, Liu XS, Zhou G, et al (2011) Osteoprotegerin deficiency attenuates strontium-mediated inhibition of osteoclastogenesis and bone resorption. Journal of Bone and Mineral Research 26:1272–1282. https://doi.org/10.1002/jbmr.325

168. Kostenuik P, Shalhoub victoria (2005) Osteoprotegerin A Physiological and Pharmacological Inhibitor of Bone Resorption. Curr Pharm Des 7:613–635. https://doi.org/10.2174/1381612013397807

169. Huang D, Zhao F, Gao W, et al (2020) Strontium-substituted sub-micron bioactive glasses inhibit ostoclastogenesis through suppression of RANKL-induced signaling pathway. Regen Biomater 7:303–311. https://doi.org/10.1093/rb/rbaa004

170. Zhao F, Lei B, Li X, et al (2018) Promoting in vivo early angiogenesis with sub-micrometer strontium-contained bioactive microspheres through modulating macrophage phenotypes. Biomaterials 178:36–47. https://doi.org/10.1016/j.biomaterials.2018.06.004

171. Li S, Li L, Guo C, et al (2017) A promising wound dressing material with excellent cytocompatibility and proangiogenesis action for wound healing: Strontium loaded Silk fibroin/Sodium alginate (SF/SA) blend films. Int J Biol Macromol 104:969–978. https://doi.org/10.1016/j.ijbiomac.2017.07.020

172. Lee CH, Kim YJ, Jang JH, Park JW (2016) Modulating macrophage polarization with divalent cations in nanostructured titanium implant surfaces. Nanotechnology 27:. https://doi.org/10.1088/0957-4484/27/8/085101

173. Berksoy Hayta S, Durmuş K, Altuntaş EE, et al (2018) The reduction in inflammation and impairment in wound healing by using strontium chloride hexahydrate. Cutan Ocul Toxicol 37:24–28. https://doi.org/10.1080/15569527.2017.1326497

174. Buache E, Velard F, Bauden E, et al (2012) Effect of strontium-substituted biphasic calcium phosphate on inflammatory mediators production by human monocytes. Acta Biomater 8:3113–3119. https://doi.org/10.1016/j.actbio.2012.04.045

175. Xia W, Chang J (2006) Well-ordered mesoporous bioactive glasses (MBG): A promising bioactive drug delivery system. Journal of Controlled Release 110:522–530. https://doi.org/10.1016/j.jconrel.2005.11.002

176. Zhao L, Yan X, Zhou X, et al (2008) Mesoporous bioactive glasses for controlled drug release. Microporous and Mesoporous Materials 109:210–215. https://doi.org/10.1016/j.micromeso.2007.04.041

177. Zhu Y, Kaskel S (2009) Comparison of the in vitro bioactivity and drug release property of mesoporous bioactive glasses (MBGs) and bioactive glasses (BGs) scaffolds. Microporous and Mesoporous Materials 118:176–182. https://doi.org/10.1016/j.micromeso.2008.08.046

178. Vallet-Regí M, Izquierdo-Barba I, Colilla M (2012) Structure and functionalization of mesoporous bioceramics for bone tissue regeneration and local drug delivery. Philosophical Transactions of the Royal Society A: Mathematical, Physical and Engineering Sciences 370:1400–1421. https://doi.org/10.1098/rsta.2011.0258

179. Sun J, Li Y, Li L, et al (2008) Functionalization and bioactivity in vitro of mesoporous bioactive glasses. J Non Cryst Solids 354:3799–3805. https://doi.org/10.1016/j.jnoncrysol.2008.05.001

180. Pereira MM, Jones JR, Orefice RL, Hench LL (2005) Preparation of bioactive glass-polyvinyl alcohol hybrid foams by the sol-gel method. J Mater Sci Mater Med 16:1045–1050

181. Baeza A, Guisasola E, Torres-Pardo A, et al (2014) Hybrid enzyme-polymeric capsules/mesoporous silica nanodevice for in situ cytotoxic agent generation. Adv Funct Mater 24:4625–4633. https://doi.org/10.1002/adfm.201400729

182. Giret S, Wong Chi Man M, Carcel C (2015) Mesoporous-Silica-Functionalized Nanoparticles for Drug Delivery. Chemistry - A European Journal 21:13850–13865. https://doi.org/10.1002/chem.201500578

183. East DA, Mulvihill DP, Todd M, Bruce IJ (2011) QD-antibody conjugates via carbodiimide-mediated coupling: A detailed study of the variables involved and a possible new mechanism for the coupling reaction under

basic aqueous conditions. Langmuir 27:13888–13896. https://doi.org/10.1021/la203273p

184. Rider P, Kačarević ŽP, Alkildani S, et al (2018) Additive manufacturing for guided bone regeneration: A perspective for alveolar ridge augmentation

185. Boga JC, Miguel SP, de Melo-Diogo D, et al (2018) In vitro characterization of 3D printed scaffolds aimed at bone tissue regeneration. Colloids Surf B Biointerfaces 165:207–218. https://doi.org/10.1016/j.colsurfb.2018.02.038

186. Roohani-Esfahani SI, Newman P, Zreiqat H (2016) Design and Fabrication of 3D printed Scaffolds with a Mechanical Strength Comparable to Cortical Bone to Repair Large Bone Defects. Sci Rep 6:1–8. https://doi.org/10.1038/srep19468

187. Vozzi G, Corallo C, Daraio C (2013) Pressure-activated microsyringe composite scaffold of poly(L -lactic acid) and carbon nanotubes for bone tissue engineering. J Appl Polym Sci 129:528–536. https://doi.org/10.1002/app.38235

188. Mazzoli A (2013) Selective laser sintering in biomedical engineering. Med Biol Eng Comput 51:245–256. https://doi.org/10.1007/s11517-012-1001-x

189. Prasad A, Sankar MR, Katiyar V (2017) State of Art on Solvent Casting Particulate Leaching Method for Orthopedic ScaffoldsFabrication. Mater Today Proc 4:898–907. https://doi.org/10.1016/j.matpr.2017.01.101

190. Hutmacher DW (2000) Scaffolds in tissue engineering bone and cartilage. The Biomaterials: Silver Jubilee Compendium 21:175–189. https://doi.org/10.1016/B978-008045154-1.50021-6

191. Akbarzadeh R, Yousefi AM (2014) Effects of processing parameters in thermally induced phase separation technique on porous architecture of scaffolds for bone tissue engineering. J Biomed Mater Res B Appl Biomater 102:1304–1315. https://doi.org/10.1002/jbm.b.33101

192. Zeugolis DI, Khew ST, Yew ESY, et al (2008) Electro-spinning of pure collagen nano-fibres - Just an expensive way to make gelatin? Biomaterials 29:2293–2305. https://doi.org/10.1016/j.biomaterials.2008.02.009

193. Ribeiro N, Sousa SR, Van Blitterswijk CA, et al (2014) A biocomposite of collagen nanofibers and nanohydroxyapatite for bone regeneration. Biofabrication 6:. https://doi.org/10.1088/1758-5082/6/3/035015

194. Braghirolli DI, Steffens D, Pranke P (2014) Electrospinning for regenerative medicine: A review of the main topics. Drug Discov Today 19:743–753. https://doi.org/10.1016/j.drudis.2014.03.024

195. Luraghi A, Peri F, Moroni L (2021) Electrospinning for drug delivery applications: A review. Journal of Controlled Release 334:463–484. https://doi.org/10.1016/j.jconrel.2021.03.033

196. Medeiros GB, Lima F de A, de Almeida DS, et al (2022) Modification and Functionalization of Fibers Formed by Electrospinning: A Review. Membranes (Basel) 12:. https://doi.org/10.3390/membranes12090861

197. Streeter BW, Xue J, Xia Y, Davis ME (2019) Electrospun Nanofiber-Based Patches for the Delivery of Cardiac Progenitor Cells. ACS Appl Mater Interfaces 11:18242–18253. https://doi.org/10.1021/acsami.9b04473

198. Liu W, Thomopoulos S, Xia Y (2012) Electrospun nanofibers for regenerative medicine. Adv Healthc Mater 1:10–25. https://doi.org/10.1002/adhm.201100021

199. Greiner A, Wendorff JH (2007) Electrospinning: A fascinating method for the preparation of ultrathin fibers. Angewandte Chemie - International Edition 46:5670–5703. https://doi.org/10.1002/anie.200604646

200. Wendorff JH, Agarwal S, Greiner A (2012) Electrospinning – Materials, Processing, and Applications

201. Doshi J, Reneker DH (1993) Electrospinning process and applications of electrospun fibers. Conference Record - IAS Annual Meeting (IEEE Industry Applications Society) 3:1698–1703. https://doi.org/10.1109/ias.1993.299067

202. Bazrafshan Z, Stylios GK (2019) Spinnability of collagen as a biomimetic material: A review. Int J Biol Macromol 129:693–705. https://doi.org/10.1016/j.ijbiomac.2019.02.024

203. Blackstone BN, Gallentine SC, Powell HM (2021) Collagen-based electrospun materials for tissue engineering: A systematic review. Bioengineering 8:1–16. https://doi.org/10.3390/bioengineering8030039

204. Stein H, Wilensky M, Tsafrir Y, et al (2009) Production of bioactive, post-translationally modified, heterotrimeric, human recombinant type-I collagen in transgenic tobacco. Biomacromolecules 10:2640–2645. https://doi.org/10.1021/bm900571b

205. Jang JH, Castano O, Kim HW (2009) Electrospun materials as potential platforms for bone tissue engineering. Adv Drug Deliv Rev 61:1065–1083. https://doi.org/10.1016/j.addr.2009.07.008

206. Stanishevsky A, Chowdhury S, Chinoda P, Thomas V (2008) Hydroxyapatite nanoparticle loaded collagen fiber composites: Microarchitecture and nanoindentation study. J Biomed Mater Res A 86:873–882. https://doi.org/10.1002/jbm.a.31657

207. Venugopal J, Low S, Choon AT, et al (2008) Mineralization of osteoblasts with electrospun collagen/hydroxyapatite nanofibers. J Mater Sci Mater Med 19:2039–2046. https://doi.org/10.1007/s10856-007-3289-x

208. Salifu AA, Lekakou C, Labeed FH (2017) Electrospun oriented gelatin-hydroxyapatite fiber scaffolds for bone tissue engineering. J Biomed Mater Res A 105:1911–1926. https://doi.org/10.1002/jbm.a.36058

209. Peng H, Yin Z, Liu H, et al (2012) Electrospun biomimetic scaffold of hydroxyapatite/chitosan supports enhanced osteogenic differentiation of mMSCs. Nanotechnology 23:. https://doi.org/10.1088/0957-4484/23/48/485102

210. Liu H, Peng H, Wu Y, et al (2013) The promotion of bone regeneration by nanofibrous hydroxyapatite/chitosan scaffolds by effects on integrin-BMP/Smad signaling pathway in BMSCs. Biomaterials 34:4404–4417. https://doi.org/10.1016/j.biomaterials.2013.02.048

211. Song JH, Kim HE, Kim HW (2008) Electrospun fibrous web of collagen-apatite precipitated nanocomposite for bone regeneration. J Mater Sci Mater Med 19:2925–2932. https://doi.org/10.1007/s10856-008-3420-7

212. Zhou Y, Yao H, Wang J, et al (2015) Greener synthesis of electrospun collagen/ hydroxyapatite composite fibers with an excellent microstructure for bone tissue engineering. Int J Nanomedicine 10:3203–3215. https://doi.org/10.2147/IJN.S79241

213. Saatchi A, Arani AR, Moghanian A, Mozafari M (2021) Synthesis and characterization of electrospun cerium-doped bioactive glass/chitosan/polyethylene oxide composite scaffolds for tissue engineering applications. Ceram Int 47:260–271. https://doi.org/10.1016/j.ceramint.2020.08.130

214. Talebian S, Mehrali M, Mohan S, et al (2014) Chitosan (PEO)/bioactive glass hybrid nanofibers for bone tissue engineering. RSC Adv 4:49144–49152. https://doi.org/10.1039/c4ra06761d

215. Chen Q, Wu J, Liu Y, et al (2019) Electrospun chitosan/PVA/bioglass Nanofibrous membrane with spatially designed structure for accelerating chronic wound healing. Materials Science and Engineering C 105:110083. https://doi.org/10.1016/j.msec.2019.110083

216. Adamiak K, Sionkowska A (2020) Current methods of collagen cross-linking: Review. Int J Biol Macromol 161:550–560. https://doi.org/10.1016/j.ijbiomac.2020.06.075

217. Jayakrishnan A, Jameela SR (1996) Glutaraldehyde as a fixative in bioprostheses and drug delivery matrices. Biomaterials 17:471–484. https://doi.org/10.1016/0142-9612(96)82721-9

218. Nimni ME, Cheung D, Strates B, et al (1987) Chemically modified collagen: A natural biomaterial for tissue replacement. J Biomed Mater Res 21:741–771. https://doi.org/10.1002/jbm.820210606

219. Dijkstra PJ, Feijen J, Biology C, et al (1995) Crosslinking of dermal sheep collagen using hexamethylene diisocyanate. J Mater Sci Mater Med 6:429–434

220. Cheung DT, Perelman N, Ko EC, Nimni ME (1985) Mechanism of crosslinking of proteins by glutaraldehyde III. Reaction with collagen in tissues. Connect Tissue Res 13:109–115. https://doi.org/10.3109/03008208509152389

221. Fukae R, Midorikawa T (2008) Preparation of Gelatin Fiber by Gel Spinning and Its Mechanical Properties. J Appl Polym Sci 110:4011–4015. https://doi.org/10.1002/app.28969

222. Stoessel PR, Raso RA, Kaufmann T, et al (2015) Fibers mechanically similar to sheep wool obtained by wet spinning of gelatin and optional plasticizers. Macromol Mater Eng 300:234–241. https://doi.org/10.1002/mame.201400240

223. Zhan J, Morsi Y, Ei-Hamshary H, et al (2016) In vitro evaluation of electrospun gelatin–glutaraldehyde nanofibers. Front Mater Sci 10:90–100. https://doi.org/10.1007/s11706-016-0329-9

224. Yang L, Fitié CFC, van der Werf KO, et al (2008) Mechanical properties of single electrospun collagen type I fibers. Biomaterials 29:955–962. https://doi.org/10.1016/j.biomaterials.2007.10.058

225. Takigawa T, Endo Y (2006) Effects of glutaraldehyde exposure on human health. J Occup Health 48:75–87. https://doi.org/10.1539/joh.48.75

226. Wang X, Zhang A, Yan G, et al (2013) Metabolomics and Proteomics Annotate Therapeutic Properties of Geniposide: Targeting and Regulating Multiple Perturbed Pathways. PLoS One 8:. https://doi.org/10.1371/journal.pone.0071403

227. Su G, Cui C, Ren J, et al (2011) Effect of xylose on the molecular and particle size distribution of peanut hydrolysate in Maillard reaction system. J Sci Food Agric 91:2457–2462. https://doi.org/10.1002/jsfa.4487

228. Yan LP, Wang YJ, Ren L, et al (2010) Genipin-cross-linked collagen/chitosan biomimetic scaffolds for articular cartilage tissue engineering applications. J Biomed Mater Res A 95 A:465–475. https://doi.org/10.1002/jbm.a.32869

229. Krishnamoorthy G, Selvakumar R, Sastry TP, et al (2014) Experimental and theoretical studies on Gallic acid assisted EDC/NHS initiated crosslinked collagen scaffolds. Materials Science and Engineering C 43:164–171. https://doi.org/10.1016/j.msec.2014.07.003

230. Ahmad Z, Shepherd JH, Shepherd D V., et al (2015) Effect of 1-ethyl-3-(3-dimethylaminopropyl) carbodiimide and N-hydroxysuccinimide

concentrations on the mechanical and biological characteristics of cross-linked collagen fibres for tendon repair. Regen Biomater 2:77–85. https://doi.org/10.1093/rb/rbv005

231. Pfeifer VF, Sohns VE, Conway HF, et al (1960) Two-Stage Process for Dialdehyde Starch Using Electrolytic Regeneration of Periodic Acid. Ind Eng Chem 52:201–206. https://doi.org/10.1021/ie50603a020

232. Lin W, Mu C, Liu F, et al (2010) Collagen cryogel cross-linked by dialdehyde starch. Macromol Mater Eng 295:100–107. https://doi.org/10.1002/mame.200900292

233. Langmaier F, Mládek M, Mokrejš P, Kolomazník K (2008) Biodegradable packing materials based on waste collagen hydrolysate cured with dialdehyde starch. J Therm Anal Calorim 93:547–552. https://doi.org/10.1007/s10973-007-8293-3

234. Langmaier F, Mládek M, Mokrejš P (2009) Hydrogels of collagen hydrolysate cross-linked with dialdehyde starch. J Therm Anal Calorim 98:807–812. https://doi.org/10.1007/s10973-009-0175-4

235. Rinaudo M (2006) Chitin and chitosan: Properties and applications. Progress in Polymer Science (Oxford) 31:603–632. https://doi.org/10.1016/j.progpolymsci.2006.06.001

236. Aranaz I, Mengibar M, Harris R, et al (2012) Functional Characterization of Chitin and Chitosan. Curr Chem Biol 3:203–230. https://doi.org/10.2174/2212796810903020203

237. Kean T, Thanou M (2010) Biodegradation, biodistribution and toxicity of chitosan. Adv Drug Deliv Rev 62:3–11. https://doi.org/10.1016/j.addr.2009.09.004

238. Arpornmaeklong P, Pripatnanont P, Suwatwirote N (2008) Properties of chitosan-collagen sponges and osteogenic differentiation of rat-bone-marrow stromal cells. Int J Oral Maxillofac Surg 37:357–366. https://doi.org/10.1016/j.ijom.2007.11.014

239. Haugh MG, Jaasma MJ, O'Brien FJ (2009) The effect of dehydrothermal treatment on the mechanical and structural properties of collagen-GAG

scaffolds. J Biomed Mater Res A 89:363–369. https://doi.org/10.1002/jbm.a.31955

240. Lutolf MP, Hubbell JA (2005) Synthetic biomaterials as instructive extracellular microenvironments for morphogenesis in tissue engineering. Nat Biotechnol 23:47–55. https://doi.org/10.1038/nbt1055

241. Weadock KS, Miller EJ, Bellincampi LD, et al (1995) Physical crosslinking of collagen fibers: Comparison of ultraviolet irradiation and dehydrothermal treatment. J Biomed Mater Res 29:1373–1379. https://doi.org/10.1002/jbm.820291108

242. Miles CA, Bailey AJ (2001) Thermally labile domains in the collagen molecule. Micron 32:325–332. https://doi.org/10.1016/S0968-4328(00)00034-2

243. Cooper DR, Davidson RJ (1965) The Effect of Ultraviolet Irradiation on Soluble Collagen. Biochem J 97:139–147

244. Weadock KS, Miller EJ, Keuffel EL, Dunn MG (1996) Effect of physical crosslinking methods on collagen-fiber durability in proteolytic solutions. J Biomed Mater Res 32:221–226. https://doi.org/10.1002/(SICI)1097-4636(199610)32:2<221::AID-JBM11>3.0.CO;2-M

245. Soloshenko IA, Bazhenov VY, Khomich VA, et al (2006) Comparative research of efficiency of water decontamination by UV radiation of cold hollow cathode discharge plasma versus that of low- and medium-pressure mercury lamps. IEEE Transactions on Plasma Science 34:1365–1369. https://doi.org/10.1109/TPS.2006.878997

246. Davidenko N, Bax D V., Schuster CF, et al (2016) Optimisation of UV irradiation as a binding site conserving method for crosslinking collagen-based scaffolds. J Mater Sci Mater Med 27:1–17. https://doi.org/10.1007/s10856-015-5627-8

247. Trackman PC (2005) Diverse biological functions of extracellular collagen processing enzymes. J Cell Biochem 96:927–937. https://doi.org/10.1002/jcb.20605

248. Siegel RC, Pinnell SR, Martin GR (1970) Cross-Linking of Collagen and Elastin. Properties of Lysyl Oxidase. Bioch 9:4486–4492

249. Garcia Y, Collighan R, Griffin M, Pandit A (2007) Assessment of cell viability in a three-dimensional enzymatically cross-linked collagen scaffold. J Mater Sci Mater Med 18:1991–2001. https://doi.org/10.1007/s10856-007-3091-9

250. Davidenko N, Schuster CF, Bax D V., et al (2015) Control of crosslinking for tailoring collagen-based scaffolds stability and mechanics. Acta Biomater 25:131–142. https://doi.org/10.1016/j.actbio.2015.07.034

251. Nair M, Johal RK, Hamaia SW, et al (2020) Tunable bioactivity and mechanics of collagen-based tissue engineering constructs: A comparison of EDC-NHS, genipin and TG2 crosslinkers. Biomaterials 254:120109. https://doi.org/10.1016/j.biomaterials.2020.120109

252. Grabska-Zielinska S, Sionkowska A, Carvalho Â, Monteiro FJ (2021) Biomaterials with Potential Use in Bone Tissue Regeneration—Collagen/Chitosan/Silk Fibroin Scaffolds Cross-Linked by EDC/NHS. Materials. https://doi.org/https:// doi.org/10.3390/ma14051105

253. Nong LM, Zhou D, Zheng D, et al (2019) The effect of different cross-linking conditions of EDC/NHS on type II collagen scaffolds: an in vitro evaluation. Cell Tissue Bank 20:557–568. https://doi.org/10.1007/s10561-019-09790-7

254. Nam K, Kimura T, Kishida A (2008) Controlling coupling reaction of EDC and NHS for preparation of collagen gels using ethanol/water co-solvents. Macromol Biosci 8:32–37. https://doi.org/10.1002/mabi.200700206

255. Hung JH, Lee CN, Hsu HW, et al (2021) Recent advances in photodynamic therapy against fungal keratitis. Pharmaceutics 13:. https://doi.org/10.3390/pharmaceutics13122011

256. Hamblin MR, Abrahamse H (2018) Inorganic salts and antimicrobial photodynamic therapy: Mechanistic conundrums? Molecules 23:1–18. https://doi.org/10.3390/molecules23123190

257. Eckes S, Braun J, Wack JS, et al (2020) Rose bengal crosslinking to stabilize collagen sheets and generate modulated collagen laminates. Int J Mol Sci 21:1–18. https://doi.org/10.3390/ijms21197408

258. Chan BP, So KF (2005) Photochemical crosslinking improves the physicochemical properties of collagen scaffolds. J Biomed Mater Res A 75:689–701. https://doi.org/10.1002/jbm.a.30469

259. Fiorilli S, Pagani M, Boggio E, et al (2021) Sr-containing mesoporous bioactive glasses bio-functionalized with recombinant ICOS-Fc: An in vitro study. Nanomaterials 11:1–23. https://doi.org/10.3390/nano11020321

260. Wu C, Chang J, Fan W (2012) Bioactive mesoporous calcium-silicate nanoparticles with excellent mineralization ability, osteostimulation, drug-delivery and antibacterial properties for filling apex roots of teeth. J Mater Chem 22:16801–16809. https://doi.org/10.1039/c2jm33387b

261. Pontiroli L, Dadkhah M, Novajra G, et al (2017) An aerosol-spray-assisted approach to produce mesoporous bioactive glass microspheres under mild acidic aqueous conditions. Mater Lett 190:111–114. https://doi.org/10.1016/j.matlet.2016.12.125

262. Zhuravlev LT (1993) Surface characterization of amorphous silica-a review of work from the former USSR. Colloids Surf A Physicochem Eng Asp 74:71–90. https://doi.org/10.1016/0927-7757(93)80399-Y

263. Pontremoli C, Izquierdo-Barba I, Montalbano G, et al (2020) Strontium-releasing mesoporous bioactive glasses with anti-adhesive zwitterionic surface as advanced biomaterials for bone tissue regeneration. J Colloid Interface Sci 563:92–103. https://doi.org/10.1016/j.jcis.2019.12.047

264. Yuan P, Southon PD, Liu Z, et al (2008) Functionalization of halloysite clay nanotubes by grafting with γ-aminopropyltriethoxysilane. Journal of Physical Chemistry C 112:15742–15751. https://doi.org/10.1021/jp805657t

265. Vergaro V, Abdullayev E, Lvov Y, et al (2010) Cytocompatibility and uptake of polycations-modified halloysite clay nanotubes. Biomacromolecules 11:820–826. https://doi.org/10.1016/j.clay.2018.12.016

266. Wang X, Liu Y, Wang S, et al (2015) CD44-engineered mesoporous silica nanoparticles for overcoming multidrug resistance in breast cancer. Appl Surf Sci 332:308–317. https://doi.org/10.1016/j.apsusc.2015.01.204

267. Bhardwaj N, Kundu SC (2010) Electrospinning: A fascinating fiber fabrication technique. Biotechnol Adv 28:325–347. https://doi.org/10.1016/j.biotechadv.2010.01.004

268. Cychosz KA, Guillet-Nicolas R, García-Martínez J, Thommes M (2017) Recent advances in the textural characterization of hierarchically structured nanoporous materials. Chem Soc Rev 46:389–414. https://doi.org/10.1039/c6cs00391e

269. Condon JB (2006) An Overview of Physisorption. Surface Area and Porosity Determinations by Physisorption 1–27. https://doi.org/10.1016/b978-044451964-1/50003-0

270. Thommes M, Kaneko K, Neimark A V., et al (2015) Physisorption of gases, with special reference to the evaluation of surface area and pore size distribution (IUPAC Technical Report). Pure and Applied Chemistry 87:1051–1069. https://doi.org/10.1515/pac-2014-1117

271. Boffito M, Gioffredi E, Chiono V, et al (2016) Novel polyurethane-based thermosensitive hydrogels as drug release and tissue engineering platforms: Design and in vitro characterization. Polym Int 65:756–769. https://doi.org/10.1002/pi.5080

272. Ismail AA, van de Voort FR, Sedman J (1997) Fourier transform infrared spectroscopy: Principles and applications. Techniques and Instrumentation in Analytical Chemistry 18:93–139. https://doi.org/10.1016/S0167-9244(97)80013-3

273. Whittig LD, Allardice WR (2018) X-ray diffraction techniques. Methods of Soil Analysis, Part 1: Physical and Mineralogical Methods 9:331–362. https://doi.org/10.2136/sssabookser5.1.2ed.c12

274. Shi M, Chen Z, Farnaghi S, et al (2016) Copper-doped mesoporous silica nanospheres, a promising immunomodulatory agent for inducing osteogenesis. Acta Biomater 30:334–344. https://doi.org/10.1016/j.actbio.2015.11.033

275. Maçon ALB, Kim TB, Valliant EM, et al (2015) A unified in vitro evaluation for apatite-forming ability of bioactive glasses and their variants.

J Mater Sci Mater Med 26:1–10. https://doi.org/10.1007/s10856-015-5403-9

276. Reen DJ (1994) Enzyme-Linked Immunosorbent Assay (ELISA). Walker JM (eds) Basic Protein and Peptide Protocols Methods in Molecular Biology™ 32:461–466

277. Chen HC (2005) Boyden chamber assay. Methods Mol Biol 294:15–22. https://doi.org/10.1385/1-59259-860-9:015

278. Ballanti P, Minisola S, Pacitti MT, et al (1997) Tartrate-resistant acid phosphate activity as osteoclastic marker: Sensitivity of cytochemical assessment and serum assay in comparison with standardized osteoclast histomorphometry. Osteoporosis International 7:39–43. https://doi.org/10.1007/BF01623458

279. Blumer MJF, Hausott B, Schwarzer C, et al (2012) Role of tartrate-resistant acid phosphatase (TRAP) in long bone development. Mech Dev 129:162–176. https://doi.org/10.1016/j.mod.2012.04.003

280. Tronci G, Russell SJ, Wood DJ (2013) Photo-active collagen systems with controlled triple helix architecture. J Mater Chem B 1:3705–3715. https://doi.org/10.1039/c3tb20720j

281. Davidenko N, Schuster CF, Bax D V., et al (2015) Control of crosslinking for tailoring collagen-based scaffolds stability and mechanics. Acta Biomater 25:131–142. https://doi.org/10.1016/j.actbio.2015.07.034

282. El-Fiqi A, Kim TH, Kim M, et al (2012) Capacity of mesoporous bioactive glass nanoparticles to deliver therapeutic molecules. Nanoscale 4:7475–7488. https://doi.org/10.1039/c2nr31775c

283. Taghvaei AH, Danaeifar F, Gammer C, et al (2020) Synthesis and characterization of novel mesoporous strontium-modified bioactive glass nanospheres for bone tissue engineering applications. Elsevier Inc.

284. Saidak Z, Marie PJ (2012) Strontium signaling: Molecular mechanisms and therapeutic implications in osteoporosis. Pharmacol Ther 136:216–226. https://doi.org/10.1016/j.pharmthera.2012.07.009

285. Kermani F, Beidokhti SM, Baino F, et al (2020) Strontium- and Cobalt-Doped Multicomponent Mesoporous Bioactive Glasses (MBGs) for Potential Use in Bone Tissue Engineering Applications. Materials 13:1–20

286. Wu C, Fan W, Gelinsky M, et al (2011) Bioactive SrO-SiO2 glass with well-ordered mesopores: Characterization, physiochemistry and biological properties. Acta Biomater 7:1797–1806. https://doi.org/10.1016/j.actbio.2010.12.018

287. Arepalli SK, Tripathi H, Hira SK, et al (2016) Enhanced bioactivity, biocompatibility and mechanical behavior of strontium substituted bioactive glasses. Materials Science and Engineering C 69:108–116. https://doi.org/10.1016/j.msec.2016.06.070

288. Taherkhani S, Moztarzadeh F (2016) Influence of strontium on the structure and biological properties of sol–gel-derived mesoporous bioactive glass (MBG) powder. J Solgel Sci Technol 78:539–549. https://doi.org/10.1007/s10971-016-3995-2

289. Zhu Y, Wu C, Ramaswamy Y, et al (2008) Preparation, characterization and in vitro bioactivity of mesoporous bioactive glasses (MBGs) scaffolds for bone tissue engineering. Microporous and Mesoporous Materials 112:494–503. https://doi.org/10.1016/j.micromeso.2007.10.029

290. Yan X, Huang X, Yu C, et al (2006) The in-vitro bioactivity of mesoporous bioactive glasses. Biomaterials 27:3396–3403. https://doi.org/10.1016/j.biomaterials.2006.01.043

291. Hu Q, Chen X, Zhao N, Li Y (2013) Facile synthesis and in vitro bioactivity of monodispersed mesoporous bioactive glass sub-micron spheres. Mater Lett 106:452–455. https://doi.org/10.1016/j.matlet.2013.04.075

292. Shih CJ, Chen HT, Huang LF, et al (2010) Synthesis and in vitro bioactivity of mesoporous bioactive glass scaffolds. Materials Science and Engineering C 30:657–663. https://doi.org/10.1016/j.msec.2010.02.006

293. Hu Q, Jiang W, Chen X, et al (2017) The effects of Sr concentration on physicochemical properties, bioactivity and biocompatibility of sub-micron

bioactive glasses spheres. Advanced Powder Technology 28:2713–2722. https://doi.org/10.1016/j.apt.2017.07.024

294. Moghanian A, Firoozi S, Tahriri M (2017) Characterization, in vitro bioactivity and biological studies of sol-gel synthesized SrO substituted 58S bioactive glass. Ceram Int 43:14880–14890. https://doi.org/10.1016/j.ceramint.2017.08.004

295. Du J, Xiang Y (2012) Effect of strontium substitution on the structure, ionic diffusion and dynamic properties of 45S5 Bioactive glasses. J Non Cryst Solids 358:1059–1071. https://doi.org/10.1016/j.jnoncrysol.2011.12.114

296. Hong W, Zhang Q, Jin H, et al (2020) Roles of strontium and hierarchy structure on the in vitro biological response and drug release mechanism of the strontium-substituted bioactive glass microspheres. Materials Science and Engineering C 107:110336. https://doi.org/10.1016/j.msec.2019.110336

297. Phetnin R, Rattanachan ST (2015) Preparation and antibacterial property on silver incorporated mesoporous bioactive glass microspheres. J Solgel Sci Technol 75:279–290. https://doi.org/10.1007/s10971-015-3697-1

298. Wu C, Chang J, Xiao Y (2011) Mesoporous bioactive glasses as drug delivery and bone tissue regeneration platforms. Ther Deliv 2:1189–1198. https://doi.org/10.4155/tde.11.84

299. Pontremoli C, Izquierdo-Barba I, Montalbano G, et al (2020) Strontium-releasing mesoporous bioactive glasses with anti-adhesive zwitterionic surface as advanced biomaterials for bone tissue regeneration. J Colloid Interface Sci 563:92–103. https://doi.org/10.1016/j.jcis.2019.12.047

300. Encinas N, Angulo M, Astorga C, et al (2019) Mixed-charge pseudo-zwitterionic mesoporous silica nanoparticles with low-fouling and reduced cell uptake properties. Acta Biomater 84:317–327. https://doi.org/10.1016/j.actbio.2018.12.012

301. Hoffmann F, Cornelius M, Morell J, Fröba M (2006) Silica-based mesoporous organic-inorganic hybrid materials. Angewandte Chemie -

International Edition 45:3216–3251. https://doi.org/10.1002/anie.200503075

302. Encinas N, Angulo M, Astorga C, et al (2019) Mixed-charge pseudo-zwitterionic mesoporous silica nanoparticles with low-fouling and reduced cell uptake properties. 84:317–327. https://doi.org/10.1016/j.actbio.2018.12.012

303. Occhipinti S, Dianzani C, Chiocchetti A, et al (2013) Triggering of B7h by the ICOS Modulates Maturation and Migration of Monocyte-Derived Dendritic Cells. The Journal of Immunology 190:1125–1134. https://doi.org/10.4049/jimmunol.1201816

304. Dianzani C, Minelli R, Gigliotti CL, et al (2014) B7h Triggering Inhibits the Migration of Tumor Cell Lines. The Journal of Immunology 192:4921–4931. https://doi.org/10.4049/jimmunol.1300587

305. Lee NK (2010) Molecular Understanding of Osteoclast Differentiation and Physiology. Endocrinology and Metabolism 25:264. https://doi.org/10.3803/enm.2010.25.4.264

306. Midha S, Kim TB, Van Den Bergh W, et al (2013) Preconditioned 70S30C bioactive glass foams promote osteogenesis in vivo. Acta Biomater 9:9169–9182. https://doi.org/10.1016/j.actbio.2013.07.014

307. Zhang J, Zhao S, Zhu Y, et al (2014) Three-dimensional printing of strontium-containing mesoporous bioactive glass scaffolds for bone regeneration. Acta Biomater 10:2269–2281. https://doi.org/10.1016/j.actbio.2014.01.001

308. Fiorilli S, Molino G, Pontremoli C, et al (2018) The incorporation of strontium to improve bone-regeneration ability of mesoporous bioactive glasses. Materials 11:678. https://doi.org/10.3390/ma11050678

309. Fiorani A, Gualandi C, Panseri S, et al (2014) Comparative performance of collagen nanofibers electrospun from different solvents and stabilized by different crosslinkers. J Mater Sci Mater Med 25:2313–2321. https://doi.org/10.1007/s10856-014-5196-2

310. Dong B, Arnoult O, Smith ME, Wnek GE (2009) Electrospinning of collagen nanofiber scaffolds from benign solvents. Macromol Rapid Commun 30:539–542. https://doi.org/10.1002/marc.200800634

311. Ming-Che W, Pins GD, Silver FH (1994) Collagen fibres with improved strength for the repair of soft tissue injuries. Biomaterials 15:507–512. https://doi.org/10.1016/0142-9612(94)90016-7

312. Matthews JA, Wnek GE, Simpson DG, Bowlin GL (2002) Electrospinning of collagen nanofibers. Biomacromolecules 3:232–238. https://doi.org/10.1021/bm015533u

313. Telemeco TA, Ayres C, Bowlin GL, et al (2005) Regulation of cellular infiltration into tissue engineering scaffolds composed of submicron diameter fibrils produced by electrospinning. Acta Biomater 1:377–385. https://doi.org/10.1016/j.actbio.2005.04.006

314. Jiang Q, Reddy N, Zhang S, et al (2013) Water-stable electrospun collagen fibers from a non-toxic solvent and crosslinking system. J Biomed Mater Res A 101 A:1237–1247. https://doi.org/10.1002/jbm.a.34422

315. Silva ZS, Botta SB, Ana PA, et al (2015) Effect of papain-based gel on type I collagen - spectroscopy applied for microstructural analysis. Sci Rep 5:1–7. https://doi.org/10.1038/srep11448

316. Jackson SD, Kelly GJ, Lennon D (2000) FTIR studies of the adsorption of acetic acid on silicas.pdf. React Kinet Catal Lett 70:207–212

317. Sobieski BJ, Noda I, Rabolt JF, Chase DB (2017) Observation of Intermolecular Hydrogen Bonding Interactions in Biosynthesized and Biodegradable Poly [(R)-3-hydroxybutyrate-co-(R)-3-hydroxyhexanoate] in Chloroform and 1,1,1,3,3,3-Hexafluoro-2-propanol (HFIP). Appl Spectrosc 71:2339–2343. https://doi.org/10.1177/0003702817702154

318. Stani C, Vaccari L, Mitri E, Birarda G (2020) FTIR investigation of the secondary structure of type I collagen: New insight into the amide III band. Spectrochim Acta A Mol Biomol Spectrosc 229:118006. https://doi.org/10.1016/j.saa.2019.118006

319. Inanc S, Keles D, Oktay G (2017) An improved collagen zymography approach for evaluating the collagenases MMP-1, MMP-8, and MMP-13. Biotechniques 63:174–180. https://doi.org/10.2144/000114597

320. Fong H, Chun I, Reneker DH (1999) Beaded nanofibers formed during electrospinning. Polymer (Guildf) 40:4585–4592. https://doi.org/https://doi.org/10.1016/S0032-3861(99)00068-3

321. Ushiki T (2002) Collagen fibers, reticular fibers and elastic fibers. A comprehensive understanding from a morphological viewpoint. Arch Histol Cytol 65:109–126

322. Robb B, Lennox B (2011) The electrospinning process, conditions and control. Electrospinning for Tissue Regeneration 51–66. https://doi.org/10.1533/9780857092915.1.51

323. Redmond RW, Kochevar IE (2019) Medical Applications of Rose Bengal- and Riboflavin-Photosensitized Protein Crosslinking. Photochem Photobiol 95:1097–1115. https://doi.org/10.1111/php.13126

324. Schiffman JD, Schauer CL (2008) A review: Electrospinning of biopolymer nanofibers and their applications. Polymer Reviews 48:317–352. https://doi.org/10.1080/15583720802022182

325. Nair AK, Gautieri A, Chang SW, Buehler MJ (2013) Molecular mechanics of mineralized collagen fibrils in bone. Nat Commun 4:1724–1729. https://doi.org/10.1038/ncomms2720

326. Kuttappan S, Mathew D, Nair MB (2016) Biomimetic composite scaffolds containing bioceramics and collagen/gelatin for bone tissue engineering - A mini review. Int J Biol Macromol 93:1390–1401. https://doi.org/10.1016/j.ijbiomac.2016.06.043